Semiconductors, Vol. 37, No. 1, 2003, pp. 1–5. Translated from Fizika i Tekhnika Poluprovodnikov, Vol. 37, No. 1, 2003, pp. 3–7.

ATOMIC STRUCTURE AND NONELECTRONIC PROPERTIES OF SEMICONDUCTORS

Multifrequency Kinks in Multifrequency External Fields

M. E. Polyakov

Lykov Institute of Mass and Heat Exchange, Belarussian Academy of Sciences, Minsk, 220072 Belarus

Submitted March 25, 2002; accepted for publication March 29, 2002

Abstract—Two-dimensional analytical equations for multifrequency kink groups were derived and solved from general principles and without simplifications for any given amplitude of multifrequency forces. Kink motion was analyzed. © *2003 MAIK "Nauka/Interperiodica".*

1. INTRODUCTION

Currently, interest in topological defects is increasing [1]. Their properties are controlled by the interfacial state of matter after violation of symmetry. In this paper, we consider a kink, whose classical example is the kink at a dislocation with a Peierls-type shape of the barrier [2], as a topological defect. It is now considered established that the motion of dislocations in GaAs-type semiconductors with a high Peierls barrier is controlled by the kink formation rate and motion velocity [3–5].

A two-dimensional (2D) static nonlinear equation of the kink for a quadratic sinusoidal barrier was derived, solved, and analyzed in [3–8]. The kink profile, which depends on an external action, was studied in the moving frame of reference. An external effect exceeding the linear tension of a kink at a pole causes the kink to rupture (a catastrophe). When writing the boundary conditions, the translational symmetry of the barrier profiles was taken into account: the y coordinates of the kink ends were displaced by equal distances. A soliton discontinuity was also detected in the external force field in the case of the one-dimensional (1D) dislocation model [9]. A 2D equation of kink motion was derived from general principles and without simplifications for any amplitude of external force [10, 11]. An analytical solution was found. Expressions for the longitudinal and transverse components of the kink velocities were determined.

Nonlinear 2D equations of motion for a group of multifrequency kinks in a stationary external field were derived, analytically solved, and analyzed in [12]. A single-phase quadratic sinusoidal barrier with different barrier amplitudes for dissimilar kinks and with the barrier amplitude varying with frequency was used. Analytical expressions for the longitudinal and transverse velocity components of the (x, y) segments of the (p–x)th kinks were derived, as were the velocity ratios and the condition for velocity equality for two arbitrary kinks. In the absence of an external force, the transverse and longitudinal velocities of the (x, y) segments of the (p–x)th kinks are nonzero and have quite definite values that depend on the minimum energies of kinks, kink masses, and maximum barrier energies. Typical current studies of kinks are based on 1D monatomic chains [9, 13, 14].

In this study, nonlinear 2D equations of motion of a group of multifrequency kinks in external multifrequency fields were derived, solved, and analyzed. A single-period quadratic sinusoidal barrier with different heights for dissimilar kinks (with the barrier height varied with frequency) was used. Analytical expressions were determined for longitudinal and transverse velocity components of the (x, y) segments of the (p–x)th kinks, which were characterized by frequencies of natural oscillations of the barrier height and the frequency shifts of the kink ends from relief valleys.

2. BASIC EQUATION

Let a 2D barrier $G(r)$ be described by the square-law sinusoidal function with the period a,

$$G(r) = \left\{ G_0(r) + [G_{mp}(r) - G_0(r)] \sin^2 \frac{\pi y}{a} \right\} \times (1 + \sin^2 q), \quad (1)$$

where $G_0(r)$ and $G_{mp}(r)$ are the minimum and maximum barrier energies, respectively; $p = 1, 2, 3,\ldots$ are the barrier indices; $\omega_p t_p + \varphi_p = q$ is the phase of natural oscillations of the pth barrier height (hereinafter, the subscript p is omitted, including other parameters); ω_p is the frequency of natural oscillations of the pth barrier amplitude; t_p is the period of natural oscillations of the pth barrier amplitude; φ_p is the initial phase of natural oscillations of the pth barrier amplitude; $r = (x, y, p, q)$; and x and y are orthogonal coordinates. The barrier energies remain unchanged along the x axis. The maximum heights $G_{mp}(r)$ depend only on the coordinate y. The coefficient $h_p > 0$ at $\sin^2 q$ is temporarily omitted. The dislocation at the valley bottom has an energy; therefore, $G_0(r)$ is generally nonzero.

The kinks are arranged so that their ends located at $x = \pm\infty$, in which case $dy/dx = 0$ at $x = +\infty$, are displaced from the valleys $y = 0, a, 2a, \ldots, (p-1)a$, where $p = 1, 2, 3, \ldots$, by $y_0\sin^2 g_1, y_1\sin^2 g_2, y_2\sin^2 g_3, \ldots$, and $y_{p-1}\sin^2 g_p$ for the 1, 2, 3,…, pth kinks, respectively, whereas the second kink ends at $x = -\infty$ are displaced from the valleys $y = a, 2a, 3a, \ldots, pa$ by $(y_0 + a)\sin^2 g_1$, $(y_1 + a)\sin^2 g_2$, $(y_2 + a)\sin^2 g_3$, …, and $(y_{p-1} + a)\sin^2 g_p$ for 1, 2, 3, …, pth kinks, respectively, $(0 \le y_{p-1}\sin^2 g_p \le a/2)$ in the case of identical maximum barrier heights; $(\theta_p t_{pq} + \phi_p) = g_p$ is the phase of forced oscillations of the $(p–x)$th kink ends; θ_p is the frequency of forced oscillations of the pth kink ends; t_{pq} is the period of forced oscillations of the pth kink ends; and ϕ_p is the initial phase of forced oscillations of the pth kink ends.

In principle, it is unnecessary to specify the phase of forced oscillations g_p of the second kink end in a fixed frame of reference. This is the case when the (x, y) segments of the pth kink jump from the pth kink to the neighboring $(p + 1)$ barrier into a pole point with a y coordinate at the jump instant in the rupture region. These segments are characterized by an energy equal to the (x, y) segment energy at the pole point at the pth barrier. Then, they are displaced to the pth valley bottom with the release of energy (dynamic catastrophe) [3–5]. The kink segment jump is similar to quicksand transport from a moving plowshare in a plowed field furrow or a shepherd lash accompanied by a bang.

Linear tensions of the $(p–x)$th kinks control the potential energies of the kink segments with natural-oscillation frequencies ω_p, natural-oscillation periods t_p, and initial phases φ_p at each point of the $(p–x)$th kink profiles. These energies are equal to the energies of the $(p–x)$ barriers characterized by the same natural-oscillation frequencies ω_p, natural-oscillation periods t_p, and initial natural-oscillation phases φ_p at the same points (dressing model). To analyze the processes in various time intervals, one should use different designations for forced and natural oscillations.

The kink profiles are controlled by the minimum energies of the kinks, while the external forces acting on the kink ends are equal to the barrier responses at corresponding points. It is obvious that the external action frequency cannot exceed the rate of response of the kink profile to the external perturbation. A natural kink differs from a model kink in that almost the entire width of the active region of the kink is within a narrow length range and only the insignificant remaining part of the width corresponds to almost passive infinity. For the $(p–x)$th kink natural-oscillation phases q at the points of the $(p–x)$th kink-end shifts of $y_{p-1}\sin^2 g_p$ at $x = +\infty$ from the valleys $y = 0, a, 2a, \ldots, (p–1)a$, the $(p–x)$th of kink oscillation energies controlled by the natural-oscillation phases q of the barrier energies at the same points are given by

$$G(x, p, q, g) = \left\{ G_0(r, g) + [G_{mp}(r, g) - G_0(r, g)] \times \sin^2 \frac{\pi y_{p-1}\sin^2 g_p}{a} \right\}(1 + \sin^2 q). \quad (2)$$

To derive the basic equations, the energy conservation conditions are written for the case when the sum of the potential and kinetic energies of the kink segment is equal to the doubled potential energy at each kink point. In a nonconservative system, the potential energy transferred to the kink is converted to kink kinetic energy and then dissipated. At each point of the (x, y) profiles of the $(p–x)$th kinks with certain natural-oscillation phases q and forced oscillation phases g_p of the kink ends, the condition for equal kinetic and potential energies of the unit lengths of the kink segments, when the $(p–x)$th kink ends begin to arrange at the pth barrier at points x and $y_{p-1}\sin^2 g_p$, is written as

$$G_{g(p)}(r)\left[1 + \left(\frac{dy}{dx}\right)^2_{g(p)}(p, q)\right]^{1/2} = M\left[\left(\frac{dy}{dt}\right)^2_{g(p)}(p, q) + \left(\frac{dx}{dt}\right)^2_{g(p)}(p, q)\right], \quad (3)$$

where M is the rest half-mass of the unit lengths of the kink (x, y) segments, $(dy/dt)_{g(p)}(p, q)$; and $(dx/dt)_{g(p)}(p, q)$ are, respectively, the transverse and longitudinal velocities of the (x, y) segments of the pth kink with a certain phase q of natural oscillations and phase g_p of forced kink-end oscillations. The condition for the zero sum of the potential and kinetic energies was also used in [15] when deriving the sine-Gordon equation to study the dislocation dynamics in a 1D approximation.

3. DISCUSSION

Since the potential energy of the (x, y) segment of the pth kink at a point near any point (x, y) at a certain phase q of natural oscillations and phase g_p of kink-end forced oscillations is conventionally written as (see [3–5])

$$G_{g(p)}(r)\left[1 + \left(\frac{dy}{dx}\right)^2_{g(p)}(p, q)\right]^{1/2},$$

where the terms $G_{g(p)}(r)$, expressing the energy of the (x, y) segment of the pth kink with the same phase q of natural oscillations and phase g_p of forced oscillations

of kink ends at points near the points $y_{p-1}\sin^2 g_p$, can be written in a similar way; i.e.,

$$G_{g(p)}(r) = G(x, y_{p-1}\sin^2 g_p, p, q) \times \left[1 + \left(\frac{dy}{dx}\right)^2_{g(p)}(p, q)\right]^{1/2}. \quad (4)$$

Substituting expressions (4) into Eqs. (3), we arrive at

$$G(x, y_{p-1}\sin^2 g_p, p, q) = M\left(\frac{dx}{dt}\right)^2_{g(p)}(p, q).$$

The expression for the longitudinal velocities $(dx/dt)_{g(p)}(p, q)$ of the (x, y) segments of the pth kink, having a natural-oscillation phase q and a forced-oscillation phase g_p of the kink ends, takes on the form

$$\left(\frac{dx}{dt}\right)_{g(p)}(p, q) = [G(x, y_{p-1}\sin^2 g_p, p, q)M^{-1}]^{1/2}$$

or

$$\left(\frac{dx}{dt}\right)_{g(p)}(p, q) = \left\{\left[G_0(r) + [G_{mp}(r) - G_0(r)] \times \sin^2\frac{\pi(y_{p-1}\sin^2 g_p)}{a}\right](1 + \sin^2 q)M^{-1}\right\}^{1/2}.$$

We now consider a particular case of the barrier energy profile $G(r)$,

$$G(r) = \left\{G_0(r) + [(pG_{m1})(r) - G_0(r)]\sin^2\frac{\pi y}{a}\right\} \times (1 + \sin^2 q).$$

In this case, the kink-end energies $G(x, y_{p-1}\sin^2 g_p, p, q)$ at points $(x, y_{p-1}\sin^2 g_p)$ with certain natural-oscillation phases q of the (x, y) segments of the $(p–x)$th kinks take on the form

$$G(x, y_{p-1}\sin^2 g_p, p, q) = \left\{G_0(r) + [(pG_{m1})(r) - G_0(r)] \times \left[\sin^2\frac{\pi(y_{p-1}\sin^2 g_p)}{a}\right]\right\}(1 + \sin^2 q),$$

and the longitudinal velocities of the (x, y) segments of the $(p–x)$th kinks for the natural-oscillation phases q and the phases g_p of forced oscillations of the kink ends can be written as

$$\left(\frac{dx}{dt}\right)_{g(p)}(p, q) = \left\{\left[G_0(r) + [pG_{m1}(r) - G_0(r)] \times \sin^2\frac{\pi(y_{p-1}\sin^2 g_p)}{a}\right](1 + \sin^2 q)M^{-1}\right\}^{1/2}. \quad (5)$$

As follows from expressions (5), the longitudinal velocities of the (x, y) segments of the $(p–x)$th kinks for the natural-oscillation phases q of the barrier heights increase under external action up to $y_p \longrightarrow y_{p-1}\sin^2 g_p$ ($y_p = y_{p-1}\sin^2 g_p$ are the singularity points) at certain pG_{m1}, G_0, and M, as well as with pG_{m1} and G_0/M when y_p remains unchanged. At constant values $y_{p-1}\sin^2 g_p$, the longitudinal velocities of the (x, y) segments of the $(p–x)$th kinks increase with the barrier heights pG_{m1} or with the barrier energies caused by changes in the phases q of natural oscillations of the barrier heights. In this case, the longitudinal velocities of the (x, y) segments of the $(p–x)$th kinks are proportional to the square root of the change in the maximum barrier heights pG_{m1}, as well as to the sinusoidal variation in the phases q. This conclusion is consistent with the experimental data on the linear dependence of the velocity of 60° and screw dislocations on the stress in high-purity crystals in the entire stress range studied [16]. In the absence of external displacement, in the case of a nonzero minimum linear tension, the longitudinal velocities of the (x, y) segments of the $(p–x)$th kinks are identical (nonzero) and depend on the sinusoidal variation of the natural-oscillation phases q of the barrier heights. Therefore, the velocities are varied (the motion is alternatively accelerated or decelerated) and independent of the maximum barrier heights (a new method for stabilizing the kink velocities) but depend on the ratio G_0/M,

$$\frac{dx}{dt}(p, q)\Big|_{g_p = 0} = \left(\frac{G_0}{M}[1 + h_p\sin^2(\omega_p t_p + \varphi_p)]\right)^{1/2}.$$

The instantaneous velocities of the (x, y) segments of the $(p–x)$th kinks increase in the course of the $(p–x)$th barrier-energy increase caused by a change of the natural-oscillation phases q of the barrier heights, whereas a decrease in the instantaneous velocities of the $(p–x)$th kinks is expected in the course of the $(p–x)$th barrier-energy decrease caused by the same change of the natural-oscillation phases q. However, when the sign in the expressions of the natural-oscillation phases of the barrier energies is reversed $(1 – \sin^2 q)$ the phase dependence of the velocity also becomes opposite.

The ratios of the longitudinal velocities of the (x, y) segments of the $(p + 1)$th and pth kinks characterized, respectively, by the velocities $(dx/dt)_{p+1}$ and $(dx/dt)_p$, maximum barrier energies $(p + 1)G_{m1}$ and pG_{m1}, natu-

ral-oscillation phases $q_{(p+1)}$ and q_p, and the phases $g_{(p+1)}$ and g_p of forced oscillations of the kink ends are written as

$$\frac{(dx/dt)_{p+1,q(p+1),g(p+1)}}{(dx/dt)_{p,q,g}} = \left\{\left(G_0[r(p+1)] + [(p+1)G_{m1}[r(p+1)] - G_0[r(p+1)]]\right.\right.$$
$$\times \sin^2\frac{\pi(y_p \sin^2 g_{p+1})}{a}\Big)(1+\sin^2 q_{(p+1)})/(G_0[r(p)] + [pG_{m1}[r(p)] - G_0[r(p)]]$$
$$\left.\left.\times \sin\frac{\pi(y_{p-1}\sin^2 g_p)}{a}\Big)(1+\sin^2 q)\right\}^{1/2}.$$

As follows from these expressions, the instantaneous velocities are higher for the kink which is characterized by either a higher maximum barrier, a stronger external action caused by the frequency field, or a higher barrier energy controlled by the natural-oscillation phase of the barrier height.

We emphasize that, although the (p–x)th kink profiles are arranged in two neighboring barriers with their origin at the pth barrier and their end at the (p + 1)th barrier, the profile of each pth kink is in fact located at the pth barrier and jumps to the (p + 1)th barrier only with a subsequent displacement to the bottom of the pth valley. Therefore, when deriving the kink profiles from the conditions for the minimization of their energy, it is possible to proceed from the identical translational symmetry of the (p–x)th barrier energy profiles for a certain pth kink with the maximum barrier amplitudes pG_{m1} for the pth kink [3–5]. In fact, only the relaxation segments of the (p–x) kink profiles, determined from the condition for kink energy minimization at the (p + 1)th barrier and revealed when the profiles are fixed at poles in the absence of external force, are arranged at the ((p + 1)–x)th barriers with maximum heights (p + 1)G_{m1} different from the maximum heights pG_{m1} of the (p–x)th barriers [3–5].

The transverse velocities $(dy/dt)_{g(p)}(p, q)$ of the (x, y) segments of the (p–x)th kinks at certain natural-oscillation phases q of linear tensions and kink-end shifts $y_{p-1}\sin^2 g_p$ are written as

$$\left(\frac{dy}{dt}\right)_{g(p)}(p,q) = \left(\frac{dy}{dx}\right)_{g(p)}(p,q)\left(\frac{dx}{dt}\right)_{g(p)}(p,q),$$

where $(dx/dt)_{g(p)}(p, q)$ are the longitudinal velocities of the (x, y) segments of the (p–x)th kinks characterized by the natural-oscillation phases q of linear tensions and the phases g_p of forced oscillations of the kink ends. The tilts $(dy/dx)g_p(p, q)$ of the (x, y) segments of the (p–x)th kinks for the natural-oscillation phases q and the phases g_p of forced oscillations of the kink ends are determined from expressions for the minimum energies of the kinks. If the barrier profile energies $G(r)$ change only along the y axis, which is defined by formulas (1) and by the kink energies $G(x, p, q, g_p)$ at points (x, p, q, g_p) according to expression (2), the energies $U_{g(p)}(p, q)$ of the (x, y) segments of the (p–x)th kinks characterized by the natural-oscillation phases q and the phases g_p of forced oscillations of the kink ends are given by

$$U_{g(p)}(p,q) = \int_{-\infty}^{+\infty} G_{g(p)}(r)\left[1+\left(\frac{dy}{dx}\right)^2_{g(p)}(p,q)\right]^{1/2} dx.$$

These energies can be minimized using the Euler equations

$$\frac{d}{dx}\left(f_{g(p)}(p,q) - \frac{\partial y}{\partial x}\frac{\partial f_{g(p)}(p,q)}{\partial(dy/dx)}\right) = 0,$$

from which the relations

$$f_{g(p)}(p,q) = G_{g(p)}(r)\left[1+\left(\frac{dy}{dx}\right)^2_{g(p)}(p,q)\right]^{1/2}$$

follow if

$$G_{g(p)}(r) = C_{0g(p)}(p,q)\left[1+\left(\frac{dy}{dx}\right)^2_{g(p)}(p,q)\right]^{1/2}. \quad (6)$$

The constants $G_{0g(p)}(p, q)$ are determined from the conditions $(dy/dx)_{g(p)}(p, q) = 0$ at $y = y_{p-1}\sin^2 g_p$, $x = +\infty$ as

$$G_{0g(p)}(p,q) = G(x, y_{p-1}\sin^2 g_p, p, q).$$

Relations (6) yield expressions for the tilts of the (x, y) segments of the (p–x)th kinks with certain natural-oscillation phases q of linear tensions and the phases g_p of forced oscillations of the kink ends,

$$\left(\frac{dy}{dx}\right)_{g(p)}(p,q) = \frac{[G^2_{g(p)}(r) - G^2(x, y_{p-1}\sin^2 g_p, p, q)]^{1/2}}{G(x, y_{p-1}\sin^2 g_p, p, q)}.$$

The formulas for the transverse velocities of the (x, y) segments of the (p–x)th kinks take on the form

$$\left(\frac{dy}{dt}\right)_{g(p)}(p,q) = \left[\frac{G^2_{g(p)}(r) - G^2(x, y_{p-1}\sin^2 g_p, p, q)}{MG(x, y_{p-1}\sin^2 g_p, p, q)}\right]^{1/2}\left(\frac{dx}{dt}\right)_{g(p)}(p,q).$$

In the particular case of the absence of displacement at $g_p = 0$ and $G_{mp} = pG_{m1}$, the transverse velocities of the (x, y) segments of the (p–x)th kinks characterized by the natural-oscillation phases q and the phases g_p of

forced oscillations are given by the nonzero expressions

$$\left(\frac{dy}{dt}\right)(p, q)\Big|_{g_p = 0}$$

$$= \left\{\left(\frac{[[pG_{m1}(r) - G_0(r)]\sin^2(\pi y/a)]^2}{MG_0(r)}\right.\right.$$

$$\left.\left. + \frac{2G_0(r)[pG_{m1}(1) - G_0(r)]\sin^2(\pi y/a)}{MG_0(r)}\right)\right.$$

$$\left.\times(1 + \sin^2 q)\right\}^{1/2} \frac{dx}{dt}(p, q, g_p = 0).$$

Specifying certain points (x, y) at the barrier surfaces, phases g_p of forced oscillations of the kink ends, and kink natural-oscillation phases q, we can determine the velocities of the (x, y) segments of the $(p–x)$th kinks for these kink points, since the shapes of the $(p–x)$th barriers characterized by the natural-oscillation phases q and the forced-oscillation phases g_p of the kink ends necessarily define the kink profiles according to the minimum kink energies.

4. CONCLUSION

Thus, in the case of multifrequency external forces g_p acting on the $(p–x)$th kink ends characterized by natural-oscillation phases of linear tensions, nonlinear equations of the kink group motion were derived for single-period quadratic sinusoidal barriers with different barrier heights in the transverse kink motion direction. Analytical expressions were derived for the longitudinal and transverse velocity components of the (x, y) segments of the $(p–x)$th kinks characterized by natural-oscillation phases q and frequency-dependent shifts of the kink ends. The ratios of the velocities of two arbitrary kinks were determined as well. In the absence of an external force, the transverse and longitudinal velocities of the (x, y) segments of the $(p–x)$th kinks are nonzero and are characterized by certain values which depend on the minimum kink energies (if these are nonzero), the kink masses M, and the barrier heights caused by the natural-oscillation phases of the barrier heights.

ACKNOWLEDGMENTS

I am grateful to A.G. Khatkevich and A.B. Gavrilovich for their fruitful participation in discussions.

REFERENCES

1. B. É. Meĭerovich, Usp. Fiz. Nauk **171**, 1033 (2001) [Phys. Usp. **44**, 981 (2001)].
2. J. P. Hirth and J. Lothe, *Theory of Dislocations* (McGraw-Hill, New York, 1967; Atomizdat, Moscow, 1972).
3. M. E. Polyakov, Preprint No. 387 (Stepanov Institute of Physics, Minsk, 1985).
4. M. E. Polyakov, Preprint No. 414 (Stepanov Institute of Physics, Minsk, 1986).
5. M. E. Polyakov, Phys. Status Solidi B **153**, 479 (1989).
6. M. E. Polyakov, Preprint No. 611 (Stepanov Institute of Physics, Minsk, 1990).
7. M. E. Polyakov, Acta Crystallogr. A **49**, 202 (1993).
8. M. E. Polyakov, Inst. Phys. Conf. Ser. **157**, 91 (1997).
9. A. Milchev and G. M. Mazzuchelli, Phys. Rev. B **38**, 2808 (1988).
10. M. E. Polyakov, in *Proceedings of International Scientific and Technical Workshop "Noise and Degradation Processes in Semiconductor Devices"* (Mosk. Énerg. Inst., Moscow, 1999), p. 163.
11. M. E. Polyakov, in *Proceedings of International Scientific and Technical Workshop "Noise and Degradation Processes in Semiconductor Devices"* (Mosk. Énerg. Inst., Moscow, 2000), p. 94.
12. M. E. Polyakov, in *Proceedings of XXXI International Scientific and Methodological Workshop "Noise and Degradation Processes in Semiconductor Devices"* (Mosk. Énerg. Inst., Moscow, 2001), p. 280.
13. O. V. Usatenko, A. V. Gorbach, and A. S. Kovalev, Fiz. Tverd. Tela (St. Petersburg) **43**, 1202 (2001) [Phys. Solid State **43**, 1247 (2001)].
14. A. S. Malishevskiĭ, V. P. Silin, and S. A. Uryupin, Fiz. Tverd. Tela (St. Petersburg) **43**, 3 (2001) [Phys. Solid State **43**, 1 (2001)].
15. A. S. Davydov, *Solitons in Molecular Systems* (Naukova Dumka, Kiev, 1988; Kluwer, Dordrecht, 1991).
16. M. Imai and K. Sumino, Philos. Mag. A **47**, 599 (1983).

Translated by A. Kazantsev

Semiconductors, Vol. 37, No. 1, 2003, pp. 103–107. Translated from Fizika i Tekhnika Poluprovodnikov, Vol. 37, No. 1, 2003, pp. 104–109.

AMORPHOUS, VITREOUS, AND POROUS SEMICONDUCTORS

The Influence of Hydrogen Plasma on the Electroreflectance Spectrum and the Spectrum of Electron States of Porous Silicon

E. F. Venger, R. Yu. Holiney*, L. A. Matveeva, and A. V. Vasin**

Institute of Semiconductor Physics, National Academy of Sciences of Ukraine, Kiev, 03028 Ukraine

**e-mail: holiney@isp.kiev.ua*

***e-mail: matveeva@isp.kiev.ua*

Submitted April 26, 2002; accepted for publication May 15, 2002

Abstract—Porous Si samples were investigated by the electroreflectance modulation spectroscopy. The presence of minibands, which are responsible for the existence of photoluminescence bands (red, green, and blue), is revealed. It is established that the miniband responsible for the blue band vanishes upon the treatment of a porous Si surface in H^+ plasma. Passivation of the surface with hydrogen also leads to strain relaxation both in porous films and in the Si substrate. The origin of electron states in the band gap of Si nanocrystallites is established. *© 2003 MAIK "Nauka/Interperiodica".*

1. INTRODUCTION

The optical properties of porous and nanocrystalline Si-based light-emitting structures have attracted particular interest from researchers [1]. Porous Si samples kept in air most often constitute nanocomposites composed of nanodimensional Si crystallites in an environment of the SiO_x oxide phase [2]. Such structures are characterized by red photoluminescence (PL) at room temperature [3]. However, blue and green PL bands have also been observed for porous Si [3–6].

For porous Si samples unexposed to air (unoxidized), the PL peak energy depends on the nanocrystallite size, owing to the quantum-confinement effect [6–10]. Due to this effect, the edge energy of indirect absorption in Si (1.14 eV) increases with decreasing nanocrystallite size [1, 6–10]. The band gap can become as wide as 2.9 eV [11]. However, as was demonstrated previously [10, 12], the indirect type of the fundamental absorption edge for Si remains.

It is known [2, 6, 13] that both the intensity and energy position of a PL peak also depend on the surface treatment. A slow-varying PL constituent (red band) is attributed to electronic states which are related to Si=O double bonds for a nanocrystallite size less than 3 nm [6, 14]. Rapid PL components for oxidized porous Si samples are attributed to defects localized at the interface between nanocrystalline Si⟩ and SiO_2 [4] or to band-to-band recombination in Si nanocrystallites [15].

Hydrogen-containing complexes, for example, polysilanes and siloxenes, or hydride bonds can be centers of radiative recombination [16, 17]. However, the exposure of porous Si samples to air leads to a decrease in the concentration of Si–H bonds and to an increase in the content of hydride and oxygen-containing complexes [13, 18]. As a result of passivation of the surface by hydrogen, the concentration of nonradiative-recombination-centers decreases and the PL intensity in the red spectral region increases [17, 19]. Theoretical calculations demonstrate [6] that H-containing complexes do not form levels in the band gap of Si nanocrystallites.

The dispersion of an imaginary part of a dielectric function calculated from transmission and absorption spectra for a porous nanocrystalline Si layer has singularities in the green and blue spectral regions [20]. Modulation spectroscopy of electroreflectance is a method which is sensitive to van Hove singularities in the energy spectrum [21, 22]. It was demonstrated that this method is also applicable to porous Si [5, 23–26].

The existence of a direct transition in the red–orange spectral region (1.7–2.0 eV) has been established [5, 26] using the method of electroreflectance modulation spectroscopy. For this reason, the electroreflectance method can also be used for investigations in the green and blue spectral regions, where PL bands are observed. The purpose of this study is to establish the influence of H-containing complexes on the energy spectrum of porous nanocrystalline Si using treatment in H^+plasma.

2. EXPERIMENTAL

Porous Si samples were obtained by electrochemical etching and stain etching. All of the samples were exposed to air for one year. Porous layers were obtained on KDB-10 (B-doped *p*-Si with a resistivity of 10 Ω cm) Si(100) substrates via the electrochemical method in an HF(20%)–C_3H_7OH (1 : 1) solution with an etching cur-

1063-7826/03/3701-0103$24.00 © 2003 MAIK "Nauka/Interperiodica"

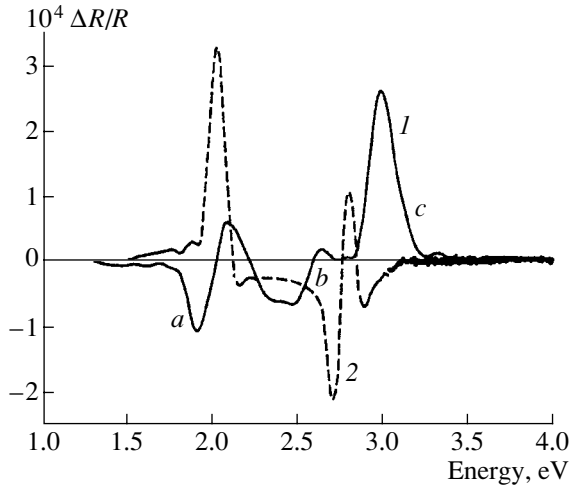

Fig. 1. Electroreflectance spectra for porous Si obtained by electrochemical etching: (*1*) prior to H^+-plasma treatment and (*2*) after treatment. *a*, *b*, and *c* denote the transitions.

rent density of 5 mA/cm^2 [27]. Other porous Si samples were obtained by stain etching. The KDB-10 Si(100) substrate was treated with the laser beam of an Nd^{3+}:YAG laser, with an emission wavelength λ = 1.06 μm and pulse duration of 125 μs, in order to generate defect regions in the substrate [25, 28]. The Si substrate was then treated in an HNO_3 : HF (3 : 1) etchant for 5 s to remove native oxide from the substrate surface. To form a porous structure, the wafer was treated in an HNO_3 : HF : H_2O (3 : 1 : 5) solution for 5 min [25, 28]. The samples were treated in dc glow-discharge H^+ plasma at a pressure of 10 Pa for 6 min at a discharge voltage of 600 V and current density of 1 mA/cm^2. The samples were placed onto a flat cathode, which allowed for their intense bombardment by positively charged H^+ ions from the plasma.

The electroreflectance spectra were measured using the standard electrolytic method at room temperature [21, 22] in a wide spectral region from 1.5 to 3.8 eV. An 0.1 N KCl solution was used as the electrolyte. The modulating voltage did not exceed 1 V, which corresponded to the weak-field measurement mode. The direct-transition energy (E_g) and phenomenological broadening parameter (Γ) were calculated for a bypolar spectrum by the three-point Aspnes method [21, 29] and for a unipolar spectrum from the peak value and half-width at half-height of the line, respectively.

3. RESULTS

The electroreflectance spectra for a porous Si sample obtained by electrochemical etching are shown in Fig. 1. In the spectral region at 3.4 eV no direct transitions, specifically the Γ_{25}–Γ_{15} transition, which is characteristic of bulk crystalline Si, were observed. Three direct transitions were observed for a starting sample in the spectral range of 1.7–3.0 eV: 1.95–2.0 eV (*a* region), 2.5–2.7 eV (*b* region), and at 3.0 eV (*c* region). After the treatment of a sample in the H^+ plasma (curve *2*), transitions in the red (*a*) and green (*b*) spectral regions shifted to shorter wavelengths by 0.07 and 0.24 eV, respectively. The electroreflectance spectrum changed its polarity sign to the opposite one in the red spectral region and was not detected in the blue region (*c*). The transition energies and phenomenological broadening parameters that were calculated from curves *1* and *2* in Fig. 1 are given in the table. Since the type of the critical points for transitions in the red, green, and blue spectral regions is unknown, the data for two-dimen-

Transition energies and phenomenological broadening parameters calculated from the electroreflectance spectra

Spectrum	Spectral region	Polarity	Transition energy E_g, eV		Broadening parameter Γ, meV	
			2D	3D	2D	3D
Fig. 1, curve *1*	a	–	1.95	1.95	200	170
	b	–	2.48	2.49	160	135
	c	Unipolar (+)	2.99		175	
Fig. 1, curve *2* (H^+-plasma)	a	Unipolar (+)	2.02		100	
	b	–	2.72	2.73	110	95
Fig. 2, curve *1*	–	–	3.33		131	
Fig. 2, curve *2* (H^+-plasma)	–	Unipolar (+)	3.39		110	
Fig. 3, curve *1*	a	Unipolar (–)	1.92		70	
	b	–	2.34	2.34	100	85
	c	Unipolar (–)	2.84		100	
Fig. 3, curve *2* (H^+-plasma)	a	Unipolar (–)	1.89		80	
	b	–	2.34	2.34	110	95

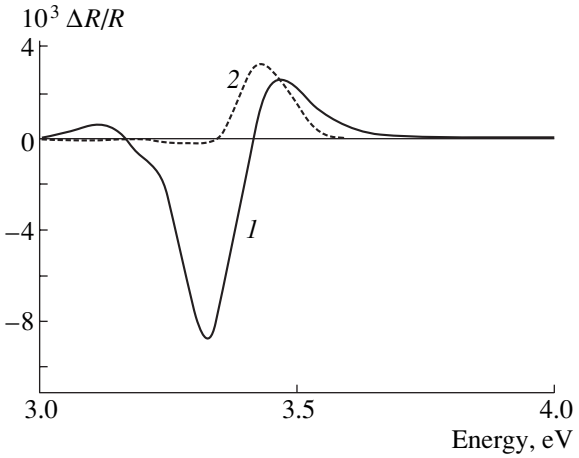

Fig. 2. Spectra of electroreflectance from the Si substrate under the porous layer obtained by stain etching (*1*) prior to H^+-plasma treatment and (*2*) after treatment.

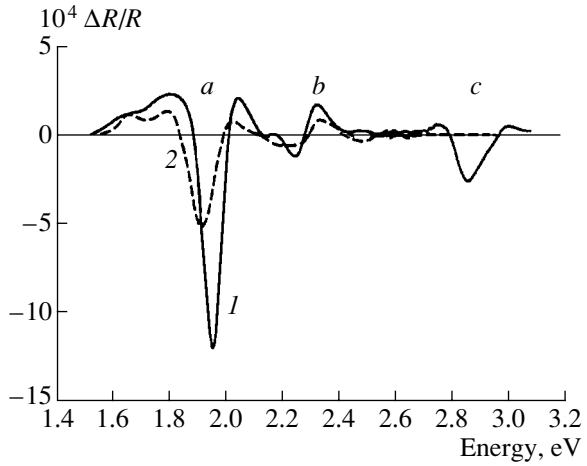

Fig. 3. Influence of hydrogen on the electroreflectance spectra of porous Si obtained by stain etching: (*1*) prior to H^+-plasma treatment and (*2*) after treatment.

sional (2D) and three-dimensional (3D) cases are given in the table for spectra with different polarities.

A transition at the center of the Brillouin zone Γ_{25}–Γ_{15} was observed in the electroreflectance spectra for a sample obtained by stain etching (Fig. 2, curve *1*). The spectrum changed its shape to a unipolar one (Fig. 2, curve *2*) after sample treatment in the H^+ plasma, and the transition energy (E_g) increased (see table).

For the samples obtained by stain etching, three direct transitions were also detected in the spectral region of 1.5–3.0 eV (Fig. 3, curve *1*) as was the case for the samples obtained by electrochemical etching. The signal intensity for this spectral region was an order of magnitude lower than that of the region at 3.4 eV in Fig. 2. After H passivation of the porous Si surface (Fig. 3, curve *2*), the transition energies and phenomenological broadening parameters remained almost unchanged (see table). An electroreflectance spectrum in the blue spectral region was also not detected after treatment of a sample surface with H^+ plasma (Fig. 3), which is similar to the case of electrochemically etched Si (Fig. 1).

4. DISCUSSION

A direct transition in the spectral region at 3.4 eV was detected only for samples prepared by stain etching (Fig. 2) and was not detected for samples prepared by electrochemical etching (Fig. 1). We may assume that the pore depth and porosity itself are lower at stain etching than at electrochemical etching. Since the thickness of the porous layer is not very large in the case of stain etching, we may argue that the electroreflectance spectrum, which is shown in Fig. 2, is related to the interface between a porous layer and Si substrate. Correspondingly, the electroreflectance signal for a sample obtained by electrochemical etching is detected only from the porous layer without participation of the substrate. It was demonstrated that the dispersion of the index of refraction for the porous layer that was removed from the Si substrate had no peak in the spectral region at 3.4 eV. This is in agreement with measurements of porous Si obtained by various methods.

A unipolar electroreflectance spectrum is characteristic of intrinsic semiconductors [30, 31]. Electron-enriched surface regions of the heterojunction between crystalline Si and oxidized nanocrystalline Si were observed (in samples obtained by stain etching) [26]. The shape of the electroreflectance signal in Fig. 2 (curve *1*) corresponds to an inversion of the surface conductivity of the *p*-Si substrate. After treatment in H^+ plasma, the spectrum becomes unipolar (Fig. 2, curve *2*), which corresponds to intrinsic surface conductivity (*i*-type) [26, 31]. A decrease in the enrichment of surface regions with electrons is caused by the H passivation of positively charged bonds (Si–F, Si–OH) on the surface of the porous layer. It is these bonds that give rise to the negative sign of the surface charge [26].

The transition energy in the unstressed Si crystalline substrate was calculated from the electroreflectance spectra and was found to be 3.38 eV [32, 33]. The transition energy in the Si substrate under the porous layer obtained by stain etching (Fig. 2, curve *1*) is equal to 3.33 eV (see table). The transition shift to lower energies (from 3.38 to 3.33 eV) is indicative of biaxial compression stresses in the Si substrate [34]. After treatment of the sample in H^+ plasma, the direct-transition energy changed to 3.39 eV (see table), which is indicative of relaxation of compressive stresses in the Si substrate [34]. The stresses are relieved due to the H passivation of defects at the interfaces between the oxide, porous nanocrystalline layer, and crystalline Si.

The energy of direct transitions in the red spectral region remained almost unchanged (see table) upon the

H passivation of the surface of a porous Si sample obtained by stain etching (Fig. 3). For an electrochemically etched sample, the transition energy in the red spectral region varied slightly; specifically, it shifted to higher energies (from 1.95 to 2.02 eV). A similar shift was observed for the direct transition in the green spectral region (Fig. 1): from 2.48 to 2.72 eV. The shift sign was the same as for the spectrum related to the Si substrate (Fig. 2).

Variation in the energies of direct transitions upon H passivation of the surface can be associated with the relaxation of stresses in the porous film itself (composite of Si nanocrystals within the SiO_x matrix). Since the thickness of a porous film after stain etching is very small, H passivates mainly the defects at the interface between crystalline silicon and the porous layer. Because of this circumstance, no variation in the energy of direct transitions is observed for this sample (Fig. 3).

The detected direct transition in the blue spectral region (at 3 eV) vanishes after H passivation of the surface (Figs. 1, 3). According to data on IR absorption [18, 35], a band peaked at 3400 cm^{-1} (0.42 eV) is observed for porous Si samples oxidized in air. This band is attributed to Si–OH bonds. Upon passivation with hydrogen, the following reaction proceeds:

$$\text{Si–OH} + \text{H}^+ = \text{Si}^+ + \text{H}_2\text{O}. \quad (1)$$

Let us assume that Si–OH bonds give rise to a miniband in the Si band gap and that this miniband is spaced at 0.42 eV from the valence band and, consequently, at 2.96 eV from the conduction band. Summation of these values yields the transition energy at the center of the Brillouin zone between the points Γ_{25} and Γ_{15} (3.38 eV). The transition energy determined from the electroreflectance spectra yields a value of 2.99 or 2.84 eV for various samples in the blue region (see table). Upon H passivation of the surface due to treatment with H^+ plasma, the Si–OH complex decomposes into pure Si and H_2O, according to formula (1). In this case, the miniband vanishes; this is detected in the electroreflectance spectra of plasma-treated samples.

It is known that Si=O bonds give rise to a miniband in the band gap of nanocrystalline Si. The energy of this miniband is close to 1.7 eV [6], whereas the transition energy, according to our measurements, is ~1.9 eV. An Si=O double bond does not require high strain energies or a large number of O or Si atoms since this bond is most stable at the interface between nanocrystalline Si and an oxide film [6]. Thus, stress relaxation in the porous film upon its passivation with hydrogen does not profoundly affect the direct transition in the red spectral region (Fig. 1).

At the same time, the transition in the green spectral region shifts to higher energies by 0.22 eV. Such a large shift can be observed for a miniband which is induced by less stable O–Si bonds on the surface of Si nanocrystals. However, these should be relatively stable bonds, since the direct transition does not vanish upon passivation with hydrogen, in contrast to what is observed in the blue spectral range (Figs. 1, 3). Such bonds can be Si–(SiO_3) bonds. It is known that the transition energy for an amorphous SiO_x film depends on x [36]. The transition energy of ~2.4–2.7 eV corresponds to $x \approx 1.25$–1.5 [36]. Using previous data [37], we can determine the approximate composition of the bonds in percent for the amorphous SiO_x film at $x = 1.5$: ~31.6% Si–(O_4), ~42% Si–(SiO_3), ~21% Si–(Si_2O_2), ~5% Si–(Si_3O), and ~0.3% Si–(Si_4). From these results, it follows that the Si–(SiO_3) bonds are the most numerous in amorphous SiO_x film at $x = 1.5$. The Si–(Si_2O_2) bonds (21%) can also give rise to a miniband which is spaced at 2.4–2.7 eV from the conduction band. To ascertain the character of the O–Si bond which gives rise to a miniband at the energy of ~2.4 eV, it is necessary to carry out additional measurements or theoretical calculations. The surface Si=O, Si–(SiO_3), and Si–OH bonds can give rise to minibands in the band gap of Si nanocrystallite, the only proviso being that an electron be localized at these levels and that they, in turn, form a superlattice-like spatial structure.

The phenomenological broadening parameter is inversely proportional to the relaxation time of electron energy ($\Gamma \propto 1/\tau_e$). Since the broadening parameters for bipolar and unipolar spectra were calculated by different methods, it is inappropriate to carry out a comparative analysis of these spectra. We can only state that the parameter Γ was almost the same prior to and after H passivation of the surface of a sample obtained by stain etching (see table). This confirms once again that, due to the small thickness of the porous layer, H passivates the defects at the interface between the crystalline substrate and the porous layer during plasma treatment.

The phenomenological broadening parameter for the transition in the green spectral region (Fig. 1, curve *1*) for an electrochemically etched sample was rather large and decreased after passivation with hydrogen from 135–160 meV to 95–110 meV (see table). The H passivation of defects leads to the following: electrons are less scattered by defects, Γ decreases, and the structure becomes closer to a perfect one.

5. CONCLUSION

The electroreflectance spectra of porous samples obtained by electrochemical or stain etching and the influence of H treatment on these samples were investigated. Based on the results of investigation, the energy spectrum of porous Si was ascertained. It was experimentally demonstrated that the following minibands, which manifest themselves in optical spectra, exist in the band gap of the Si nanocrystal:

(i) A miniband at 1.9 eV (red–orange PL band). According to Wolkin *et al.* [6], this miniband can be related to a double Si=O bond.

(ii) A miniband in the green spectral region (2.4–2.7 eV). This miniband can be induced by Si–(SiO_3) or

Si–(Si_2O_2) bonds. The accurate determination of the origin of this miniband is the subject of further investigations.

(iii) A miniband at 2.9 eV (blue PL region). This miniband is related to Si–OH bonds and is spaced by 0.42 eV from the valence band.

The H passivation of a porous Si surface by plasma treatment leads to the relaxation of compression stresses in porous films and in Si substrate. Scattering of charge carriers decreases, and the miniband which is caused by the presence of Si–OH bonds on the Si nanocrystallite surface vanishes.

REFERENCES

1. S. V. Sveshnikov, A. V. Sachenko, G. A. Sukach, *et al.*, Optoélektron. Poluprovodn. Tekh. **27**, 3 (1994).
2. A. V. Sachenko, É. B. Kaganovich, É. G. Manoĭlov, and S. V. Svechnikov, Fiz. Tekh. Poluprovodn. (St. Petersburg) **35** (12), 1445 (2001) [Semiconductors **35**, 1383 (2001)].
3. L. T. Canham, Appl. Phys. Lett. **57**, 1046 (1990).
4. A. J. Kontkiewicz, A. M. Kontkiewicz, J. Siejka, *et al.*, Appl. Phys. Lett. **65** (11), 1436 (1994).
5. R. Yu. Holiney, L. A. Matveeva, and E. F. Venger, in *Abstract Book of Frontiers in Molecular-Scale Science and Technology of Fullerene, Nanotube, Nanosilicon and Biopolymer (DNA, Protein) Multifunctional Nanosystem, Kiev, 2001*, p. SC-P4.
6. M. V. Wolkin, J. Jorne, P. M. Fauchet, *et al.*, Phys. Rev. Lett. **82** (1), 197 (1999).
7. M. S. Bresler and I. N. Yassievich, Fiz. Tekh. Poluprovodn. (St. Petersburg) **27** (5), 873 (1993) [Semiconductors **27**, 475 (1993)].
8. R. T. Collins, P. M. Fauchet, and M. A. Tischler, Phys. Today **50** (1), 24 (1997).
9. G. D. Sanders and Yia-Chung Chang, Appl. Phys. Lett. **60** (20), 2525 (1992).
10. M. Ben-Chorin, B. Averboukh, D. Kovalev, *et al.*, Phys. Rev. Lett. **77** (4), 763 (1996).
11. P. H. Hao, X. Y. Hou, F. L. Zang, and X. Wang, Appl. Phys. Lett. **64** (26), 3602 (1994).
12. X. L. Wu, S. J. Xiong, D. L. Fan, *et al.*, Phys. Rev. B **62** (12), R7759 (2000).
13. P. K. Kashkarov, E. A. Konstantinova, and V. Yu. Timoshenko, Fiz. Tekh. Poluprovodn. (St. Petersburg) **30** (8), 1479 (1996) [Semiconductors **30**, 778 (1996)].
14. Y. Kanemitsu, T. Ogawa, K. Shiraishi, and K. Takeda, Phys. Rev. B **48** (7), 4883 (1993).
15. X. Zhao, O. Schoenfeld, S. Nomura, *et al.*, Mater. Sci. Eng. B **35**, 467 (1995).
16. P. Gupta, A. C. Dilon, A. S. Bracker, and S. M. George, Surf. Sci. **245**, 360 (1991).
17. S. M. Prokes, O. J. Glembocki, and V. M. Bermudes, Phys. Rev. B **45** (23), 13788 (1992).
18. A. A. Kopylov and A. N. Kholodilov, Fiz. Tekh. Poluprovodn. (St. Petersburg) **31** (5), 556 (1997) [Semiconductors **31**, 470 (1997)].
19. Y. Takeda and H. N. Suzuki, J. Appl. Phys. **73** (4), 1924 (1993).
20. M. I. Strashnikova, V. L. Voznyĭ, V. Ya. Reznichenko, and V. Ya. Gaĭvoronskiĭ, Zh. Éksp. Teor. Fiz. **120** (2), 409 (2001) [JETP **93**, 363 (2001)].
21. D. E. Aspnes, Surf. Sci. **37**, 417 (1973).
22. V. Ya. Tyagaĭ and O. V. Snitko, *Electroreflection of Light in Semiconductors* (Naukova Dumka, Kiev, 1980), p. 304.
23. E. F. Venger, T. Ya. Gorbach, L. A. Matveeva, *et al.*, Zh. Éksp. Teor. Fiz. **116**, 1750 (1999) [JETP **89**, 948 (1999)].
24. R. Yu. Holiney, L. A. Matveeva, E. F. Venger, *et al.*, Appl. Surf. Sci. **172**, 214 (2001).
25. R. Yu. Holiney, L. L. Fedorenko, L. A. Matveeva, *et al.*, J. Phys. D **33**, 2875 (2000).
26. E. F. Venger, R. Yu. Golineĭ, and L. A. Matveeva, Optoélektron. Poluprovodn. Tekh. **36**, 199 (2001).
27. V. Lehmann and H. Foll, J. Electrochem. Soc. **137** (2), 653 (1990).
28. L. L. Fedorenko, A. D. Sardary, É. B. Kaganovich, *et al.*, Fiz. Tekh. Poluprovodn. (St. Petersburg) **31** (1), 6 (1997) [Semiconductors **31**, 4 (1997)].
29. D. E. Aspnes and J. E. Rowe, Phys. Rev. Lett. **27** (4), 188 (1971).
30. N. P. Garbar, L. A. Matveeva, V. F. Mitin, *et al.*, Fiz. Tekh. Poluprovodn. (Leningrad) **21** (3), 393 (1987) [Sov. Phys. Semicond. **21**, 245 (1987)].
31. R. Yu. Holiney, A. Szekeres, L. A. Matveeva, *et al.*, in *Proceedings of 11th International School on Condensed Matter Physics: Materials for Information Technology in the New Millennium, Varna, 2000*, p. 240.
32. R. Yu. Holiney, L. A. Matveeva, and E. F. Venger, Semicond. Phys. Quantum Electron. Optoelectron. **2** (4), 10 (1999).
33. V. I. Gavrilenko, V. A. Zuev, and V. G. Litovchenko, Poluprovodn. Tekh. Mikroélektron. **18**, 49 (1974).
34. L. A. Matveeva, E. F. Venger, and R. Yu. Holiney, Vopr. At. Nauki Tekh. **3**, 103 (1999).
35. T. Ya. Gorbach, G. Yu. Rudko, P. S. Smertenko, *et al.*, Semicond. Sci. Technol. **11**, 601 (1996).
36. G. Zuther, Phys. Status Solidi A **59**, K109 (1980).
37. H. R. Philipp, Phys. Chem. Solids **32**, 1935 (1931).

Translated by N. Korovin

Semiconductors, Vol. 37, No. 1, 2003, pp. 108–111. Translated from Fizika i Tekhnika Poluprovodnikov, Vol. 37, No. 1, 2003, pp. 110–113.

AMORPHOUS, VITREOUS, AND POROUS SEMICONDUCTORS

Optical Properties of Polydimethylphenyleneoxide Free-Standing Films Containing Fullerene

Yu. F. Biryulin*^, E. Yu. Melenevskaya*, S. N. Mikov**, S. E. Orlov**, V. D. Petrikov*, D. A. Syckmanov*, and V. N. Zgonnik*****

** Ioffe Physicotechnical Institute, Russian Academy of Sciences, St. Petersburg, 194021 Russia*
^e-mail:biryulin@mail.ioffe.ru
*** Ul'yanovsk State University, Ul'yanovsk, 432700 Russia*
**** Institute of Macromolecular Compounds, Russian Academy of Sciences, St. Petersburg, 199004 Russia*
Submitted June 17, 2002; accepted for publication June 19, 2002

Abstract—The interaction of fullerene C_{60} with poly(2,6-dimethyl)-phenyleneoxide (PPO) in free films was studied by optical methods. The electronic structure of C_{60} in these polymer films was shown to have two states, with the energy state of C_{60} bound to PPO being independent of the C_{60} content. Comparison of the photoluminescence spectra of PPO–C_{60} and polystyrene–C_{60} systems makes it possible to assert that the interaction between the components of these systems occurs via π electrons of fullerene and π electrons of benzene rings of the polymers. It is assumed that C_{60} in the polymer exists in two forms that differ in their electronic structure: a molecular-dispersed state (in the form of complexes with the polymer) and as crystals (aggregates) of fullerene. *© 2003 MAIK "Nauka/Interperiodica".*

1. INTRODUCTION

Combining known properties of polymers (elasticity and film-and fiber-forming ability) with such properties of fullerenes as electron deficiency and the ability to interact with free radicals, one can obtain new polymer materials with specific properties. Numerous studies of polymer–fullerene composites have been carried out with this aim. The objective of this study was to gain insight into the state of fullerene in composite materials.

In this paper, we present the results of optical studies of free films (without substrates) prepared from such polymers as poly(2.6-dimethyl)-phenyleneoxide (PPO) and polystyrene (PS) and containing different amounts of fullerene C_{60}.

2. EXPERIMENTAL

The PPO–C_{60} and PS–C_{60} films were prepared by evaporating the solvent from a mixture of solutions of polymers in chloroform and fullerenes in toluene with subsequent drying of the films deposited on cellophane substrates in a vacuum dryer to a constant weight [1]. We used PPO and PS with a molecular mass of 112000 and 230000, respectively. A microcrystalline powder of fullerene C_{60} with 99.95% purity was used to prepare the toluene solutions. The thickness of the films varied in the range of 120–160 μm.

IR spectra of the PPO–C_{60} complexes were measured at room temperature with a Specord-M80 spectrometer.

Photoluminescence (PL) of the PPO–C_{60} films was studied at a sample temperature of T = 300 and 77 K. Two experimental setups were employed. In one of them, the PL spectra were excited by an argon laser (radiation wavelength λ = 488 nm) and were recorded using a synchronous phase detector and a FÉU-62 photomultiplier. The other setup used a DFS-52 spectrometer that was equipped with an FÉU-79 photomultiplier, which operated in the photon-counting mode. In this case, a correction for the spectral sensitivity of the photomultiplier was introduced. An LCS-DTL-316 solid-state Nd:YAG laser (λ = 532 nm) pumped by semiconductor lasers served as an excitation source. The radiation power of the laser beam could be varied from 1 to 200 mW, which, upon focusing this radiation to a spot 0.06 mm in diameter, corresponded to a power density varying in the range of 35–7000 W/cm^2. A better signal-to-noise ratio was attained in the second case.

3. DISCUSSION

The PL spectra of free-standing PPO–C_{60} films at 300 K excited by laser radiation with λ = 532 nm are shown in Fig. 1. A pure polymer (PPO–C_{60}(0.0%)) exhibits a PL band peaked at an energy of 1.915 eV.[1] Addition of fullerene leads to the appearance of another band (located at 1.76 eV in the spectrum of the PPO–C_{60}(0.5%) film). When the content of C_{60} in the PPO films increases, this additional band increases

[1] Hereafter, we will be dealing with mole fractions expressed in percent.

in intensity and steadily shifts to lower photon energies. At the same time, the intensity of the PL band of pure PPO slowly decreases according to nearly the same law. The additional band in the film with the highest content of fullerene, PPO–C_{60}(4.0%), is located at 1.694 eV, with the band intensity of pure PPO being nearly zero.

At the liquid nitrogen temperature (T = 77 K), the PL spectra of the PPO–C_{60} films have a more complex structure (Fig. 2). Two bands peaked at 1.69 and 1.75 eV, respectively, are dominant in the spectra. In the sample with the lowest content of fullerene, PPO–C_{60}(0.5%), the peak at 1.75 eV is the highest, while the 1.69-eV band appears in the spectrum as a weak long-wavelength shoulder of this 1.75-eV peak. As the content of fullerene increases, the 1.75-eV band decreases in intensity, whereas the 1.69-eV shoulder increases and transforms into a dominant band (peaked at 1.70 eV in PPO with 4% of C_{60}).

Figure 2 also shows the PL spectrum of a PS–C_{60} film obtained by using a similar procedure. It can be clearly seen that this spectrum virtually coincides in the structure and energy position of its bands with the spectrum of PPO with 2% of C_{60}.

The PL bands at 1.69 and 1.75 eV can be attributed to radiative transitions in fullerene C_{60}, some portion of which is in an unbound (aggregated) state and the rest is chemically bound to PPO. In the latter case, the electronic structure of fullerene changes in such a way that the HOMO–LUMO gap increases, which we observed previously for C_{60}–$(PS)_n$ samples synthesized with the opening of double bonds of fullerene [2–5]. Therefore, we should assume that the fullerene molecules in PPO with 4% of C_{60} are predominantly unbound to this polymer; i.e., this film represents a mechanical mixture of fullerene and PPO. By contrast, in PPO with 0.5% of C_{60}, fullerene is chemically bound to PPO (i.e., it exists in a molecular-dispersed form), with a very small fraction of C_{60} aggregates remaining unreacted.

The spectra of nearly all the samples in Fig. 1 indicate that pure PPO contributes to PL. This contribution decreases as the content of C_{60} in the films increases. This fact indicates that the films contain PPO macromolecules that do not interact with the fullerene molecules. A PPO–C_{60}(1.0%) system is the most homogenous (Figs. 1, 2): in this case, the largest amount of fullerene is dispersed to a molecular level, interacting with nearly all the PPO macromolecules.

The preparation of films from combined polymer–fullerene solutions evidently cannot result in a chemical reaction between the components accompanied with the opening of double bonds in C_{60}. Therefore, the spectral changes observed result from interactions at the level of π bonds. Identical energy positions of the peaks in the PL spectra of PPO–C_{60} and PS–C_{60} systems (both containing 2% of fullerene) are indicative of the similar nature of the interaction of these polymers with fullerene. In this context, one may evidently

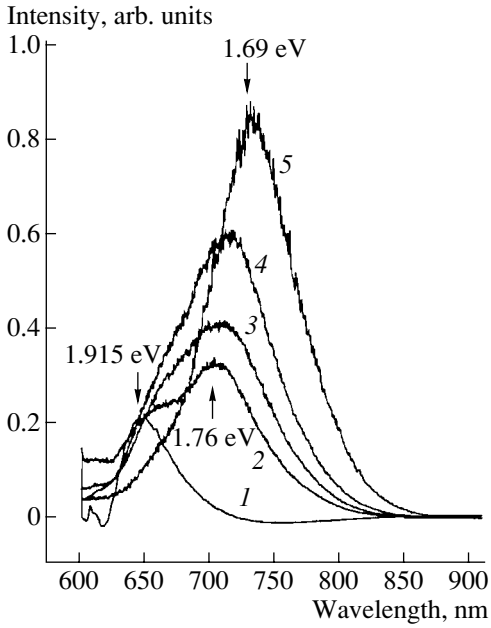

Fig. 1. Photoluminescence spectra of PPO–C_{60} films at 300 K. The content (%) of C_{60}: (*1*) 0.0, (*2*) 0.5, (*3*) 1.0, (*4*) 2.0, and (*5*) 4.0.

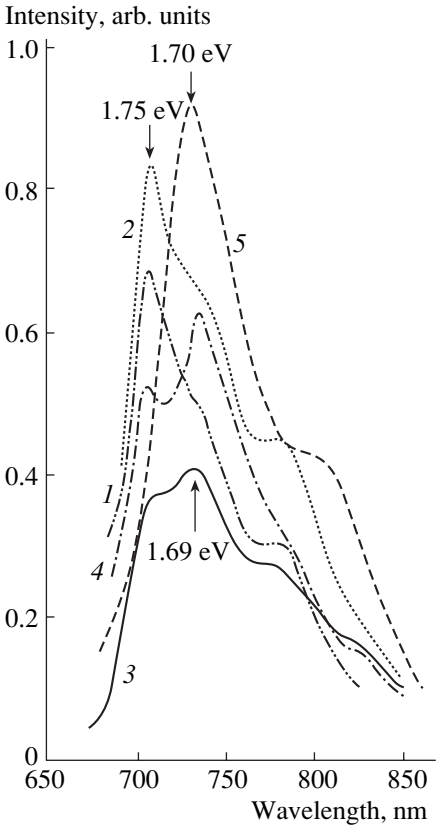

Fig. 2. Photoluminescence spectra of (*1–3, 5*) PPO–C_{60} and (*4*) PS–C_{60} films at 77 K. The content (%) of C_{60}: (*1*) 0.5, (*2*) 1.0, (*3, 4*) 2.0, and (*5*) 4.0.

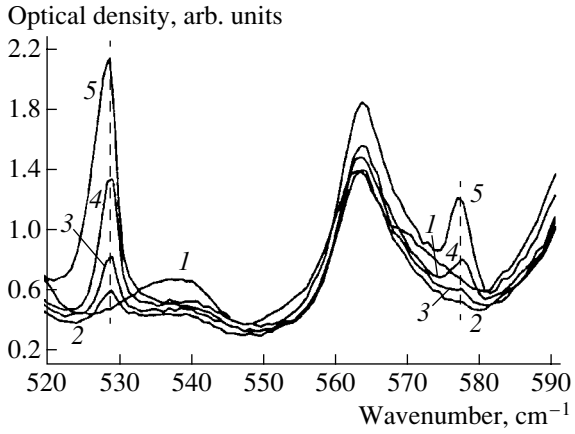

Fig. 3. IR absorption spectra of PPO–C_{60} films at 300 K. The content (%) of C_{60}: (*1*) 0.0, (*2*) 0.5, (*3*) 1.0, (*4*) 2.0, and (*5*) 4.0.

assume that oxygen atoms from simple ester bonds in PPO do not markedly contribute to the complexation.

Figure 3 shows the IR absorption spectra of the same samples in the region of 520–590 cm^{-1}. It can be clearly seen that the IR absorption bands of fullerene in the PPO film with 4% of C_{60} are located at 528 and 577 cm^{-1}. This corresponds to the position of these bands in the absence of interaction between fullerene and PPO. As the content of fullerene decreases, these bands undergo a slight shift, so that their positions in the spectrum of the PPO–C_{60}(0.5%) system correspond to 528.5 and 578 cm^{-1}, respectively. Thus, this shift does not exceed 1.0 cm^{-1} (this experimental fact was repeatedly verified). Therefore, the IR absorption spectra of C_{60} also indicate that PPO chemically affects the electronic–vibrational system of fullerene; i.e., they point to the formation of PPO–C_{60} complexes. This interaction manifests itself most clearly at low contents of fullerene; however, the small shift of the IR bands of C_{60} indicates that the resultant complex is more likely molecular in nature rather than a charge-transfer complex.

As can be seen from the PL spectra of the films at 77 K, the 1.75-eV band corresponds to the energy state of the electronic structure of fullerene involved in the PPO–C_{60} complexes. The position of this band does not change, which indicates that the stoichiometry in all of the cases remains the same, whereas the intensity of this band corresponds to the efficiency of the chemical process of complexation, i.e., to the concentration of the complexes formed.

From these results we can draw the following preliminary conclusions.

(i) Regardless of the ratio between the content of C_{60} and that of PPO during the preparation of the films (during synthesis), the complexes formed are characterized by the same number of coordination bonds between the fullerene molecule and PPO (or PS) and by the same stoichiometry.

(ii) One can assume that the number of such bonds in each complex is constant and exceeds unity. The number of contacts between the surface of the fullerene molecule with monomeric units of the polymer can attain three to four or higher. The interaction between the fullerene molecules with the polymer in their contact areas occurs owing to overlap of the π systems of C_{60} and benzene rings of PPO (or PS).

(iii) Fullerene has a low sensitivity to the structure of a polymer with which it interacts. The system of π electrons of fullerene interacts with the clouds of π electrons of conjugated polymers, which surround the fullerene molecules and form an envelope of π electrons around them. The interaction of the two π systems over the entire surface of C_{60} results in the formation of polymer–C_{60} complexes. This causes the electronic system of fullerene to change to a new state that is characterized by the appearance of a 1.76 eV band in the PL spectra of C_{60}. One may assume that this state is universal, weakly depends on the type of conjugated polymer, and is governed only by the interaction of the π system of fullerene with the envelope of π electrons of the polymer.

4. CONCLUSION

A comparison of the PL spectra corresponding to different mole fractions of fullerene in films prepared from poly(2,6-dimethyl)-phenyleneoxide shows that the PPO–C_{60}(1.0%) film is the most homogenous. In this film, a macromolecule of PPO efficiently interacts with a C_{60} molecule.

Therefore, in the sample PPO–C_{60} with 0.5% of fullerene, molecular complexes of the components are formed. In this case, fullerene in the polymer occurs mainly in a molecular-dispersed form. By contrast, in the PPO film with 4% of C_{60}, the ratio $[C_{60}]/[PPO] = 6$ and fullerene in this film forms crystallites (aggregates) consisting of several C_{60} molecules that predominantly interact with each other. In this case, the film is a mechanical mixture of polymer macromolecules and fullerene crystallites. Therefore, by employing an appropriate molecular relationship between fullerene and polymer and by choosing corresponding synthesis conditions of complexation, one can ensure the dispersion of fullerene to a molecular level.

5. ACKNOWLEDGMENTS

This study was supported by the State Scientific and Technical Program “Controlled Synthesis of Fullerenes and Atomic Clusters” and by the Presidium of the RAS program “Low-Dimensional Quantum Structures” (project: “Investigation of the Interaction of Fullerenes with Substrates and the Electronic Properties of Such Heterosystems”).

REFERENCES

1. V. N. Zgonnik, L. V. Vinogradova, E. Yu. Melenevskaya, *et al.*, in *Abstracts of International Workshop on Fullerenes and Atomic Clusters, IWFAC-2001*, p. 187.
2. Yu. F. Biryulin, V. M. Lebedev, S. N. Mikov, *et al.*, Fiz. Tverd. Tela (St. Petersburg) **42** (10), 1904 (2000) [Phys. Solid State **42**, 1958 (2000)].
3. S. S. Moliver and Yu. F. Biryulin, Fiz. Tverd. Tela (St. Petersburg) **43** (5), 944 (2001) [Phys. Solid State **43**, 982 (2001)].
4. D. A. Sykmanov, Yu. F. Biryulin, L. V. Vinogradova, and V. N. Zgonnik, Fiz. Tekh. Poluprovodn. (St. Petersburg) **35** (6), 671 (2001) [Semiconductors **35**, 643 (2001)].
5. L. V. Vinogradova, V. N. Zgonnik, D. A. Sykmanov, and Yu. F. Biryulin, Vysokomol. Soedin., Ser. A **43** (6), 1002 (2001).

Translated by V. Rogovoĭ

Semiconductors, Vol. 37, No. 1, 2003, pp. 112–114. Translated from Fizika i Tekhnika Poluprovodnikov, Vol. 37, No. 1, 2003, pp. 114–116.

PHYSICS OF SEMICONDUCTOR DEVICES

Electroluminescence of Injection Lasers Based on Vertically Coupled Quantum Dots near the Lasing Threshold

N. Yu. Gordeev*^, S. V. Zaĭtsev, L. Ya. Karachinsky*, V. I. Kopchatov*, I. I. Novikov*, V. M. Ustinov*, and P. S. Kop'ev***

** Ioffe Physicotechnical Institute, Russian Academy of Sciences, St. Petersburg, 194021 Russia*

^ e-mail: gordeev@switch.ioffe.rssi.ru

*** Nova Crystals, Inc., 174 Component Dr., San José, CA 95131 USA*

Submitted May 28, 2002; accepted for publication June 3, 2002

Abstract—Electroluminescence spectroscopy has been used in a wide range of temperatures (77–300 K) and driving current densities to study a laser heterostructure based on vertically coupled self-assembled InGaAs quantum dots (QD). It has been found that lasing occurs via the QD ground state in the entire temperature range. The temperature-independent position of the emission peak corresponding to the second excited state in QDs is explained. © *2003 MAIK "Nauka/Interperiodica".*

1. INTRODUCTION

In studies of laser heterostructures with a QD active region, much attention is being given to determining which states are responsible for emission, in general, and lasing, in particular [1, 2]. For example, a transition from lasing via QD states to lasing via the states in a wetting layer (WL) has been observed in such structures with a rise in temperature [3]. This was assigned primarily to the considerable ejection of nonequilibrium carriers out of QDs. As shown in [4], the use of arrays of vertically coupled QDs (VCQD) in an InGaAs/GaAs system provided substantial reduction of the carrier ejection from QDs to the WL.

In this paper, we report experimental results concerning the emission spectrum of a heterostructure with an InGaAs/GaAs VCQD active region. Special attention was given to a thorough study of the temperature dependence of emission peaks. The main task was to define which QD states are responsible for lasing at different temperatures.

2. EXPERIMENTAL

A separate-confinement InGaAs/GaAs heterostructure with a lasing wavelength $\lambda = 0.98$ μm was grown by MBE on an Si-doped (001) GaAs substrate. The structure comprised 1.5-μm-thick $Al_{0.4}Ga_{0.6}As$ *n*- and *p*-emitters, a 0.4-μm-thick gradient-index waveguide, and a 0.6-μm GaAs contact layer. QDs were grown at a temperature of 485°C, and all the other layers, at 700°C. VCQDs were obtained by the Stranski–Krastanow method with self-assembly in the course of deposition of ten (In,Ga)As QD layers separated by 50-Å-thick GaAs buffer layers [4].

Stripe-contact samples (with a cavity length of 300–500 μm) were pumped in the quasi-CW mode by 1.5-μs driving current pulses at a 5-kHz repetition rate. To study the electroluminescence (EL) spectra in a wide temperature range, $T = 77$–300 K, the samples were soldered with their layers facing down onto a heat sink and placed into a cryostat. The emission in the direction normal to the epitaxial layers was investigated. Particular attention was given to suppressing feedback: the mirrors were etched and covered with black paint having a high refractive index. This method, eliminating reemission and reducing the influence of the waveguide to zero, has been described in detail elsewhere [5]. It also provided a substantial increase in the lasing threshold in the samples under study, thus widening the possible range of driving currents. In several samples, a "window" was etched through the epitaxial layers to the waveguide. This allowed study of the emission spectrum, with the effects of the emitter and contact layer excluded.

3. RESULTS AND DISCUSSION

Figure 1 shows the emission spectra at the lasing threshold. As can be seen, the number of peaks in the EL spectrum increases as the temperature rises due to the filling of higher levels. Figure 2 shows the temperature dependence of the peak position for peaks *I–IV*. It was obtained using the emission spectrum simulation method described in [6].

Figure 3 presents the proposed structure of energy levels. We believe that an electron state and three hole states exist in a QD, with transitions (*I–III*) possible between these states. Transition *I* corresponds to the QD ground state, and transitions *II* and *III*, to the first and second excited states, respectively. Transition *IV* is the transition between the electron state of a QD and the wetting layer (WL).

1063-7826/03/3701-0112$24.00 © 2003 MAIK "Nauka/Interperiodica"

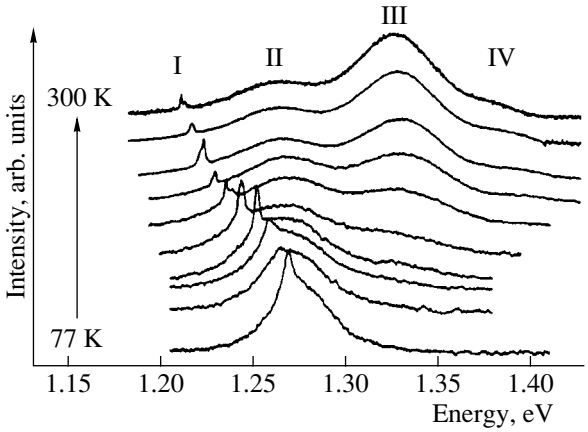

Fig. 1. EL spectra of an InGaAs/GaAs QD laser heterostructure at the lasing threshold.

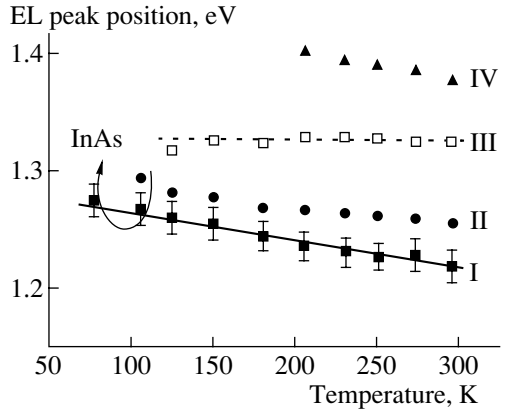

Fig. 2. Temperature dependence of the peak positions of EL spectra.

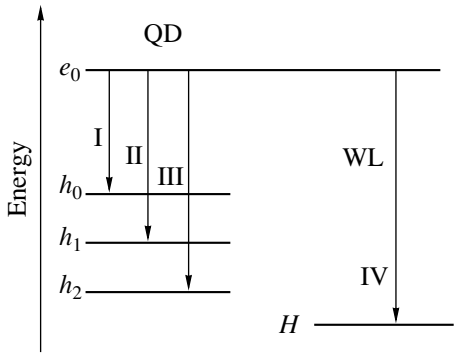

Fig. 3. Energy levels responsible for radiative recombination in the heterostructure under study. e_0 and h_0: ground states of electrons and holes in a QD, respectively; h_1 and h_2: excited states of holes in a QD; H denotes the hole subband in the wetting layer (WL).

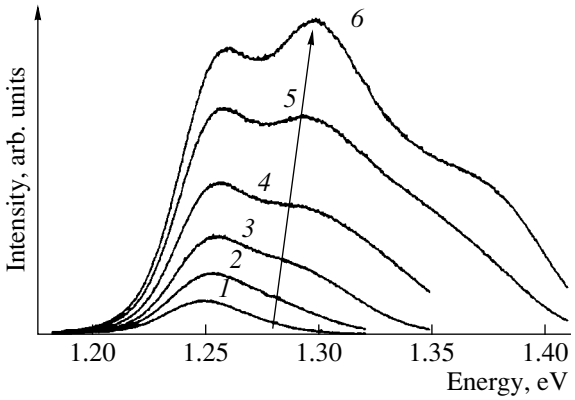

Fig. 4. EL spectra of an InGaAs/GaAs QD laser heterostructure at $T = 77$ K. Driving current density: (*1*) 40, (*2*) 80, (*3*) 160, (*4*) 320, (5) 640, and (*6*) 980 A cm^{-2}.

As seen in Fig. 2, the shift of the first peak (*I*) with rising temperature correlates with the temperature dependence of the InAs band gap. The temperature shift of the second peak (*II*) is much weaker, and the position of peak *III* is temperature-independent.

A weak temperature dependence of the lasing wavelength in QD heterostructures has been observed in [7–9]. In [9], for a heterostructure with a single InGaAs QD layer, this effect was explained as an active region by the temperature-independent position of the maximum of gain. With temperature varied, the QD states are modified in such a way that, at constant gain, the distance between the quasi-Fermi levels (ΔE_f) corresponding to the electron and hole distributions in a QD remains virtually unchanged. This means that the shape of the energy distribution of these states follows the increase in the broadening of the Fermi function as the temperature rises. The energy distribution of states in a QD is determined by inhomogeneous broadening caused by inhomogeneities in the shape, size, and composition of a QD.

The data obtained show that the temperature dependence of the lasing wavelength virtually coincides with that of the band gap. Most likely, the distinctions between our data and those from [9] are related to different experimental and pumping conditions. An anomalous temperature dependence of transitions *II* and *III* can also be explained by strong inhomogeneous broadening. A higher driving current density corresponds to a spectrum recorded at an elevated temperature, since the spectra were recorded at the lasing threshold, which increases as the temperature rises. As seen in Fig. 4, raising the driving current at a fixed temperature results in a short-wavelength shift of the emission peak related to a higher energy level. It can be assumed that this shift may be on the order of the inhomogeneous broadening of the corresponding level (up to 40–50 meV) [2]. As the temperature rises, variation in the band gap and the above-described effect of level filling are mutually compensated. In the temperature range $T = 77$–300 K, the band gap narrows by ~50 meV. We believe that the above-described mechanism, according to which a shift

of the EL peaks is compensated for by a change in the band gap with a rise in temperature and by an increase in the driving current, results in the position of peak *II* depending only slightly on temperature and that of peak *III* remaining invariable over the entire temperature range.

4. CONCLUSION

The emission spectra of a laser heterostructure based on vertically coupled InGaAs/GaAs QDs have been studied. The origin of spectral peaks related to carrier excitation from the QD ground state with temperature increasing has been thoroughly investigated. In the whole temperature range under study, lasing occurs via the ground state of QDs. The temperature independence of the position of the emission peak corresponding to the second excited state of a QD is explained.

ACKNOWLEDGMENTS

We are grateful to R.A. Suris, G.G. Zegrya, and E.Yu. Kotel'nikov for discussing the results, and to N.D. Il'inskaya for her assistance in the preparation of samples.

This study was supported by the Russian Foundation for Basic Research (project no. 01-02-17764) and by the Sixth Competition of the Projects of Young Scientists of the Russian Academy of Sciences (grant no. 26). L.Ya.K. acknowledges the support of INTAS (grant YSE no. 2001/2-97).

REFERENCES

1. S. Raymond, S. Fafard, P. J. Poole, *et al.*, Phys. Rev. B **54**, 11548 (1996).
2. N. N. Ledentsov, V. M. Ustinov, V. A. Shchukin, *et al.*, Fiz. Tekh. Poluprovodn. (St. Petersburg) **32**, 385 (1998) [Semiconductors **32**, 343 (1998)].
3. Zh. I. Alferov, N. Yu. Gordeev, S. V. Zaĭtsev, *et al.*, Fiz. Tekh. Poluprovodn. (St. Petersburg) **30**, 357 (1996) [Semiconductors **30**, 197 (1996)].
4. S. V. Zaitsev, N. Yu. Gordeev, Yu. M. Shernyakov, *et al.*, Superlattices Microstruct. **21**, 559 (1997).
5. A. M. Georgievskiĭ, S. V. Zaĭtsev, N. Yu. Gordeev, *et al.*, Fiz. Tekh. Poluprovodn. (St. Petersburg) **33**, 847 (1999) [Semiconductors **33**, 779 (1999)].
6. S. V. Zaitsev, H. Yu. Gordeev, L. Ya. Karachinsky, *et al.*, Appl. Phys. Lett. **76**, 2514 (2000).
7. D. Bimberg, N. N. Ledentsov, M. Grundmann, *et al.*, Jpn. J. Appl. Phys. **35**, 1311 (1996).
8. H. Shoji, Y. Nakaata, K. Mukai, *et al.*, IEEE J. Sel. Top. Quantum Electron. **3**, 188 (1997).
9. J. D. Thomson, H. D. Summers, P. M. Smowton, *et al.*, J. Appl. Phys. **90**, 4859 (2001).

Translated by D. Mashovets

Semiconductors, Vol. 37, No. 1, 2003, pp. 115–118. Translated from Fizika i Tekhnika Poluprovodnikov, Vol. 37, No. 1, 2003, pp. 117–120.

PHYSICS OF SEMICONDUCTOR DEVICES

Tunneling Recombination in Silicon Avalanche Diodes

S. V. Bulyarskiĭ*, V. K. Ionychev*, and V. V. Kuz'min**

** Mordovian State University, Saransk, 430000 Russia*

*** Ul'yanovsk State University, Ul'yanovsk, 432700 Russia*

Submitted February 18, 2002; accepted for publication June 10, 2002

Abstract—Distribution of the tunneling-recombination current over the space-charge region in a *p–n* junction was simulated mathematically. It is shown that the recombination rate saturates if the probability of tunneling is low. An expression for current–voltage characteristics of the *p–n* junction in the case of tunneling recombination is derived. The current–voltage characteristics of silicon avalanche diodes containing dislocations were studied experimentally. The results of numerical calculations based on the tunneling-recombination model are consistent with experimental data. © *2003 MAIK "Nauka/Interperiodica"*.

1. INTRODUCTION

Recently, the theory of recombination processes in the space-charge region (SCR) of semiconductor structures has been modified radically. The Shockley–Read–Hall theory is inapplicable to the structures in which electrons and holes are spatially separated at localized states and have to tunnel through potential barriers in order to recombine. At the same time, portions of the current–voltage (*I–V*) characteristics, when related to the recombination in the SCR, provide useful and important information about properties of recombination centers. Bulyarskiĭ and Grushko [1] suggested a generalized model of recombination for structures with tunneling-connected regions. In this paper, we report the results of studying the tunneling recombination in silicon avalanche diodes that contain dislocations.

2. CHARACTERISTICS OF THE SAMPLES UNDER INVESTIGATION

In our investigations, we used commercial KD 2978 avalanche rectifying diodes as samples (Fig. 1). The latter incorporated silicon epitaxial p^+–*n* junctions. The structure is based on the *p*-Si:B substrate with a resistivity of 0.005 Ω cm. The *p–n* junction was formed by growing an *n*-Si epitaxial film with a thickness of 18 μm and resistivity of 0.07 Ω cm. A groove was etched off at the site where the *p–n* junction emerged at the surface; this groove was then overgrown with silicon oxynitride using plasma-chemical deposition in an O_2 and N_2 atmosphere. The results of studying the capacitance–voltage (*C–V*) characteristics showed that, in spite of advances in epitaxial growth technology, the exponential model of a *p–n* junction [2] best fitted the diodes under investigation; according to this model, we have

$$N_a(x) - N_d = N_0\left[\exp\left(-\frac{x - x_j}{\lambda}\right) - 1\right], \qquad (1)$$

where, in the case under consideration, $N_0 = 1 \times 10^{17}$ cm^{-3} and $\lambda = 0.25$ μm. In expression (1), $x = 0$ corresponds to the interface between the epitaxial film and the substrate.

The samples from the prepared batch were sorted according to the value of the reverse current. On the basis of an analysis of *C–V* characteristics, we found that the samples with increased reverse currents had increased values of the parameter N_0. This indicates that the *p–n* junction is closer to the film–substrate interface in these samples than in the samples with smaller reverse currents. It is well known [3] that, invariably, there are defects and imperfections (dislocations, stacking faults, and so on) at the interface between the epitaxial film and substrate. As the distance from the interface increases, the density of these defects decreases. Numerical estimations performed by us showed that the displacement of the metallurgical *p–n* junction x_j from the film–substrate interface for all samples did not exceed 1.3 μm; i.e., the *p–n* junction

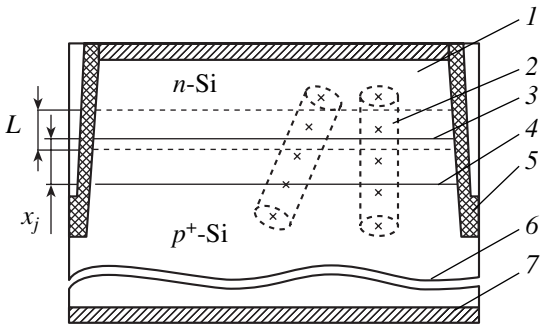

Fig. 1. The structure of the diodes under investigation: (*1*) epitaxial film, (*2*) dislocation, (*3*) metallurgical *p–n* junction, (*4*) film–substrate interface, (*5*) oxynitride, (*6*) substrate, and (*7*) metallization layer. *L* stands for the width of the space-charge region; and x_j, for the displacement of the metallurgical *p–n* junction.

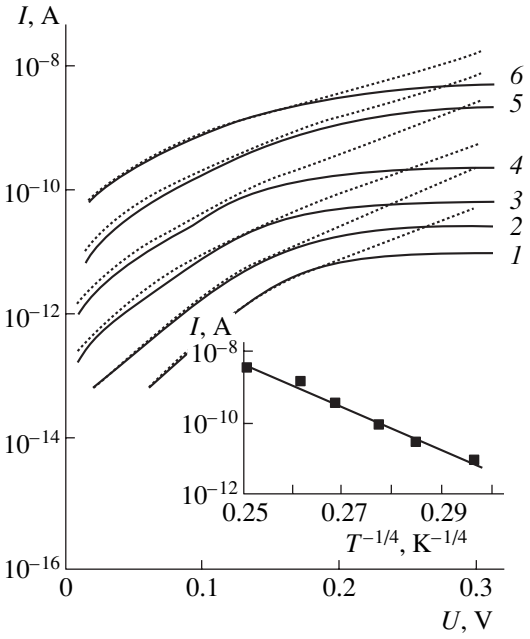

Fig. 2. Experimental (dots) and theoretical (solid lines) forward *I–V* characteristics of diodes with large reverse currents; the voltage dependences of the forward current are shown for T = (*1*) 129.2, (*2*) 151.7, (*3*) 168.8, (*4*) 184.8, (*5*) 214.0, and (*6*) 250.5 K. The temperature dependence of the forward current at the bias voltage U = 0.2 V is shown in the inset.

was always located in the region with a potentially high density of defects. The difference in reverse currents can be attributed to a nonuniform distribution of defects over the area of the initial wafer. The defect density in the SCR is higher in the samples with inferior characteristics; correspondingly, the reverse current is larger.

In order to assess the role of surface currents, we used the same technology to fabricate several batches of samples that differed in their area. The results of measurements showed that the forward current increased in proportion to the structure area. This means that this current has a volume origin; i.e., the contribution of the surface current to the total current is negligibly small.

3. HOPPING CONDUCTION ALONG DISLOCATIONS

We measured the forward *I–V* characteristics in the dc mode in the low-temperature range (130–150 K). During measurements, the samples were installed in a light-tight cryostat. The sample temperature was measured using a TSPN-5 platinum resistance thermometer. The temperature was maintained constant to within 0.1 K.

The low-voltage portions of the measured *I–V* characteristics are shown in Fig. 2 (points). The temperature dependence of the current is linear when plotted as $\ln I$ versus $T^{-1/4}$ (see Fig. 2, inset); i.e., the Mott law

$$I = I_0 \exp\left[-\left(\frac{T_0}{T}\right)^{1/4}\right], \qquad T_0 = \frac{\beta}{kg(E_F)a^3} \tag{2}$$

is obeyed. In (2), $g(E_F)$ is the density of states at the Fermi level, k is the Boltzmann constant, a is the localization radius for an electron [4], and β is a constant calculated on the basis of the percolation theory [5] (β = 21 for a three-dimensional problem).

Such a temperature dependence of the current indicates that we have variable-range hopping conductivity. The latter can be caused by dislocations that are located along the flow direction of the current and intersect the *p–n* junction (Fig. 1).

We found that $T_0 = 3.7 \times 10^8$ K from the slope of the curve in the inset of Fig. 2. The calculated density of states at the Fermi level is $g(E_F) = 6.4 \times 10^{16}$ eV^{-1} cm^{-3}. It has been shown by Shklovskii and Efros [5] that percolation occurs in a narrow energy range in the vicinity of the Fermi level; this range can be estimated using the formula

$$\Delta = -\frac{d\ln I}{d(kT)^{-1}}. \tag{3}$$

The mean energy is Δ = 0.1 eV in the case under consideration, which yields a trap concentration $N_t = 6.4 \times 10^{15}$ cm^{-3}.

Edge dislocations most profoundly affect the *p–n*-junction parameters [6]. In the case of these dislocations, the density of states within the dislocation core is comparable to the intrinsic-atom density, whereas the traps originate from the bond splitting by an atomic plane. In the case under consideration, the density of states is much lower. We may assume that the dislocations under investigation are of the edge type; however, a fraction of the dangling bonds are completed by uncontrolled impurities and are electrically inactive.

4. SIMULATION OF TUNNELING RECOMBINATION IN A *p–n* JUNCTION

If there is a high density of localized states in the SCR of a *p–n* junction, with this density exceeding the concentration of free charge carriers, the latter are rapidly captured by traps [7]. Electrons and holes become localized within different spatial regions. The charge carriers have to tunnel in order to recombine.

An expression for the tunneling-recombination rate in the situation where the energy distribution of local states may be ignored can be written as [8]

$$R = \frac{c_n c_p w N_t^2 [pp - n_1 p_1]}{c_n c_p (n + n_1)(p + p_1) + w N_t [c_n (n + n_1) + c_p (p + p_1)]}, \quad (4)$$

where $w = w_0/N_t$ is the probability of tunneling divided by the concentration of states over which transport occurs, N_t is the concentration of local states, and n_1 and p_1 are the concentrations of electrons and holes referred to the localized-state level.

The concentrations of free electrons n and holes p and p in the SCR can be found by solving the Poisson equations. The probability of a tunneling hop per unit time w_0 is defined by an overlap integral, which can be estimated from the formula [5]

$$w_0(r) = \nu \exp(-2r/a), \quad (5)$$

where ν is the frequency of a characteristic phonon, r is the hop range, and a is the electron-localization radius. The hop range is equal to the mean distance between impurity atoms, $r \approx N_t^{-1/3}$.

In Fig. 3a, we show the results of numerical simulation of the distribution of the tunneling-recombination rates over the SCR width (L) in an exponential p–n junction for various forward-bias voltages. In contrast to the form of formula (1), the origin of the x axis is chosen hereinafter at the SCR boundary in the p-type region (the lower dashed line in Fig. 1). The p–n junction was approximated using the following parameters: $N_0 = 1 \times 10^{17}$ cm^{-3} and $\lambda = 0.25$ μm. It was assumed that the temperature of the p–n junction was equal to 150 K. Parameters of deep-level centers were specified as $E_t = E_c - 0.7$ eV and $N_t = 5 \times 10^{15}$ cm^{-3}. The obtained dependence features portions of steep rise, which are narrowed with increasing forward bias applied to the p–n junction, and a plateau portion. As was previously noted [1], the tunneling-recombination rate levels off for a low tunneling probability w.

For large values of w, expression (4) transforms into the formula for the classical Shockley–Read recombination,

$$R = \frac{c_n c_p (np - n_1 p_1) N_t}{c_n (n + n_1) + c_p (p + p_1)}, \quad (6)$$

and the plateau for R disappears. In Fig. 3b, we show the results of the $R = f(x)$ simulation for a forward bias of 0.2 V applied to the junction at a temperature of 150 K and for several values of w. As the tunneling probability increases, the recombination rate ceases to be limited by the tunneling transitions, the width of the plateau in the dependence $R = f(x)$ decreases, and the curve takes a characteristic bell-like shape.

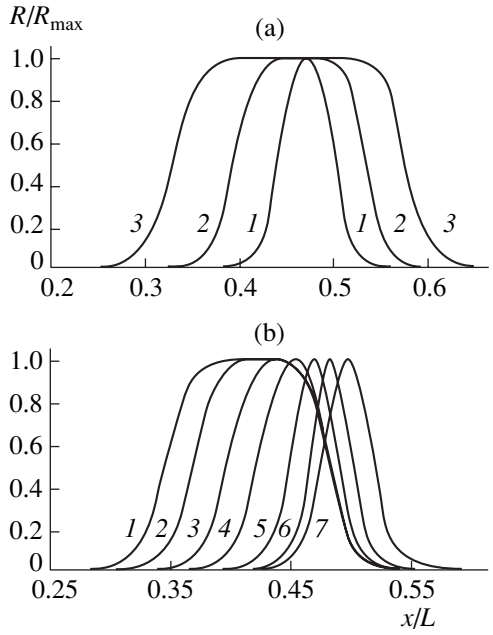

Fig. 3. Distribution of the tunneling-recombination rate throughout the space-charge region of an exponential p–n junction (the normalized coordinates are used). (a) U = (*1*) 0.1, (*2*) 0.2, and (*3*) 0.3 V. (b) U = 0.2 V; w = (*1*) 1.6×10^{-28}, (*2*) 4.6×10^{-27}, (*3*) 8.4×10^{-26}, (*4*) 1.1×10^{-24}, (*5*) 3.2×10^{-23}, (*6*) 5.8×10^{-22}, and (*7*) 6.9×10^{-20} cm^3 s^{-1}.

Formula (4) can be used to calculate the I–V characteristic of the p–n junction in the situation where tunneling recombination occurs in the SCR. The recombination-current density can be determined by integrating the recombination rate (4) over the SCR, taking into account expressions for concentrations of the free charge carriers; i.e.,

$$j_r = e\int_0^L R(x)dx. \quad (7)$$

The distribution curve $R = f(x)$ cannot be approximated using an analytically integrable function. This function is defined by the specific form of the p–n junction. Therefore, it has been suggested [1] that integral (7) be calculated using the half-falloff procedure, in which case only the behavior of the maximum in the dependence $R = f(x)$ needs to be known. Performing this procedure, we determine the values of the concentrations of free charge carriers at the point corresponding to the maximum of the recombination rate; i.e.,

$$n = n_i \sqrt{\frac{c_p(E)}{c_n(E)}\left[\frac{c_n(E)n_1(E) + wN_t}{c_p(E)p_1(E) + wN_t}\right]} \exp\left(\frac{eU}{2kT}\right),$$
$$p = n_i \sqrt{\frac{c_n(E)}{c_p(E)}\left[\frac{c_p(E)p_1(E) + wN_t}{c_n(E)n_1(E) + wN_t}\right]} \exp\left(\frac{eU}{2kT}\right). \quad (8)$$

Taking expressions (4) and (8) into account, we obtain the following formula for the current density in the case of tunneling recombination [1]:

$$j_r = \frac{2kTL}{U_d - U} \times \frac{wN_t^2 c_n c_p n_i^2 [\exp(eU/kT) - 1]}{c_n c_p (n + n_1)(p + p_1) + wN_t [c_n (n + n_1) + c_p (p + p_1)]}. \quad (9)$$

The theoretical *I–V* characteristic was calculated using expression (9) and by taking formula (5) into account. The results of simulation are shown in Fig. 2 (solid lines). The parameters of the deep-level centers were chosen to be $E_t = E_v + 0.45$ eV and $N_t = 6.1 \times 10^{15}$ cm^{-3}. As can be seen from Fig. 2, the low-voltage (near-origin) portions of the experimental and theoretical *I–V* characteristics are in good agreement with each other. The previously determined parameters of the traps are consistent with the parameters used in simulation. Thus, the assumption that tunneling recombination and hopping conduction occur along dislocations in the SCR of the *p–n* junction seems to be valid.

Theoretically calculated values of current are found to be too large when higher forward voltages are applied to the *p–n* junction ($U > 0.3$ V). Apparently, other mechanisms of charge transport contribute significantly to the total current in this region of bias voltages.

5. CONCLUSION

In this paper, the model of tunneling recombination is extended to semiconductor structures with *p–n* junctions. We studied the mechanism of charge transport in silicon avalanche diodes. We determined the parameters of deep-level centers involved in the formation of recombination current. The results of analytical calculations of the *I–V* characteristics on the basis of the model under consideration are found to be in good agreement with experimental data, which validates the choice of this model.

REFERENCES

1. S. V. Bulyarskiĭ and N. S. Grushko, Zh. Éksp. Teor. Fiz. **118**, 1222 (2000) [JETP **91**, 1059 (2000)].
2. P. V. Akimov, Yu. N. Serezhkin, and V. M. Fedoseev, Available from VINITI, No. 8126-V (1985).
3. K. V. Ravi, *Imperfections and Impurities in Semiconducting Silicon* (Wiley, New York, 1981; Mir, Moscow, 1984).
4. S. D. Baranovskiĭ, V. G. Karpov, and B. I. Shklovskiĭ, Zh. Éksp. Teor. Fiz. **94** (3), 278 (1988) [Sov. Phys. JETP **67**, 588 (1988)].
5. B. I. Shklovskiĭ and A. L. Efros, *Electronic Properties of Doped Semiconductors* (Nauka, Moscow, 1979; Springer-Verlag, New York, 1984).
6. H. F. Matare, *Defect Electronics in Semiconductors* (Wiley, New York, 1971; Mir, Moscow, 1974).
7. S. D. Baranovskiĭ, E. L. Ivchenko, and B. I. Shklovskiĭ, Zh. Éksp. Teor. Fiz. **92**, 2234 (1987) [Sov. Phys. JETP **65**, 1260 (1987)].
8. N. S. Grushko, in *Critical Technology and Fundamental Problems in the Physics of Condensed Matter: Proceedings of Lecturers of the School* (Ul'yanovsk. Gos. Univ., Ul'yanovsk, 1999), p. 81.

Translated by A. Spitsyn

Semiconductors, Vol. 37, No. 1, 2003, pp. 15–19. Translated from Fizika i Tekhnika Poluprovodnikov, Vol. 37, No. 1, 2003, pp. 17–21.

ATOMIC STRUCTURE AND NONELECTRONIC PROPERTIES OF SEMICONDUCTORS

Determination of Deformation Potential Constants for *n*- and *p*-Si from the Concentration Anharmonicity

A. A. Skvortsov*, O. V. Litvinenko, and A. M. Orlov

Ul'yanovsk State University, ul. Tolstogo 42, Ul'aynovsk, 432700 Russia

**e-mail: scvor@sv.uven.ru*

Submitted February 27, 2002; accepted for publication April 24, 2002

Abstract—The contribution of charge carriers to the fourth-order modulus of elasticity β for *n*- and *p*-type silicon under uniaxial tension along the [110] direction was analyzed in the approximation of small strains. The effect of concentration on β was measured using spontaneous excitation of Lamb waves in bent plates with different doping levels. Experimental curves were used to determine the deformation potential constants of the conduction band $\Xi_u = 7 \pm 1$ eV and the averaged value of the deformation potential of the valence band $\sqrt[4]{\langle \Phi^4 \rangle} = 5.6 \pm 0.8$ eV at room temperature. © *2003 MAIK "Nauka/Interperiodica".*

1. INTRODUCTION

The deformation of semiconductive crystals generally lowers their symmetry, which results in a shift of the energy band edges of a semiconductor and the redistribution of charge carriers [1–4]. A change in carrier energy is linear in strain and is determined by the values of deformation potential constants. These constants play a decisive role in the description of kinetic effects [1], and also in acoustooptical and acoustoelectronic processes [5]. However, the determination of numerical values of these constants presents considerable difficulties and sometimes is very approximate.

This study is devoted to a theoretical analysis of the redistribution of charge carriers in semiconductors with isoenergy surfaces described by a multivalley model, or by a model of corrugated spheres [1–4], and to the experimental determination of some of the deformation-potential constants in *n*- and *p*-type silicon.

2. REDISTRIBUTION OF ELECTRONS BY DEFORMATION IN A MULTIVALLEY MODEL

The contribution of charge carriers to the properties of lightly doped semiconductors is completely determined by a comparatively small number of electrons which transfer to the conduction band and by holes formed in the valence band. Therefore, almost all carriers are located at the levels near the extrema of corresponding bands.

It is known [1, 2] that the minima of the conduction band in undistorted silicon (valleys) in quasi-momentum space at a given energy have the form of ellipsoids of revolution oriented along the ⟨100⟩ axes. In an unstrained state, all valleys are equally occupied by electrons. Neglecting the term (equal for all valleys) caused by the isotropic compression of a crystal, the shift of a band edge under deformation can be expressed as [1]

$$\Delta E_c = \frac{1}{3}\Xi_u(2\varepsilon_{11} - \varepsilon_{22} - \varepsilon_{33}), \tag{1}$$

where Ξ_u is the deformation potential constant of the conduction band characterizing the influence of uniaxial deformation and ε_{ij} are the components of the strain tensor in the coordinate system linked to the principal axes of a chosen ellipsoidal isoenergy surface.

Let us consider the redistribution of electrons between six potential wells under the tension of a crystal along the [110] direction. We introduce a coordinate system (*x*, *y*, *z*) related to the principle crystal axes. In this system, for a given deformation, we have $\varepsilon_{xx} = \varepsilon_{yy}$ and $\Delta E_c^{[100]} = \Delta E_c^{[010]}$. For nonequivalent valleys, relation (1) takes the form

$$E_c^{[100]} = \frac{1}{3}\Xi_u(\varepsilon_{xx} - \varepsilon_{zz}); \quad E_c^{[001]} = -\frac{2}{3}\Xi_u(\varepsilon_{xx} - \varepsilon_{zz}). \tag{2}$$

In the nondegenerate case, the equilibrium ratio of populations is determined by the Boltzmann principle [1, 2]; i.e.,

$$\frac{n_{[100]}}{n_{[001]}} = \frac{\exp[-(E_c^0 + \Delta E_c^{[100]})/k_B T]}{\exp[-(E_c^0 + \Delta E_c^{[001]})/k_B T]} = \exp\left(-\frac{\Xi_u(\varepsilon_{xx} - \varepsilon_{zz})}{k_B T}\right), \tag{3}$$

1063-7826/03/3701-0015$24.00 © 2003 MAIK "Nauka/Interperiodica"

where E_c^0 is the energy of the valley bottom for an undeformed semiconductor, k_B is the Boltzmann constant, and T is the temperature.

The quantity $\varepsilon_{xx} - \varepsilon_{zz}$ can be expressed in terms of the relative tension of a crystal along the [110] direction [3]:

$$\varepsilon = \varepsilon_{[110]} - \frac{1}{2}(\varepsilon_{[1\bar{1}1]} + \varepsilon_{[\bar{1}12]}) = \frac{1}{2}(\varepsilon_{xx} - \varepsilon_{zz}) + \frac{3}{2}\varepsilon_{xy}. \quad (4)$$

Since the shear strain ε_{xy} equally affects all valleys (see (1)) and does not cause redistribution of electrons, we have

$$\varepsilon_{xx} - \varepsilon_{zz} = 2\varepsilon. \quad (5)$$

Expressions (3) and (5) and the electron conservation law $n_0 = 4n_{[100]} + 2n_{[001]}$ determine the equilibrium populations of valleys in a deformed semiconductor:

$$4n_{[100]} = \frac{2n_0\exp(-2\Xi_u\varepsilon/k_BT)}{2\exp(-2\Xi_u\varepsilon/k_BT) + 1};$$
$$2n_{[001]} = \frac{n_0}{2\exp(-2\Xi_u\varepsilon/k_BT) + 1}. \quad (6)$$

Redistribution of charge carriers under deformation results in an additional contribution to the elastic energy density of a crystal; this contribution is equal to the product of the change in electron energy (defined by Eqs. (2)–(5)) and the electron concentration (defined by Eq. (6)):

$$\Delta W = 4n_{[100]}\frac{2\Xi_u\varepsilon}{3} - 2n_{[001]}\frac{4\Xi_u\varepsilon}{3}$$
$$= -\frac{8n_0\Xi_u^2\varepsilon^2}{9k_BT} - \frac{8n_0\Xi_u^2\varepsilon^3}{27(k_BT)^2} + \frac{16n_0\Xi_u^4\varepsilon^4}{81(k_BT)^3}. \quad (7)$$

This quantity can be expanded into a series in powers of small parameter ε.

To clarify the meaning of the terms in expression (7), the nonlinear Hooke law and the elastic energy density can be written as

$$\sigma = E_0\varepsilon + \alpha\varepsilon^2 + \beta\varepsilon^3;$$
$$W = \frac{1}{2}E_0\varepsilon^2 + \frac{1}{3}\alpha\varepsilon^3 + \frac{1}{4}\beta\varepsilon^4. \quad (8)$$

Here, E_0 is the Young modulus, and α and β are the linear combinations of the third- and fourth-order moduli of elasticity. The addition of ΔW (7) to W (8), which alters the coefficients at different powers of ε, accounts for the influence of charge carriers on moduli of elasticity under the deformation of a crystal. Irrespective of the nature of the impurity, E_0 and α decrease linearly with increasing concentration of free electrons n_0, while β increases by

$$\Delta\beta = \frac{64n_0\Xi_u^4}{81(k_BT)^3}. \quad (9)$$

Moreover, the relative change of β is much greater than the change of low-order moduli. Indeed, the value of the deformation potential Ξ_u for silicon lies within the range from 8.5 to 9.57 eV [1, 4]. The ratio of moduli of elasticity of the crystals are about $\alpha/E_0 \approx -6$ and $\beta/E_0 \approx 200$ [6]. Consequently, in a semiconductor doped up to $n_0 = 10^{17}$ cm^{-3}, the relative change of moduli of elasticity at room temperature will be of the order

$$\frac{\Delta E_0}{E_0} \approx 5\times10^{-4}, \quad \frac{\Delta\alpha}{\alpha} \approx 10^{-2}, \quad \frac{\Delta\beta}{\beta} \approx 10^{-1}. \quad (10)$$

Therefore, in the following calculations we assume the Young modulus to be independent of the charge-carrier concentration.

It should also be emphasized that the modulus α in (8) is a coefficient when there is an odd power of elastic strain, therefore the alternating-sign contribution of this term to elastic energy depends on the sign of ε. For example, in the case of bending deformation, the upper part of a plate is compressed with respect to the neutral layer ($\alpha\varepsilon^3 < 0$), while the lower part is stretched ($\alpha\varepsilon^3 > 0$), so that averaging over the cross section yields zero. In contrast to this, any alternating-sign deformation for the term containing β results in the same change in W. This feature was used in this study for the determination of the contribution of nonlinear fourth-order moduli of elasticity.

3. REDISTRIBUTION OF HOLES UNDER DEFORMATION IN THE MODEL OF CORRUGATED SPHERES

The isoenergy surfaces in a silicon valence band are corrugated spheres. Being averaged over various directions of the wave vector k, they can be approximated by the spheres [2]

$$E_v^0 = -k^2(A \pm \sqrt{B^2 + C^2/6}), \quad (11)$$

where A, B, and C are the constants of the band structure; and the signs "+" and "–" correspond to the surfaces of light and heavy holes. In silicon, heavy holes predominantly contribute to elastic properties; the fraction of these holes amounts to 85% of their total number [1, 2].

In a high energy approximation, i.e., when the kinetic energy of charge carriers k_BT is considerably larger than band splitting due to the deformation ΔE_v, the distortion of the surface of heavy holes has the form [3]

$$\Delta E_v = \frac{1}{2}(E_v^0 + Ak^2)\{Bb[3(k_x^2\varepsilon_{xx} + k_y^2\varepsilon_{yy} + k_z^2\varepsilon_{zz}) - k^2(\varepsilon_{xx} + \varepsilon_{yy} + \varepsilon_{zz})] + 2Dd[k_xk_y\varepsilon_{xy} + k_xk_z\varepsilon_{xz} + k_yk_z\varepsilon_{yz}]\}. \quad (12)$$

Here, the term associated with isotropic compression of a semiconductor is omitted; b are d are the deformation potential constants for the valence band, $D^2 = C^2 + 3B^2$.

For the tension of a crystal along the [110] direction, we have

$$\Delta E_v^{[110]} = \frac{1}{2}(E_v^0 + Ak^2)[Bb(k^2 - 3k_z^2) \times (\varepsilon_{xx} - \varepsilon_{zz}) + 2Ddk_xk_y\varepsilon_{xy}]. \quad (13)$$

The components of the strain tensor should be expressed in terms of relative elongation along the [110] direction described by formula (4). For the tension in this direction, the following relation ensues from the theory of elasticity [7]:

$$\frac{(1/2)(\varepsilon_{xx} - \varepsilon_{zz})}{(3/2)\varepsilon_{xy}} = \frac{2c_{44}}{3(c_{11} - c_{12})}. \quad (14)$$

Here, $c_{11} = 165.7$ GPa, $c_{12} = 63.9$ GPa, and $c_{44} = 79.6$ GPa [8] are the values of the elastic stiffness constants for silicon. The ratio (14) is very close to 1 / 2.

Substituting expressions (4), (14), and (11) into formula (13), and performing conversion to the spherical coordinate system of the quasi-momentum space, we find that the change in energy becomes proportional to the strain

$$\Delta E_v^{[110]} = \frac{\sqrt{2}\varepsilon}{\sqrt{3(3B^2 + D^2)}}\left[Bb(1 - 3\cos^2\theta) + \frac{2}{3}Dd\sin^2\theta\sin 2\varphi\right] = \Phi(\varphi, \theta)\varepsilon; \quad (15)$$

therefore, it is possible to introduce the deformation potential Φ for a heavy-hole band.

In the high-energy approximation, carrier exchange between surfaces of light and heavy holes is impossible [3]; therefore, the carriers relax by executing transitions between different points of the same surface. The number of these carries in the element of a solid angle $d\Omega$ in the space of quasi-momenta in the absence of strains and for isotropic dispersion law (11) is equal to $(p_0/4\pi)d\Omega$, where p_0 is the total hole concentration within the surface. Redistribution of holes due to deformation is determined by the Boltzmann distribution

$$\frac{dp(\Omega)}{p_0 d\Omega} = \frac{\exp((E_v^0 + \Delta E_v^{[110]})/k_BT)}{\exp(E_v^0/k_BT)} = \exp\frac{\Delta E_v^{[110]}}{k_BT}. \quad (16)$$

The integration of the product of $dp(\Omega)$ into $\Delta E_v^{[110]}$ over the entire surface yields a deformation-induced change of the elastic energy

$$\Delta W = \frac{1}{4}p_0\int_\Omega \Delta E_v^{[110]}\exp\left(\frac{\Delta E_v^{[110]}}{k_BT}\right)d\Omega. \quad (17)$$

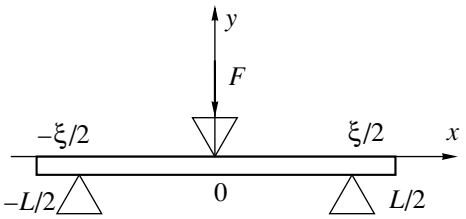

Fig. 1. Schematic diagram of crystal loading.

Expanding the exponent in (17) into a series in powers of ε and comparing the coefficient at the fourth-power term with formula (8), we obtain the increment of the fourth-order modulus of elasticity:

$$\Delta\beta = \frac{2p_0}{3(k_BT)^3}\frac{1}{4\pi}\int_\Omega \Phi^4 d\Omega = \frac{2p_0}{3(k_BT)^3}\langle\Phi^4\rangle. \quad (18)$$

In view of formula (15), integration of (18) yields

$$\langle\Phi^4\rangle = \frac{64}{315[(3B/D) + 1]^2} \times \left[3\left(\frac{B}{D}\right)^4 b^4 + \frac{4}{9}\left(\frac{B}{D}\right)^2 b^2 d^2 + \frac{16}{243}d^4\right]. \quad (19)$$

If deformation is directed along the [100] axis, the magnitude of $\langle\Phi^4\rangle$ is determined only by the constant b; for the [111] direction, only by the constant d. This provides the possibility of experimentally determining one of these constants from the concentration dependence of β.

4. EXPERIMENT, RESULTS, AND DISCUSSION

The modulus of elasticity β was measured by the self-excitation of longitudinal oscillations in a combined vibrator consisting of a single-crystal silicon bar elastically bent by the three-point method (Fig. 1) and piezoelectric transducers attached to the bar ends. Details of the experiment are described elsewhere [6, 9].

The silicon bars were cut from Czochralski-grown dislocation-free single-crystal *n*- and *p*- Si wafers with surfaces parallel to the (111) plane. The bars were cut along the [110] direction, which coincides with the x axis in Fig. 1. The parameters of the samples and the results obtained are given in Tables 1 and 2.

The change in resonance frequency f of a longitudinal wave in a combined vibrator [9] depends on the sagging deflection l of a silicon bar in the following way:

$$\frac{\Delta f}{f} = \frac{f - f_0}{f} = \frac{6h^2l^2\beta}{\xi^3 LE_0}. \quad (20)$$

Here, f_0 is the resonance frequency in a system with undeformed crystal, L and h are the length and width of a crystal bar, and ξ is the distance between the supports (Fig. 1).

Table 1. Parameters of *n*-type silicon bars doped with phosphorus

Sample parameters	Samples			
	1	2	3	4
Resistivity, Ω cm	30	0.1	0.05	0.03
Carrier concentration n_0, m^{-3}	2×10^{20}	9×10^{22}	3×10^{23}	8×10^{23}
Length L, mm	67	68	66	65
Width w, mm	11	12	14	12
Thickness h, μm	330	450	480	500
Distance between supports ξ, mm	65	65	61	60
Resonance frequency f_0, Hz	5253514	5343871	5243273	5578154
Modulus β_L, Pa	4.9×10^{13}	6.2×10^{13}	6.4×10^{13}	6.9×10^{13}

Table 2. Parameters of *p*-type silicon bars doped with boron

Sample parameters	Samples			
	1	2	3	4
Resistivity, Ω cm	3	0.5	0.1	0.05
Carrier concentration p_0, m^{-3}	4×10^{21}	4×10^{22}	5×10^{23}	1×10^{24}
Length L, mm	68	68	66	60
Width w, mm	10	12	14	12
Thickness h, μm	450	450	450	450
Distance between supports ξ, mm	67	65	60	55
Resonance frequency f_0, Hz	7695353	7635351	7832791	7057815
Modulus β_L, Pa	2.9×10^{13}	3.1×10^{13}	3.3×10^{13}	3.4×10^{13}

The experimental dependences of the frequency change Δf in the generation of longitudinal waves on the squared sagging deflection l^2 are shown in Fig. 2. The observed distinctions in the slopes for doped and lightly doped silicon of *n*- and *p*-types are caused by the contribution of charge carriers to the fourth-order modulus of elasticity (see formulas (9), (18)). As can be seen from formula (20), the slopes of the experimental curves allow the nonlinear β_L modulus for the doped samples to be determined (the lower index L); i.e.,

$$\beta_L = \beta_0 + \Delta\beta = \beta_0 + \frac{E_0 \xi_L^3 L_L}{6 f_L h_L^2} \left(\frac{\Delta f}{l^2} \right)_L, \qquad (21)$$

where β_0 is the fourth-order modulus of elasticity of an undoped semiconductor.

The Young modulus in silicon for the (111) plane, which is isotropic with respect to elastic properties, is equal to E_0 = 169 GPa [10]. Using this value and expression (21), we calculated the dependence of β_L on the concentration of charge carriers (see Table 2).

By using Eq. (9) and the slopes of the approximating straight line in Fig. 3, we found $\beta_0 = (3.8 \pm 0.6) \times 10^{13}$ GPa and the constant of the deformation potential Ξ_n of the conduction band for silicon at a temperature of T = 288 K. The value $\Xi_n = 7 \pm 1$ eV, obtained for the first time by concentration anharmonicity, correlates with the available data [1, 4].

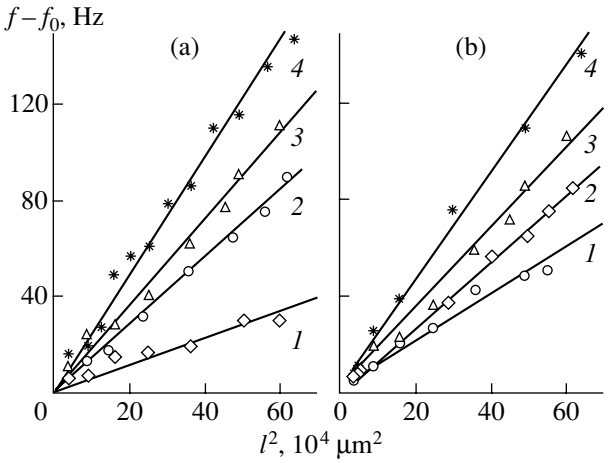

Fig. 2. Resonance frequency of the combined vibrator as a function of squared sagging deflection for silicon; (a) *n*-Si with resistivity ρ = (*1*) 30, (*2*) 0.1, (*3*) 0.05 and (*4*) 0.03 Ω cm; (b) *p*-Si with resistivity ρ = (*1*) 3, (*2*) 0.5, (*3*) 0.1, and (*4*) 0.05 Ω cm.

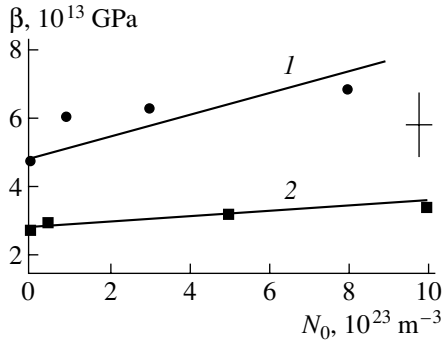

Fig. 3. Concentration dependence of the fourth-order elasticity modulus for (*1*) *n*- and (*2*) *p*-type silicon at $T = 288$ K. N_0 stands for the charge-carrirer concentration.

We will now clarify the applicability of the high-energy approximation (and, consequently, formula (18)) to *p*-type silicon. The kinetic energy of carriers at room temperature is $k_BT = 0.026$ eV, and the valence band splitting under deformation (formula (15)) is on the order of $b\varepsilon$, where $b \approx 2$ eV [4]. In our experiments, the strain in a bent bar at the point of maximum curvature (at $x = 0$, $y = h/2$, Fig. 1) is no greater than $\varepsilon = 0.0003$. Consequently, $b\varepsilon \approx 0.0006$ eV is considerably smaller than the kinetic energy of holes. Therefore, we can use Eq. (18) to calculate the deformation potential for the band of heavy holes as $\sqrt[4]{\langle \Phi^4 \rangle} = 5.6 \pm 0.8$ eV. This value is on the same order of magnitude as that reported in [2, 4] for Φ in silicon under tension along the [111] axis.

The procedure suggested in this study can be used to determine other constants of deformation potential by choosing the proper direction of deformation.

REFERENCES

1. K. Seeger, *Semiconductor Physics* (Springer-Verlag, Berlin, 1974; Mir, Moscow, 1977).
2. *Physical Acoustics: Principles and Methods*, Vol. IV: *Applications to Quantum and Solid State Physics*, Ed. by W. P. Mason (Academic, New York, 1966; Mir, Moscow, 1969).
3. G. L. Bir and G. E. Pikus, *Symmetry and Strain-induced Effects in Semiconductors* (Nauka, Moscow, 1972; Wiley, New York, 1975).
4. A. L. Polyakova, *Deformation of Semiconductors and Semiconductor Devices* (Énergiya, Moscow, 1979).
5. V. É. Gusev and A. A. Karabutov, *Laser Optical Acoustics* (Nauka, Moscow, 1991).
6. K. E. Nikitin, Fiz. Tverd. Tela (St. Petersburg) **36**, 3587 (1994) [Phys. Solid State **36**, 1909 (1994)].
7. L. D. Landau and E. M. Lifshitz, *Course of Theoretical Physics*, Vol. 7: *Theory of Elasticity* (Nauka, Moscow, 1987; Pergamon, New York, 1986).
8. *Physical Acoustics: Principles and Methods*, Vol. III, Part B: *Lattice Dynamics*, Ed. by W. P. Mason (Academic, New York, 1965; Mir, Moscow, 1968).
9. A. A. Skvortsov, A. M. Orlov, K. E. Nikitin, and O. V. Litvinenko, Pis'ma Zh. Tekh. Fiz. **26**, 82 (2000) [Tech. Phys. Lett. **26**, 974 (2000)].
10. Yu. A. Kontsevoĭ, Yu. M. Litvinov, and É. A. Fattakhov, *Plasticity and Strength of Semiconductor Materials and Structures* (Radio i Svyaz', Moscow, 1982).

Translated by A. Zalesskiĭ

Semiconductors, Vol. 37, No. 1, 2003, pp. 20–27. Translated from Fizika i Tekhnika Poluprovodnikov, Vol. 37, No. 1, 2003, pp. 22–28.

ELECTRONIC AND OPTICAL PROPERTIES OF SEMICONDUCTORS

Influence of Electronic (Charge) State of *E* Traps on Their Introduction Rate in Irradiated *n*-GaAs

V. N. Brudnyi* and V. V. Peshev**

** Kuznetsov Physicotechnical Institute, pl. Revolyutsii 1, Tomsk, 634050 Russia*

e-mail: brudnyi@ic.tsu.ru

*** Tomsk Polytechnical University, Tomsk, 634050 Russia*

Submitted March 14, 2002; accepted for publication April 24, 2002

Abstract—A complex temperature dependence of the introduction rate of *E* traps in the neutral and space-charge regions of Schottky diodes based on *n*-GaAs and subjected to high-energy irradiation was observed at 77–580 K in the situation where the recoil-atom energies were close to the threshold energies for radiation-defect production. The experimental data were interpreted quantitatively using a model of metastable Frenkel pairs. This model accounts for the processes of annihilation, recharging, and stabilization of a Frenkel pair in the material in relation to the electronic (charge) state of the Frenkel pair components; this state is governed by the position of the Fermi (quasi-Fermi) level and the sample temperature. © *2003 MAIK "Nauka/Interperiodica".*

1. INTRODUCTION

The influence of the electronic (charge) state of radiation defects on the processes of their formation and subsequent annealing in semiconductors has long attracted the attention of scientists. This attention is caused by the fact that the efficiencies of radiation-defect annihilation and migration in a semiconductor crystal lattice may depend to a great extent on the defects' charge state, which, in turn, can govern both the accumulation rates of these defects in the material and the types of radiation defects which are prevalent under the specified conditions of irradiation. Variations in the doping level or in the conductivity type of the material and the presence of neutral regions or space-charge regions (SCRs) in the material give rise to variation in the position of the Fermi (quasi-Fermi) level in reference to the levels of radiation defects, which can not only radically affect the efficiency of the defects' buildup but also govern the spectrum of radiation defects in the material. Originally, measurements of integral characteristics (such as the electrical conductivity and the carrier removal rate) were used to study the radiation effects in semiconductors with various levels of initial doping and different conductivity types. These studies were mainly concerned with elemental semiconductors, Si and Ge; notably, a high mobility of intrinsic lattice defects is characteristic of these materials at room temperature. As a result, the dominant radiation defects in these semiconductors are complexes involving intrinsic defects and chemical impurities and they come into existence as a result of secondary defect-formation processes [1]. The development of deep-level transient spectroscopy (DLTS) has opened up fresh opportunities for studying the efficiencies of radiation-defect buildup and annealing in the same material by changing the charge state of the defect; this state can be changed if the position of the quasi-Fermi level is varied by applying a reverse bias to the structure in the course of both irradiation and subsequent annealing of the sample. In contrast to previous measurements of the electrical conductivity and the magnitude of the Hall effect DLTS measurements make it possible to keep track of the evolution of specific radiation defects.

2. EXPERIMENTAL

In this paper, we report the results of studying the influence of the electronic (charge) state of so-called *E* traps [2] on the efficiency of the buildup of these traps in *n*-GaAs irradiated in a wide temperature range. Extensive experimental data on the parameters of these defects have been obtained; however, all measurements have been performed for neutral regions of semiconductor structures. In this study, we performed a comparative analysis of the efficiency of buildup of *E* traps in the neutral regions and SCRs of Schottky diodes based on *n*-GaAs irradiated with gamma quanta and various particles.

We may note that, even as far back as 1962, Aukerman and Graft [3] observed the effect of the Fermi level position on the outcome of annealing of radiation defects at temperatures in the vicinity of 500 K in *n*-GaAs irradiated with electrons; measurements of electrical conductivity were used. Subsequently [4], two types of radiation defects were identified in *n*-GaAs samples irradiated with fast neutrons and annealed in the aforementioned temperature region. These are (i) the defects whose annealing is sensitive to the position of the Fermi level in the band gap of the semiconductor and (ii) the defects that are insensitive to the Fermi level position; these specific characteristics of radiation

1063-7826/03/3701-0020$24.00 © 2003 MAIK "Nauka/Interperiodica"

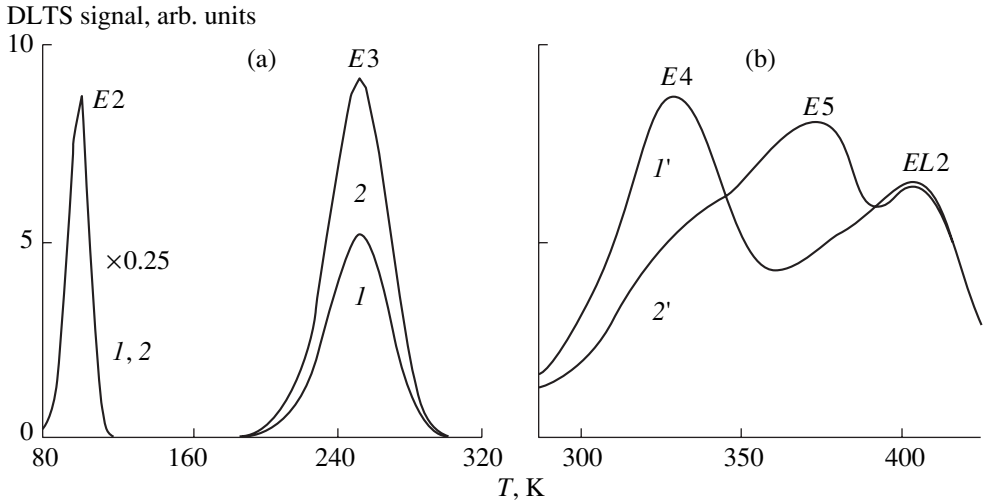

Fig. 1. The (a) low-temperature and (b) high-temperature regions of DLTS spectra for the Schottky diodes based on *n*-GaAs and irradiated with ^{60}Co gamma quanta (T = 300 K, $D = 6.5 \times 10^{16}$ cm^{-2}). Curves *1* and *1*' correspond to the data obtained for the Schottky diodes reverse-biased by a voltage of 9 V during irradiation; curves *2* and *2*' are for the diodes unbiased during irradiation. The *EL2* trap is related to a growth defect.

defects were attributed to special features of neutron irradiation, in particular, to formation of clusters of radiation defects [4]. It was shown later using DLTS [5] that the annealing stage under consideration corresponded to annihilation of *E* traps; moreover, using the example of an *E*3 trap, it was shown that the thermal stability of this particular defect at about 500 K depended on whether this defect is located in the neutral region or in the SCR of diodes based on *n*-GaAs. Mamontov *et al*. [6] showed for the first time that the electronic state of the *E* traps affects not only the efficiency of their subsequent annealing but also the rate of their buildup in the case of gamma-ray and electron irradiation [6].

In this paper, we generalize the previous results of our studies, which were aimed at gaining insight into the efficiency of the buildup of *E*3, *E*4, and *E*5 traps in the neutral region and SCR of Schottky diodes based on *n*-GaAs and subjected to irradiation in the temperature range of 77–580 K, and show that the observed special features of radiation-defect buildup can be accounted for quantitatively in the context of the model of metastable Frenkel pairs.

2.1. Samples and Experimental Procedure

In our studies, we used Au/Ti/*n*-GaAs(3×10^{15} cm^{-3})/n^+-GaAs(2×10^{18} cm^{-3}) structures, the active region of which was formed by vapor-transport epitaxy using an $AsCl_3$ system. The diodes were irradiated with ^{60}Co gamma-ray photons; 0.6- to 6.0-MeV electrons; protons with energies of 5, 10, and 63 MeV; 12.4-MeV deuterons; 22-MeV alpha particles; and fast neutrons from a pulsed nuclear reactor ($E \approx 1$ MeV). During irradiation, the diode structures were either unbiased (U = 0) or a reverse bias with a magnitude of up to 40 V was applied to these structures. After cessation of irradiation, the reverse voltage was switched off and then DLTS measurements were performed. Experiments showed that there was a difference between the efficiencies of buildup of the *E* traps in the neutral region and the SCR of Schottky diodes under conditions of isodose irradiation (Fig. 1). Since there are data on the electrodiffusion of certain growth defects in reverse-biased surface-barrier structures based on *n*-GaAs [7], we measured the profiles of *E* traps in the diodes irradiated with a reverse bias of various magnitudes that was applied to the structures. In addition, we studied the influence of external bias applied to the diodes irradiated without a bias applied on the DLTS signal (trap concentration) in these diodes during a postirradiation period equal to the irradiation time. These studies showed that the observed difference between the introduction rates of defects in the neutral region and the SCR could not be caused by the electrodiffusion of *E* traps under the specified experimental conditions [8].

2.2. Model-based Estimates

In order to interpret the experimental dependences of the buildup efficiency on various factors for the *E* traps in the neutral region and SCR of diodes, we used the model of metastable Frenkel (vacancy–interstitial) pairs; in this model, it is assumed that the Frenkel pairs that formed during irradiation can, with certain probability, either annihilate or separate, depending on the ratio between the corresponding barrier heights and the value of *kT*. It should be noted that this model was suggested at the inception of studies of radiation defects and was aimed at explaining the experimental data obtained under various irradiation condi-

tions (variations in the sample temperature, the radiation flux density, and the doping level of the material) [9, 10]. A detailed analysis of such models and their applicability to various semiconductors can be found in the book by Emtsev and Mashovets [11]. Numerous experiments have shown that, due to a high mobility of intrinsic defects in elemental semiconductors, secondary processes of defect formation acquire great importance; these processes include the formation of complexes that consist of radiation defects and chemical impurities and clusterization of intrinsic defects (e.g., formation of divacancies in Si). As a result, the model of metastable Frenkel pairs has been used mainly for low-temperature experiments.

The applicability of the metastable-pair models to GaAs, including the case where irradiation is performed at temperatures around 300 K, is based on the following factors: (i) the experimental introduction rates of E traps in neutral regions of diodes based on n-GaAs are close to calculated rates, and the energy spectrum of these traps is almost independent of irradiation temperature (4–300 K), impurity types in the material, and the method of its growth [2]; and (ii) experimentally determined energy released during annealing of a radiation defect at temperatures in the region of 500 K is equal to about 8 eV [12] and is close to theoretical estimates of the energy stored per Frenkel pair [13, 14] and to the threshold energy for the formation of E traps (approximately 10 eV) [2]. All of this suggests that the E traps observed in n-GaAs can be assigned to the simplest intrinsic lattice defects. Moreover, a study of the orientation effects at the energies of bombarding electrons of 0.2–0.5 MeV [2] and the independence of the introduction rate of the E traps from the composition of the $Ga_{1-x}Al_xAs$ [15] solid solution made it possible to relate these traps to the Frenkel pairs of the V_{As}–I_{As} type, which have various distances between the components of the pair [2].

In quantitative estimations, we have taken into account that a Frenkel pair is formed in several stages. In the first stage, a protopair in the (V^-, I^+) charge state is formed in a time which is close to the characteristic time of interaction between a bombarding particle and a lattice atom (the latter time is on the order of 10^{-14} s) [16]. The protopair can then either annihilate or transform into the stationary charge state in a time $\tau \approx [e_n^{V,I} + k_p^{V,I}]^{-1} + [e_p^{V,I} + k_n^{V,I}]^{-1}$, which is governed by irradiation conditions, i.e., by the position of the Fermi (quasi-Fermi) level in reference to the defect levels and by the sample temperature (here, $e_{np}^{V,I}$ and $k_{np}^{V,I}$ are the rate constants for the emission and capture of electrons and holes for a vacancy (V) or an interstitial atom (I), respectively). Thus, the concentrations of Frenkel pairs in different charge states may vary owing both to recombination in the course of irradiation and to recharging of these pairs; as a result, the pairs are transformed into the stationary charge state by capturing (emitting) the electrons (holes) with subsequent possible annihilation of the pair.

Since the aforementioned processes depend on the spatial separation of the Frenkel pair components, we studied the distribution of the pairs using the mean distance between the components ($\langle r \rangle$) as a function of the mean energy of recoil atoms ($\langle E \rangle$). To this end, we took into account that $\langle E \rangle \approx E_m \ln(E_m/E_d)$ for irradiation with charged particles and $\langle E \rangle \approx (E_m - E_d)/2$ for irradiation with neutrons, where E_m is the highest recoil-atom energy and E_d is the threshold energy for the atom displacement. Using the expression $r_f = (1/\pi r_0^2 N_0)\ln(E_0/E_f)$, where E_0 is the initial energy of a recoil atom, r_0 is the collision radius, and E_f is the recoil-atom energy after this atom has traversed the distance r_f [17], we can derive a relation for estimating the mean distance between the components of a Frenkel pair; i.e., $\langle r \rangle \approx (1/\pi r_0^2 N_0)\{\ln[(\langle E \rangle - E_d + E_M)/E_M + 1]\}$ or $\langle r \rangle \approx 0.5a\{\ln[(\langle E \rangle - E_d + E_M)/E_M + 1]\}$, where E_M is the barrier height for the migration of defects in the lattice and a is the lattice constant. These estimates, as applied to the $E3$ trap in GaAs ($E_d \approx 10$ eV and $E_M \approx 1.5$ eV, with a being equal to 0.564 nm), made it possible to plot experimental dependences of the ratio between the introduction rates of $E3$ traps into the SCRs and neutral regions of the Schottky diodes versus $\langle E \rangle$ and $\langle r \rangle/a$ (Fig. 2). It follows from these data that, for $\langle E \rangle \approx 80$–$90$ keV and $\langle r \rangle/a > 2.5$, the rates of introduction of the $E3$ traps into the SCRs and neutral regions of the Schottky diodes become equal. In contrast, for $\langle E \rangle < 80$–90 keV ($\langle r \rangle/a < 2.5$), we have pairs for which the rates of introduction into the neutral region and SCR of a diode differ, with this difference increasing as the $\langle r \rangle/a$ ratio decreases. In what follows, we will refer to these pairs as closely spaced pairs. Since the value of $\langle E \rangle \approx E_d (\approx 10$ eV) is close to the threshold energy for formation of E traps in GaAs irradiated with ^{60}Co gamma quanta, a large portion of protopairs formed under gamma-quantum irradiation are closely spaced pairs, which can either annihilate or be recharged and convert into a stationary charge state, depending on the irradiation conditions. As the recoil-atom energy increases, the fraction of protopairs with large separation of their components increases, so that the probability of annihilation for such pairs decreases. Thus, by varying the recoil-atom energy and the position of the Fermi (quasi-Fermi) level in the neutral region and SCR, we can change the lifetime of Frenkel pairs in different charge states depending on the sample temperature. According to the data shown in Fig. 2b, Frenkel pairs with closely spaced components can be conventionally divided into two groups: (I) pairs with $\langle r \rangle/a < 1.25$ ($\langle r \rangle \leq 0.6$ nm), for which the rates of their introduction into the neutral region and SCR differ appreciably; and (II) pairs with $\langle r \rangle/a > 1.25$ ($\langle r \rangle > 0.6$ nm), for which this difference is of lesser importance. We used

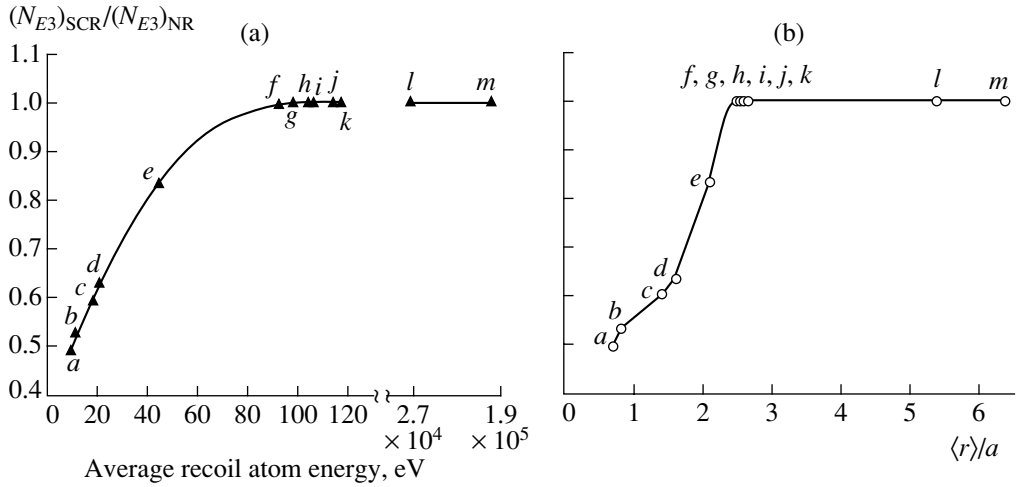

Fig. 2. Dependences of the ratio between the concentrations of the *E*3 centers in the space-charge region (SCR) and in the neutral region (NR) on (a) the average recoil-atom energy and (b) the mean distance between the Frenkel pair components *r* divided by the GaAs lattice parameter *a*. GaAs was irradiated with (*a*, *b*, *c*, *d*, and *e*) electrons with energies *E* = 0.33, 0.56, 1, 1.4, and 6 MeV, respectively; (*f*, *g*, and *j*) protons with energies *E* = 5, 10, and 63 MeV, respectively; (*h* and *k*) alpha particles with energies *E* = 5.1 and 22 MeV; (*i*) 12.4-MeV deuterons; and (*l* and *m*) neutrons with *E* = 1 and 7 MeV.

the above reasoning to construct diagrams of the corresponding reactions for the neutral region and SCR and to choose the parameters of these reactions.

The processes of buildup, recharging, and annealing of radiation defects in the neutral region can be represented in the following way:

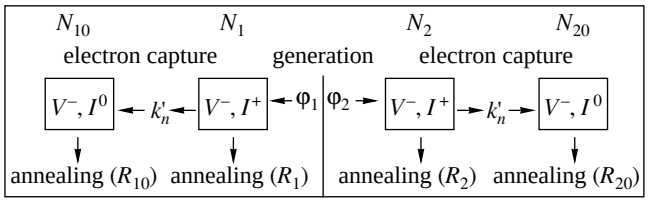

Here, N_1 and N_2 are the concentrations of protopairs of types I and II, respectively; φ_1 and φ_2 are the generation rates of these protopairs; N_{10} and N_{20} are the corresponding concentrations of these pairs in the equilibrium charge states 1 and 2; and $k_n^1 = n\langle v\rangle\sigma_1$ is the rate of electron capture by an interstitial atom, where n is the electron concentration in the conduction band, $\langle v\rangle$ is the thermal velocity of electrons, and σ_1 is the cross section of electron capture by an interstitial atom. According to the theory of annealing of correlated pairs, we have taken into account that, if we consider the pairs with closely spaced components and if the mobility of one of the components (supposedly, the interstitial atom) is higher than that of the other component, the following relation is valid: $R_i(T) = \nu_i\exp(-E_i/kT)$; here, $R_i(T)$ is the annealing-rate constant, ν_i is the frequency factor, and E_i is the barrier for recombination. We have also taken into account that the barrier height depends on electrostatic interaction between *V* and *I*.

Similarly, the scheme of the corresponding reactions proceeding in the SCR can be represented by the following diagram:

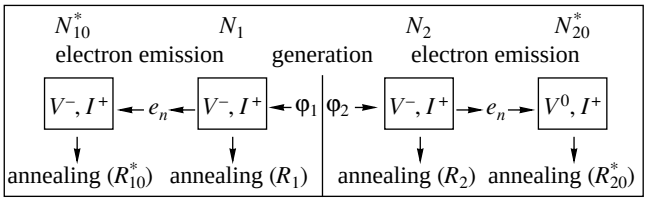

Here, N_{10}^* and N_{20}^* are the concentrations of pairs I and II in the stationary charge state; and $e_n^V = b\sigma_V T^2\exp(-E_V/kT)$ is the rate of electron emission from the trap level E_V to the conduction band, where σ_V is the emission cross section and $b = 2.28\times10^{20}$ cm^{-2} s^{-1} K^{-2} for GaAs.

On the basis of the above models, we numerically processed the temperature dependences of the buildup efficiencies for the *E*3, *E*4, and *E*5 traps in the neutral region and SCR of the *n*-GaAs Schottky diodes under irradiation.

2.3. Studies of Temperature Effects

2.3.1. The *E*3 trap (E_c – 0.38 eV). The *E*3 trap is a deep-level acceptor (supposedly, V_{As}) and is formed in irradiated GaAs as a result of a single displacement of an atom in the As sublattice [18]. The parameters of this defect in the neutral region have been much studied [2]. It has been shown that, in GaAs irradiated with 1-MeV electrons, the *E*3 traps are annealed at about 500 K more efficiently in the neutral region of diodes than in the SCR [5]. Mamontov *et al*. [6] were the first to find that the efficiencies of buildup of this trap in the neutral

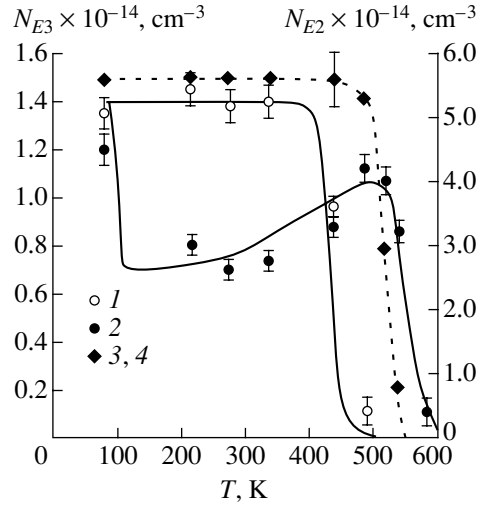

Fig. 3. Temperature dependences of concentrations of the (*1*, *2*) $E3$ and (*3*, *4*) $E2$ centers in the (*1*, *3*) neutral and (*2*, *4*) space-charge regions of diodes subjected to isodose irradiation with ^{60}Co gamma quanta ($D = 1.4 \times 10^{17}$ cm^{-2}, $t_{irr} = 1.5 \times 10^5$ s). The circles and diamonds represent experimental data; the solid and dashed lines correspond to the results of calculations based on Eqs. (1)–(8).

region and in the SCR of Schottky diodes based on *n*-GaAs and irradiated with ^{60}Co gamma quanta differ significantly. An increase in the recoil-atom energy (in the sequence of irradiations with electrons with $E >$ 6 MeV, protons, alpha particles, deuterons, and fast neutrons) causes the introduction rates of $E3$ traps in the neutral region of Schottky diodes to become equal to those in the corresponding SCR [19], which supposedly results from a larger separation of V from I under given irradiation conditions. This phenomenon was studied in detail by us in a wide temperature range for diodes irradiated with ^{60}Co gamma quanta [20]. It follows from experimental data and the results of simulations shown in Fig. 3 for gamma-ray irradiation that the efficiency of buildup of the $E3$ trap (and, for the sake of comparison, the $E2$ trap) in the neutral region is independent of the temperature of the irradiated sample in the range of 77–470 K. At higher temperatures, the introduction rate for these defects decreases, which is related to their annealing at temperatures in the vicinity of 500 K. As follows from Fig. 3, the temperature dependence of the introduction rate for the $E3$ trap in an SCR has a complex form.

In order to quantitatively interpret the obtained data, we used a model in which it is taken into account that the $E3$ trap determined from the DLTS measurements is related to V_{As} perturbed by the presence of neighboring I_{As} [2]. In the neutral region of the diode under investigation, the Fermi level is located higher than $E_c - 0.38$ eV in the band gap, so that the stationary charge state of the acceptor level of this trap corresponds to $E3^-$, whereas the position of the Fermi level in the band gap of the SCR is lower than $E_c - 0.38$ eV, which corresponds to the $E3^0$ state. There is no reliable data on the position of the I_{As} level in the band gap of GaAs. For the model we are using, it is necessary that I_{As} be a donor with a deep level in the lower half of the band gap.

On the basis of the scheme of reactions for the neutral region, we can write the corresponding kinetic equations, the solutions to which have the following form for the $E3$ centers in the neutral region under the condition that $R_{10} = R_{20}$:

$$N_1(T, t) = \varphi_1\{1 - \exp[-(k_n^I + R_1)t]\}/(k_n^I + R_1), \quad (1)$$

$$N_2(T, t) = \varphi_2\{1 - \exp[-(k_n^I + R_2)t]\}/(k_n^I + R_2), \quad (2)$$

$$\begin{aligned} N_{10}(T, t) &= \varphi_1 k_n^I\{[1 - \exp(-R_{10}t)]/R_{10} \\ &+ \{\exp[-(k_n^I + R_1)t] - \exp[-R_{10}t]\}/(k_n^I \\ &+ R_1 - R_{10})\}/(k_n^I + R_1), \end{aligned} \quad (3)$$

$$\begin{aligned} N_{20}(T, t) &= \varphi_2 k_n^I\{[1 - \exp(-R_{10}t)]/R_{10} \\ &+ \{\exp[-(k_n^I + R_2)t] - \exp[-R_{10}t]\}/(k_n^I \\ &+ R_2 - R_{10})\}/(k_n^I + R_2). \end{aligned} \quad (4)$$

Kinetic equations for the SCR can be written similarly; under the condition that $R_{10}^* = R_{20}^* \approx R_2^* = R_2$, these equations have the following solutions:

$$N_1(T, t) = \varphi_1\{1 - \exp[-(e_n^V + R_1)t]\}/(e_n^V + R_1), \quad (5)$$

$$N_2(T, t) = \varphi_2\{1 - \exp[-(e_n^V + R_2)t]\}/(e_n^V + R_2), \quad (6)$$

$$\begin{aligned} N_{10}^*(T, t) &= \varphi_1 e_n^V\{[1 - \exp(-R_2t)]/R_2 \\ &+ \{\exp[-(e_n^V + R_1)t] - \exp[-R_2t]\}/(e_n^V \\ &+ R_1 - R_2)\}/(k_n^I + R_1), \end{aligned} \quad (7)$$

$$\begin{aligned} N_{20}^*(T, t) &= \varphi_2 e_n^V\{[1 - \exp(-R_2t)]/R_2 \\ &+ \{\exp[-(e_n^V + R_2)t] - \exp[-R_2t]\}/e_n^V\}/(e_n^V + R_2). \end{aligned} \quad (8)$$

Substituting the irradiation time $t = t_{irr} = 1.5 \times 10^5$ s into the above solutions, we can obtain calculated temperature dependences (see Fig. 3) for the $E3$ trap in the situation where GaAs is irradiated with ^{60}Co gamma quanta; the following parameter values were used in calculations: $E_V = 0.38$ eV, $\sigma_V = 6.2 \times 10^{-15}$ cm^2, $\sigma_I = 1.9 \times 10^{-12}$ cm^2, $E_2 = 1.75$ eV, $\nu_2 = 10^{11}$ s^{-1}, $E_{10} = E_{20} =$ 1.55 eV, $\nu_{10} = \nu_{20} = 10^{13.5}$ s^{-1}, $\varphi = 9.4 \times 10^8$ cm^{-3} s^{-1}, and $\varphi_1/\varphi_2 \approx 1$. Most of the above-listed parameters (E_V, σ_V, E_2, $E_{10} = E_{20}$, and φ) are consistent with known results of calculations [2] and experimental data; other adjustable parameters have reasonable values. In the general case, the shape of the temperature-dependence curves for the efficiency of buildup for the $E3$ traps in the neutral region and the SCR depends on the irradiation intensity (for the same concentration of introduced

defects). As the duration of isodose irradiation is decreased, the calculated curves shift to higher temperatures.

Qualitatively, the obtained temperature dependence of the introduction rate of *E*3 centers in the SCR can be explained in the following way. In the low-temperature region ($T < 80$ K), pairs of type I are "frozen," since the recombination time $\tau_R(1/R_1) > t_{irr} = 1.5 \times 10^5$ s. In the temperature range of 80 K < T < 200 K, N_1 pairs recombine intensely, which manifests itself in a decrease in the introduction rate of *E*3 centers. In the temperature range of 200 K < T < 490 K, electrons are emitted from the level of V_{As} to the conduction band, which leads to a decrease in the concentration of charged pairs N_1 and to an increase in the concentration of neutral (more stable) pairs N_{10}^*. As a result, the introduction rate for the *E*3 centers increases. Indeed, since $N_1 \longrightarrow 0$ with increasing irradiation temperature, most Frenkel pairs should disappear with the annealing-rate constants $R_{10}^* = R_{20}^* \approx R_2^* = R_2$, which is conducive to the survival of an *E*3 trap in the temperature range under consideration. Finally, at $T > 500$ K, the intense annealing of *E*3 centers sets in.

A similar analysis can be performed in order to describe the temperature dependence of the introduction rate for the *E*3 traps in the neutral region of Schottky diodes. A high introduction rate of the *E*3 traps in the neutral region in the temperature range of 77–500 K is caused by the fact that the time of capture of a conduction-band electron by an *E*3 center (the time necessary for conversion of this center to the stationary charge state) is shorter than the time constant for annihilation of a pair through the barrier *E*1. It also follows from the results of the analysis that, in the well-known annealing stage in the vicinity of 500 K, the fraction of *E*3 defects residing in the SCR and having an annealing-activation energy of 1.75 eV increases in comparison with the traps annealed with an activation energy of 1.55 eV, which manifests itself in a corresponding shift of the curves describing the introduction rate for the *E*3 traps to higher temperatures (see Fig. 3).

2.3.2. The *E*4 trap (E_c – 0.76 eV). This trap is also related to a defect in the As sublattice. However, the trap under consideration has a number of special features, namely, the characteristics of its annealing differ from those of other *E* traps, the threshold energy of its formation has not been accurately determined, and the *E*4 center is not susceptible to recombination annealing [21]. It is assumed that this defect has a more complex structure than that of other *E* traps and belongs to the class of associated defects. It has also been shown that an increase in the energy of bombarding electrons leads to a more efficient buildup of *E*4 traps in the neutral region of diodes compared to the buildup of *E*3 and *E*5 traps, which indicates that the threshold energy of formation of the *E*4 defect is higher [22]. In addition, it is found that the introduction rate for the *E*4 trap is higher in the neutral region than in the SCR when the diodes are irradiated with 1-MeV electrons at 300 K (Fig. 4); these data differ from those for the *E*3 trap (Fig. 3). Temperature dependences of the introduction rate for the *E*4 defect in the temperature range of 77–500 K also differ from those for the *E*3 trap. Specifically, the introduction rate for *E*4 traps in the neutral region increases with increasing temperature, which indicates that formation of this defect is activation-controlled (Fig. 4). These experiments demonstrate that the formation of the *E*4 defect requires higher recoil-atom energies and irradiation temperatures. We may assume that, in order to form the defect under consideration, two neighboring atoms should be displaced in a single collision event with the subsequent formation of an associated center. A plausible model for formation consists in the following. As a result of a single displacement event, two neighboring Frenkel pairs come into existence with the subsequent formation of an associated defect (a complex). The latter may be represented by $V_{Ga} - V_{As}$ or $V_{As} - V_{As}$ divacancies. However, the fact that the formation of a *E*4 defect requires overcoming a potential barrier makes a model involving an antisite defect (in particular, the $As_{Ga} - V_{As}$ defect, which has been identified in irradiated GaAs using the ESR method [23]) preferential. Notably, the *E*4 defect is formed in the SCR almost athermally, which is possibly caused by a lowering of the barrier of formation of this defect as a result of the Coulomb interaction between V_{Ga}^- and I_{As}^+. By contrast, the formation of the defect under consideration in the neutral region requires overcoming a potential barrier with a height of 0.02–0.03 eV (Fig. 4).

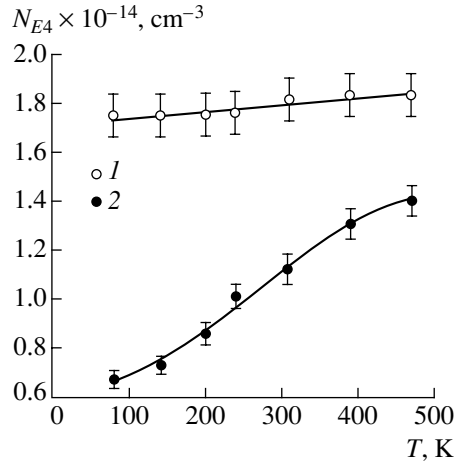

Fig. 4. Experimental temperature dependences of the concentration of *E*4 centers in the (*1*) space-charge and (*2*) neutral regions of diodes subjected to isodose irradiation with electrons (E = 1 MeV, $D = 1.2 \times 10^{15}$ cm^{-2}, t_{irr} = 180 s).

2.3.3. The *E*5 trap (E_c – 0.90 eV). The characteristics of the introduction rate for *E*5 traps are quite similar to those of *E*3 traps; specifically, the parameters of

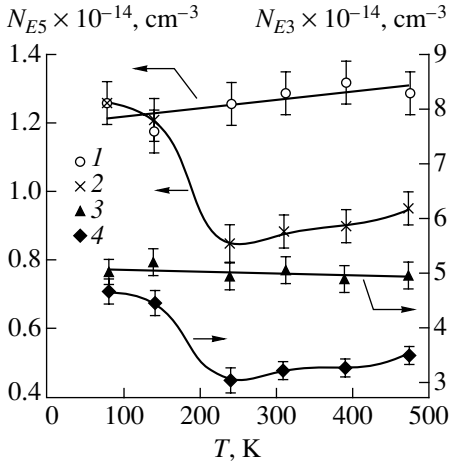

Fig. 5. Experimental temperature dependences of concentrations of the (*1*, *2*) *E*5 and (*3*, *4*) *E*3 centers in the (*1*, *3*) neutral and (*2*, *4*) space-charge regions of diodes subjected to isodose irradiation with electrons (E = 1 MeV, D = 1.2×10^{15} cm^{-2}, t_{irr} = 180 s).

500-K annealing of these traps in the neutral region of the diodes coincide, the annealing rates for both traps in the SCR are lower than those in the neutral region, and the buildup efficiency of these traps introduced by electron irradiation at 300 K into the neutral region is approximately twofold higher than those introduced by gamma-ray irradiation into the SCR. Temperature dependences of the introduction rates for the *E*3 and *E*5 traps in the neutral region and SCR of the Schottky diodes based on *n*-GaAs and exposed to 1-MeV electron irradiation are shown in Fig. 5. It can be seen that the data for the traps *E*3 and *E*5 are almost identical and are qualitatively similar to the data shown in Fig. 3 for the *E*3 trap in the case of gamma-quantum irradiation, which is consistent with the model concepts developed for the *E*3 trap. The main difference between the data shown in Fig. 5 and those shown in Fig. 3 consists in the fact that the temperature dependences of the introduction rate for the *E* traps in the SCR are much less pronounced in the case of electron irradiation. These results can be easily interpreted using the data shown in Fig. 2, according to which the value of $\langle E \rangle$ is larger for 1-MeV electron irradiation than for ^{60}Co gamma-quantum irradiation ($E \approx 0.56$ MeV); this circumstance gives rise to a certain equalization of the rates of introduction of the traps into the neutral region and SCR. As the value of $\langle E \rangle$ increases further, the introduction rates for the traps in the neutral region and SCR become exactly the same.

3. CONCLUSION

Our studies have shown that the introduction rate for the *E* traps in the neutral region of Schottky diodes based on *n*-GaAs and irradiated with particles whose energies are close to the threshold energies for radiation-defect production differs significantly from the corresponding rate in the space-charge region in a wide temperature range. We observed a complex temperature dependence of the introduction rate for the *E*3 and *E*5 traps in the space-charge region of diodes and for the *E*4 defect in the corresponding neutral region. As a result of an increase in the recoil-atom energy (an increase in the bombarding-electron energy or irradiation with protons, alpha particles, and fast neutrons), the introduction rates of *E* traps in the neutral regions of diodes tend to become equal to those in the space-charge regions, which is caused by a wider separation of the Frenkel pair components with increasing recoil-atom energy. Thus, the introduction rates for the *E* traps in *n*-GaAs irradiated with particles whose energies are close to the threshold energies for the displacement of lattice atoms depend heavily on the position of the Fermi (quasi-Fermi) level in reference to the radiation-defect levels. This circumstance should be taken into account when studying the effects of high-energy radiation on semiconductor structures that contain regions differing in their doping level and conductivity type, i.e., neutral and space-charge regions. Moreover, experimental data show that, when studying the dose dependences of the GaAs electrical parameters, one should keep in mind the following circumstance: the introduction rates for the *E* traps may vary as the Fermi level position changes and approaches its limiting (pinned) position in the vicinity of E_V + 0.6 eV in the band gap of irradiated GaAs [24].

REFERENCES

1. L. S. Smirnov, *Physical Processes in Irradiated Semiconductors* (Nauka, Novosibirsk, 1977).
2. D. Pons and J. C. Bourgoin, J. Phys. C **18** (20), 3839 (1985).
3. L. W. Aukerman and R. D. Graft, Phys. Rev. **127**, 1576 (1962).
4. L. W. Aukerman, in *Semiconductors and Semimetals*, Ed. by R. K. Willardson and A. C. Bear (Academic, New York, 1968), Vol. 4, p. 343.
5. D. Pons, Inst. Phys. Conf. Ser. **59**, 269 (1981).
6. A. P. Mamontov, V. V. Peshev, and I. P. Chernov, Fiz. Tekh. Poluprovodn. (Leningrad) **16** (12), 2126 (1982) [Sov. Phys. Semicond. **16**, 1371 (1982)].
7. S. L. Pearton and A. J. Tavendale, Phys. Status Solidi A **73**, K75 (1982).
8. A. P. Mamontov and V. V. Peshev, Fiz. Tekh. Poluprovodn. (Leningrad) **19** (1), 147 (1985) [Sov. Phys. Semicond. **19**, 90 (1985)].
9. G. K. Wertheim, Phys. Rev. **115** (3), 568 (1959).
10. J. W. Mackay and E. E. Klontz, in *Radiation Effects in Semiconductors*, Ed. by F. L. Vook (Plenum, New York, 1968), p. 175.
11. V. V. Emtsev and T. V. Mashovets, *Impurities and Point Defects in Semiconductors* (Radio i Svyaz', Moscow, 1981).

12. L. H. Lim, Y. J. von Bardeleben, and J. C. Bourgoin, Phys. Rev. Lett. **58**, 2315 (1987).
13. G. A. Baraff and M. Schluter, Phys. Rev. Lett. **55**, 1327 (1985).
14. P. Pons and J. C. Bourgoin, J. Phys. C **38**, 7839 (1985).
15. S. Loualiche, G. Guiillot, A. Nouilhat, and J. C. Bourgoin, Phys. Rev. B **26** (12), 7090 (1982).
16. J. W. Corbett, J. C. Bourgoin, and W. C. Weigel, Inst. Phys. Conf. Ser. **16**, 1 (1973).
17. V. L. Vinetskiĭ and G. A. Kholodar', *Radiation Physics of Semiconductors* (Naukova Dumka, Kiev, 1979).
18. D. Pons and J. C. Bruemer, Phys. Rev. Lett. **47**, 1293 (1981).
19. A. P. Mamontov and V. V. Peshev, Fiz. Tekh. Poluprovodn. (Leningrad) **17** (10), 1771 (1983) [Sov. Phys. Semicond. **17**, 1131 (1983)].
20. V. N. Brudnyi and V. V. Peshev, Phys. Status Solidi B **118** (1), 219 (1990).
21. D. Stievenard and J. C. Bourgoin, Phys. Rev. B **33**, 8410 (1986).
22. V. N. Brudnyi and V. V. Peshev, Phys. Status Solidi A **105**, K57 (1988).
23. H. J. von Bardeleben and J. C. Bourgoin, Phys. Rev. B **38**, 2800 (1980).
24. V. N. Brudnyi, S. N. Grinyaev, and V. E. Stepanov, Physica B (Amsterdam) **202**, 429 (1995).

Translated by A. Spitsyn

Semiconductors, Vol. 37, No. 1, 2003, pp. 28–30. Translated from Fizika i Tekhnika Poluprovodnikov, Vol. 37, No. 1, 2003, pp. 29–31.

SEMICONDUCTOR STRUCTURES, INTERFACES, AND SURFACES

Study of Photocapacitance in Diodes Fabricated from Silicon Doped with Vanadium

Kh. T. Igamberdiev, A. T. Mamadalimov, R. A. Muminov, T. A. Usmanov, and Sh. A. Shoyusupov

Ulugbek National University of Uzbekistan, Tashkent, 700174 Uzbekistan

Submitted March 12, 2002; accepted for publication March 28, 2002

Abstract—The levels of vanadium in the band gap of *n*- and *p*-Si were determined using photocapacitance measurements. It is shown that vanadium introduces levels only in the upper half of the band gap of *n*-Si; these levels have ionization energies of about $E_c - 0.21$ eV, $E_c - 0.32$ eV, and $E_c - 0.52$ eV. By contrast, V levels are located both in the upper and lower halves of the *p*-Si band gap: $E_c - 0.26$ eV, $E_v + 0.52$ eV, $E_v + 0.42$ eV, and $E_v + 0.31$ eV. It is ascertained that the photoionization cross sections of all vanadium levels are larger for electrons than for holes. It is shown that the concentration of electrically active vanadium centers in *n*- and *p*-Si depends on both the concentration of shallow-level impurities and the time of vanadium diffusion into Si. © *2003 MAIK "Nauka/Interperiodica".*

Vanadium levels in the silicon band gap have been inadequately studied so far [1–4]. The ionization energies for these levels reported in several publications are indicated in Fig. 1a. Henceforth, we report the results of using the photocapacitance method to study the characteristics of silicon doped with vanadium.

Crystals of Si:P and Si:B with a resistivity ρ = 5–100 Ω cm were doped with vanadium using diffusion from a vanadium layer deposited onto the silicon surface; the diffusion was performed for 2–20 h at T = 1200–1250°C with subsequent cooling in atmospheric air at a rate of about 10 K/s. The diffusion coefficient of vanadium in silicon varies from 3.4×10^{-11} to 4.4×10^{-10} cm^2/s as the temperature increases from 1100 to 1250°C [5]. The resistivity of *n*- and *p*-Si increased insignificantly after vanadium diffusion. This indicates that both acceptor and donor levels are formed in the silicon band gap as a result of doping with vanadium.

The Schottky barriers that formed after vanadium diffusion were used as rectifying contacts to the *n*-Si:V samples. These barriers were obtained via the vacuum evaporation of gold onto the *n*-Si surface. In the *p*-Si samples, *p–n* junctions were preliminarily formed by diffusion of phosphorus for 30 min at a temperature of 1250°C. The depth of the *p–n* junctions did not exceed 3–4 μm. The parameters and concentrations of the levels were determined from measurements of photocapacitance [6, 7].

The concentration of electrically active vanadium centers depends on the conductivity type of as-grown silicon crystals. We found that the concentration of electrically active vanadium centers decreased in *p*-Si as the boron concentration increased, whereas the concentration of these centers increased in *n*-Si as the phosphorus concentration increased.

In Fig. 2, we show the photocapacitance spectra of diodes based on *n*-Si:V. The measured values of the increment in the capacitance ΔC were recalculated to the concentration of vanadium centers N using the conventional method. It can be seen from Fig. 1b that vanadium introduces three levels into the upper half of the band gap; the ionization energies of these levels are

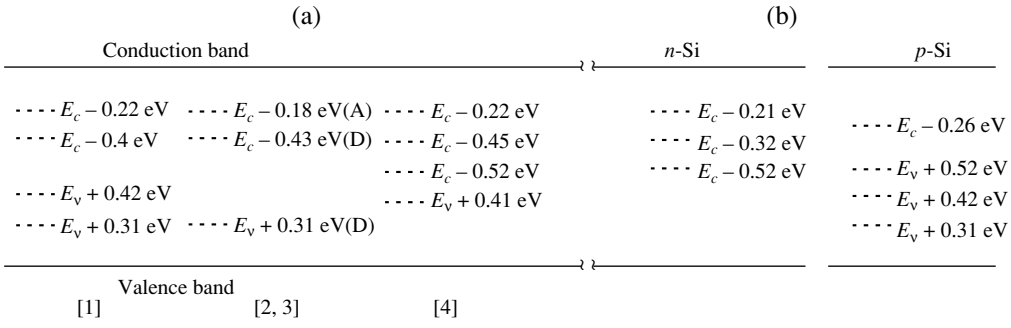

Fig. 1. Ionization energies of vanadium levels in silicon according to (a) the data reported in [1–4] and (b) the results of this study.

1063-7826/03/3701-0028$24.00 © 2003 MAIK "Nauka/Interperiodica"

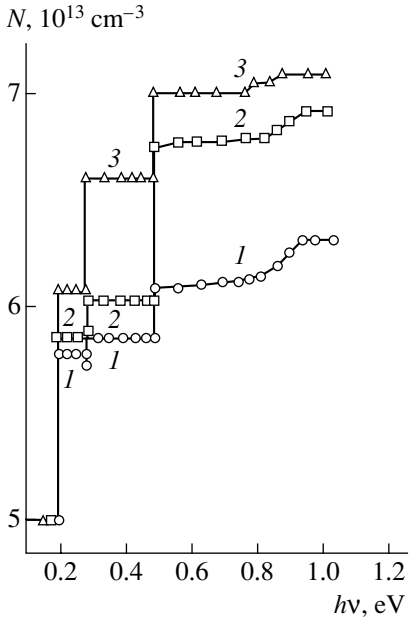

Fig. 2. Photocapacitance spectra of diodes based on *n*-Si:V. The vanadium diffusion times were (*1*) 2, (*2*) 10, and (*3*) 20 h. The spectra were measured at $T = 77$ K.

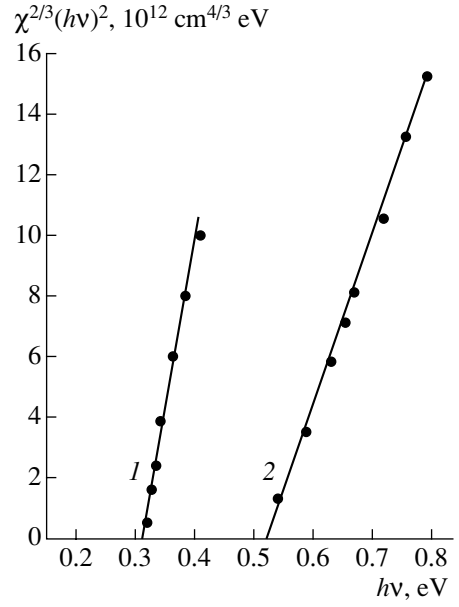

Fig. 3. Dependences $\chi^{2/3}(h\nu)^2 = f(h\nu)$ for vanadium levels in the band gap of *n*-Si; the levels have ionization energies of (*1*) $E_c - 0.32$ eV and (*2*) $E_c - 0.52$ eV.

$E_c - 0.21$ eV, $E_c - 0.32$ eV, and $E_c - 0.52$ eV (Fig. 1b). The total vanadium concentration increases as the diffusion time increases. Induced photocapacitance [7] was not observed in any of the *n*-Si:V diodes under investigation; this means that either there are no vanadium levels in the lower half of the band gap or the hole-capture cross section for these levels is smaller than 10^{-19} cm^2.

Measurements of the kinetics of photocapacitance buildup in the diodes exposed to light with a wavelength corresponding to extrinsic absorption made it possible to determine the spectral dependence of photoionization cross sections χ for vanadium levels. According to the Lucovsky theory [8], we have

$$\chi \propto (h\nu - \Delta E_{\text{opt}})^{3/2}/(h\nu)^3;$$

consequently,

$$\chi^{2/3}(h\nu)^2 \propto h\nu - \Delta E_{\text{opt}}.$$

Extrapolation of the function $\chi^{2/3}(h\nu)^2 = f(h\nu)$ to zero makes it possible to determine the ionization energy of deep levels ΔE_{opt}. In Fig. 3, we show the measured dependences $f(h\nu)$ for χ_n and $\chi_n + \chi_p$ in *n*-Si; here, χ_n and χ_p are the cross sections for photon capture by an impurity center when an electron and a hole are emitted, respectively. It can be seen from Fig. 3 that experimental dependences $\chi(h\nu)$ are in good agreement with the theory [8]. Extrapolation yields $\chi_n = 10^{-17}$–10^{-16} cm^2 for the level $E_c - 0.32$ eV in the range of 0.32 eV $< h\nu <$ 0.45 eV and $\chi_n + \chi_p = 10^{-17}$–$1.02 \times 10^{-16}$ cm^2 for the level $E_c - 0.52$ eV with allowance made for dual optical transitions. The ascending dependence $N(h\nu)$ for the diodes based on *n*-Si:V is caused by the fact that the relation $\chi_n \gg \chi_p$ is characteristic of vanadium levels.

Measurements of photocapacitance have shown that vanadium introduces levels at $E_v + 0.31$ eV, $E_v +$

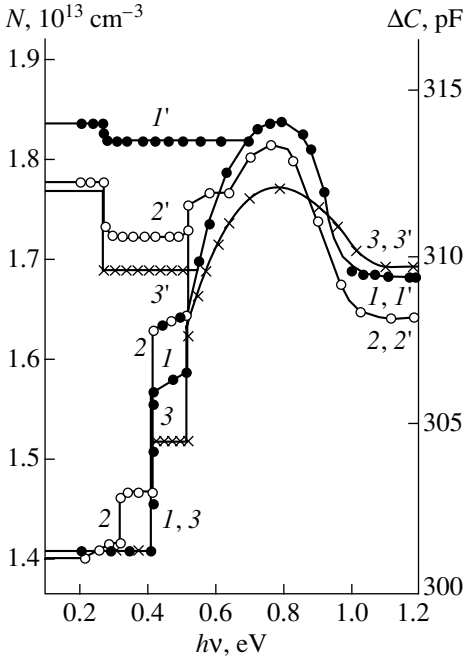

Fig. 4. The spectra of (*1*, *2*, *3*) photocapacitance and (*1'*, *2'*, *3'*) induced photocapacitance of diodes based on *p*-Si:V. The times of vanadium diffusion were (*1*, *1'*) 2, (*2*, *2'*) 10, and (*3*, *3'*) 20 h. The spectra were measured at $T = 77$ K.

0.42 eV, and $E_v + 0.52$ eV into the lower half of the *p*-Si band gap; notably, the level at $E_v + 0.31$ eV is formed only if vanadium diffusion lasts for 10 h. If the diffusion time is longer (20 h), this level is not observed in the photocapacitance spectrum and the concentrations of the $E_v + 0.42$ eV and $E_v + 0.52$ eV levels increase simultaneously. An analysis of the photocapacitance spectra for *p*-Si:V shows that the relation $\chi_n > \chi_p$ is characteristic of the $E_v + 0.52$ eV level as well. This follows from the observation of descending portions in the dependence $\Delta C(h\nu)$ in the photocapacitance spectra [7, 9]. The levels in the upper half of the band gap, which are observed in the measured photocapacitance spectra of *p*-Si:V, have an ionization energy equal to $E_c - 0.26$ eV.

Generally, the results of studying the spectra of photocapacitance and induced photocapacitance for diodes based on *n*- and *p*-Si suggest that the relation $\chi_n > \chi_p$ is indeed characteristic of all vanadium levels in the band gap of silicon.

REFERENCES

1. J.-W. Chen and A. G. Milnes, Annu. Rev. Mater. Sci. **10**, 157 (1980).
2. H. Lemke, Phys. Status Solidi A **64** (2), 549 (1981).
3. H. Lemke, Phys. Status Solidi A **75** (1), 473 (1983).
4. Kh. S. Daliev, A. A. Lebedev, N. A. Sultanov, and W. Ecke, Fiz. Tekh. Poluprovodn. (Leningrad) **19** (2), 338 (1985) [Sov. Phys. Semicond. **19**, 211 (1985)].
5. G. K. Azimov, S. Z. Zaĭnabidinov, and Yu. I. Kozlov, Fiz. Tekh. Poluprovodn. (Leningrad) **23** (10), 1890 (1989) [Sov. Phys. Semicond. **23**, 1169 (1989)].
6. A. T. Mamadalimov, A. A. Lebedev, and E. V. Astrova, *Spectroscopy of Deep Centers in Semiconductors* (Universitet, Tashkent, 1999).
7. L. S. Berman and A. A. Lebedev, *Capacitance Spectroscopy of Deep-Centers* (Nauka, Moscow, 1981).
8. G. V. Lucovsky, Solid State Commun. **3**, 299 (1965).
9. A. T. Mamadalimov, S. S. Kakharov, Sh. Makhkamov, and P. K. Khabibullaev, Izv. Akad. Nauk Uz. SSSR, Ser. Fiz.-Mat. Nauk, No. 4, 53 (1980).

Translated by A. Spitsyn

Semiconductors, Vol. 37, No. 1, 2003, pp. 31–37. Translated from Fizika i Tekhnika Poluprovodnikov, Vol. 37, No. 1, 2003, pp. 32–38.

SEMICONDUCTOR STRUCTURES, INTERFACES, AND SURFACES

Investigation of Magnetosensitivity of Transistor Structures with Diffusive Transport of Injected Charge Carriers

M. A. Glauberman, V. V. Yegorov, V. V. Kozel, and N. A. Kanishcheva

Training, Research, and Production Center at the Mechnikov National University, ul. Petra Velikogo 2, Odessa, 65063 Ukraine

Submitted January 8, 2002; accepted for publication March 28, 2002

Abstract—A new approach to the magnetosensitivity of transistor structures with diffusive transport of injected charge carriers is suggested. It is shown that the conventional explanation of this mechanism for magnetosensitivity, which is thought to be based on deflection of the charge-carrier diffusion flow by a magnetic field, is basically incorrect. Specifically, the term accounting for this deflection in the continuity equation vanishes; thus, the conventional theory predicts the absence of magnetosensitivity if there is no electric field in the base. This fact is interpreted physically as being due to the circulation of currents excited by a magnetic field along the lines of a level in the concentration field. In the suggested theory, boundary conditions of the third kind (instead of the Dirichlet conditions) are specified at the collector junction. Notably, the absolute sensitivity is governed by the difference between the concentrations of injected charge carriers at the most distant points of the collector. *© 2003 MAIK "Nauka/Interperiodica".*

1. INTRODUCTION

Magnetotransistors are bipolar transistors whose structure and operating conditions are optimized in order to obtain the highest sensitivity of collector current to a magnetic field; these transistors have been attracting much attention for the last two decades as the most promising semiconductor magnetic-field sensors [1]. The operation of magnetotransistors is based on the effect of the Lorentz force on moving injected charge carriers. One can differentiate drift- and diffusion-related magetotransistors, depending on the type of transport of injected charge carriers. The magnetosensitivity of drift magnetotransistors is caused by redistribution of the injected-carrier concentration in the base bulk under the effect of a magnetic field, which brings about a variation in the gradients of this concentration at the interface with a collector and, thus, produces changes in the collector current.

Until recently, the above viewpoint had also been extended to diffusive magnetotransistors. The assumption that there is a redistribution of the charge-carrier concentration in the bulk (or, which amounts to the same, that the carrier flux is deflected by a magnetic field) was first used in the optimization of the simplest structures of diffusive magnetotransistors [2]. This assumption was then used later on in developing subsequent structural modifications and calculation procedures (see, e.g., [3, 4]). However, when closely examined, this approach is found to be incorrect, which impels one to reconsider the established concepts.

In this study, we determine more exactly the characteristics of the magnetic-field effect on the diffusion flow of charge carriers in the base bulk, demonstrate the inconsistency of the assumption that this flow is deflected by a magnetic field, and suggest a consistent interpretation of the magnetosensitivity of magnetotransistors with idealized (purely diffusive) transport of injected charge carriers (we ignore the effect of electric fields, including those caused by the recombination current of the majority charge carriers).

2. EXPERIMENTAL DATA AND THEIR CONVENTIONAL INTERPRETATION

Magnetotransistor structures can be formed both with longitudinal (Fig. 1a) and transverse (Fig. 1b) magnetic axes (according to [2] and [6, 7], respectively), depending on the mutual orientation of the magnetic-induction vector and the structure surface.

In the absence of a magnetic field, the vector fields of the current density of injected charge carriers **J** are symmetric with respect to the symmetry plane of the structure, which causes the collector currents for electrons and holes to be equal to each other. For diffusive transport, we have

$$\mathbf{J} = \pm eD\,\mathrm{grad}c, \qquad (1)$$

where the upper and lower signs correspond to electrons and holes, respectively; e is the elementary charge; and D and c are the diffusion (generally, ambipolar) coefficient and the injected-carrier concentration, respectively.

In the context of the mechanism under consideration, it is generally agreed that a magnetic field gives rise to redistribution of concentrations c; as a result, the vectors **J** gain increments (deflections in the carrier

1063-7826/03/3701-0031$24.00

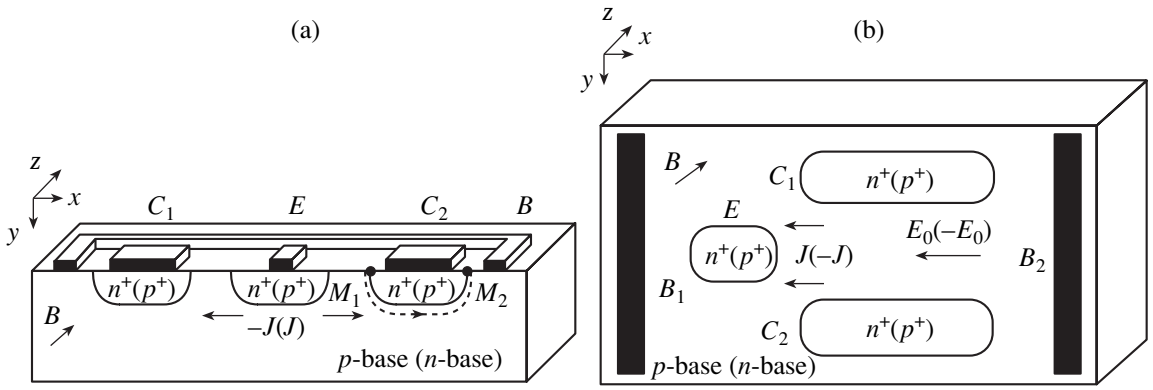

Fig. 1. Structure of a horizontal diffusive magnetotransistor of *n–p–n* (*p–n–p*) type with (a) longitudinal and (b) transverse magnetic axes. *E* stands for emitter; C_1 and C_2, for collectors; and *B*, B_1, and B_2 denote ohmic contacts to the base (external voltage is applied to the contacts B_1 and B_2 if the drift-based operation is chosen; in contrast, these contacts are shorted to each other in the case of diffusion-based operation).

flows) which are perpendicular to the initial direction of these vectors, so that the balance between the collector currents becomes disturbed.[1] First of all, we will clarify to what extent this viewpoint is consistent with experimental data.

The electrical mode of a diffusive magnetotransistor is specified uniquely by the emitter current I_E (by the injection level). It is conventional to characterize the magnetosensitivity by the absolute sensitivity

$$S_A \equiv \left.\frac{\partial I_C}{\partial B}\right|_{B=0} \tag{2}$$

and the conversion efficiency

$$S_R \equiv I_C^{-1}\left.\frac{\partial I_C}{\partial B}\right|_{B=0} = \frac{S_A}{I_C}, \tag{3}$$

where I_C is the collector current and *B* is the magnetic-field induction.

Experimental dependences of S_R on the emitter current (for the structures corresponding to Fig. 1a and having the parameters listed in the table, with the dopants for the *p*- and *n*-type regions being boron and phosphorus, respectively) are shown in Fig. 2 (the data for the *p–n–p* structures were adopted from [8]).

The choice of the conversion efficiency S_R as the characteristic of magnetosensitivity is preferable since S_R depends the least on specific parameters of the structure and the electric-operation mode (on the collector extent, the diffusion length, and the emitter current) in comparison with other characteristics. Generalizing numerous theoretical results for various layouts of the drift structures (see, e.g., [6, 9]), we can write

$$S_R = \frac{rb}{\varphi_T}\nu. \tag{4}$$

Here, *r* is the scattering factor, *b* is a characteristic geometrical parameter (most often, the distance between the collector and emitter), φ_T is the temperature potential, and ν is the mean velocity of injected charge carriers. An expression for S_R in terms of velocity is convenient because the latter is a kinematic parameter and, as such, is independent of the specific features of charge-carrier motion (diffusion or drift) and is quite reasonable since S_R is defined by the Lorentz force, which depends exactly on the velocity.

Using the assumption that the excess concentration of minority charge carriers is much higher than the equilibrium concentration and is equal to the excess concentration of majority charge carriers, the condition $mc_0/N \ll 1$ (*m* is the ratio between the drift mobilities of the minority and majority charge carriers, c_0 is the equilibrium concentration of minority charge carriers, and *N* is the doping-impurity concentration), and on the basis of the well-known expression for ambipolar diffusivity, we can write

$$D(\rho) = \varphi_T\mu\frac{2\rho+1}{\rho(m+1)+1}, \tag{5}$$

where $\rho \equiv \Delta c/N$ is the injection level; and Δc and μ are the excess concentration and the drift mobility of minority charge carriers, respectively. Assuming that $\nu = D/L$, where *L* is the diffusion length of minority charge carriers, we obtain

$$S_R(\rho) = \frac{\mu^* b}{L}\frac{2\rho+1}{\rho(m+1)+1}. \tag{6}$$

[1] An alternative mechanism suggested by Vinal and Masnary [12] is based on spatial modulation of the emitter current by the Hall field E_H. In turn, this field has its origin in the spatial separation of charges under the effect of a magnetic field. As will be shown in what follows, the charges are not separated under the conditions of purely diffusive transport; taking this into account, we will disregard this mechanism.

Here, $\mu^* \equiv r\mu$ is the Hall mobility. $S_R(\rho)$ increases steadily for $m < 1$ and decreases steadily for $m > 1$. Notably, the ratio of the limiting values of S_R is equal to

$$\frac{S_R(\infty)}{S_R(0)} = \frac{2}{m+1}. \quad (7)$$

Assuming that the mobilities of electrons and holes in silicon are equal to 1500 and 500 $cm^2\ V^{-1}\ s^{-1}$, we obtain 2/3 for this ratio in *p–n–p* structures and 3/2 in *n–p–n* structures (correspondingly, we have an increase and decrease in S_R as ρ increases).

Since the values of ρ are proportional to the emitter current and taking into account the run of the curves in Fig. 2 and the ratio between the limiting values of S_R, we may conclude that the notion about the deflection of the flow of injected charge carriers by the Lorentz force in the bulk (with allowance made for drift in the Dember field) is consistent with experimental data.

3. INFLUENCE OF A MAGNETIC FIELD ON CARRIER FLOW IN THE BULK

It is conventional to base the theory of bipolar magnetosensitive semiconductor structures on the solution of a system of equations [1, 10, 11] which includes, in particular, the continuity equation for the charge carriers of both types,

$$\mathrm{div}\mathbf{J} \mp e\partial c/\partial t = \pm eR, \quad (8)$$

and expressions for the current densities of these carriers,

$$\mathbf{J} = \mathbf{J}_0 \mp \mu^*[\mathbf{J} \times \mathbf{B}], \quad (9)$$

where

$$\mathbf{J}_0 = ec\mu\mathbf{E} \pm eD\mathrm{grad}c \quad (10)$$

is the current density in the absence of a magnetic field, t is time, R is the recombination rate, and $\mathbf{E}$ is the electric-field strength.

In order to solve analytically the problem concerning the concentration distribution, we have to substitute (9) and (10) into (8), which yields

$$\mu\mathrm{div}(c, \mathbf{E}) \pm D\mathrm{div}\,\mathrm{grad}c \mp \mu^*\mu\mathrm{div}\{c[\mathbf{E} \times \mathbf{B}]\} - \mu^* D\mathrm{div}[\mathrm{grad}c \times \mathbf{B}] \mp \partial c/\partial t = \pm R. \quad (11)$$

Here, we use the assumption that the vectors $\mathbf{J}$ and $\mathbf{B}$ are mutually perpendicular, which makes it possible, without loss of generality, to solve expression (9) for $\mathbf{J}$ and transform this expression into the following convenient form in the case of weak magnetic fields ($\mu^*\mathbf{B} \ll 1$):

$$\mathbf{J} = \{\mathbf{J}_0 \mp \mu^*[\mathbf{J}_0 \times \mathbf{B}]\}/\{1 + (\mu^*\mathbf{B})^2\} \approx \mathbf{J}_0 \mp \mu^*[\mathbf{J}_0 \times \mathbf{B}]. \quad (12)$$

Let us consider the fourth term on the left-hand side of (11); this term accounts for the influence of a magnetic field on the diffusion-related component of the current. We obtain the following expression for divergence:

$$\nabla[\nabla c \times \mathbf{B}] = \mathbf{B}[\nabla \times \nabla c] - \nabla c[\nabla \times \mathbf{B}] = \mathbf{B} \cdot \mathrm{curl}\,\mathrm{grad}c - \mathrm{grad}c \cdot \mathrm{curl}\mathbf{B}. \quad (13)$$

The first term on the right-hand side of (13) is equal to zero identically, whereas the second term vanishes if the magnetic fields are uniform. Thus, the magnetodiffusion term disappears from the continuity equation and further transformations, which theoretically excludes the influence of a magnetic field on the distribution of the injected-carrier concentration. An attempt to attribute the magnetosensitivity of these structures to the drift of charge carriers in the Dember field (taking into account that, in general, drift makes an explicit contribution to magnetosensitivity because the third term in (11) is nonzero) runs into the same problem, since the vector of this field is proportional to the concentration gradient.

Thus, the existing view about the origin of magnetosensitivity in diffusive magnetotransistors is consistent with experimental data but is inconsistent with the theory. In order to resolve this contradiction, we refine the characteristics of the carrier transport described by Eq. (11).

Table

The structure type		*n–p–n*	*p–n–p*
The base resistivity, Ω cm		7.5	20
Electrode dimensions, μm	Depth of doping	≈3	
	Length of electrodes h	100	
	Effective base width x_1	50	20
	Width of collectors x_2–x_1	12	6
	Emitter width	18	12

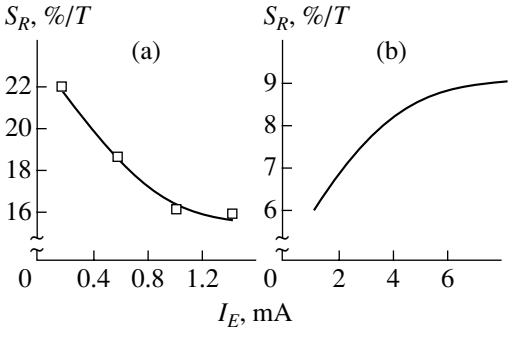

Fig. 2. Magnetoelectrical characteristics of a magnetotransistor: conversion efficiency as a function of emitter current for the (a) *n–p–n* and (b) *p–n–p* structures.

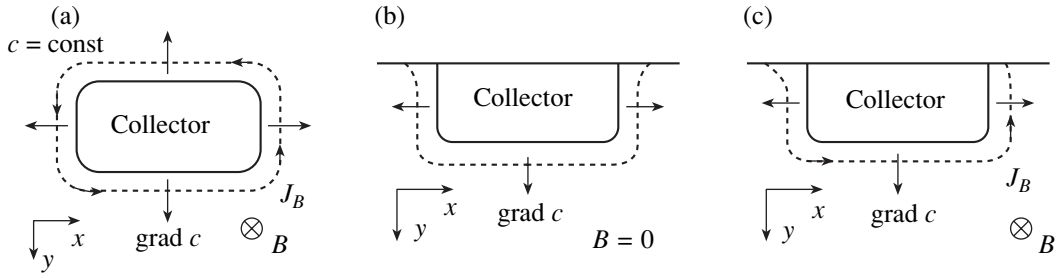

Fig. 3. The level lines and the flow of the majority-carrier current when the charge-carrier concentration is constant at the interface with collector (a) in the absence of isolating walls (according to Fig. 1b) and (b, c) in the presence of these walls (see Fig. 1a) in (b) the absence and (c) presence of a magnetic field.

The fourth term in Eq. (11) is obtained from the expression for the Lorentz force; the latter acts on the charges that move with the velocity

$$\mathrm{v}_{\mathrm{dif}} = -Dc^{-1}\mathrm{grad}c, \tag{14}$$

which is directed perpendicularly to the level surface in the concentration field (the isoconcentration surface established before the magnetic field was switched on). Thus, the Lorentz force is found to be directed at a tangent to this surface. Obviously, the currents induced by this force will only flow over the level surface (in the plane perpendicular to **B**); since this surface is closed, the currents will circulate and, thus, the divergence of their densities will vanish.

Since a magnetic field does not cause the carrier concentrations in the base bulk to redistribute, we have to clarify the characteristics of carrier transport at the base boundaries.

4. INFLUENCE OF A MAGNETIC FIELD ON THE CHARGE-CARRIER FLOW THROUGH THE BOUNDARY

When simulating magnetotransistors [10, 11], it is most common to treat the boundary of the space-charge region of the collector junction as a surface with a constant concentration of minority charge carriers (the Dirichlet conditions). Taking into account the foregoing, the switching on of a magnetic field should only give rise to circulating currents $\mathbf{J}_B$ of these charge carriers around the collectors (Fig. 3a) without perturbing the concentration field. The presence of isolating walls in the structure (Fig. 3b) cannot disturb the flow of these currents and should only perturb the carrier concentration in the vicinity of the walls (Fig. 3c), which neutralizes the isolation effect owing to variation in the surface-recombination rate. Obviously, the collector current, which depends on the carrier-concentration distribution, will not change in the former case at all and will not change in the latter case at least in the first approximation. When there are walls, the collector-current increments differing in sign are compensated at opposite ends, whereas, in the case of incomplete compensation, the response to a magnetic field is found to be independent of the **B** direction, which is inconsistent with experimental data. Consequently, the Dirichlet conditions are inapplicable to the solution of the problem concerning the magnetosensitivity of diffusive magnetotransistors.

It is clear from the above reasoning that the collector-current response to a magnetic field is possible only if the component of the minority-carrier velocity (and, consequently, the concentration gradient) in the collector-surface plane is nonzero. If the formulated condition is satisfied, then

$$J_C = J_{0n} + J_B = J_{0n} \mp J_{0\tau}\mu^*_{mn}B, \tag{15}$$

where the normal component of the boundary current

$$J_{0n} = \pm eD\frac{\partial c}{\partial n} \tag{16}$$

gives rise to a collector current in the absence of a magnetic field, whereas the tangential component

$$J_{0\tau} = \pm eD\frac{\partial c}{\partial l} \tag{17}$$

gives rise to an additional component J_B, which depends on **B**. Here, $\partial/\partial l$ and $\partial/\partial n$ are derivatives along the direction of the M_1M_2 curve (Fig. 1a) and along the normal to this curve.

The collector current can then be expressed in terms of a curvilinear integral along the M_1M_2 curve as

$$\begin{aligned} J_C(B) &= I_C(0) - e\mu^*_{mn}DhB\int\limits_{M_1M_2}\frac{\partial c}{\partial l}dl \\ &= I_C(0) + e\mu^*_{mn}DhB[c(M_1) - c(M_2)], \end{aligned} \tag{18}$$

where

$$I_C(0) = \pm eDh\int\limits_{M_1M_2}\frac{\partial c}{\partial n}dl \tag{19}$$

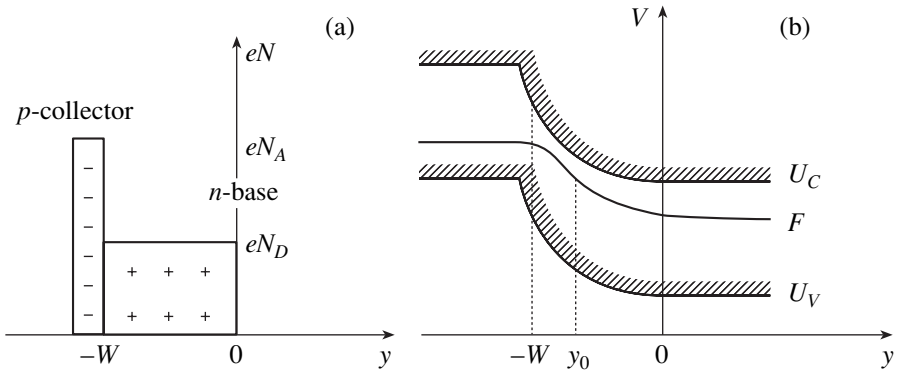

Fig. 4. Distribution of (a) the space charge and (b) the electric and electrochemical potentials in the space-charge region of the collector junction. The coordinate $y = 0$ corresponds to the boundary of the space-charge region. A minimum of the hole concentration is attained at the point y_0.

is the value of this integral at $\mathbf{B} = 0$; h is the extent of electron motion along the OZ axis; and the absolute sensitivity of the diffusive structure

$$S_A = \frac{\partial I_C}{\partial B} = e\mu^*_{mn} Dh[c(M_1) - c(M_2)] \qquad (20)$$

is governed by the difference of concentrations at the collector ends.

We will now show that the assumption about nonuniformity of the minority-carrier concentration at the interface with a collector

$$\frac{\partial c}{\partial l} \neq 0 \qquad (21)$$

is indeed valid.

5. THE BOUNDARY CONDITIONS

Physically, condition (21) can be satisfied if the following two requirements are met:

(i) the concentration distribution along x (Fig. 1) is nonuniform in the bulk; and

(ii) the concentration at the boundary depends on the concentration in the bulk.

The first requirement is met by choosing an appropriate device structure, i.e., one that is in accordance with the principle of its operation. The second requirement makes it necessary to reject the Dirichlet conditions in favor of the boundary conditions of the third kind. Such conditions seem to be reasonable taking into account the fact that the diffusion-related flow should be matched to the drift-related flow in the collector space-charge layer; i.e.,

$$eD\frac{\partial c}{\partial n} = e\nu_{dr} c(l), \qquad (22)$$

so that

$$\frac{\partial c}{\partial n} = \frac{\nu_{dr}}{D} c(l), \qquad (23)$$

where ν_{dr} is a parameter that characterizes the charge-carrier drift in the space-charge region of the collector (in a rough approximation, this parameter corresponds to the drift velocity in the junction); and l is a curvilinear coordinate at the interface with the space-charge region of the collector. We then obtain (21) taking into account the first requirement that defines the dependence of $\partial c/\partial n$ on l.

However, condition (23), as it is written, is practically unacceptable as a consequence of the uncertainty in ν_{dr} caused by the appreciable nonuniformity of the electric field in the junction and, thus, needs to be reformulated.

To this end, we will determine more accurately the concentration distribution in the space-charge region of a reversely biased abrupt p–n junction (Fig. 4a). For the sake of definiteness, we consider the junction portion in the "bottom" part of the collector in Fig. 1a, where the x and y axes define the tangential and normal directions to the n-type base. The frequently used assumption that electrochemical potentials are constant in the p–n junction results in the Dirichlet conditions and cannot be accepted for the following reason. In the case of extraction from an electrically neutral base (Fig. 4b), we have

$$\left.\frac{\partial c}{\partial y}\right|_{y=0} > 0. \qquad (24)$$

With allowance made for $c(x, -W) > c(x, 0)$, where W is the width of the space-charge region, we find that there is a minimum in the charge-carrier concentration for a fixed x at a certain point $y_0 \in (-W, 0)$. At the same time, ignoring recombination in the depletion layer, we obtain the following expression for the collector-current density:

$$J_C = e\mu c\frac{\partial F}{\partial y} = \text{const}(y). \qquad (25)$$

Here, F is the electrochemical potential of minority charge carriers. It follows from (25) that there exists an inflection in F at $y = y_0$, such that

$$\left.\frac{\partial F}{\partial y}\right|_{y = y_0} = \left.\frac{\partial U}{\partial y}\right|_{y = y_0}, \tag{26}$$

where U is the electric potential.

Thus, the assumption that the potential F is constant (or almost constant) in the space-charge layer, which corresponds to the Dirichlet conditions, cannot be considered even *a priori* valid since this assumption is radically inconsistent with the fact that there is an inflection point in this region, which follows from physically significant condition (24). In order to determine the concentration distribution in the depletion region, we rewrite (25) as

$$eD\frac{\partial c}{\partial y} - e\mu cE(y) = eD\left.\frac{\partial c}{\partial y}\right|_{y = 0}. \tag{27}$$

The conventional expression for the depletion-region width in the case of parabolic bending of the energy bands can be written as

$$W = \sqrt{\frac{2\varepsilon\varepsilon_0}{eN_B}\Delta\varphi}, \tag{28}$$

where $\Delta\varphi \equiv \Delta\varphi_0 + V_C$, $\Delta\varphi_0$ is the equilibrium potential difference across the junction, V_C is an external bias applied to the collector junction, and N_B is the ionized-impurity concentration in the base. As an example, we consider the simplest situation where $\mu = \text{const}(E)$. Then, using the dimensionless variables

$$q \equiv y/W, \quad \zeta \equiv c/N_B, \tag{29}$$

we transform Eq. (27) into

$$\frac{d\zeta}{dq} - \frac{2\Delta\varphi}{\varphi_T}q\zeta = \left.\frac{d\zeta}{dq}\right|_{q = 0}. \tag{30}$$

On condition that $\zeta(-1) = \zeta_0$, the solution to Eq. (30) is given by

$$\zeta(q) = \exp\left(\frac{\Delta\varphi}{\varphi_T}q^2\right)\left[\zeta_0\exp\left(-\frac{\Delta\varphi}{\varphi_T}\right) + \left.\frac{d\zeta}{dq}\right|_{q = 0} \times \int_{-1}^{q}\exp\left(-\frac{\Delta\varphi}{\varphi_T}q^2\right)dq\right]. \tag{31}$$

It follows from (31) that

$$\zeta(0) = \zeta_0\exp\left(-\frac{\Delta\varphi}{\varphi_T}\right) + \left.\frac{d\zeta}{dq}\right|_{q = 0}\int_{-1}^{0}\exp\left(-\frac{\Delta\varphi}{\varphi_T}q^2\right)dq = \zeta_0\exp\left(-\frac{\Delta\varphi}{\varphi_T}\right) + \left(\frac{\varphi_T}{\Delta\varphi}\right)^{1/2}\left.\frac{d\zeta}{dq}\right|_{q = 0}\frac{\sqrt{\pi}}{2}\Phi\left[\left(\frac{\Delta\varphi}{\varphi_T}\right)^{1/2}\right], \tag{32}$$

where Φ is the probability integral.

Since Φ tends monotonically toward 0.5 and takes a value in excess of 0.4999997 even at $V_C = 0$ (in which case, $(\Delta\varphi/\varphi_T)^{1/2} \approx 5$ for silicon at room temperature), we may set $\Phi = 1/2$. Then, returning to natural variables, we obtain the following final expression for the boundary condition of the third kind:

$$c(x, 0) = c_c\exp\left(-\frac{\Delta\varphi}{\varphi_T}\right) + l_D\sqrt{\frac{\pi}{2}}\left.\frac{\partial c}{\partial y}\right|_{y = 0}. \tag{33}$$

Here, $c_c = c(x, -W)$ is the concentration of majority charge carriers in the near-boundary region of the collector and l_D is the Debye length in the base. It can be seen that boundary condition (33) becomes homogeneous in the limiting case of very large values of V_C. This makes it possible to use expression (23) assuming that

$$\frac{v_{dr}}{D} = \frac{1}{l_D}\sqrt{\frac{2}{\pi}}. \tag{34}$$

5. CONCLUSION

We have shown that the mechanism of magnetosensitivity for transistor structures with drift-based transport of charge carriers differs radically from the corresponding mechanism in structures with diffusion-based transport. In the former case, the sensitivity is caused by the influence of a magnetic field on the motion of injected charge carriers in the base bulk, whereas, in the latter case, the field affects the charge-carrier motion in the layer that adjoins the space-charge region of the collector junction.

This circumstance impels one to reconsider the established procedure for simulating diffusive magnetotransistors. In order to determine the absolute sensitivity, one has to calculate the concentration field of injected charge carriers in the absence of a magnetic field; the boundary conditions at the collector given by (23) should be used with allowance made for expression (34). Thereafter, the value of this sensitivity should be determined using formula (20).

REFERENCES

1. H. P. Baltes and R. S. Popovic, Proc. IEEE **74**, 1107 (1986).
2. I. M. Mitnikova, T. V. Persiyanov, G. I. Rekalova, and G. Shtyubner, Fiz. Tekh. Poluprovodn. (Leningrad) **12**, 48 (1978) [Sov. Phys. Semicond. **12**, 26 (1978)].
3. Lj. Ristic, T. Smy, H. P. Baltes, and I. Filanovsky, in *Proceedings of IEEE Bipolar Circuits & Technology Meeting, Minneapolis, Minnesota, USA, 1988*, p. 199.
4. Lj. Ristic, M. T. Doan, and M. Paranjape, in *Proceedings of 32nd Midwest Symposium on Circuits and Systems, New York, 1989*, Vol. 2, p. 701.
5. M. A. Glauberman, V. V. Yegorov, N. A. Kanischeva, and V. V. Kozel, in *Proceedings of 2nd International*

Smakula Symposium, Ternopol, Ukraine, CIS, 2000, p. 143.

6. L. W. Davies and M. S. Wells, Proc. IREE Aust. **32**, 235 (1971).
7. I. M. Vikulin, N. A. Kanishcheva, and M. A. Glauberman, Fiz. Tekh. Poluprovodn. (Leningrad) **10**, 785 (1976) [Sov. Phys. Semicond. **10**, 467 (1976)].
8. D. M. Kozlov, N. N. Kuz'mina, T. V. Persiyanov, *et al.*, Return on Research, No. GR 0186.0050291 (1988).
9. R. S. Popovic and R. Widmer, IEEE Trans. Electron Devices **ED-33**, 1134 (1986).
10. W. Allegretto, A. Nathan, and H. P. Baltes, in *NASECODE V: Proceedings of 5th International Conference on the Numerical Analysis of Semiconductor Devices and Integrated Circuit, Dublin, Ireland, 1987*.
11. M. G. Guvenc, IEEE Trans. Electron Devices **35**, 1851 (1988).
12. A. W. Vinal and N. A. Masnary, IEEE Electron Device Lett. **EDL-3**, 203 (1982).

Translated by A. Spitsyn

Semiconductors, Vol. 37, No. 1, 2003, pp. 38–43. Translated from Fizika i Tekhnika Poluprovodnikov, Vol. 37, No. 1, 2003, pp. 39–43.

SEMICONDUCTOR STRUCTURES, INTERFACES, AND SURFACES

Size Effect in Two-Photon Absorption of Recombination Radiation in Graded-Gap $Al_xGa_{1-x}As$ Solid Solutions

V. F. Kovalenko* and S. V. Shutov

Institute of Semiconductor Physics (Kherson Branch), National Academy of Sciences of Ukraine, Kherson, 73008 Ukraine

**e-mail: mickle@semicond.kiev.ua*

Submitted March 25, 2002; accepted for publication March 29, 2002

Abstract—The influence of the size effect in photoluminescence on two-photon absorption in the course of reradiation in undoped graded-gap $Al_xGa_{1-x}As$ solid solutions was studied. It is shown that the efficiency of two-photon absorption increases as the extent of the crystal region under excitation increases. The factors affecting the ratio between the contributions of the frequency- and polarization-related components of probability for two-photon absorption to its spectral dependence were determined. © *2003 MAIK "Nauka/Interperiodica".*

1. INTRODUCTION

It is well known [1–3] that the process of reradiation of electroluminescence and photoluminescence (PL) in graded-gap semiconductors brings about an increase in the external quantum yield of radiation with increasing size of the excitation region (the size effect of luminescence). It has been shown by Kovalenko *et al*. [4] that two-photon absorption makes an appreciable contribution to the PL reradiation at high excitation levels in such semiconductors.

In this paper, we report the results of studying the effect of the PL size effect on two-photon absorption in the course of reradiation in graded-gap $Al_xGa_{1-x}As$ solid solutions.

2. EXPERIMENTAL

We studied undoped (with an electron concentration $n \le 1 \times 10^{16}$ cm^{-3}) epitaxial layers (epilayers) of $Al_xGa_{1-x}As$ solid solutions grown on GaAs substrates from the bounded volume of the solution–melt. The aluminum content decreased from $x \approx 0.36$ at the heterointerface to $x = 0$ at the surface of the layers. Variation in composition over the layer thickness was almost linear within the layer portion extending from the substrate–layer boundary to the depth of $\sim 0.7d_0$ (d_0 is the total thickness of the epilayer). The band-gap gradient ∇E_g within this layer portion amounted to 350 eV/cm $< \nabla E_g <$ 400 eV/cm; the value of ∇E_g decreased gradually when approaching the narrow-gap layer surface.

The chosen values of ∇E_g ensured, first, the drift mechanism of transport of nonequilibrium charge carriers in the built-in quasi-electric field $F = e^{-1}\nabla E_g$ (e is the elementary charge) and, second, the equality between the extent of the excitation region of the crystal and the thickness of the layer portion d' confined between the rear narrow-gap and the front wide-gap (illuminated) surfaces. This was based on the fact that the effective displacement length of nonequilibrium charge carriers l_+ determined from the low-energy falloff of the emission spectrum [5] ($l_+ \approx 9$–12 μm) was comparable to d' for the specified values of ∇E_g, which was favorable for the transport of a high proportion of nonequilibrium charge carriers to the rear (narrow-gap) surface without their recombination in the crystal bulk.

We studied the influence of the size effect on two-photon absorption while varying the extent of the excitation region in the crystal on both the front (wide-gap) and rear (narrow-gap) surfaces. To this end, each epitaxial structure was cleaved into two parts, the surface narrow-gap portion of the epilayer with a thickness of $(0.2$–$0.3)d_0$ was then removed from one of the parts, and, finally, reverse angular lappings [6] were formed on both parts of the structure in order to excite the PL from the wide-gap side of the layers. Various sizes of the excitation region d' were effected by scanning the optical probe over the wide-gap surface of the reverse angular lapping of the structure.

The PL was excited at 300 K by an optical beam with a diameter of ~30 μm using argon-laser radiation (the wavelength $l_{exc} = 0.488$–0.514 μm). The excitation intensity J was varied within the range of $1 \times 10^{21} < J < 5 \times 10^{22}$ cm^{-2} s^{-1}. The PL spectra were measured conventionally using an SDL-1 spectrometer and an FÉU-62 photomultiplier.

3. RESULTS

The PL spectra of the solid solutions under investigation included an edge-emission band caused by

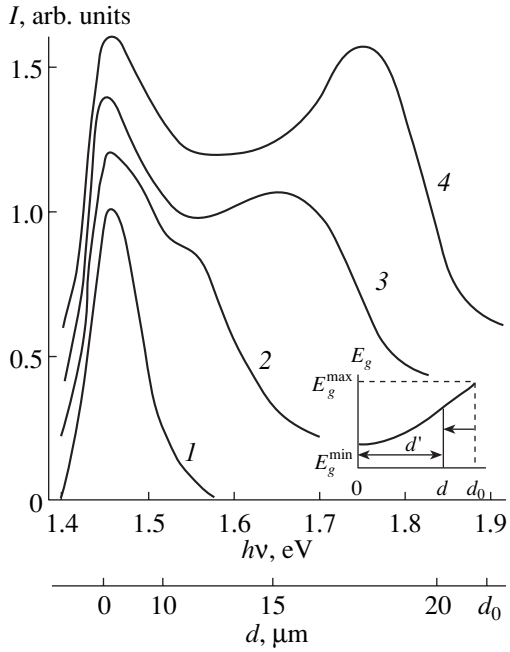

Fig. 1. The shape of photoluminescence spectra for a layer with full thickness (∇E_g = 380 eV/cm) for several values of the excitation-region extent; d' = (*1*) 8, (*2*) 11, (*3*) 15, and (*4*) 19 μm. The excitation intensity $J = 1.6 \times 10^{22}$ cm^{-2} s^{-1}. The spectra are normalized to unity and are arbitrarily shifted along the vertical axis. Variations in the band-gap width over the depth in the layer from the minimal value $E_g^{\min}$ to the maximal value $E_g^{\max}$ are shown in the inset; the excitation region is also outlined. The arrows indicate the excitation direction.

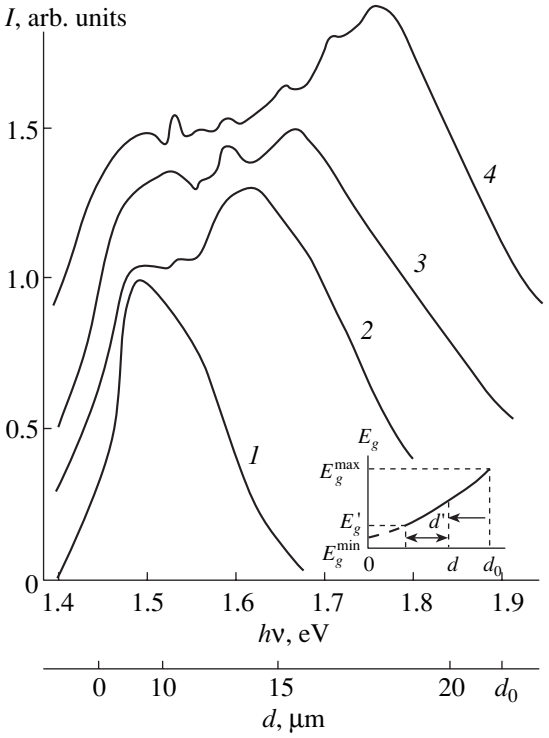

Fig. 2. The shape of photoluminescence spectra for a layer with a removed narrow-gap region with a thickness of about 10 μm (∇E_g = 380 eV/cm) for several values of the excitation-region extent: d' = (*1*) 5, (*2*) 8, (*3*) 10, and (*4*) 12 μm. The excitation intensity $J = 1.6 \times 10^{22}$ cm^{-2} s^{-1}. The spectra are normalized to unity and are shifted arbitrarily along the vertical axis. In the inset, we show variations in the band-gap width over the layer depth from the minimal value $E_g^{\min}$ to the maximal value $E_g^{\max}$ and indicate the excitation region. The dashed line in the inset represents the portion of the $E_g(d)$ curve which corresponds to the removed narrow-gap region. The arrow in the inset indicates the excitation direction.

band-to-band transitions. In Figs. 1 and 2, we show the PL spectra $I(h\nu)$ of the same layer without removing the narrow-gap portion (in the following, the layer with full thickness) and with a removed narrow-gap region for various values of d' and J = const. It can be seen that the band width is governed by the extent of the excitation region d': as d' increases, the short-wavelength wing of the band shifts to higher energies in the spectrum.

The shape of the epilayer-related emission band for the full-thickness layer was similar to that reported by Kovalenko *et al*. [4]. The PL spectrum of the layers with a removed narrow-gap region had a fine structure. Specifically, spikes with various intensities I and with the number of spikes increasing as the value of d' increased were observed against the background of the continuous spectrum. The features of the fine structure of the spectrum depended markedly on the excitation level (Fig. 3). The fine structure was hardly observed at small values of J. This structure was most pronounced at intermediate excitation levels; a further increase in J lead to smoothing of the fine structure; i.e., the number and intensity of the peaks decreased. As the excitation level increased, the spectra of the layers with a removed narrow-band region were also distinguished by a greater shift of the short-wavelength peak to lower energies (Fig. 3). The integrated PL intensity I_Σ increased with increasing d'. The exception was the transition region with a thickness of about 4 μm in the vicinity of the layer–substrate interface; the PL intensity decreased in this region as the substrate was approached. Removal of the narrow-gap region from the epilayer resulted in a decrease in I_Σ; however, the shape of the dependence $I_\Sigma(d')$ remained unchanged (Fig. 4). As J increased, the integrated PL intensity increased according to a power law; i.e.,

$$I_\Sigma = CJ^{m_\Sigma}, \quad (1)$$

where C is a proportionality coefficient [4]. The exponent m_Σ depended on the extent of the excitation region d' similarly to the dependence $I_\Sigma(d')$; i.e., this exponent increased with increasing d' and decreased as the het-

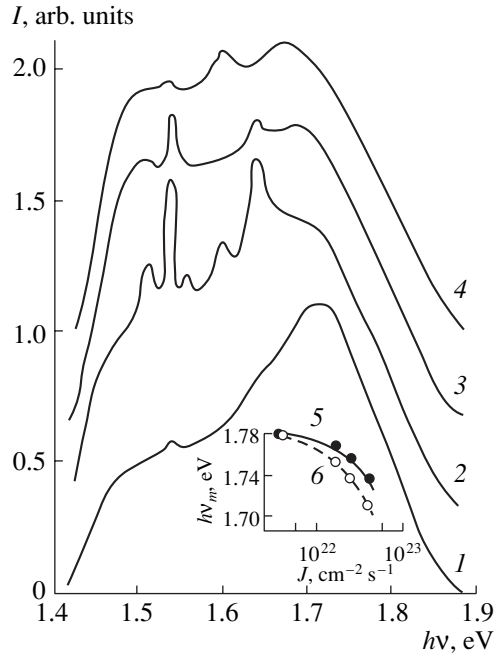

Fig. 3. The shape of the photoluminescence spectrum for a layer with a removed narrow-gap region in relation to the excitation intensity $J = (1)\ 1 \times 10^{21}$, (*2*) 1.6×10^{22}, (*3*) 2.2×10^{22}, and (*4*) 3.6×10^{22} cm^{-2} s^{-1}. Dependences of the position of the short-wavelength peak $h\nu_m$ in the photoluminescence spectrum on the excitation intensity for the same layer (*5*) with full thickness and (*6*) with a removed narrow-gap region are shown in the inset.

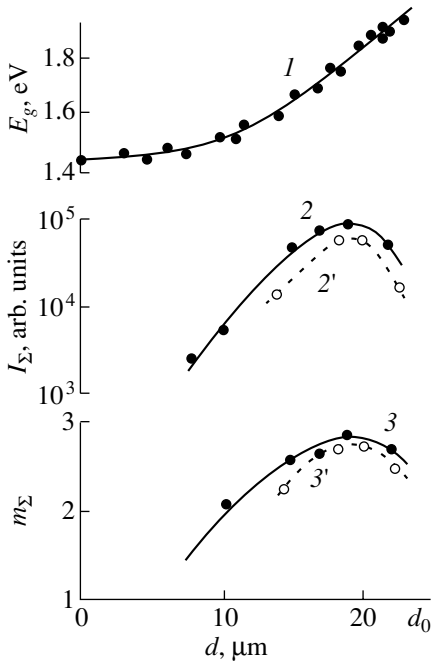

Fig. 4. Variations in (*1*) the band gap E_g, (*2*, *2*') integrated photoluminescence intensity I_Σ, and (*3*, *3*') the parameter m_Σ over the depth in one of the layers (*2*, *3*) with full thickness and (*2*', *3*') with a removed narrow-gap region.

erointerface was approached. Removal of the narrow-gap region from the epilayer resulted in a decrease in m_Σ; however, the shape of the dependence $m_\Sigma(d')$ remained intact (Fig. 4). It can be seen from Fig. 4 that dependence (1) changes from superlinear ($m_\Sigma > 1$) for the smallest values of d' to superquadratic ($m_\Sigma > 2$) as d' increases for the layers with full thickness; at the same time, this dependence is superquadratic in the entire range of variations in d' for the layers with a removed narrow-gap region.

The spectral PL intensity I_λ also increased with increasing excitation level; i.e.,

$$I_\lambda = C_1 J^{m_\lambda}. \qquad (2)$$

The degree to which the spectral intensity I_λ is superquadratic is characterized by the parameter m_λ in dependence (2) and is different for various wavelengths of the same emission spectrum. The removal of the narrow-gap region from the epilayer and a variation in d' affected the shape of the dependence $m_\lambda(h\nu)$ (Fig. 5). The degree to which the dependence $I_\lambda(h\nu)$ was superquadratic in the PL spectra of the layers with full thickness was minimal in the region of the short-wavelength peak and increased with increasing emission wavelength. A similar dependence $m_\lambda(h\nu)$ was observed in the layers with a removed narrow-gap region for small values of d'. As the values of d' increased, the shape of the dependence $m_\lambda(h\nu)$ changed radically; specifically, the exponent m_λ had a minimum in the short-wavelength region and decreased with increasing emission wavelength. The exponent m_λ was virtually indepen-

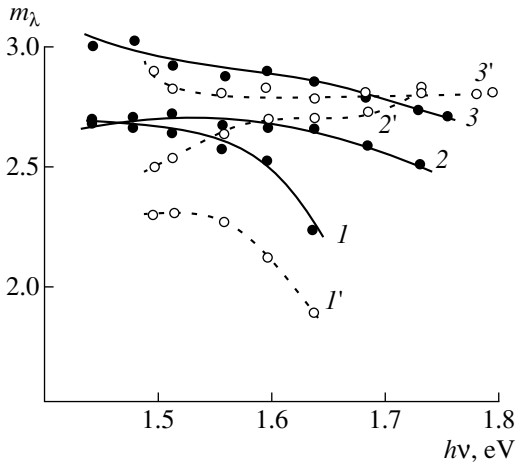

Fig. 5. Spectral dependences of the parameter m_λ for several values of the excitation-region extent d' for photoluminescence spectra of the same layer (*1*–*3*) with full thickness and (*1*'–*3*') with a removed narrow-gap region. $d' = (1)$ 11, (*2*) 15, (*3*) 19, (*1*') 8, (*2*') 10, and (*3*') 12 μm.

dent of the energy of emitted quanta for the largest values of d'.

4. DISCUSSION

An increase in the integrated PL intensity I_λ with increasing d' (the PL size effect) is caused by reradiation, special features of extraction of radiation, and a decrease in the recombination-related losses at the rear (narrow-gap) surface of a graded-gap semiconductor [1–3].

The superquadratic dependence $I_\Sigma(J)$ indicates that radiation resulting from the recombination of nonequilibrium charge carriers generated owing to the two-photon absorption of PL in the course of multiple reradiation contributes to the measured emission intensity [4]. An increase in the contribution of two-photon absorption (an increase in the parameter m_λ) to PL with increasing d' is caused by the following factors. As the extent of excitation region d' increases, the number of sequential reradiation events increases as well; these events ensure that the nonequilibrium charge carriers reach the rear (narrow-gap) surface and lead to a decrease in nonradiative recombination losses at this surface [3]. The latter circumstance brings about an increase in the internal quantum yield η_{in} as a result of saturation of the channels for the volume nonradiative recombination. This is confirmed by an increase in the effective displacement of nonequilibrium charge carriers as J increases (similarly to what was observed by Kovalenko *et al*. [4]) and by a shift of the short-wavelength peak in the PL spectrum to longer wavelengths, which is caused by the coordinate dependence of the probability of recombination for nonequilibrium charge carriers [7]. An increase in the number of reradiation events and in η_{in} brings about an increase in the photon density in the crystal bulk and, consequently, in the probability of two-photon PL absorption.

Smaller values of I_Σ and m_Σ for the layers with a removed narrow-gap region are caused by a lower internal quantum yield of PL. As a result of the smaller value of d' in these layers, a larger (than in the epilayers with full thickness) fraction of nonequilibrium charge carriers drifting in the electric field F reach the rear surface, which brings about higher nonradiative losses. The decrease in I_Σ and m_Σ with increasing d' in the vicinity of the heterointerface is related to a decrease in η_{in}, which is caused by a higher concentration of defects in this region [8].

The difference between the form of dependences $m_\lambda(h\nu)$ in the spectra of the layers with full thickness and in those of the layers with a removed narrow-gap region indicate that there are special features of two-photon absorption which are caused by geometrical factors. In the full-thickness layers, two-photon absorption increases as the distance from the illuminated wide-gap surface increases; this absorption is most significant in the narrow-gap region due to the predominance of the following frequency dependence of two-photon absorptivity [9]:

$$K_2(h\nu) = A\rho[h(\nu_1 + \nu_2) - E_g]^{1/2}. \quad (3)$$

Here, A is a coefficient which depends on the orientation of polarization vectors for both photons ($h\nu_1$ and $h\nu_2$), and ρ is the flux density of primary PL.

In the layers with a removed narrow-gap region, two-photon absorption is highest in the wide-gap region and decreases as the distance from the illuminated wide-gap surface increases. In our opinion, the cause of this discrepancy consists in the fact that the absorption of photons generated in the energy range of $E_g' < h\nu \le E_g^{\max}$ (E_g' and $E_g^{\max}$ are the band gaps at the rear surface of an epilayer with a removed narrow-gap region and at the illuminated front of the wide-gap surface, respectively) occurs identically when these photons are reradiated both in the full-thickness layer and in the layer with a removed narrow-gap region; i.e., the mechanism of absorption of photons propagating into the crystal regions with $E_g < h\nu$ in the direction of the drift of nonequilibrium charge carriers is of the one-photon type. Photons propagating in the $E_g^{\max}$ direction at angles that are larger than the angle α_0 of total internal reflection are reflected from the wide-gap surface back to the crystal. Thereafter, the photons can undergo two-photon absorption in the layer regions with $E_g > h\nu$ and one-photon absorption in the regions with $E_g < h\nu$, which is similar to the absorption of photons that propagate initially in the direction of the drift of nonequilibrium charge carriers. Thus, reflection of these photons from the wide-gap surface is of the single-stage type, whereas the reabsorption process is of the single-pass type.

Differences between the PL absorption in the full-thickness layers and in the layers with a removed narrow-gap layer manifest themselves for the photons $h\nu \approx E_g'$. Photons are absorbed in the full-thickness layers similarly to the above-considered mechanism. In the layers with a removed narrow-gap region, the photons outside the angle α_0 are reflected from both the wide-gap surface with $E_g = E_g^{\max}$ and the rear narrow-gap surface with $E_g = E_g'$. The reflection process can be multiple and completed either with two-photon absorption or with the photons found within the angle α_0 and with their subsequent escape from the crystal. A higher volume density of photons in the wide-gap region of the crystal, which is ensured by the multipass type of reradiation, brings about a higher probability of two-photon

absorption; this, in turn, leads to an increase in the concentration of nonequilibrium charge carriers in the wide-gap region as compared with the concentration of these carriers in the corresponding region of the full-thickness layers for the same excitation level. The latter circumstance gives rise to a more significant shift of the short-wavelength peak to longer wavelengths as J increases in the PL spectra of epilayers with a removed narrow-gap region. The origin of this shift was considered by Kovalenko *et al*. [10].

Apparently, the probability of two-photon absorption within regions with a narrower band gap is governed to a great extent by polarizations of absorbed photons. On the assumption that the allowed–allowed transitions are vertical and all the bands with extrema at $\mathbf{k} = 0$ are parabolic, we have the following expression for the probability of two-photon absorption [11]:

$$W \approx A_1 \frac{N_1 N_2 V}{\nu_1 \nu_2 \varepsilon_1 \varepsilon_2} \sqrt{h\nu_1 + h\nu_2 - E_g} \times \left[\frac{(\mathbf{e}_1 \mathbf{p}_{cm})(\mathbf{p}_{cm} \mathbf{e}_2)}{E_m + h\nu_2 - E_g} + \frac{(\mathbf{e}_2 \mathbf{p}_{cm})(\mathbf{p}_{cm} \mathbf{e}_1)}{E_m + h\nu_1 - E_g} \right]^2. \quad (4)$$

Here, A_1 = const; N_1 and N_2 are the volume density of photons with frequencies ν_1 and ν_2, respectively; ε_1 and ε_2 are the dielectric constants at the frequencies ν_1 and ν_2; $\mathbf{p}$ is the electron momentum (the subscript m stands for an intermediate state; c, for the conduction band; and ν, for the valence band); E_m is the energy interval between the conduction-band bottom and the intermediate state m; and V is the volume of the excitation region. It can be seen from expression (4) that the value of W depends on the volume density and frequency of absorbed photons and also on the orientations of photons' polarization vectors $\mathbf{e}_1$ and $\mathbf{e}_2$. We believe that it is the polarization factor which gives rise to the fine structure in the PL spectrum of the layers with a removed narrow-gap region. Obviously, the mechanism of the effect of this factor consists in the following. Each reflection of a photon changes its polarization. In addition, photons propagate within a crystal whose refractive index varies; as a result, their paths in the crystal are curvilinear, which leads to continuous variations in the polarization. If the values of J are small, in which case the probability of two-photon absorption W is low, the aforementioned mechanisms are responsible for nonmonotonic variation in this probability along the drift of nonequilibrium charge carriers. In the crystal regions where the electron-momentum vector is parallel to the polarization vectors of absorbed photons, the probability W is higher than in the regions where these vectors are not parallel; as a result, "surges" in the concentration of nonequilibrium charge carriers appear in these regions, which manifest themselves in the form of spikes against the continuous spectrum of PL.

At high excitation levels, the probability W increases owing to an increase in the volume densities of photons N_1 and N_2, which brings about an increase in the number of crystal regions where the vectors $\mathbf{p}$ and $\mathbf{e}_1$ (and $\mathbf{e}_2$) are parallel, an increase in the frequency factor, and a resulting smoothing of the fine structure in the spectrum.

The absence of a fine structure in the PL spectrum and the pronounced effect of the excitation-region extent d' on the frequency dependence of the coefficient of two-photon absorption in the full-thickness layers are related to two circumstances. First, the reradiation is a single-pass process in these layers. Second, the paths of the low-frequency photons that are reflected from the wide-gap surface and traverse a longer distance in these layers than in the layers with a removed narrow-gap region become more rectilinear and oriented along the ∇E_g vector. These circumstances exclude a local increase in the probability W, which is caused by a polarization-related factor in two-photon absorption in such layers.

5. CONCLUSION

Thus, the two-photon photoluminescence absorption involving reradiation depends on a geometrical factor in graded-gap $Al_xGa_{1-x}As$ solid solutions in the case of drift transport of nonequilibrium charge carriers in the built-in electric field F in the crystal. This geometrical factor amounts to the following: a change in the extent of the excitation region brings about variations both in the efficiency and in the characteristics of the spectral dependence of two-photon absorption of recombination radiation.

REFERENCES

1. V. N. Bessolov, V. G. Gutov, A. I. Imenkov, *et al.*, Fiz. Tekh. Poluprovodn. (Leningrad) **11** (5), 939 (1977) [Sov. Phys. Semicond. **11**, 552 (1977)].
2. R. G. Roedel and V. G. Keramidas, J. Appl. Phys. **50** (10), 6359 (1973).
3. A. I. Bazyk, V. F. Kovalenko, and G. P. Peka, Ukr. Fiz. Zh. **27** (7), 1007 (1982).
4. V. F. Kovalenko, A. Yu. Mironchenko, and S. V. Shutov, Fiz. Tekh. Poluprovodn. (St. Petersburg) **36** (5), 513 (2002) [Semiconductors **36**, 481 (2002)].
5. G. P. Peka, V. F. Kovalenko, and A. N. Smolyar, *Graded-Gap Semiconductors* (Vishcha Shkola, Kiev, 1989).

6. V. F. Kovalenko, G. P. Peka, and L. G. Shepel', Fiz. Tekh. Poluprovodn. (Leningrad) **14** (7), 1350 (1980) [Sov. Phys. Semicond. **14**, 798 (1980)].
7. A. I. Bazyk, V. F. Kovalenko, A. Yu. Mironchenko, and S. V. Shutov, Fiz. Tekh. Poluprovodn. (St. Petersburg) **35** (1), 53 (2001) [Semiconductors **35**, 54 (2001)].
8. F. P. Kesamanly, V. F. Kovalenko, I. E. Maronchuk, *et al.*, Fiz. Tekh. Poluprovodn. (Leningrad) **12** (7), 1318 (1978) [Sov. Phys. Semicond. **12**, 780 (1978)].
9. V. P. Gribkovskiĭ, *The Theory of Emission and Absorption of Light in Semiconductors* (Nauka i Tekhnika, Minsk, 1975).
10. V. F. Kovalenko, A. Yu. Mironchenko, and S. V. Shutov, Fiz. Tekh. Poluprovodn. (St. Petersburg) **36** (2), 192 (2002) [Semiconductors **36**, 185 (2002)].
11. V. I. Ponomarenko, Kvantovaya Élektron. (Kiev), No. 1, 13 (1966).

Translated by A. Spitsyn

Semiconductors, Vol. 37, No. 1, 2003, pp. 44–49. Translated from Fizika i Tekhnika Poluprovodnikov, Vol. 37, No. 1, 2003, pp. 44–49.

SEMICONDUCTOR STRUCTURES, INTERFACES, AND SURFACES

Mathematical Simulation of the Kinetics of High-Temperature Silicon Oxidation and the Structure of the Boundary Layer in the Si–SiO_2 System

G. Ya. Krasnikov, N. A. Zaitsev, and I. V. Matyushkin*

Research and Development Institute for Molecular Electronics and MICRON Corp., Moscow (Zelenograd), 103460 Russia

**e-mail: mivmiv@aport.ru*

Submitted March 27, 2002; accepted for publication April 22, 2002

Abstract—Structural complexes formed in the Si–SiO_2 boundary layer under high-temperature thermal oxidation of silicon are considered. A mathematical model of the kinetics of silicon–oxygen cluster polymerization was suggested using the boundary-layer concept. The influence of the diffusion flow of these clusters on the percentage of SiO_4 tetrahedral chains of various lengths in the SiO_2 bulk was noted. © *2003 MAIK "Nauka/Interperiodica".*

1. INTRODUCTION

The Si/SiO_2 interface structure is a subject of active studies in submicrometer technology [1–14]. First of all, this is caused by the fact that the SiO_2 gate layer thickness typical of modern MOS structures is comparable to the transition layer thickness in the Si–SiO_2 system. However, a consensus on the transition layer structure has not been reached yet.

As previously [1], we adhere to the model of a continuous Si/SiO_2 interface. There exists a boundary layer at the Si/SiO_2 interface in the course of silicon thermal oxidation after which this layer naturally transforms into a transition layer. Thus, to extend the knowledge on the transition layer, attention should be focused on the physicochemical structure and the processes in the boundary layer during silicon oxidation.

Experimental data in this field are very scanty, since the oxidation temperature is high (1200–1300 K) and processing of spectral curves is complicated. Therefore, either formed Si/SiO_2 structures or low-rate oxidation at lower temperatures (up to 900 K) were studied. For example, the kinetics of layer-by-layer silicon oxidation was studied by scanning reflection electron microscopy combined with Auger electron and photoelectron X-ray spectroscopy [2]. A number of interesting results were obtained in the study of the SiO_2–gas interface [2, 3, 14]. In particular, a case of bifurcation related to the surface charge state was described in [3] while studying the dynamics of variation in the coverage of silicon with silicon dioxide. Notwithstanding the evident recent tendency to study low-temperature oxidation (800–100 K) at a low partial oxygen pressure (10^{-7}–10^{-6} Torr), it is high-temperature oxidation which yields highly uniform (over area) and high-quality nanometer layers of gate silicon dioxide.

The interrelation between the kinetics of high-temperature silicon oxidation, polymerization in the boundary layer, and its structural features is the subject of inquiry in this paper.

2. MODEL OF THE Si–SiO_2 BOUNDARY LAYER

The SiO_2 layer grows in the course of silicon thermal oxidation due to the interaction of the silicon surface with O_2 molecules or probably with O* radicals or O_2^- ions that diffused to the surface through the already grown insulator layer. The Si–Si bond breakage and Si–O bond formation proceed simultaneously, which is accompanied by the release of thermal energy. This energy is spent on the additional heating of atomic layers adjacent to the interface. Thus, elementary oxidation stages are thermally activated and active particles of O_2^-, O_2^*, and (SiO)* are generated. The layer phase state changes: a viscoelastic pseudoliquid emerges instead of a solid amorphous phase characteristic of silicates. In moving away from the active zone of the reaction, the viscosity increases and the insulator is vitrified. However, the viscoelastic (even if cooled) liquid phase is retained in the SiO_2 layer lying at a certain distance from the Si–SiP_2 interface. We refer to this layer, together with the active reaction zone, as the boundary layer (see Fig. 1). The active zone probably consists of various clusters of incompletely oxidized SiO_x ($x < 2$) silicon, which can be either rigidly linked to the silicon lattice or exist as a melt. The polymerization zone is permanently "fed" by monomers from the interface due to thermally activated diffusion of these clusters. Formation of polymer molecules in the active zone is impossible since the locally high temperature prevents chain elongation. Existence of active particles of vari-

ous types, e.g., NaO^-, can also be assumed. The influence of sodium accumulation, as well as hydrogen and potassium cations at the Si/SiO_2 interface, on gate insulator degradation has already been elucidated in the literature (see, e.g., [1, 5, 8]). These particles can promote destruction of Si–Si bonds in the active zone, as well as initiate or, on the contrary, inhibit polymeric chain formation in the polymerization zone.

Receding from the $Si–SiO_2$ interface, the active zone gradually transfers to the polymerization zone. The latter represents a viscoelastic pseudoliquid characterized by rather slow reactions of polymeric-chain elongation effected by trapping of various monomeric units (clusters). Furthermore, an important role in the formation of the structure typical of bulk SiO_2 is played by oxidation of incompletely oxidized polymeric chains. The transition of the polymerization zone to the bulk SiO_2 structure is caused by two factors: (i) full completion of Si–O chain oxidation and (ii) a drastic increase in the viscosity caused by cyclization of polymer molecules. However, it is not clear what mechanism has the most significant influence on the spatial confinement of a boundary layer: either polymeric chains are cycled when they are still suboxidized or when they represent an already formed chain of SiO_4 tetrahedra. In our opinion, the former scenario takes place. If the oxidation rate is low, a polymer network or gel can arise due to the formation of covalent Van der Waals bonds between polymeric chains or linking of rings to each other. At high oxidation rates, polymerization does not proceed to completion and polymeric clusters are not large. At the final oxidation stage, the diffusive flow of oxygen particles comes to an end and suboxidized polymeric chains emerge in the polymerization zone.

We now briefly and qualitatively discuss the probable structures of both monomeric clusters and polymeric molecules (this qualitative analysis is consistent with quantum-chemical calculations). The energy (4.6 eV) of a single Si–O bond formation is sufficient to break two Si–Si bonds (2.3 eV), i.e., to transfer a silicon atom to an *sp*-hybridized state. In other words, the energy released during the oxygen–silicon interaction is sufficient to break the bonds with a lattice for a fraction of silicon atoms. This can give rise to Si_xO_y low-molecular clusters, which can freely migrate in the boundary layer. The oxidation conditions are nonequilibrium; therefore, the Si atom in such clusters, e.g., $^+Si{\equiv}Si–O^-$, can have hybridization which differs from sp^3. Then, these clusters can form a linearly branched polymer (Fig. 2), which, being oxidized, yields either a linear (Fig. 3) or folded (Fig. 4) $(Si_2O_2)_n$ polymer. The molecules shown in Figs. 2–4 do not exhaust the diversity of polymer structures. These polymers, when oxidized, ultimately produce the SiO_4 tetrahedron chains characteristic of a Zahariasen network of bulk layers of silicon dioxide.

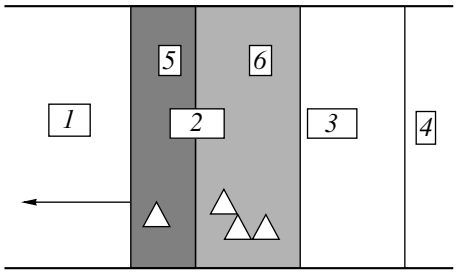

Fig. 1. Boundary layer in the $Si–SiO_2$ system: (*1*) silicon, (*2*) boundary layer, (*3*) grown SiO_2 layer, (*4*) gas medium, (*5*) active zone, and (*6*) polymerization zone. The arrow indicates the SiO_2 growth direction. The triangle symbolically shows the SiO_4 lattice structure tetrahedron. The layer thickness scale is not obeyed.

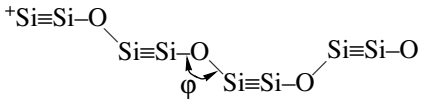

Fig. 2. Polymeric chain of four monomeric SiO_2 units. The rightmost monomeric unit is parallel to the plane of the drawing. Rotation of the plane angle φ about the Si–O bond allows multiplicity of rotational-isomeric chain states.

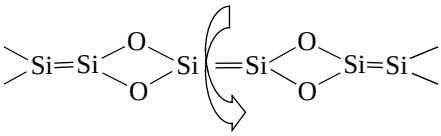

Fig. 3. A fragment of the polymeric $(Si_2O_3)_n$ molecules. The arrow shows the possibility of rotation about the double Si=Si bond.

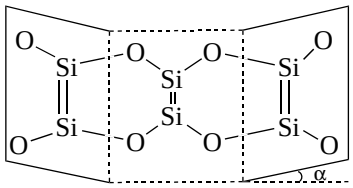

Fig. 4. A fragment of the cyclic $(Si_2O_3)_n$ structure. Each Si_2O_2 unit is planar (the corresponding planes are shown by parallelograms). The dihedral angle between planes is designated as α.

3. MATHEMATICAL MODEL OF POLYMERIZATION IN THE BOUNDARY LAYER IN A $Si–SiO_2$ SYSTEM

We now consider an arbitrary cross section in the polymerization zone. Since the $Si–SiO_2$ interface permanently moves (to the left, to be precise) into the semiconductor depth during oxidation, the horizontal coordinate of this section increases. Hence, motion

along the temporal coordinate t on the assumption of a constant oxidation rate is equivalent to motion along the spatial coordinate (Fig. 1). Let there be a monomer inflow to this cross section j. We denote the concentrations of the monomer and the polymer composed of monomeric units $i + 1$ in the layer by x_0 and x_i, respectively. Considering the cross section with a certain finite thickness to be homogeneous as a whole, we write the reactions up to the formation of the $(n + 1)$-unit polymer ($n \le N = 9$) as

$$\begin{cases} x_0 + x_0 \xrightarrow{k_0} x_1 \\ x_1 + x_0 \xrightarrow{k_1} x_2 \\ \ldots\ldots\ldots\ldots\ldots \\ x_{N-1} + x_0 \xrightarrow{k_{N-1}} x_N, \end{cases} \tag{1}$$

where $k_0, \ldots, k_{N-1}$ are the rate constants of corresponding chemical reactions. When receding from the $Si–SiO_2$ interface, the local viscosity increases in this zone, since the number of 8-, 9-, or 10-unit polymeric molecules increases. The further elongation of the chain is limited by cyclization of polymer molecules and the formation of a polymeric network; therefore, the local viscosity drastically increases and chemical reactions of chain elongation become sterically (spatially) difficult. The reactions are assumed to be irreversible, their rate is calculated by the mass action law (bimolecular reaction), and the rate constants are considered to be different. In order to take into account the restriction on chain elongation, we set $k_N = 0$. Then, we can write

$$\begin{cases} dx_0/dt = j(x_0, t) - k_0x_0^2 - k_1x_0x_1 - \ldots - k_{N-1}x_{N-1}x_0 \\ dx_1/dt = k_0x_0^2 - k_1x_1x_0 \\ \ldots\ldots\ldots\ldots\ldots\ldots\ldots\ldots \\ dx_n/dt = k_{n-1}x_{n-1}x_0 - k_nx_nx_0 \\ \ldots\ldots\ldots\ldots\ldots\ldots\ldots\ldots \\ dx_N/dt = k_{N-1}x_{N-1}x_0. \end{cases} \tag{2}$$

The viscoelastic properties of the growing SiO_2 layer suggest that reactions (1) are diffusion-controlled ($i > 0$),

$$k_i = \frac{2RT}{3\eta}(i + 1). \tag{3}$$

We note that the constant k_0 can in fact be defined by another expression, since the monomer–monomer interaction is probably controlled by chemical reaction kinetics rather than by diffusion. The viscosity of the boundary layer, in turn, depends on the variables of the problem, i.e., the polymer molecule concentrations. We employ the dependence

$$\eta = \eta_0\left(1 + \frac{\sum_{n=1}^{N-1} x_n(t)n^3}{\sum_{n=1}^{N-1} x_n(t)}\right), \tag{4}$$

which is known in the physics of polymers as an approximation for the case under study.

Model equations (2) incorporate the monomer flux $j(x_0, t)$, which arrives at the cross section from the outside and generally depends on time (since the farther the cross section is from the interface, the weaker the diffusion flow of monomer will be into this cross section from the active zone) and on the monomer concentration itself. It is evident that the temporal dependence of the flux j is a steadily decreasing function, which vanishes when the cross section passes from the polymerization zone into the region of already formed SiO_2 layers.

We use a simplifying assumption and consider the boundary-layer viscosity as constant. Although this assumption is not quite justified physically, it is undoubtedly interesting to consider this case (allowing an analytical solution) as an initial approximation. Then, system (1) becomes a second-order, autonomous, and homogeneous system. We then substitute the variable as $d\xi = dx_0(t)dt$. To make the substitution correct, we also assume that $k_0x_0 \gg k_ix_i$ ($i > 0$); i.e., the monomer amount decreases mainly due to dimerization. We then have one equation for $x_0(\xi)$, another for $x_1(\xi)$, and $(N–1)$ equations for $x_i(t)$, $(i > 1)$; i.e.,

$$\begin{aligned} dx_1/d\xi &= f(\xi) - k_1x_1, \\ dx_i/d\xi &= k_{i-1}x_{i-1} - k_ix_i, \quad i = \overline{2, N-1}, \end{aligned} \tag{5}$$

where the summand k_0x_0 written in terms of the new coordinate ξ serves as $f(\xi)$. First, we solve a homogeneous linear set, i.e., with $f(\xi) = 0$. It has n roots $\lambda_i = –k_i$, where the ith eigenvector $\mathbf{u}_i$ has the following kth component:

$$u_{ik} = \begin{cases} 0, & k < i \\ \prod_{l=i+1}^{k} \frac{k_l}{k_l - k_i}, & k > 1. \\ 1, & k = i \end{cases} \tag{6}$$

For example, the quantities $\lambda_n = –k_n$ and $\lambda_1 = –k_1$ correspond to the vectors (0, 0, 0,…, 0, 1) and 1, $k_1/(k_2 – k_1)$, $k_1k_2/((k_2 – k_1)(k_3 – k_1))$, …, $k_1 \cdot \ldots \cdot k_n/((k_2 – k_1) \cdot \ldots \cdot (k_n –$

k_1)). The general solution to the homogeneous equation is given by

$$x_i(\xi) = \sum_{k=1}^{n} C_k u_{ik} \exp(-k_i \xi). \quad (7)$$

We note that the first component $\boldsymbol{x}(\xi)$ depends only on the first of the constants C_k. This facilitates the application of the Cauchy formula to solving the heterogeneous set. Thus, we arrive at the following formula:

$$\mathbf{x}(\xi) = C_{11}\mathbf{u}_1 \exp(-k_1\xi) + \int_0^{\xi} f(\xi')\exp(k_1(\xi' - \xi))d\xi' + \sum_{k=2}^{n} C_k \exp(-k_k\xi)\mathbf{u}_k. \quad (8)$$

At the initial condition $x_i(0) = 0$, $x_1(0) = 0$, we have $C_1 = C_k = 0$. We now return to the dependence $z_0(\xi)$. It is evident that

$$dt = \frac{dx_0}{j(x_0) - k_0 x_0^2}, \qquad d\xi = x_0 dt = \frac{1}{2}\frac{d(x_0^2)}{j(\sqrt{x_0^2}) - k_0 x_0^2}. \quad (9)$$

If j = const and $x_0(0) = c$, we have

$$x_0(t) = \sqrt{\frac{j}{k_0}}\frac{1 - \exp(-bt)}{1 + \exp(-bt)}, \quad b = 2\sqrt{jk_0}\frac{j + ck_0}{j - ck_0}, \quad (10)$$

$$f(\xi) = k_0 x_0(\xi) = \sqrt{k_0 j(1 - \exp(-2k_0\xi)) + k_0 x^2 \exp(-2k_0\xi)}. \quad (11)$$

In particular, it follows from (10) that the rate of decrease in the monomer amount significantly depends on its initial concentration since the quantity c is in the exponent. The same is also valid for the effect of flux j.

4. RESULTS OF CALCULATION

The experimental determination of the rate constants of chain-propagation reactions is rather complicated, particularly when the specific features of each n-unit polymer are taken into account. We assumed that $T = 1273$ K and $\eta_0 = 10^9$ kg/(m s) [4, 6]. In order to specify the initial conditions for the Cauchy problem (2), we have to know $c = x_0(0)$; we assume that $x_i(0) = 0$ ($i > 0$). The dimension of concentration x_0 is [cm^{-3}], the value of c is 2.2×10^{22} cm^{-3}. This dimension makes it possible to retain the conventional dimensions of the reaction rate constant and the flux j. Furthermore, there is an additional parameter τ responsible for the decrease of the rate of flux j, e.g., according to the dependence

$$j = j_0 \exp(-t/\tau). \quad (12)$$

Let the total oxidation time be 300 s, which in practice yields an SiO_2 layer with a thickness of several nanometers. We take τ equal to one tenth of the duration of oxidation. We considered the parameter j_0 to be proportional to the initial monomer concentration c. In our opinion, the relation of these two parameters in many respects defines the adequacy of any thermal oxidation model.

In view of the above, calculations were carried out in dimensionless quantities: the concentrations were normalized to c, the time was normalized to a second, the flux was normalized to $[x_0(0)/c]$, and the rate constants were defined in terms of the parameter Q,

$$Q = \frac{2RT}{3\eta_0}c. \quad (13)$$

The dimensionless representation of the system shows that the changes in the quantities c and Q are equivalent; i.e., they imply identical changes in the curve dynamics (in dimensionless variables). The calculation was carried out by the conventional Runge–Kutta method of the fourth order of accuracy at a step corresponding to 1/10 s.

Figures 5 and 6 display typical calculation results for the exponentially decreasing dependence of the monomer flux j. The abscissa and ordinate axes are the time (s) and the molar or mass fractions of polymeric chains of various lengths (relative units), respectively. This representation allows us to take into account the problem of excluded volume; i.e., the cross section is permanently fed with material and simultaneously expands. The molar W and mass U fractions are cal-

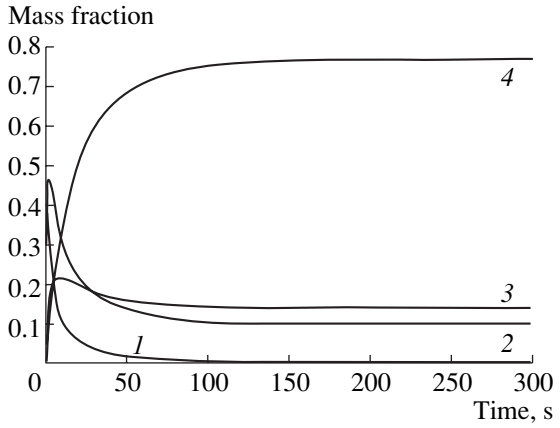

Fig. 5. Dependence of the mass fractions of polymers on the reaction coordinate at $c = 1$, $Q = 1$, $\tau = 30$ s, and $j = 10c\exp(-t/\tau)$: the monomer fraction (*1*), fractions of 2- to 4- (*2*), 5- to 7- (*3*), and of 8- to 10-unit (*4*) polymers. "Time" is the reaction coordinate.

Dependence of the polymer fraction in the asymptotics on the model coefficients

Coefficients and their values			Polymer fractions in the asymptotics			
Q	τ	j_0	Monomer	2–4-unit polymers	5–7-unit polymers	8–10-unit polymers
0	30	$0.1c$	0.001/0.000	0.591/0.356	0.231/0.288	0.177/0.356
10	30	$0.1c$	0.000/0.000	0.387/0.184	0.236/0.227	0.377/0.589
0.1	30	$0.1c$	0.114/0.033	0.658/0.524	0.117/0.279	0.062/0.165
1	3	$0.1c$	0.000/0.000	0.777/0.602	0.179/0.287	0.044/0.111
1	30	$0.01c$	0.001/0.000	0.725/0.532	0.210/0.315	0.064/0.152
1	30	$10c$	0.000/0.000	0.245/0.098	0.174/0.138	0.581/0.765
1	30	0	0.000/0.000	0.801/0.640	0.165/0.274	0.033/0.086

Note: The slash (/) separates the molar (left) and mass (right) fractions of polymers.

culated according to the following expressions (14) and (15):

$$W_\alpha = \sum_{i \in \alpha} x_i / \sum_{0 \le i \le N} x_i, \quad (14)$$

$$U_\alpha = \sum_{i \in \alpha} (i+1)x_i / \sum_{0 \le i \le N} (i+1)x_i. \quad (15)$$

The molar fraction accounts to a greater extent for the final structure of the transition layer, whereas the mass fraction better represents the balance of material in the boundary layer during thermal oxidation. Here, α is a set of indices over which aggregation is carried out. The sets {0}, {1,2,3}, {4,5,6}, and {7,8,9} were considered. The general run of the curves is as follows: the monomeric fraction decreases (with the possible exception of the initial range), the fraction of 8-, 9-, and 10-unit polymers increases steadily, while the fractions of 2-, 3-, 4- and 5-, 6-, 7-unit polymers have a more or less pronounced maximum (the instants of time when the molar and mass fraction maxima occur are noncoincident). The fraction of 2-, 3-, and 4-unit polymers drastically increases in the first few seconds, while the monomer fraction abruptly decreases. As t asymptotically tends toward infinity, a quasi-steady state is established, which now corresponds to the formation of bulk layers of silicon dioxide. Furthermore, if the variation dynamics of polymer fractions of various lengths in this cross section is known, one can indirectly determine the distribution of these fractions over the transition layer thickness.

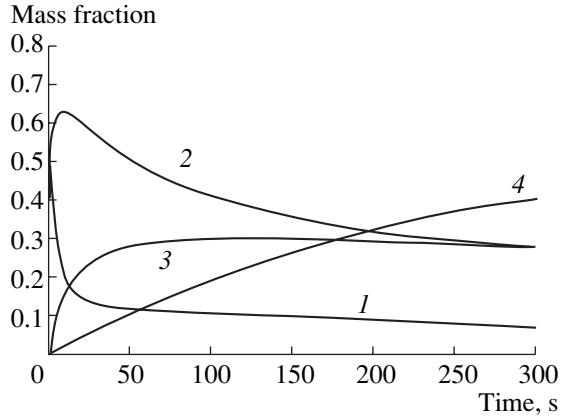

Fig. 6. Initial region of the dependence of Fig. 5. $j = 0.1c\exp(-t/\tau)$. Other parameters and designations are the same as in Fig. 5.

The model was studied for various values of parameters (see table). For example, when chain propagation (parameter Q) becomes more and more active, all the maxima become pronounced and the fraction of 8-, 9-, and 10-unit polymers increases. The quasi-steady state is established more quickly. Figures 5 and 6 show the special features of the initial oxidation stage; however, these features are characteristic of only a few values of the parameters. The physical cause of the Q increase consists, e.g., in an increase in oxidation temperature or a decrease in viscosity; the latter can also be caused by an increase in temperature. As the monomer flux (coefficient j_0) increases, which, e.g., can be caused by an increase in the partial pressure of oxygen in the gas mixture, the fraction of heavy polymers also increases and a local concentration maximum of 2-, 3-, and 4-unit polymers can take place. Without the monomer diffusion flow ($j = 0$), 2-, 3-, and 4-unit polymers dominate, and the quasi-steady state is rapidly reached. A similar factor decreases the parameter τ, which corresponds to the case of relative separation of various cross sections when there is a quick falloff of the monomer flux from the active zone.

The dependences displayed in Figs. 5–6 and in the table are related, first of all, to features of the polymerization reaction kinetics and monomer diffusion into the boundary layer from the active zone. These dependences can be used to predict the final distribution of polymers with various numbers of monomeric units over the transition layer thickness, which is of impor-

tant practical significance for optimization of the electrical properties of the gate insulator.

5. CONCLUSION

The numerical experiment shows that the diffusion flow of monomers from the active zone into the polymerization zone has a significant effect on the ratio of fractions of polymeric molecules of various lengths even in the case of growth of rather thick silicon dioxide layers. This conclusion, which also takes into account the fact that the active zone naturally transforms into a polymerization zone with time, seems to be of interest. As was also shown, the fraction of heavy polymers increases with the temperature and oxidation rate.

Currently, a mathematical model that solves the problem of the percentage of these rings in various cross sections of the transition layer does not exist. Furthermore, the mechanisms influencing the formation of rings of various sizes are also unclear. The mathematical model developed in this study of structural inhomogeneities that form in thermally oxidized silicon layers qualitatively answers the above questions. A more adequate quantitative solution requires extending the model we suggested with technologically clearer parameters, in particular, the oxidation temperature and the partial pressure of oxygen in the gas mixture.

REFERENCES

1. N. A. Zaĭtsev and I. O. Shurchkov, *Structural–Extrinsic and Electrical Properties a Si–SiO_2 System* (Radio i Svyaz', Moscow, 1993), p. 193.
2. H. Watanabe, K. Kato, T. Uda, *et al.*, Phys. Rev. Lett. **80**, 345 (2000).
3. M. Suemitsi, Y. Enta, Y. Takegawa, and N. Miyamoto, Appl. Phys. Lett. **77**, 3179 (2000).
4. N. Kwok-On and D. Vanderbilt, Phys. Rev. B **59**, 10132 (1999).
5. D.-A. Luh, T. Miller, and T.-C. Chang, Phys. Rev. Lett. **79**, 3014 (1997).
6. J. P. Perdew, K. Burke, and M. Ernzerhof, Phys. Rev. Lett. **77**, 3865 (1996).
7. H. Nishikawa, R. Tohmon, Y. Ohki, *et al.*, J. Appl. Phys. **65**, 4672 (1989).
8. P. J. Grunthaner, M. Hecht, F. J. Crunthaner, and N. Johnson, J. Appl. Phys. **61**, 629 (1987).
9. G. Hollinger and F. Himpsel, Appl. Phys. Lett. **44**, 93 (1984).
10. F. Himpsel, F. McFeely, A. Taleb-Ibraimi, *et al.*, Phys. Rev. B **38**, 6084 (1988).
11. S. Iwata and A. Ishizaka, J. Appl. Phys. **79**, 6653 (1996).
12. A. Pasquarello, M. Hybertsen, and R. Car, Phys. Rev. Lett. **74**, 1024 (1995).
13. N. Miyata, H. Watanabe, and M. Ichikawa, Phys. Rev. Lett. **84**, 1043 (2000).
14. R. Tromp, G. Rubloff, P. Balk, and F. K. LeGoues, Phys. Rev. Lett. **55**, 2332 (1985).

Translated by A. Kazantsev

Semiconductors, Vol. 37, No. 1, 2003, pp. 50–52. Translated from Fizika i Tekhnika Poluprovodnikov, Vol. 37, No. 1, 2003, pp. 50–52.

SEMICONDUCTOR STRUCTURES, INTERFACES, AND SURFACES

Effect of Thermal Annealing of Radiation Defects on the Noise Characteristics of Silicon *p–n* Structures with a Thin Multiplication Region

A. K. Baranouskiĭ*, P. V. Kuchinskiĭ, and E. D. Savenok****

** Belarussian State University, ul. Leningradskaya 14, Minsk, 220080 Belarus*

*** Institute of Applied Physics, Belarussian Academy of Sciences, ul. F. Skoriny 16, Minsk, 270072 Belarus*

e-mail: baranouski@bsu.by

Submitted April 9, 2002; accepted for publication May 15, 2002

Abstract—Specific features of changes in the noise spectral density and the lifetime of minority charge carriers in Si *p–n* structures with a thin multiplication region under thermal annealing of radiation defects were studied. It is shown that the change in the frequency characteristics of noise in *p–n* structures is related to the recovery of surface states. A qualitative explanation of self-limitation of the avalanche process in *p–n* structures with a thin multiplication region is suggested. © *2003 MAIK "Nauka/Interperiodica".*

Avalanche semiconductor devices operating in the mode of microplasma breakdown are used in electronics as sources of broadband noise. Studying the mechanisms of influence of external factors on the parameters of physical processes that occur under avalanche multiplication is of practical interest for the development and application of such devices.

In [1], changes in the noise characteristics of Si *p–n* structures with different *p–n*-junction areas irradiated with gamma-ray photons from a ^{60}Co source were reported. The features of changes in the width of a low-frequency plateau in the curves of the noise spectral density (NSD), as well as the relationship between these changes and the changes in the lifetime of minority charge carriers in structures with small-area *p–n* junctions (about 10^{-6} cm^2), are of much interest. Accordingly, the aim of this study was to investigate the behavior of the NSD and the lifetime of minority charge carriers under the isochronous annealing of radiation defects.

We studied samples of *p*-Si:B with a B concentration of 10^{18} cm^{-3}. The main *p–n* junction was obtained by the thermal diffusion of P at 900°C; the area of this junction amounted to $\approx 10^{-6}$ cm^2. The samples differed from each other by the time of thermal diffusion, which manifested itself in different amplitudes and frequencies of microplasma pulses. The *p–n*-junction depth amounted to 1.33×10^{-4} and 1.50×10^{-4} cm for samples prepared using different thermal-diffusion times. The dopant concentration amounted to $\approx 2 \times 10^{17}$ cm^{-3} in the region of charge multiplication, which corresponded to a breakdown voltage of ≈8 V. Under these conditions, the width of the multiplication region amounted to $\approx (1–2) \times 10^{-5}$ cm.

The samples were irradiated with gamma photons from a ^{60}Co source with an energy of 1.2 MeV at doses in the range of 1.8×10^{16}–1.7×10^{18} cm^{-2}. The irradiated samples were annealed for 30 min in the temperature range of 80–380°C. Output oscillograms of the noise current in the structures were measured at 20 ± 1°C by passing an electric current with an average value of 50 μA through the structures. The calculation of the NSD was performed using a standard algorithm of fast Fourier transformation [2] on the basis of measurements of the noise current in the *p–n* structures under investigation. Figure 1 illustrates the changes in the NSD due to irradiation and subsequent annealing.

The lifetime of minority carriers was measured using the transient-response method with current switching [3].

The diffusion length L_d is related to the lifetime τ of minority charge carriers as follows:

$$L_d = \sqrt{(kT/e)\mu\tau}. \quad (1)$$

Here, k is the Boltzmann constant, T is the temperature, e is the elementary charge, and μ is the charge-carrier mobility. As calculations show, irradiation leads to a decrease in the diffusion length from 1.1×10^{-3} (initial samples before irradiation) to 0.4×10^{-3} cm (samples irradiated with the highest dose). According to the previously obtained [1] dependence of the change in the lifetime of charge carriers on the irradiation dose, the diffusion length becomes smaller than the linear dimension of the *p–n* junction when the irradiation dose Φ exceeds 1.5×10^{17} cm^{-2}. In this case, the change in the lifetime of minority charge carriers caused by irradiation is inversely proportional to the concentration of introduced radiation defects. A change in the frequency

of microplasma pulses (or the width of the low-frequency plateau in the NSD curves) is directly proportional to the concentration of the introduced radiation defects.

We introduce the following designations: τ_0, τ_{flow}, and τ_T are the effective lifetimes of minority charge carriers before irradiation, after irradiation with the highest dose, and after annealing, respectively; $\Delta\omega_0$, $\Delta\omega_{flow}$, and $\Delta\omega_T$ are the widths of the low-frequency plateau in the NSD curves (at the level of 0.7 of the maximum) before irradiation, after irradiation with the highest dose, and after annealing, respectively. The curves shown in Figs. 2 and 3 represent the recovery of the lifetime of minority charge carriers and the recovery of the width of the low-frequency plateau in the NSD curves as a result of thermal annealing:

$$f(\tau) = (1/\tau_T - 1/\tau_0)/(1/\tau_{flow} - 1/\tau_0), \quad (2)$$

$$f(\omega) = (\Delta\omega_T - \Delta\omega_0)/(\Delta\omega_{flow} - \Delta\omega_0). \quad (3)$$

Two stages of defect annealing are quite distinct in Fig. 2. These are the stage in the range of 150–260°C and the stage in the range of 300–340°C. As can be seen, the annealing at 300–340°C does not provide for the complete recovery of the lifetime of charge carriers. This may be due to the fact that, in this temperature range, the diffusion length becomes larger than the linear dimension of the *p–n* junction and expression (2) cannot be used for accurate estimations in this case.

At the same time, a nearly complete recovery of the frequency of microplasma pulses is observed in the annealing stage in the temperature range of 100–260°C (see Fig. 3).

It was established using capacitance spectroscopy that irradiation of *p*-Si with gamma photons from a ^{60}Co source results in the formation of acceptor radiation defects with emission-activation energies E_v + 0.35 eV and E_v + 0.21 eV having production rates of $\approx 10^{-4}$ and 3×10^{-5} cm^{-1}, respectively [4]. The above-mentioned defects are commonly related to oxygen–vacancy centers (E_v + 0.35 eV) and divacancies (E_v + 0.21 eV). Accordingly, the observed stage of recovery of the lifetime of minority carriers in the range of 150–260°C can be attributed to the annealing of divacancies, while the stage at 300–340°C can be attributed to the annealing of centers with an emission-activation energy of E_v + 0.35 eV [5]. However, Figs. 2 and 3 show a broadening of the annealing stage in the range of 100–260°C, which is inconsistent with the features of annealing of divacancies in the sample bulk. Such behavior of the annealing of defects produced by gamma irradiation may be related to the annealing of defects introduced at the surface [6].

The assumption that the annealing stage in the range of 300–340°C corresponds to annealing of defects in the bulk is confirmed by an analysis of oscillograms of output pulses. Indeed, the probability of initiating an avalanche decreases, which can be attributed to a decrease in the number of bulk centers of reemission of charge carriers that are responsible for initiating subsequent avalanches.

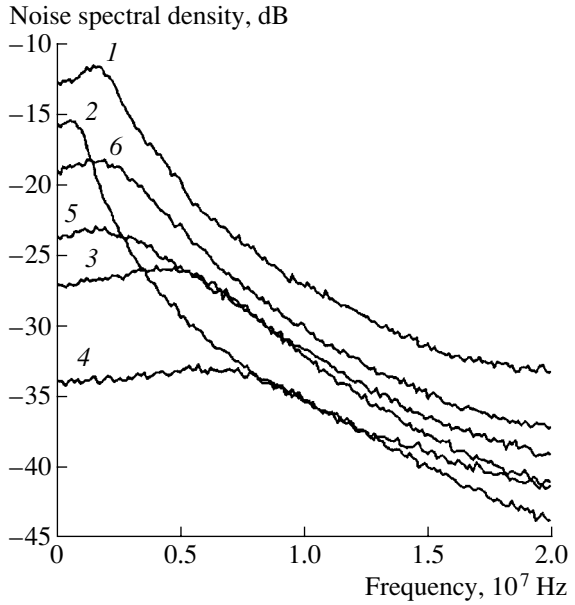

Fig. 1. Noise spectral density for samples with 1.33×10^{-4}-cm-deep *p–n* junctions irradiated at doses of (*1*) 0, (*2*) 1.8×10^{16}, (*3*) 6.0×10^{17}, and (*4*) 1.14×10^{18} cm^{-2} and annealed at (*5*) 240 and (*6*) 340°C.

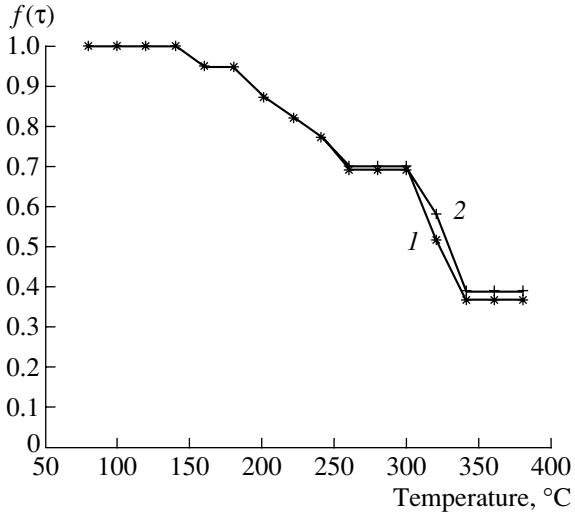

Fig. 2. Change in the effective lifetime of minority charge carriers as a result of isochronous annealing of radiation defects. The thermal-diffusion times for the main *p–n* junction are (*1*) 120 and (*2*) 75 min.

The data on the annealing studies make it possible to refine the model suggested in [1]. The decrease in the lifetime of minority charge carriers with the increase in the irradiation dose, as well as the decrease in the steepness of the trailing edge of microplasma pulses after the

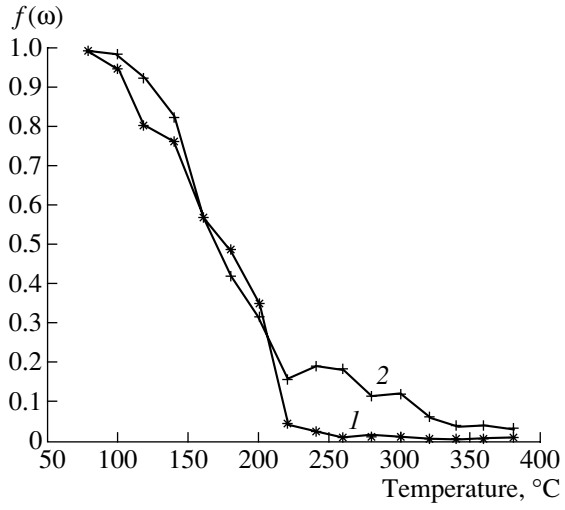

Fig. 3. Change in the width of the low-frequency plateau in the NSD curve as a result of isochronous annealing of radiation defects. The thermal-diffusion times for the main *p–n* junction are (*1*) 120 and (*2*) 75 min.

first stage of irradiation (see [1]), suggest that the surface serves as the region where majority charge carriers (i.e., holes) accumulate. In other words, the surface has a negative potential [7]. In this case, a local decrease in an electric field results in the avalanche multiplication being switched off (the thickness of the multiplication region amounts to $\approx(1–2) \times 10^{-5}$ cm). A comparison of the thermal-relaxation time and the time of the trailing edge of pulses makes it possible to exclude the effect of lattice heating [8]. The irradiation-caused exclusion of the surface effect diminishes the role of the space charge; i.e., the number of charge carriers increases due to impact ionization by holes, which increases the trailing-edge time of microplasma pulses. Under these conditions, the lifetime τ of minority charge carriers changes more significantly in comparison with the bulk lifetime [9]: $\Delta(1/\tau) = \kappa\Phi$. Here, κ is the damage factor and Φ is the irradiation dose. Such behavior of the lifetime can be caused by the formation of positively charged radiation defects at the surface. These defects not only balance the negatively charged centers, but also affect the results of measurements of the lifetime of minority charge carriers. A further increase in the irradiation dose leads to the formation of bulk traps for minority charge carriers, which serve as effective centers of trapping and recombination of majority charge carriers, as well as centers of initiation of subsequent avalanches.

Thus, the investigations performed here show that the recovery of noise characteristics of Si *p–n* structures with a thin multiplication region, irradiated with gamma photons from a ^{60}Co source and subjected to thermal annealing, occurs in the temperature range of 100–120°C. We ascertained the dominant effect of the surface on the frequency characteristics of noise. However, it is necessary to take into account the influence of radiation defects on the time distribution of noise pulses, because the time of initiation of repeat avalanches is governed to a greater extent by reemission of electrons from trapping centers rather than by thermal electrons. The results obtained may be used in designing noise semiconductor devices.

REFERENCES

1. O. K. Baranovskiĭ, P. V. Kuchinskiĭ, V. M. Lutkovskiĭ, *et al.*, Fiz. Tekh. Poluprovodn. (St. Petersburg) **35**, 352 (2001) [Semiconductors **35**, 338 (2001)].
2. J. Bendat and A. Piersol, *Random Data. Analysis and Measurement Procedures* (Wiley, New York, 1986; Mir, Moscow, 1989).
3. S. M. Krakauer, Proc. IEEE **50** (7), 1665 (1962).
4. P. V. Kuchinskiĭ, Author's Abstract of Candidate's Dissertation (Belarusskiĭ Gos. Univ., Minsk, 1984).
5. V. I. Gubskaya, P. V. Kuchinskiĭ, and V. M. Lomako, Fiz. Tekh. Poluprovodn. (Leningrad) **20**, 1055 (1986) [Sov. Phys. Semicond. **20**, 664 (1986)].
6. V. S. Pershenkov, V. D. Popov, and A. V. Shal'nov, *Surface Radiation Effects in Integrated Circuits* (Énergoatomizdat, Moscow, 1988).
7. Z. Ya. Sadygov, M. K. Suleĭmanov, and T. Yu. Bokova, Pis'ma Zh. Tekh. Fiz. **26** (7), 75 (2000) [Tech. Phys. Lett. **26**, 305 (2000)].
8. B. I. Datsko, Fiz. Tekh. Poluprovodn. (St. Petersburg) **31**, 186 (1997) [Semiconductors **31**, 146 (1997)].
9. V. S. Vavilov and N. A. Ukhin, *Radiation Effects in Semiconductors and Semiconductor Devices* (Atomizdat, Moscow, 1969).

Translated by Yu. Sin'kov

Semiconductors, Vol. 37, No. 1, 2003, pp. 53–56. Translated from Fizika i Tekhnika Poluprovodnikov, Vol. 37, No. 1, 2003, pp. 53–56.

SEMICONDUCTOR STRUCTURES, INTERFACES, AND SURFACES

Photoelectric Properties of Heterojunctions between Silicon and Polyhomoconjugated Organometallic Compounds

N. V. Blinova*, E. L. Krasnopeeva*, Yu. A. Nikolaev, A. Yu. Osadchev*, V. Yu. Rud'***, Yu. V. Rud'**, E. I. Terukov**, and V. V. Shamanin***

** Institute of Macromolecular Compounds, Russian Academy of Sciences, Bol'shoi proezd 31, St. Petersburg, 119004 Russia*

*** Ioffe Physicotechnical Institute, Russian Academy of Sciences, Politekhnicheskaya ul. 26, St. Petersburg, 194021 Russia*

**** St. Petersburg State Technical University, ul. Polytekhnicheskaya 29, St. Petersburg, 195251 Russia*

Submitted April 26, 2002; accepted for publication May 15, 2002

Abstract—Rectifying photosensitive heterojunctions were obtained for the first time by depositing films of polyhomoconjugated organometallic compounds onto Si waters. The photoelectric properties of the obtained structures were studied, and the basic photoelectric parameters of these structures were determined. The new heterojunctions are shown to be promising candidates for developing natural-radiation photoconverters. © *2003 MAIK "Nauka/Interperiodica".*

The development of novel heterojunctions based on diamond-like semiconductors and other materials is a promising line of inquiry in modern optoelectronics [1–4], since such heterojunctions make it possible to expand the functional range of optoelectronic devices. It was found recently that a direct contact of inorganic semiconductors with materials of biological origin gives rise to the photovoltaic effect [5–7].

In this study, we report the first results from investigations of the photoelectric properties of heterojunctions formed by the deposition of recently synthesized polyhomoconjugated organometallic polymers [8, 9] onto single-crystal Si wafers.

Polymers were prepared by the Wurtz–Fittig reaction according to the scheme

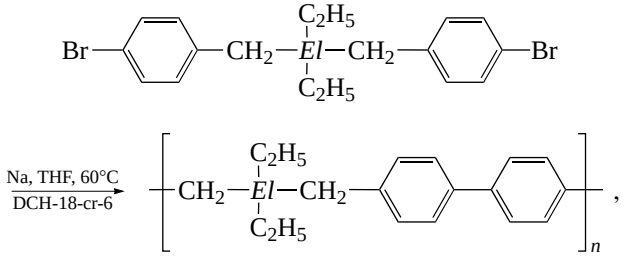

where *El* = Si, Ge.

The reactions were carried out in an inert gas using dehydrated tetrahydrofurane (THF) as a solvent and dicyanohexyl-18-crown-6 (DCH-18-cr-6) as an interphase-transport catalyst. Polymers were purified by redeposition, and solvent residues were removed by vacuum drying down to an unchanged weight. The structure of macromolecules was confirmed by the data obtained using UV, IR Fourier, ^{1}H, and ^{13}C NMR spectroscopic methods.

The polymer layers were grown on substrates by the flow coating technique using a fresh filtered solution of the polymer in $CHCl_3$ (C_W = 5%). Solvent residues evaporated from the layers at room temperature in air. Final drying was carried out in a vacuum chamber with a residual pressure of 2×10^{-2} Torr.

The optical absorption was studied in polymeric layers deposited onto glass plates. The synthesis method developed has made it possible to obtain layers with a uniform yellow color, a thickness $d = 50$ μm, and an area of 2×2 cm^2. The measured optical transmittance T_0 of the polymeric layers was used to calculate the optical-absorption coefficient

$$\alpha = \frac{1}{d}\ln\left\{\frac{(1-R)^2}{2T_0} + \sqrt{\frac{(1-R)^2}{2T} + R^2}\right\}, \qquad (1)$$

where R is the optical reflectance; $R \approx 0.3$ in the studied spectral range. Typical spectral dependences of the optical-absorption coefficient for the polymers under study are shown in Fig. 1. The absorption coefficient of the polymer layers begins to significantly increase at photon energies $\hbar\omega > 2.8$ eV (Fig. 1, curves *1*, *2*). We can use this fact to evaluate, in a first approximation, the band gap E_G of two different novel organic compounds. One can see from Fig. 1 (curves *1*, *2*) that the short-wave length portions of the optical-absorption spectra in the coordinates $((\alpha\hbar\omega)^2, \hbar\omega)$ are close to linear and the extrapolation $(\alpha\hbar\omega)^2 \longrightarrow 0$ yields virtually the same value of the band gap for these materials,

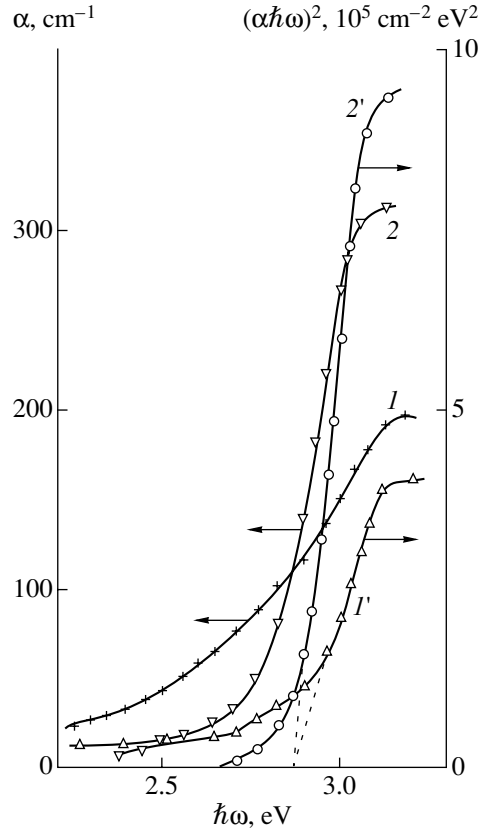

Fig. 1. Spectral dependences of the optical-absorption coefficient of polymer layers (*1*, *1*') *P*⟨Ge⟩ and (*2*, *2*') *P*⟨Si⟩ at *T* = 300 K.

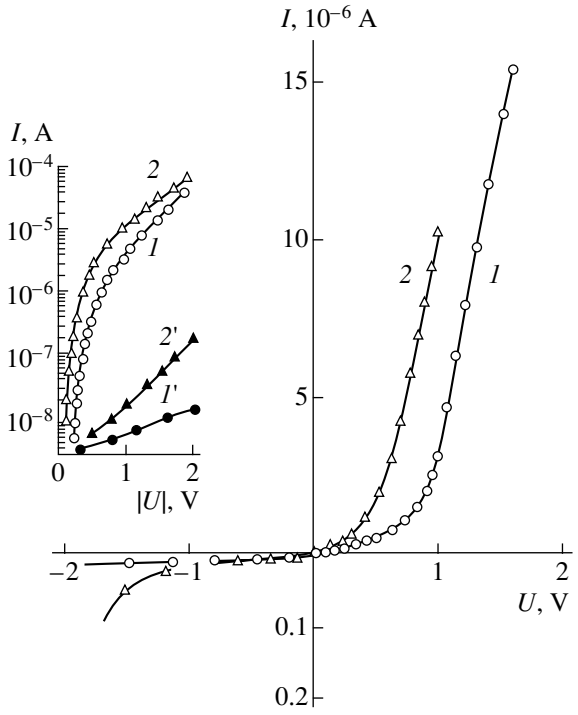

Fig. 2. Steady-state *I–V* characteristics of the (*1*, *1*') *P*⟨Ge⟩/*p*-Si and (*2*, *2*') *P*⟨Si⟩/*p*-Si heterojunctions at *T* = 300 K. The inset shows the (*1*, *2*) forward and (*1*', *2*') reverse portions of the *I–V* characteristics plotted in semilogarithmic coordinates.

$E_G \cong 2.85$ eV at *T* = 300 K (Fig. 1, curves *1*', *2*'). It is worth noting that in the long-wavelength region of the $\alpha(\hbar\omega)$ spectra the absorption coefficient of the polymer layers containing Ge is higher than that of the Si-containing layers (see curve *1* in Fig. 1). This may be caused by a higher concentration of defects in the Ge-containing layers. We should note that a more adequate interpretation of the data on the optical absorption in the obtained organic polymers calls for further investigations.

The polymer–crystalline-Si heterojunctions were formed by depositing polymer layers onto the chemically polished surfaces of KDB-10 Si(111) (i.e., *p*-Si(111):B, ρ = 10 Ω cm) wafers. The heterojunction area was about 1 cm^2. Aluminum layers up to ≈0.1 μm thick, deposited through masks onto the polymer layers, as well as a silver paste, were used as ohmic contacts. The current–voltage (*I–V*) characteristics of the Al(Ag)/polymer/Al(Ag) systems showed that Ohm's law is valid in the range of bias voltages up to *U* = 100 V. The resistivity of the polymer layers of different types deposited on glass was evaluated at ρ = 10^8–10^9 Ω cm at *T* = 300 K. Notably, the Si- and Ge-containing polymers were found to have similar resistivities.

The steady-state *I–V* characteristics of the new heterojunctions showed pronounced rectification. The forward direction was the same for all the structures and corresponded to the negative polarity of the applied bias at the *p*-Si substrates. Typical steady-state *I–V* characteristics for the heterojunctions based on polymers (*P*) containing Si (*P*⟨Si⟩) and Ge (*P*⟨Ge⟩) are shown in Fig. 2. Typical parameters of the heterojunctions are listed in the table. The initial portions of the

Photoelectric properties of the heterojunctions based on organic polymers and Si (*T* = 300 K, illumination from the polymer-layer side)

Structure type	*n*	I_s, A	R_0, Ω	U_0, V	*K* (*U* ≅ 1 V)	S_U^m, V/W	$\hbar\omega^m$	δ, eV
P⟨Ge⟩/*p*-Si	1.0, 1.35	4.6×10^{-11}	10^5	0.9	2800	80	1.26	1.6
P⟨Si⟩/*p*-Si	2.0	1.5×10^{-9}	10^5	0.5	550	250	1.26	0.6

I–V characteristics ($U < 0.4$ V) are described by the equation for conventional semiconductor diodes:

$$I = I_s\left[\exp\left(\frac{eU}{nkT}\right) - 1\right]. \quad (2)$$

The ideality factor n determined from the slope of the forward portions of the I–V characteristics in the coordinates ($\log I$–U) ranges from 1 to 2 (see table), which can be caused by competition between diffusion and recombination components of the forward current [10]. It is not improbable that the value of n can be controlled not only by the parameters of deposition of polymer layers on the Si wafers, but also by features of the elements of Group IV of the periodic system incorporated in the polymer. The deviation from relation (2), observed at $U > 0.5$ V, is caused by the effect of the rather high series resistance of these structures. The values of the saturation current I_s (see table), as well as the rather low reverse currents ($\leq 10^{-9}$ A) at biases up to 20 V at $T = 300$ K in the best structures, are indicative of the high quality of the obtained heterojunctions. The reverse current typically increases with the voltage by a power law, which is probably caused by the effect of leakage currents at the structure periphery.

When the bias voltage exceeds certain values characteristic of specific structures (see Fig. 2, curves *1* and *2*), the exponential dependence (2) transforms into the linear one:

$$I = \frac{U - U_0}{R_0}. \quad (3)$$

The $P\langle$Ge$\rangle$/p-Si and $P\langle$Si$\rangle$/p-Si heterojunctions turned out to have similar and rather high values of the residual resistance R_0 (see table), while the cutoff voltage U_0 (generally associated with the energy-barrier height) turned out to be higher for the heterojunctions based on the Ge-containing polymer. As follows from the steady-state I–V characteristics, the rectification factor K (defined as the forward-to-reverse current ratio at $U \cong 1$ V) is higher for the $P\langle$Ge$\rangle$/p-Si heterojunctions (see table).

The exposure of the obtained heterojunctions to natural light resulted in the photovoltaic effect, due to which negative photovoltage arose on the Si substrate. It is also noteworthy that the photovoltage sign is independent of the location of the probe beam of light (about 0.2 cm in diameter) on the surfaces of these structures. As a rule, the photovoltage is higher in the case of illumination of the polymer-layer side. The established features of the I–V characteristics suggest that the photovoltaic effect is controlled by the energy barrier arising at the semiconductor–organic-polymer contact. The highest photovoltaic sensitivity S_U^m of the best heterojunctions (see table) amounts to 250 V/W at 300 K when the polymer-layer side is illuminated.

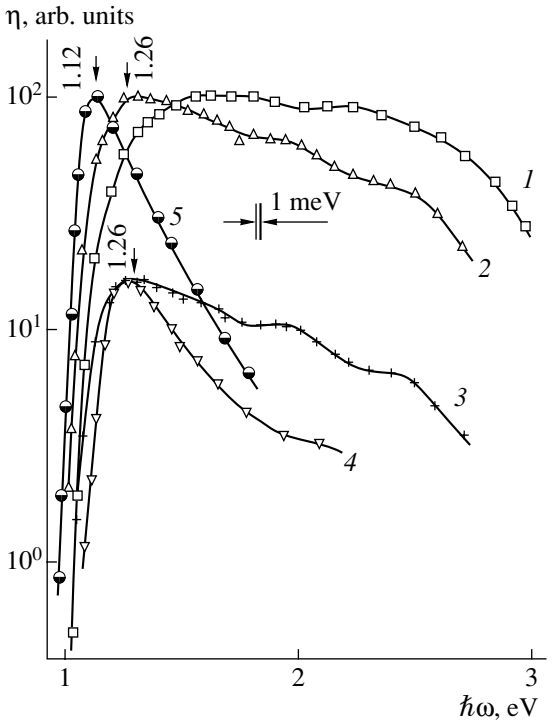

Fig. 3. Spectral dependences of the relative quantum efficiency η of the $P\langle$Ge$\rangle$/p-Si (sample 1, curves *1*, *5*; sample 2, curve *2*) and $P\langle$Si$\rangle$/p-Si (sample 3, curve *3*; sample 4, curve *4*) heterojunctions exposed to unpolarized light from the polymer-layer side (curves *1–4*) and from the silicon-wafer side (curve *5*) at $T = 300$ K. The spectra are shifted along the ordinate axis to avoid overlapping.

Typical spectral dependences of the relative quantum efficiency of conversion η for the obtained heterojunctions are shown in Fig. 3. One can see that the broadband photovoltaic effect arises in the heterojunctions when the polymer layers are illuminated (curves *1–4*). The long-wavelength limit of the photosensitivity in such heterojunctions is caused by the interband absorption in Si. On the coordinates $((\eta\hbar\omega)^{1/2}, \hbar\omega)$, the long-wavelength portions of the spectra of the obtained heterojunctions are linearized and the extrapolation $((\eta\hbar\omega)^{1/2} \longrightarrow 0)$ yields a cutoff on the energy axis, which is consistent with the value of the band gap of bulk crystalline Si [11] (see Fig. 4). When the Si sides of the $P\langle$Ge$\rangle$/p-Si and $P\langle$Si$\rangle$/p-Si heterojunctions are illuminated, as a rule, the photosensivity spectra become narrow-band (Fig. 3, curve *5*) and the FWHM of the η spectra, δ, amounts to ≅0.22 eV and decreases with an increase in the silicon-substrate thickness. When the polymer-layer side is illuminated, the value of δ is larger than in the preceding case (see curves *1–4* in Fig. 3 and table). One can see from Fig. 3 that the η spectra of the heterojunctions studied here differ from each other when the energy of incident photons $\hbar\omega$ exceeds 1.26 eV. Correspondingly, the value of δ changes too. This difference in the η spectra can be caused by the effect of conditions in which polymer

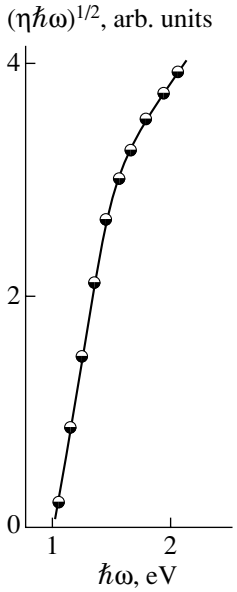

Fig. 4. Dependence of $(\eta\hbar\omega)^{1/2}$ on $\hbar\omega$ for the $P\langle Ge\rangle/p$-Si heterojunction at $T = 300$ K (illumination from the $P\langle Ge\rangle$-layer side).

layers were deposited onto Si. It is noteworthy that the short-wavelength falloff of the photosensitivity in the structures with the broadest band spectrum (Fig. 3, curve *1*) is located near the value corresponding to the band gap $E_G \cong 2.85$ eV (determined from the polymer absorption spectra). Therefore, the observed short-wavelength falloff of η can be explained by the effect of light absorption in the polymeric layer. Hence, the new heterojunctions exhibit high photosensitivity in the range between the band gaps of contacting materials, which is, in general, typical of perfect heterojunctions [10]. We also emphasize that the values of δ, as well as the spectral-peak location obtained for the best Si/polymer heterojunctions, are indicative of the applicability of the developed systems to the design of high-efficiency solar cells.

Thus, we have suggested and developed a new type of semiconductor–organic-polymer heterojunctions. These heterojunctions can be used in the development of high-efficiency thin-film photoconverters of natural light.

ACKNOWLEDGMENTS

This study was supported by the Russian Foundation for Basic Research, project nos. 01-03-32376, 01-03-32292, and 02-03-06498.

REFERENCES

1. Zh. I. Alferov, Fiz. Tekh. Poluprovodn. (St. Petersburg) **32**, 3 (1998) [Semiconductors **32**, 1 (1998)].
2. Zh. I. Alferov, V. M. Andreev, and N. N. Ledentsov, *Semiconductor Heterostructures. Ioffe Institute 1918–1988. Development and Research Activities* (Ioffe Physicotechnical Inst., Russ. Acad. of Sci., St. Petersburg, 1998), p. 276.
3. A. G. Milnes and D. L. Feucht, *Heterojunctions and Metal-Semiconductor Junctions* (Academic, New York, 1972; Mir, Moscow, 1975).
4. J. Simon and J.-J. Andre, *Molecular Semiconductors: Photoelectrical Properties and Solar Cells* (Springer-Verlag, Berlin, 1985; Mir, Moscow, 1988).
5. V. Yu. Rud', Yu. V. Rud', and V. Kh. Shpunt, Fiz. Tekh. Poluprovodn. (St. Petersburg) **29**, 1178 (1995) [Semiconductors **29**, 608 (1995)].
6. V. Yu. Rud', Yu. V. Rud', V. Ch. Shpunt, and S. Iida, Inst. Phys. Conf. Ser. **152**, 997 (1998).
7. V. Yu. Rud', Yu. V. Rud', and V. Kh. Shpunt, Zh. Tekh. Fiz. **70** (2), 114 (2000) [Tech. Phys. **45**, 255 (2000)].
8. A. Yu. Osadchev, A. R. Pushkarev, Yu. Yu. Nikitina, *et al.*, Zh. Obshch. Khim. **70**, 1470 (2000).
9. V. V. Shamanin, A. Yu. Osadchev, and S. S. Skorokhodov, Dokl. Akad. Nauk **380** (1), 71 (2001).
10. S. Sze, *Physics of Semiconductor Devices* (Wiley, New York, 1981; Mir, Moscow, 1984).
11. *Physicochemical Properties of Semiconductor Materials: a Handbook*, Ed. by A. V. Novoselova and V. B. Lazarev (Nauka, Moscow, 1975).

Translated by A. Kazantsev

Semiconductors, Vol. 37, No. 1, 2003, pp. 57–64. Translated from Fizika i Tekhnika Poluprovodnikov, Vol. 37, No. 1, 2003, pp. 57–64.

SEMICONDUCTOR STRUCTURES, INTERFACES, AND SURFACES

Optical Transparency of Macroporous Silicon with Through Pores

E. V. Astrova, L. I. Korovin, I. G. Lang, A. D. Remenyuk*, and V. B. Shuman

Ioffe Physicotechnical Institute, Russian Academy of Sciences, St. Petersburg, 194021 Russia

**e-mail: arem@pop.ioffe.rssi.ru*

Submitted May 15, 2002; accepted for publication May 16, 2002

Abstract—Optical transmission spectra of macroporous silicon with through pores has been studied experimentally and theoretically in the spectral range 0.3–0.8 μm (in which single-crystal Si is opaque). The spectra are discussed in terms of the general diffraction theory. Expressions taking into account the diffraction at the entrance and exit of pores and the influence exerted by deviation of the angle of light incidence from the normal are derived. The transmission spectrum is fairly well described by the results of calculation. © *2003 MAIK "Nauka/Interperiodica".*

1. INTRODUCTION

Macroporous silicon (*ma*-Si) is a type of porous Si in which vertical or slightly inclined pores form a two-dimensional (2D) periodic structure on the surface, and the pore depth is larger than the interpore distance and pore diameter by orders of magnitude [1]. The combination of a high-quality 2D periodic structure with high refractive index contrast in *ma*-Si opens the way to its application as a 2D photonic crystal, where a photonic band gap appears during light propagation in a direction perpendicular to the pore axis. The spectral position and width of the gap are defined by the structure symmetry, interpore distance, and pore radius [2]. For the light propagating parallel to the pore axis, *ma*-Si can be used as a sharp-cutoff high-pass filter that is transparent in the short-wavelength range and blocks long-wavelength radiation [3]. Filters with spectral characteristics of this kind are used in various imaging systems. Conventionally, these have been multilayer thin-film structures deposited on a glass substrate. In the short-wavelength range, the filter materials themselves block the transmission. In *ma*-Si filters, light propagates in the air in pores surrounded by silicon that is opaque to visible light. The pore dimensions, i.e., their diameter and length, define the filter transmission spectrum. To date, we know of only one study devoted to *ma*-Si transmission in the visible range [3], and another, to its popularization [4]. The present study is devoted to further experimental and theoretical investigations of *ma*-Si transmission in the visible range for light propagating parallel to the pore axis.

2. EXPERIMENTAL

The samples under study were 300-μm-thick *n*-Si wafers 25 mm in diameter with 15Ω-cm resistivity and deep periodically arranged channels produced by photoelectrochemical etching. The technology of *ma*-Si preparation was described in [5]. The periodical pore structure had a hexagonal symmetry, with a distance of $d = 12$ μm between the pore centers and a pore diameter $2R$ ranging from 5 to 8.6 μm. In the as-grown *ma*-Si, the diameter of pores was about 3 μm; their average depth was $L \approx 150$–200 μm. To obtain uniform through pores, the pore-free part of a substrate and the layer with seeding pits were removed by mechanical polishing. Further, the pore diameter was enlarged by repeated oxidation of a sample, with subsequent oxide removal from the sample surface and pore walls by etching. The parameters of the samples are presented in the table.

Figure 1 shows a SEM image of a sample with a pore diameter of 4.0 μm. As is seen, the pores are parallel and their diameter varies only slightly along their length, though the walls are somewhat corrugated.

Transmission spectra in the wavelength range of 0.3–0.8 μm were recorded with an SF-26 spectrophotometer. The beam of light from a monochromator, with a divergence of about 3.1°, was incident normal to the surface and was not additionally focused after passing through the sample. Figure 2 shows the transmission spectra of four samples whose through pores have different diameters and lengths. As seen, the transmission of *ma*-Si is at a maximum in the ultraviolet and violet

Table

Sample no.	R, μm	L, μm	Porosity, %
1	2.5	170	15.6
2	3.4	180	29.0
3	4.3	180	46.0
4	4.1	208	41.8

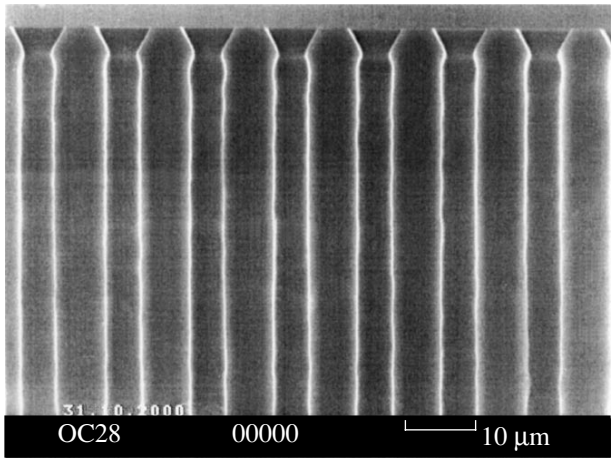

Fig. 1. SEM image of an *ma*-Si sample before the removal of seeding pits.

spectral ranges, and it decreases as the wavelength increases.

3. DISCUSSION

The behavior and nature of *ma*-Si optical transmission in the visible range differ radically from the cases of single-crystal (*c*-Si) and nanoporous Si. For comparison, Figure 3 presents the transmission spectra for *c*-Si [6], luminescing nanoporous Si [7], and *ma*-Si (this study). In interpreting the *ma*-Si transmission spectra, it is important that, during the propagation of visible light along the pore axis, the radiation is transmitted through absolutely transparent channels with a refractive index $n = 1$ and surrounded by silicon absorbing in this spectral range. The pore diameter (the minimum was 5 μm), the interpore distance $d = 12$ μm, and the wafer thickness substantially exceed the wavelength (in the transmission study, the maximum wavelength was $\lambda = 0.8$ μm). Therefore, the general theory of diffraction [8] can be used for a theoretical interpretation of the *ma*-Si transmission spectra. A circular aperture is assumed. Figure 4 schematically shows a pore with a radius R in a plate with a thickness L.

It is convenient to resolve the problem in several steps. At the first step, we consider normal incidence of light onto an *ma*-Si wafer and consider only the light diffraction by the entrance of a single pore. The light intensity distribution $I(r)$ in the pore exit plane is determined taking only the diffraction by the pore entrance under normal incidence into account, i.e., at $\theta = 0$. Starting with the relation (59.2) from [8], we obtain

$$I(r) = I_0 Z(r). \quad (1)$$

Here, I_0 is the intensity of incident light,

$$Z(r) = \left[\int_0^\beta dt \cos t J_0(\sqrt{at})\right]^2 + \left[\int_0^\beta dt \sin t J_0(\sqrt{at})\right]^2, \quad (2)$$

where $t = \pi r_i^2/\lambda L$ is the integration variable, $a = 4\pi r^2/\lambda L = 4\beta r^2/R^2$, $\beta = \pi/R^2/\lambda L$, and $J_0(z)$ the Bessel function. Let us consider different limiting cases. At $\lambda \longrightarrow 0$, a transition to the geometrical optics must

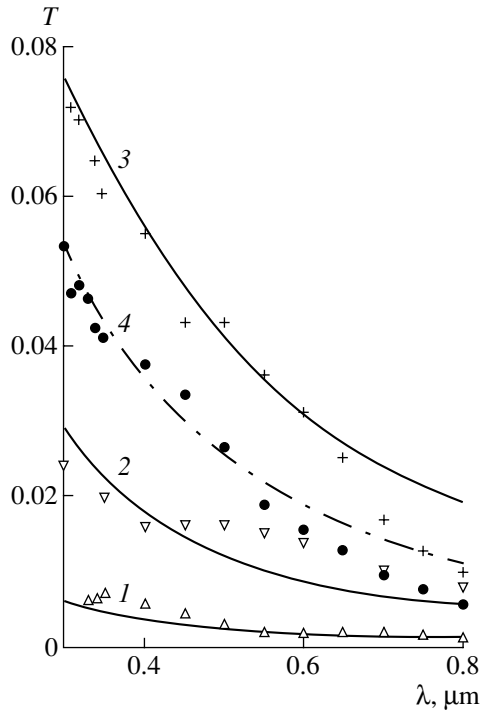

Fig. 2. Transmission spectra of four *ma*-Si samples. Points: experiment; curves: calculation by relation (7). Indices at curves are the sample numbers.

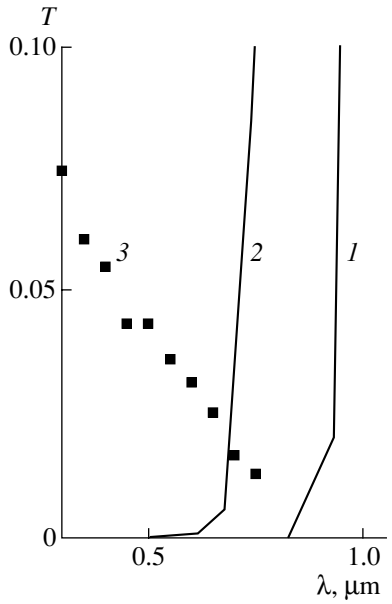

Fig. 3. Transmission spectra of (*1*) single-crystal Si [6], (*2*) nanoporous Si [7], and (*3*) *ma*-Si.

occur. Indeed, in this limit, the function $Z(r)$ becomes a step function

$$Z_{\lambda\to 0}(r) = \begin{cases} 1, & r < R \\ 0, & r > R \end{cases}; \quad (3)$$

i.e., $I(r) = I_0$ within the pore exit, and $I(r) = 0$ outside it. To prove relation (3), we note that at $r < R$, which corresponds conditionally to $\beta > a/4$, in the limit $\lambda \longrightarrow 0$, the integrals in (2) are (see [9, p. 749])

$$\int_0^\infty dt \cos t J_0(\sqrt{at}) = \sin\frac{a}{4},$$
$$\int_0^\infty dt \sin t J_0(\sqrt{at}) = \cos\frac{a}{4}, \quad (3a)$$

which yields $Z_{\lambda\to 0} = 1$ upon being substituted into (2). At $\lambda \longrightarrow 0$, but with $\beta < a/4$, the same integrals are zero, which yields $Z_{\lambda\to 0} = 0$.

Analyzing (2), we find that the light intensity distribution at the pore exit is defined by the parameter β. It is a product of small R/L and large $\pi R/\lambda$ parameters; therefore, in terms of diffraction theory, it may be both much smaller and much greater than unity. At $\beta \gg 1$, the Fresnel and, at $\beta \ll 1$, the Fraunhofer diffraction takes place [8]. In the latter case, (2) approximately yields

$$Z_B(r) = \frac{R^2}{r^2} J_1^2\left(\frac{2\pi Rr}{\lambda L}\right), \quad (4)$$

where $J_1(z)$ is the Bessel function. If the argument of function $z = (2\pi Rr/\lambda L) \ll 1$, then $J_1(z) \approx z/2$ and we approximately obtain

$$Z_A(r) \approx \frac{\pi^2 R^4}{\lambda^2 L^2} = \beta^2; \quad (5)$$

i.e., at small r in the Fraunhofer diffraction case, the quantity $Z_A(r)$, which determines the intensity distribution in the pore exit plane, is independent of r.

The aforesaid is illustrated by Figure 5, which shows $Z(r)$ functions found by numerical integration of (2) with different β values. Curve *1* corresponds to $\beta = 0.1$. Within the limits of $r < R$, $Z(r) \approx 0.01$; i.e., it is very small and remains virtually constant. Nearly all the light energy goes outside the limits of the circle with radius R in the bottom plane; i.e., it does not reach the pore exit, but falls onto side walls. Curve *1* is well described by approximate relation (4), and within $r < R$, by (5). Curve *2* corresponds to $\beta = 1$. This case is intermediate between the Fraunhofer and Fresnel types of diffraction. As seen in the figure, the fraction of energy falling within the circle $r < R$ is comparable with unity. Finally, curve *3* corresponds to a very large $\beta = 50$ (unattained in our experiment, the actual β values being within 0.15–1.6). In this case, nearly all of the energy falls within the circle $r < R$, $Z(r)$ being very small at $r > R$. This is an approximation of the geometrical optics, with the entire amount of energy incident on the pore entrance reaching the exit orifice.

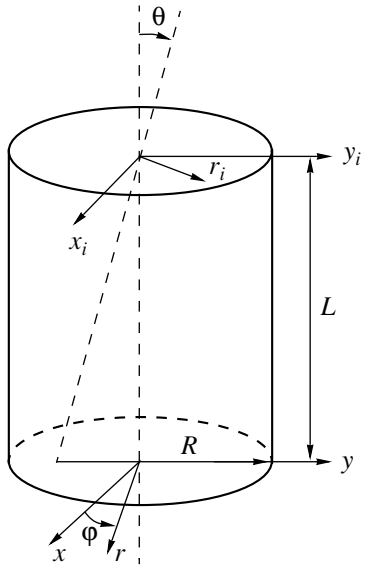

Fig. 4. Transmission of light through a pore at oblique incidence.

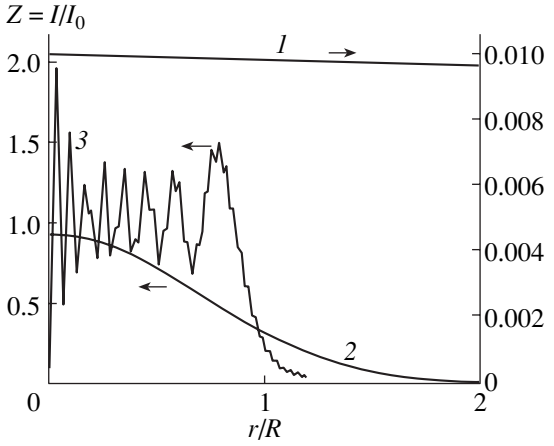

Fig. 5. $Z(r)$ at different β: (*1*) $\beta = 0.1$ (right scale), (*2*) $\beta = 1$ (left scale), and (*3*) $\beta = 50$ (left scale).

In the general case, only the radiation reaching the exit of a pore with radius R passes through a pore. The fraction of energy reaching the pore exit equals $(2\pi/S_0)\int_0^R r\,dr Z(r)$, where $S_0 = \pi r^2$ is the area of the pore orifice. Multiplying this value by the porosity, which equals

$$P = (2\pi/\sqrt{3})(R/d)^2 \quad (6)$$

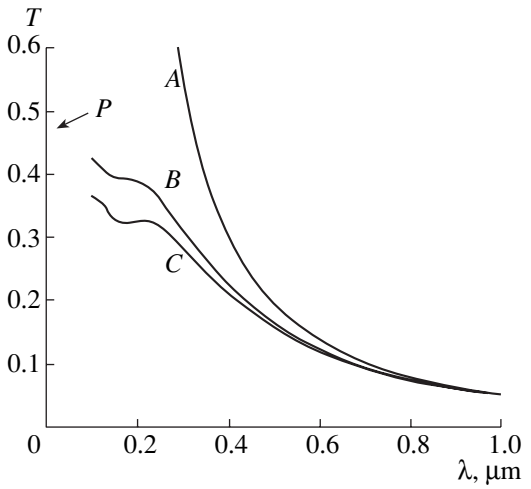

Fig. 6. Transmission spectra of sample no. 3 calculated in approximations of (*A*) geometrical optics and (*B*) Fraunhofer and (*C*) calculated by general relation (7).

in the case of a hexagonal arrangement of pores, we find that the transmission of a *ma*-Si wafer is

$$T(\lambda) = \frac{4\pi}{\sqrt{3}d^2}\int_0^R rdrZ(r). \quad (7)$$

At $\lambda \longrightarrow 0$, i.e., in the limit of geometrical optics, when the function $Z(r)$ has the form (3), we obtain

$$T(\lambda \longrightarrow 0) = P. \quad (8)$$

At $\beta \ll 1$, when the Fraunhofer diffraction takes place,

$$T_B(\lambda) = \frac{4\pi R^2}{\sqrt{3}d^2}\int_0^R \frac{dr}{r} J_1^2\left(\frac{2\pi Rr}{\lambda L}\right). \quad (9)$$

It is noteworthy that, in the limit $\lambda \longrightarrow 0$, relation (9) also yields $T_B(\lambda \longrightarrow 0) = P$. Comparing expressions (2) and (4), we can conclude that in the limit of geometrical optics, i.e., at $\lambda \longrightarrow 0$, relation (4), which describes the Fraunhofer diffraction, yields erroneous results for the light intensity distribution in the pore exit plane. According to (4), at $\lambda \longrightarrow 0$, the intensity is nonzero only at the point $r = 0$ (because $J_1(r) \longrightarrow 0$ at $z \longrightarrow \infty$), whereas according to (2), the intensity is nonzero within a circle of radius R centered at the point $r = 0$. However, the integration of expressions $Z(r)$ and $Z_B(r)$ over the coordinate r yields the same results in the limiting case of $\lambda \longrightarrow 0$. At last, in approximation (5), we obtain

$$T_A(\lambda) = P\beta^2 = \frac{2\pi^3 R^6}{\sqrt{3}d^2\lambda^2 L^2}, \quad (10)$$

which shows that the transparency of *ma*-Si is proportional to the sixth power of R and depends on the wavelength as λ^{-2}. Formulas (9) and (10) were used for interpreting the data in [3].

Figure 6 shows $T(\lambda)$ curves calculated using three different formulas: curve *C* by (7) with substitution of (2), curve *B* by (9), and curve *A* by (10). As is seen, the curves merge when λ is high enough, which indicates Fraunhofer diffraction. At small λ, curve *A* strongly deviates from *B* and *C*, and, at $\lambda \longrightarrow 0$, these latter tend toward the point $T(\lambda \longrightarrow 0) = P$ at the ordinate axis.

In Fig. 2, the experimental data (transmissivity values) are compared with the theoretical $T(\lambda)$ curves that were plotted using the most accurate formulas [(2) and (7)]. The theory describes fairly well the shape of $T(\lambda)$ curves, but the absolute experimental values of transmission (points) are smaller than those predicted theoretically (curves) by a factor of 3.5 for sample nos. 3 and 1 (curves *3*, *1*) and a factor of 4 for sample no. 2 (curve *2*). The theoretical values in Fig. 2 are reduced in order to bring them into coincidence with the experimental data.

Now we will discuss possible reasons as to why the experimental transmissivities are much smaller than the calculated values.

The first reason is the following: the condition of normal incidence of a parallel beam onto the surface of a sample, which is assumed to be met in deriving formula (2), is not fulfilled in the experiment. In actual fact, the beam divergence at the output slit of the spectrometer is 3.1°. This can reduce the transmission in comparison with its calculated value, especially in the short-wavelength range where the geometrical optics is valid and the transmission equals zero if the angle of incidence $\theta > 2R/L$. For example, the critical angle $2R/L$ equals 2.7° for $R = 4.3$ μm and $L = 180$ μm (for $R = 2.5$ μm and $L = 170$ μm, $2R/L = 1.7°$).

The calculations of transmission for oblique incidence of light onto the surface of a sample confirm this assumption. Using relation (59.2) [8, p. 194], we obtain an expression for light intensity in the lower plane of a pore:

$$I(\mathbf{r}, \theta) = I_0 Z(\mathbf{r}, \theta), \quad (11)$$

$$Z(\mathbf{r}, \theta) = Z(r, \varphi, \theta) = \left[\int_0^\beta dt \cos t J_0(\sqrt{a(r, \varphi)t})\right]^2 \times \left[\int_0^\beta dt \sin t J_0(\sqrt{a(r, \varphi)t})\right]^2, \quad (12)$$

where

$$a(r, \varphi) = \frac{4\pi}{\lambda L}(r^2 + L^2\theta^2 + 2rL\theta\sin\varphi); \quad (13)$$

θ is the angle of incidence, which we assume to be small: $\theta \ll 1$, so that $\sin\theta \approx \tan\theta \approx \theta$, $\cos\theta \approx 1$; and φ is the azimuth angle (see Fig. 4). Relation (12) has a

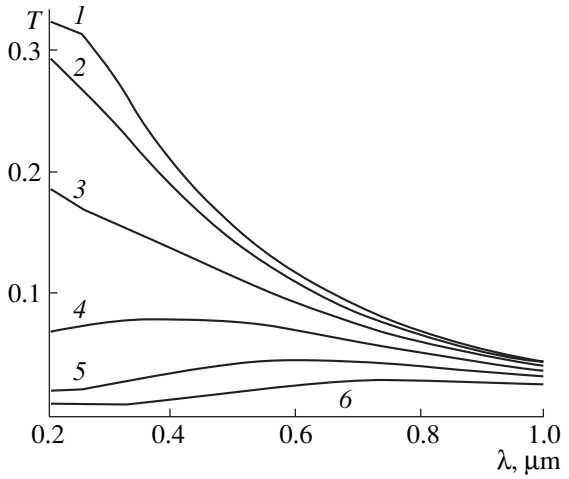

Fig. 7. The transmission of a pore of sample no. 3 calculated with Eq. (14). Angle of incidence θ: (*1*) 0°, (*2*) 0.62°, (*3*) 1.24°, (*4*) 1.86°, (*5*) 2.48°, and (*6*) 3.1°.

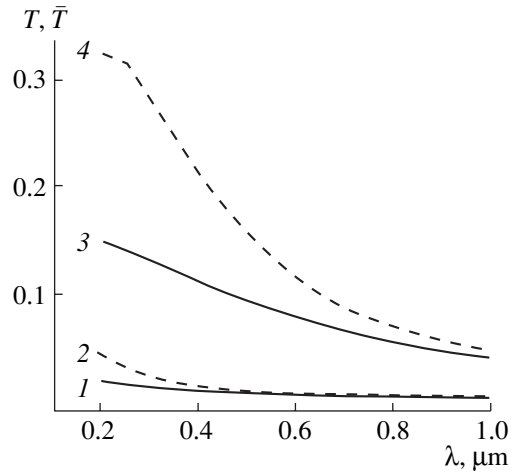

Fig. 8. Calculated transmission spectra: (*1*, *2*) sample no. 1, (*3*, *4*) sample no. 3. (*1*, *3*) (Solid lines) averaged over the polar angle; (*2*, *4*) (dashed lines) normal incidence of the light beam.

very simple interpretation: the intensity distribution in the lower plane under oblique incidence is the same as that under normal incidence, but with the center at the point with coordinates $x = 0$, $y = -L\theta$, instead of the point $\mathbf{r} = 0$.

In the limit of geometrical optics, from (11) and (12) we find that the intensity of light in the output plane equals I_0 within a circle of radius R centered at $x = 0$, $y = -L\theta$. The transition from expression (12) for $Z(\mathbf{r}, \theta)$ to relations $Z_B(\mathbf{r}, \theta)$ and $Z_A(\mathbf{r}, \theta)$ occurs in the same way as in the case of normal incidence of light.

To calculate the transmission for a fixed angle θ, $Z(\mathbf{r}, \theta)$ must be integrated within the circle of radius R in the vicinity of the origin of coordinates $\mathbf{r} = 0$, i.e., within the pore exit; the result must then be divided by πR^2 and multiplied by the porosity P defined by (6). We obtain

$$T(\lambda, \theta) = \frac{2}{\sqrt{3}d^2}\int_0^{2\pi} d\varphi \int_0^R r dr Z(r, \varphi, \theta) \qquad (14)$$

and also

$$T_B(\lambda, \theta) = \frac{2}{\sqrt{3}}\frac{R^2}{d^2}\int_0^{\pi} d\varphi \int_0^R \frac{r dr}{r^2 + L^2\theta^2 + 2rL\theta\sin\varphi} \times J_1^2\left(\frac{2\pi R\sqrt{r^2 + L^2\theta^2 + 2rL\theta\sin\varphi}}{\lambda L}\right), \qquad (15)$$

$$T_A(\lambda, \theta) = \frac{2\pi^3 R^6}{\sqrt{3}d^2\lambda^2 L^2}. \qquad (16)$$

In the last approximation, which we denote by the index *A*, the transmission is independent of angle θ. It is necessary to note, however, that this approximation is valid only under the condition $\frac{2\pi R\sqrt{R^2 + L^2\theta^2 + 2RL\theta\sin\varphi}}{\lambda L} \ll 1$, which is more stringent than $2\pi R^2/\lambda L \ll 1$, applicable in the case of normal incidence. In the geometrical optics limit, we use (14) to obtain an evident result:

$$T(\lambda \longrightarrow 0, \theta) = P\frac{S(R, L\theta)}{\pi R^2}, \qquad (17)$$

where $S(R, L\theta)$ is the overlapping area of two circles of radius R with centers spaced by $L\theta$. Elementary calculations yield

$$S(R, L\theta) = \begin{cases} 2R^2\arccos\dfrac{L\theta}{2R} - L\theta\sqrt{R^2 - (L\theta)^2/4} & \text{at} \quad \theta < \dfrac{2R}{L}, \\ 0 \quad \text{at} \quad \theta > \dfrac{2R}{L}. \end{cases} \qquad (18)$$

Figure 7 shows the transmission T as a function of wavelength λ for sample no. 3 at fixed θ values. As seen, all the curves merge at large λ; i.e., the dependence of transmission on the angle of incidence θ decreases with λ increasing. At small λ, the dependence of transmission on the angle θ is very strong. In order to perform a comparison with the experimental data, the values of $T(\lambda)$ are averaged over θ within the range from 0 to θ_0; i.e., it is necessary to calculate

$$\bar{T}(\lambda) = \frac{1}{\theta_0}\int_0^{\theta_0} d\theta T(\lambda, \theta). \qquad (19)$$

Figure 8 shows data obtained in this manner for sample nos. 1 and 3. Curves *1* and *3* were calculated by

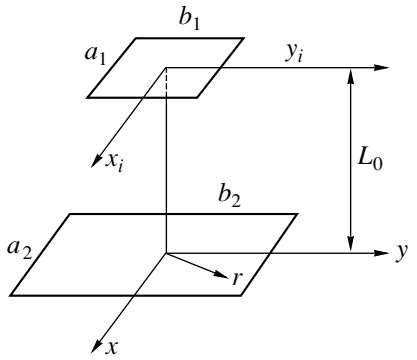

Fig. 9. Model of the experiment: rectangle a_1b_1 is the sample as a source of light and a_2b_2 is the detector.

averaging over the polar angle within the range from 0 to 3.1°; curves *2* and *4* correspond to normal beam incidence. As seen in Fig. 8, at $\lambda \approx 0.2$ μm, the scatter of the angles of incidence nearly halves the transmission for both samples; the effect of scatter in angles may be considered insignificant at $\lambda \approx 1$ μm.

The second possible reason for the discrepancy between theoretical and experimental data may be the neglecting of the diffraction by pore exits. This is indicated by the deflection of a theoretical curve from the experiment in the long-wavelength range (see Fig. 2). This diffraction must lead to beam divergence at the exit of each pore, and this divergence increases as the wavelength increases. Therefore, at long wavelengths, some fraction of the beam transmitted through the sample bypasses the detector, which causes an apparent reduction in the transmission *T*. In further calculations, we disregard the interference of light coming from separate pores; i.e., we sum up the intensities, rather than electric fields, from all pores, since the interference should not considerably affect the total power incident on the detector.

Let us model the experimental conditions using a rectangular source and a detector of light placed in parallel planes spaced by L_0 (Fig. 9). The source is an *ma*-Si wafer emitting light from its pore exits. The intensity distribution at the exit of a single pore situated at the point $x_i = 0, y_i = 0$ is given by relations (1) and (2), with the wafer thickness L replaced by the distance L_0, which is 11 cm in our experiment. Let us estimate the parameter $\beta = \pi R^2/\lambda L_0$. Using, as an example, $R = 4.3$ μm, $\lambda = 0.3$ μm, and $L_0 = 11$ cm, we obtain $\beta \approx 1.7 \times 10^{-3}$. The condition $\beta \ll 1$ is satisfied very well, so we can use the Fraunhofer relation (4), with L replaced by L_0. Evidently, the intensity at point (x, y) in the lower plane, produced by a single pore lying at point (x_i, y_i), equals $IZ_B(\mathbf{r}, \mathbf{r}_i)$, where I is the intensity at the pore exit and

$$Z_B(\mathbf{r}, \mathbf{r}_i) = \frac{R^2}{(x-x_i)^2 + (y-y_i)^2} \times J_1^2\left(\frac{2\pi R\sqrt{(x-x_i)^2 + (y-y_i)^2}}{\lambda L_0}\right). \quad (20)$$

The intensity at point (x, y) in the *ma*-Si output plane, produced by all the pores located inside the rectangle with sides a_1 and b_1, is

$$I(x, y) = nI\int_{-a_1/2}^{a_1/2} dx_i \int_{-b_1/2}^{b_1/2} dy_i Z_B(\mathbf{r}, \mathbf{r}_i), \quad (21)$$

where n is the number of pores per unit of the surface area. Instead of $I(x, y)$, we introduce the function $Q(x, Y) = KI(x, y)$, which is normalized so as to fulfill the condition

$$\int_{-\infty}^{\infty} dx \int_{-\infty}^{\infty} dy Q(x, y) = 1. \quad (22)$$

The constant K is determined from normalizing condition (22). After simple calculations, we find K and finally obtain

$$Q(x, y) = \frac{1}{\pi a_1 b_1} \times \int_{-a_1/2}^{a_1/2} dx_i \int_{-b_1/2}^{b_1/2} dy_i \frac{J_1^2\left(\frac{2\pi R\sqrt{(x-x_i)^2 + (y-y_i)^2}}{\lambda L_0}\right)}{(x-x_i)^2 + (y-y_i)^2}. \quad (23)$$

Integrating $Q(x, y)$ within the rectangle with the sides a_2 and b_2, we obtain the fraction of energy emitted from the sample and reaching the detector. This fraction is given by

$$H(\lambda) = \int_{-a_2/2}^{a_2/2} dx \int_{-b_2/2}^{b_2/2} dy Q(x, y). \quad (24)$$

At $a_2 \longrightarrow \infty$ and $b_2 \longrightarrow \infty$, $H(\lambda) \longrightarrow 1$. This means that all the energy emitted from the source reaches the detector.

Figure 10 presents $H(\lambda)$ curves for samples of various dimensions: no. 3, with $a_1 = 0.6$ cm, $b_1 = 1.5$ cm, $a_2 = 1$ cm, $b_2 = 3.5$ cm, and $L_0 = 11$ cm; and no. 1, with $a_1 = 0.3$ cm, $b_1 = 1.5$ cm, $a_2 = 1$ cm, $b_2 = 3.5$ cm, and $L_0 = 11$ cm. The energy losses increase as the wavelength λ increases. These losses are no more than 10% for both samples near $\lambda = 0.2$ μm, while at $\lambda = 1$ μm they reach 50% for the sample with $R = 2.5$ μm. The losses are substantially heavier for a sample with a smaller pore radius.

Figure 11 presents the final theoretical curves for two samples with account taken of two types of corrections: that for deviation from normal incidence of light and that for the energy losses associated with diffraction by pore exits. These curves have been constructed using the relation

$$T_{re}(\lambda) = \bar{T}(\lambda)H(\lambda). \quad (25)$$

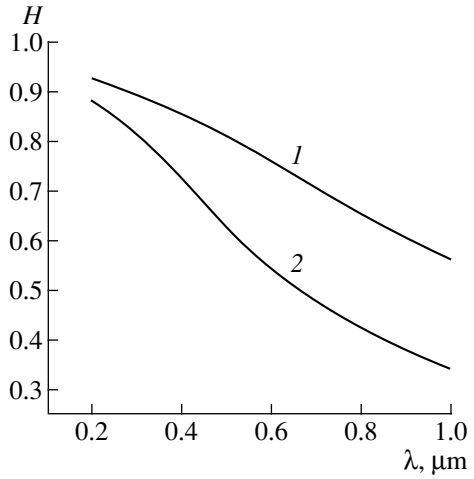

Fig. 10. Intensity of light incident on the detector related to that exiting from the sample: (*1*) sample no. 3, $a_1 = 0.6$ cm; (*2*) sample no. 1, $a_1 = 0.3$ cm.

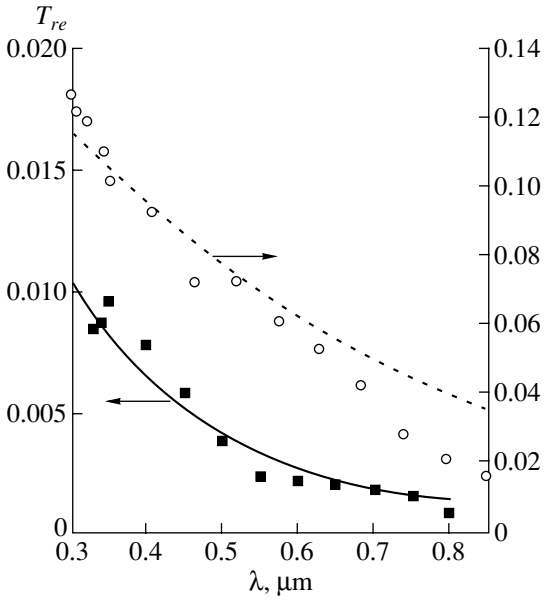

Fig. 11. Comparison of transmission spectra calculated with account of the corrections for the beam divergence and for the diffraction at the pore exit for samples no. 3 [dashed line (calculation) and circles (experiment)] and no. 1 [solid line (calculation) and squares (experiment)]. The calculated data were reduced to bring them in coincidence with the experimental values.

Corrections of the first and second types make the $T_{re}(\lambda)$ values smaller at small and large λ, respectively. Therefore, taking into account both corrections simultaneously does not significantly modify the shape of the $T_{re}(\lambda)$ curves, compared with that obtained without corrections, but only reduces the absolute value of $T_{re}(\lambda)$ by a factor of about 2.5 for all λ. Nevertheless, despite the fact that the spectral behavior is qualitatively the same in both cases, the experimental transmission values differ by a factor of ≅1.2–1.7 from those calculated by the formulas with corrections. Possible reasons for this discrepancy are the following.

(i) A small fraction of pores (≅20%) does not penetrate through the sample to its back surface.

(ii) As can be seen in Fig. 1, the surface of channels is not strictly cylindrical, rather, it is slightly corrugated, which was disregarded in our theory.

(iii) The precision in determining the pore radius may be insufficient. Even slight imprecision in the value of the radius causes strong variations of transmission both at small and large wavelengths. At small λ, when the geometrical optics is "operative," this can occur due to scatter in the angles of incidence and a strong dependence of the transmission on the parameter $2R/L$ [see (17)–(18)]. At high enough λ, when Fraunhofer diffraction takes place and relations (10) and (16) are valid, the transmission is proportional to R^6, i.e., depends very strongly on the pore radius. For example, if the pore radius decreases by 10%, the transmission is halved.

(iv) The condition $\lambda \ll 2R$ is poorly satisfied at high λ ($\lambda/2R = 0.16$ at $\lambda = 0.8$ μm and $R = 2.5$ μm); therefore, deviations from the basic diffraction relation taken from [8] are possible.

(v) In the calculation of the energy losses at the pore exit $H(\lambda)$, we disregarded oblique incidence of light onto the pore exit aperture, which may result in even stronger divergence of the light beam at each pore exit and thus reduce the energy incident on the detector.

On the other hand, our theory disregards the reflection of light from the inner surfaces of pores, since we have assumed that the light falling onto these surfaces does not reach the pore exits. However, multiple reflections from the inner surfaces with subsequent emergence from pores can, in principle, somewhat enhance transmission.

4. CONCLUSION

In *ma*-Si, light with a wave vector parallel or slightly inclined to the pore axis propagates in air, i.e., in a medium which exhibits neither absorption nor dispersion in the visible spectral range. Since the geometric parameters of pores can be preset experimentally, it is possible to obtain *ma*-Si with a diameter and length of pores that ensure that visible light is diffracted by orifices in the opaque screen; this diffraction determines the transmission spectrum. Indeed, the experimental transmission spectra recorded when the beam of light was parallel to the pore axis are fairly well described in terms of the general theory of diffraction with account taken of the diffraction at the pore entrance and exit and the influence exerted by deviation of the angle of light incidence from the normal to the sample surface.

ACKNOWLEDGMENTS

This study was supported by the Russian Foundation for Basic Research (project nos. 00-15-96770 and 00-02-16904), by programs of the St. Petersburg Scientific Center ("Low-Dimensional Quantum Structures") and the Ministry of Industry and Science of the Russian Federation ("Physics of Solid-State Nanostructures" and "Design of Components for Communication Networks, Software, and Databases for Fundamental Science and Education"), and by INTAS (grant no. 01-642).

REFERENCES

1. V. Lehman and U. Gruning, Thin Solid Films **297**, 13 (1997).
2. N. Winn, R. D. Meade, and J. D. Joannopoulos, J. Mod. Opt. **41**, 257 (1994).
3. V. Lehman, R. Stengl, H. Reisinger, *et al.*, Appl. Phys. Lett. **78**, 589 (2001).
4. J. Wallace, Laser Focus World, April, 36 (2001).
5. E. V. Astrova, A. D. Remenyuk, A. G. Tkachenko, and I. L. Shul'pina, Pis'ma Zh. Tekh. Fiz. **26** (24), 31 (2000) [Tech. Phys. Lett. **26**, 1087 (2000)].
6. T. S. Moss, *Optical Properties of Semiconductors* (Butterworths, London, 1959; Inostrannaya Literatura, Moscow, 1961).
7. E. V. Astrova, S. V. Belov, A. A. Lebedev, *et al.*, Thin Solid Films **255**, 196 (1995).
8. L. D. Landau and E. M. Lifshitz, *Course of Theoretical Physics*, Vol. 2: *The Classical Theory of Fields* (Nauka, Moscow, 1973; Pergamon, Oxford, 1975).
9. I. S. Gradshteyn and I. M. Ryzhik, *Table of Integrals, Series, and Products* (Nauka, Moscow, 1962; Academic, New York, 1980).

Translated by D. Mashovets

Semiconductors, Vol. 37, No. 1, 2003, pp. 6–14. Translated from Fizika i Tekhnika Poluprovodnikov, Vol. 37, No. 1, 2003, pp. 8–16.

ATOMIC STRUCTURE AND NONELECTRONIC PROPERTIES OF SEMICONDUCTORS

Electrical Activity of Dislocations and Point Defects of Deformation Origin in $Cd_xHg_{1-x}Te$ Crystals

S. G. Gasan-zade*, S. V. Staryĭ, M. V. Strikha, and G. A. Shepel'skiĭ

Institute of Semiconductor Physics, National Academy of Sciences of Ukraine, Kiev, 01650 Ukraine

** e-mail: gassan@class.semicond.kiev.ua*

Submitted February 26, 2002; accepted for publication April 11, 2002

Abstract—The generation of dislocations with even a relatively low density ($N_{dis} \le 10^7$ cm^{-2}) leads to significant variations in the kinetic coefficients of $Cd_xHg_{1-x}Te$ (x = 0.20–0.21) crystals. In *n*-type crystals, a substantial decrease in electron mobility takes place along with a marked growth in electron concentration. For *p*-type crystals, the transition from the activation conductivity to the metal one is observed in the low-temperature range of 4.2–40 K, as is the alternating-sign behavior of the Hall coefficient R_H depending on temperature and magnetic-field strength. A dominant role in the observed modifications is played by electronic states of point defects formed during the dislocation motion rather than the dislocations themselves. The totality of the data can be explained in terms of the formation of connected channels of an opposite-type conductivity in the form of a three-dimensional dislocation network in the matrix of the main crystal. © *2003 MAIK "Nauka/Interperiodica".*

1. INTRODUCTION

The narrow-gap compound $Cd_xHg_{1-x}Te$ (MCT), which is widely used in infrared semiconductor optoelectronics, is a semiconductor material that is difficult to work with. This fact is associated with the mechanical properties of MCT and, above all, with its high plasticity. Even under insignificant mechanical action, a marked number of dislocations can arise in MCT crystals. Macroscopic plastic deformation, which results in the generation of dislocations in the crystal bulk, easily proceeds in MCT at room temperature. Moreover, as was shown in [1, 2], the plasticity range is extended in MCT also to a region of much lower temperatures (to T = 80–100 K). Thus, during various conventional operations necessary for fabricating semiconductor devices, for example, mechanical treatment of a surface, thermal treatments, ion implantation, etc., a significant number of defects with a deformation origin can be generated in the semiconductor element. Such defects arise in the active region of a device and during the operation of the semiconductor devices themselves, for example, in the case of thermal cycling. The indicated problem is also of current concern for depositing epitaxial layers. Due to mismatch in the lattice parameters for the materials of the substrate and epitaxial layers, elastic stresses arise in the boundary region. Their relaxation leads to the formation of a dislocation network.

Deformation defects can markedly affect the characteristics of devices and the processes of their degradation. In addition, the available data on the electrical activity of linear and point defects formed under plastic deformation and also on the influence of such defects on the electrical properties of MCT are rather scarce [2–5]; moreover, the results of these studies are contradictory. Such a situation is explained by the complexity of this problem: the generation and motion of dislocations induces several mechanisms of defect formation at the same time. Especially contradictory are the results of investigations for *p*-type crystals. In our opinion, the indicated problems can also be explained, in particular, by the fact that the lower boundary of the temperature range of investigation of deformation defects in MCT, as a rule, was restricted to T = 77 K. At the same time, an extension of the low-temperature range to T = 4.2 K may facilitate identification of the types of defects arising during deformation, because the "freezing out" of free holes at acceptors occurs exactly in this temperature region. As a result, most of the uncompensated acceptors convert to the neutral charge state, whereas the donors remain ionized.

In this study, we investigate the influence of deformation defects on the kinetic coefficients of MCT in the temperature range T = 4.2–300 K and for a magnetic field whose strength can be as high as 70 kOe. Our main goal is to establish the type of defects that form during the plastic flow of the crystal and to determine the electrical activity of such defects and their influence on the basic electrical parameters of MCT crystals.

2. EXPERIMENTAL

MCT (as CdTe) single crystals are deformed plastically under the action of a mechanical load along the $\langle 110 \rangle \{111\}$ slip system. In the experiments under consideration, $Cd_xHg_{1-x}Te$ (x = 0.20–0.21) crystals were plastically deformed by uniaxial compression at T = 300 K. In this case, as a result of selective etching, the

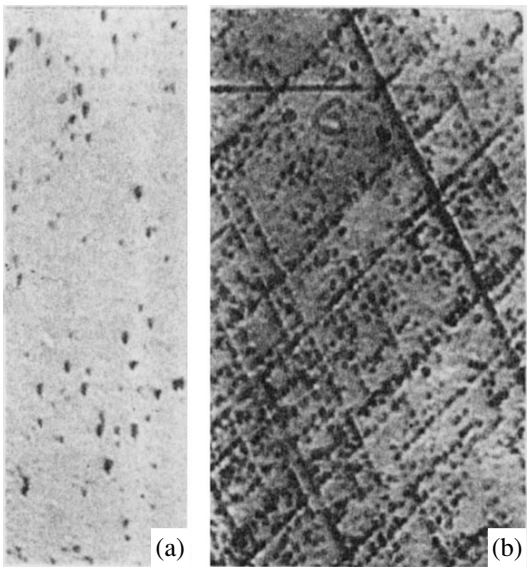

Fig. 1. Microphotograph of the $Cd_xHg_{1-x}Te$ (111) surface with magnification of 370X: (a) before deformation and (b) after deformation ($N_{dis} \approx 10^7$ cm^{-2}).

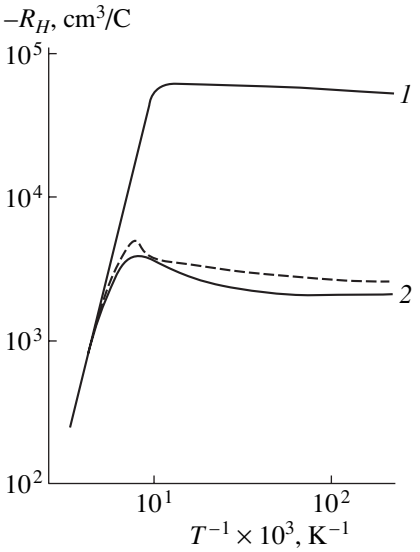

Fig. 2. Temperature dependences of R_H for the *n*-$Cd_xHg_{1-x}Te$ sample 4: (*1*) before and (*2*) after generation of dislocations with $N_{dis} \approx 7 \times 10^6$ cm^{-2}; solid lines are experimental, and the dashed curve is calculated.

(111) crystal surface contains a system of slip bands formed by etching pits and oriented along equivalent [110] directions (Fig. 1). Such a pattern corresponds to the concept of the predominant generation of 60° dislocations in the MCT ⟨110⟩{111} slip system [6]. The average density of growth dislocations in the original crystals was within $(3–5) \times 10^5$ cm^{-2}. We measured the temperature (T = 4.2–300 K) and magnetic-field dependences of conductivity σ and the Hall coefficient R_H for samples before and after plastic deformation. The dislocation density N_{dis} in the crystal was determined by metallography, i.e., by selective etching. In these experiments, N_{dis} was lower than 10^7 cm^{-2}, which corresponds to the situations actually arising in crystals and structures. Attempts to obtain a much higher degree of strain at T = 300 K resulted, as a rule, in the appearance of microcracks. The choice of such a low deformation temperature was motivated, first of all, by the problem of obtaining the primary pattern of defect formation in the crystal, which is affected only slightly by the diffusion and annihilation processes for the defects formed.

3. RESULTS

3.1. n-type Crystals

In Fig. 2, we show typical temperature dependences of R_H for an *n*-type sample before (curve *1*) and after (curve *2*) plastic deformation. In Fig. 3, we show the temperature dependences of the electron mobility μ_n in the same sample. The mobility was determined as the product of the experimentally measured σ and R_H. Since the sample maintains the electron type of conductivity within the entire temperature range, determining mobility in this way seems quite acceptable.

Our attention is drawn to several features in the dependences $\mu_n(1/T)$ and $R_H(1/T)$, which manifest themselves in a sample with dislocations (curves *2* in Figs. 2, 3). From the shape of the $R_H(1/T)$ dependence, it follows that the type of conductivity of the sample remains unchanged, while its electron concentration increases after introducing dislocations. The parameters of several *n*-type samples at T = 77 K before and after deformation are listed in the table. It can be seen that an increase in electron concentration n and a simultaneous decrease in electron mobility μ_n is observed for

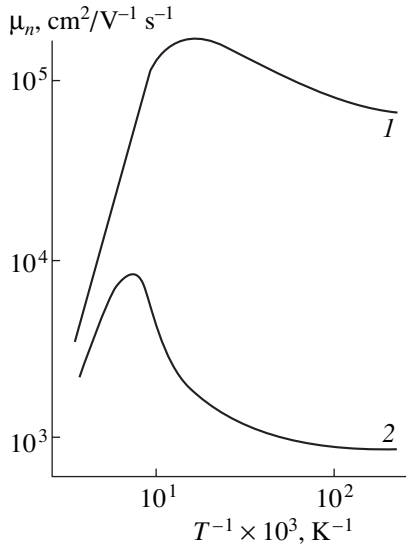

Fig. 3. Temperature dependences of electron mobility for sample 4 (*1*) before and (*2*) after deformation.

Table

Sample no.	$n \times 10^{-14}$, cm^{-3}		$\mu_n \times 10^{-4}$, cm^2 V^{-1} s^{-1}	
	before	after	before	after
4	1.4	27	18	0.2
12	1.1	3.8	7.6	0.3
14	3.1	19	23	1.1
17	21	41	14	0.65

all the samples. As for μ_n itself, Fig. 3 shows that the character of its temperature dependence is more strongly modified after deformation when compared with $R_H(1/T)$. A distinct peak in μ_n appears and shifts to higher temperatures with increasing dislocation density. Our attention is also drawn to the fact that an abrupt fall in μ_n takes place on the low-temperature side of the peak, the activation section being observed in the $\mu_n(1/T)$ dependence. The latter fact points to the appearance of a new supplementary mechanism of charge-carrier scattering which may have a barrier character. It should be noted that the original *n*-type MCT crystal had a very high electron mobility of 2×10^5 cm^2 V^{-1} s^{-1} at $T = 77$ K with relatively less pronounced scattering by ionized impurities in the low-temperature range (Fig. 3, curve *1*).

From the dependences shown in Figs. 2 and 3 and the data in the table, it can also be seen that, as a rule, relative changes in the mobility of carriers turn out to be larger than those in the concentration when the same

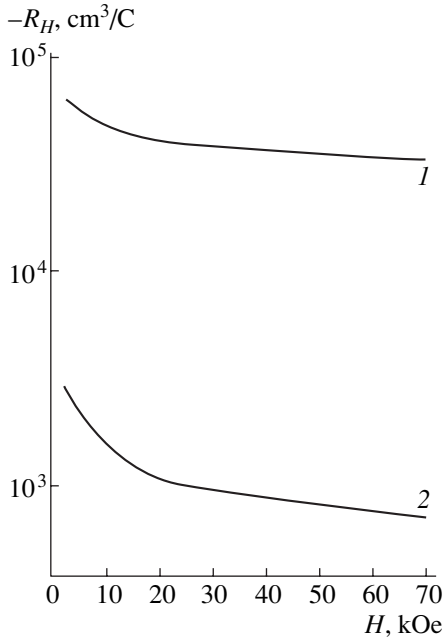

Fig. 4. Field dependences of R_H at $T = 77$ K for sample 4 (*1*) before and (*2*) after deformation.

dislocation density is formed in the crystal. This behavior is especially pronounced for samples whose initial concentration of extrinsic electrons exceeds 10^{14} cm^{-3}. This fact implies the mutual compensation of most of the defects formed under deformation. As a result, such defects contribute only to the scattering of charge carriers, leaving their concentration virtually unaffected. It should be noted that direct estimations of sample parameters must be made with caution. This applies, for example, to the estimation of mobility μ_n from the product of σ and R_H in the deformed samples. In fact, the temperature dependence $R_H(1/T)$ for samples with dislocations generally reveals a small characteristic peak (Fig. 2), which points to the presence in the sample of at least two types of charge carriers that have different mobility [7].

From the above data it follows that defects of both donor and acceptor types are simultaneously formed in MCT crystals during the motion of dislocations. Therefore, it is of interest to estimate the resultant electrical activity of the totality of defects formed with the aim of trying to single out one component of the conductivity. To this end, we measured the magnetic-field dependences for the Hall coefficient at $T = 77$ K in a field whose strength could reach 70 kOe (Fig. 4). Such a strong magnetic field in the temperature region of depletion of impurities ($T > 50$–60 K) usually makes it possible to easily reveal the MCT hole conductivity, which is obscured in the absence of a field by the contribution from the electron component to the conductivity. Such an effect can be explained by the large ratio $b = \mu_n/\mu_h \approx 100$ between the mobilities of electrons and holes. For this reason, electrons can dominate in the conductivity even in the case when their concentration in the sample is markedly lower than that of holes; i.e., when the inequality $N_A > N_D$ is fulfilled. However, in a magnetic field which is strong for electrons ($\mu_n H/c \ll 1$) but simultaneously weak for holes ($\mu_h H/c \ll 1$), the "magnetization" of electrons takes place. As a result, the electron component turns out to be virtually neglected in the conductivity even for $H > 4$–6 kOe and the Hall coefficient can be described by the simple expression $R_H = 1/e(p - n)$ in the strong-field limit [8]. Experimentally, the magnetization effect for electrons should manifest itself in *p*-type crystals as a change in the Hall-coefficient sign in a strong field from negative to positive and in the leveling off of the $R_H(H)$ dependence [8]. However, as the field dependences of R_H (Fig. 4) show, these experiments do not reveal a tendency toward a change in the sign of R_H. The stronger field dependence of R_H for a deformed crystal when compared with the original one is associated with either an increase in the degree of inhomogeneity of the crystal or the presence of at least two types of charge carriers with different mobilities in the sample. The latter conclusion is consistent with the data in Figs. 2 and 3.

On the basis of the results obtained and the metallography data, we will try to make certain quantitative estimates with the aim of clarifying the nature of the

electronic states of defects introduced into MCT crystals during deformation. It is generally agreed that the plastic deformation of a semiconductor simultaneously generates a significant number of point defects [9] in addition to dislocations. There are several mechanisms for point-defect formation by mobile dislocations. An important role in these mechanisms is played by dislocation jogs. In II–VI compounds (in particular, $Cd_xHg_{1-x}Te$), the jogs are sources of vacancies and interstitial defects. In addition, they themselves can act as donors and acceptors [10]. The problem is essentially reduced to the following: which of the two types of electron states predominantly contributes to the observed changes in the concentration and mobility of electrons—those belonging directly to the dislocation core or to the intrinsic point defect formed during dislocation motion. If we start from the dangling-bond model, which is the most acceptable for MCTs, it turns out that there are 2×10^7 cm^{-1} ionic sites, i.e., the atoms with violated coordination of the chemical bond in the dislocation core, per unit of dislocation length. In this case, the charge density per state is much lower than unity and is equal to 0.12 (the latter fact is associated with the Coulomb repulsion of like charges and follows from the Read statistics for the electronic states in a dislocation core [11]). Therefore, the maximum number of electronic states at the dangling bonds is less than 2×10^{13} cm^{-3} for a dislocation density of 10^7 cm^{-2}. However, it follows from experimental values of R_H that the density of electronic states introduced by deformation exceeds this value by at least two orders of magnitude: $(2–4) \times 10^{15}$ cm^{-3}. In fact, this excess can be even larger if allowance is made for the observed increase in the degree of compensation. The estimate of an ionized-defect density $N_D - N_A$ from the Brooks–Herring relationship for electron mobility requires a defect concentration of $(7–8) \times 10^{15}$ cm^{-3}. The latter value turns out to be close to the estimated density of point defects introduced in the crystal lattice by dislocation jogs under a degree of strain such that it provides generation of dislocations with $N_{dis} \approx 10^7$ cm^{-2} [9].

Thus, we may conclude that the conductivity of *n*-type MCT crystals subjected to plastic deformation is mainly affected by point defects of deformation origin rather than by dislocations themselves; these defects are generated in corresponding slip planes as a result of the motion of dislocations.

3.2. p-Type Crystals

In the as-grown state, the *p*-type crystals had a relatively low hole concentration $p = (4–8) \times 10^{15}$ cm^{-3} defined by the difference $N_A - N_D$. The temperature dependences of electrical conductivity ρ and R_H for such crystals had a shape typical of homogeneous *p*-type MCT samples before deformation (Fig. 5). In addition, as the temperature decreases, characteristic regions appear consecutively in the temperature dependences of ρ and R_H; these are the intrinsic-conductivity region, the region of depleted impurities (acceptors), the region of freezing out of holes at acceptors, and, finally, the region of conductivity over the impurity band (hopping conductivity). The first and third regions are characterized by exponential dependences, with the slope of the ρ(T) lines on a logarithmic scale corresponding to the band gap E_g for the first region and to an approximate acceptor-level depth E_A for the third region. The value of E_A depends on the degree of compensation and on the concentration of acceptors and is within 6–8 meV for the crystals under investigation.

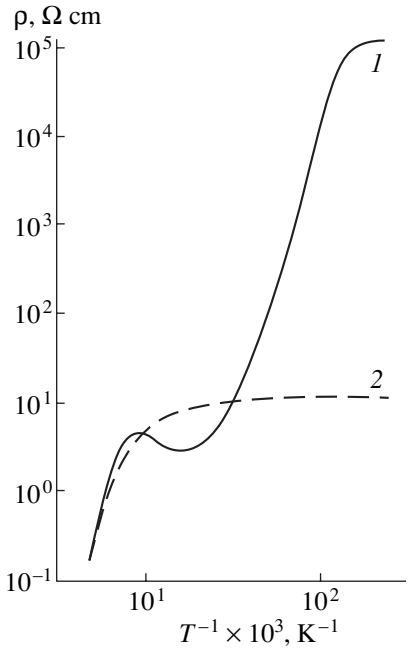

Fig. 5. Temperature dependences of ρ for a *p*-$Cd_xHg_{1-x}Te$ sample (*1*) before and (*2*) after deformation. The initial parameters of the sample at 77 K: $p = 3.8 \times 10^{15}$ cm^{-3} and $\mu_p = 4.2 \times 10^2$ cm^2 V^{-1} s^{-1}.

In *p*-type crystals, the Hall coefficient is always negative due to the large value of the ratio μ_n/μ_h in the intrinsic-conductivity region. When the temperature decreases, R_H changes its sign (the passage from the intrinsic to impurity conductivity). For the further decrease in T, rapid growth in R_H occurs due to the freezing out of holes at the acceptor level. In the temperature region of $T < 10$ K, where the electric resistance of a sample attains high values, while the conductivity is defined by the hopping mechanism, it becomes impossible, as a rule, to reliably measure the Hall coefficient.

After introducing dislocations, the shape of the temperature dependences of R_H and ρ markedly change. The following modifications should be cited.

(i) The temperature at which the sign of $R_H(1/T)$ changes as a result of a passage from intrinsic to impurity (hole-type) conductivity shifts towards lower tem-

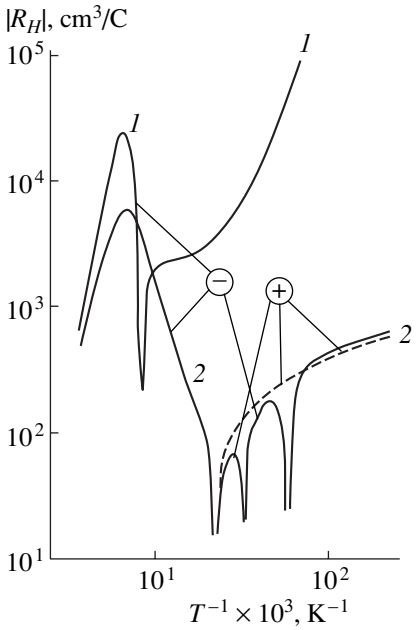

Fig. 6. Temperature dependences of $|R_H|$. The same sample as in Fig. 5: (*1*) before and (*2*) after deformation; the solid curves correspond to H = 1.5 kOe; the dashed curve, to H = 6 kOe.

peratures. In this case, the magnitude of R_H turns out to be smaller than that for the original crystal in the hole-conductivity region.

(ii) For a reasonably high dislocation density ($N_{dis} \geq (7–8) \times 10^6$ cm^{-2}), the activation regions in the curves for R_H and ρ associated with freezing out of the holes at acceptors and also the hopping-conductivity region virtually disappear; i.e., a transition to metal-type conductivity takes place.

(iii) By virtue of the above, at the lowest temperatures (4.2–30 K), the conductivity of a deformed sample increases by several orders of magnitude as compared with that of the original crystal. However, in the temperature region of impurity depletion (50–110 K), the conductivity of a sample with dislocations, on the contrary, is lower than that of the original sample. At the same time, measurements of the Hall coefficient at $T < 40$ K run into serious difficulties due to its sign-altering behavior (R_H changes its sign several times) in spite of the reasonably high conductivity of a sample with dislocations. Moreover, in this temperature range, the electron sign of R_H can be changed for the hole sign by a magnetic field with H = 5–6 kOe.

(iv) In the range of T = 4.2–40 K for $N_{dis} \geq (6–8) \times 10^6$ cm^{-2}, a transverse magnetoresistance of *p*-type MCT in the region of fields with H = 1–5 kOe has, as a rule, a negative sign, which is characteristic of conductivity over the impurity band.

4. DISCUSSION

A crystal with a reasonably high density of dislocations should evidently be considered as an inhomogeneous system. However, when the degree of plastic deformation in the sample bulk is constant, the aforementioned inhomogeneity can be considered as ordered instead of chaotic. From the selective-etching pattern (Fig. 1), it can be seen that a network consisting of virtually equidistant lines with approximately the same density of etching pits is superimposed upon the sample, which was homogeneous before the deformation. Thus, we may consider a crystal with dislocations as being divided into a main matrix, with the initial parameters of the crystal, and a network of extended microclusters with electronic properties, which differ radically from those of the main matrix. In terms of such a model, we will discuss the experimental features of kinetic coefficients in the MCT samples with dislocations. Attention should be concentrated primarily on the $R_H(1/T)$ and $\mu(1/T)$ dependences.

It should be noted that problems from the emergence of anomalies in the $R_H(1/T)$ dependences for MCT (an additional small peak in the region of transition to intrinsic conductivity in an *n*-type material and the double inversion of the sign in a *p*-type material), observed in nominally homogeneous MCT samples, have been discussed for a long time. The different theoretical approaches for describing such anomalies were based on several models: the presence of microinhomogeneities with various types of conductivity in a sample, the layered structure of the sample itself, and the presence of a surface layer whose carrier properties differ from those of majority carriers in the bulk (see, for example, [12, 13]). However, for all the apparent diversity of the models used, we are, in essence, dealing with various ways of averaging the known expression for the Hall coefficient on the assumption that there are several types of carriers:

$$R_H = \sum \sigma^{(i)} \mu_H^{(i)} / c[(\sum \sigma^{(i)})^2 + (H/c)^2 (\sum \sigma^{(i)} \mu_H^{(i)})^2]. \quad (1)$$

Here, summation is performed over all i various types of carriers involved in the sample, $\sigma^{(i)} = en^{(i)}\mu^{(i)}$, and μ_H is the Hall mobility.

Important information about which groups of carriers are involved in the samples under investigation is provided by the field dependence of the Hall coefficient shown in Fig. 4. It should be noted that $R_H = -\gamma/en$, where $\gamma = \mu_H/\mu$ is the Hall factor for electrons if, in the *n*-type sample, there are only electrons in the limit of weak magnetic fields. Consideration of the dependence of γ on a magnetic-field strength H can lead to a certain decrease in R_H with increasing H. However, the magnitude of such an increase must not exceed 1.93 for scattering of the carriers by charged impurities in the range of temperatures and fields under consideration (see [14]). In experiment, a much more abrupt decrease in the Hall coefficient is observed.

At the same time, the presence of a characteristic peak in the $R_H(1/T)$ curve for an *n*-type semiconductor (Fig. 2, curve *2*) in the temperature region of transition from intrinsic to impurity conductivity cannot be explained if only carriers of like sign, for example, electrons, are considered [7].

The totality of the above experimental data can be explained by assuming that there are also hole-conductivity regions along with electron-conductivity ones in a plastically deformed sample. In principle (see [12]), *p*-type regions can have the form of surface layers; however, chemical etching of the samples does not lead to significant changes in the experimental results, which makes it possible to neglect the role of the surface. At the same time, the dislocations introduced into the sample by plastic deformation are extended defects and they can generally be related to "channels" having modified conductivity properties.

In fact, the 60° edge dislocation arising in MCT can terminate both at the Te atomic row and at the Cd and Hg rows [15]. In the first case, the unsaturated bonds form a negative charge in the dislocation core and, in the second case, a positive charge. Such charged cores form "tubes" of space charge along their length. The negatively charged line of acceptors repulses free electrons and forms a positive charge in *n*-type material; the averaged magnitude of this charge per unit of volume is equal to $e(N_D - N_A)$.

Around the dislocation, it is possible to construct a cylinder of radius *r*, which is defined from the condition for equality between the positive charge of the cylinder and the negative charge of the dislocation. This radius is equal to $r = [a\pi(N_D - N_A)]^{-1/2}$. Here, *a* is the spacing between the charges in the dislocation line. An estimate for the above parameters of *n*-type MCT yields a tube radius of about a half of a micrometer, which exceeds the characteristic sizes of a dislocation core by orders of magnitude. For $N_{dis} \approx 10^7$ cm^{-2}, this means that the tubes with a positive space charge (their number is equal to the number of negative-charge tubes) cover only 4% of the area of a plane intersecting them perpendicularly. In this case, the acceptors inside the space-charge region (SCR) are ionized owing to valence-band bending even when they are frozen out in the remaining volume with decreasing temperature. As a result, the tube becomes a hole-conductivity channel.

Thus, we can consider the *n*-type sample as penetrated uniformly over its bulk by channels with different types of conductivity, both hole and electron (due to the fact that the extended dipole layer is linked to the dislocation). Evidently, the presence of additional "electron" channels related to dislocations only negligibly affects the electron properties of the *n*-type samples due to the smallness of their volume as compared with the matrix volume; however, this influence can manifest itself in *p*-type samples.

We assign the hole conductivity σ_p to the "hole" tubes. In this case, the concentration of *p* carriers in such channels is controlled by point defects of deformation origin. It should be noted that a similar model was used for explaining the Hall effect anomalies in MCT films [7] irrespective of dislocations. In this case, a model of *p–n* junctions was considered in which its rectifying effect could be neglected down to the lowest temperatures for small currents. The electron scattering by *p–n* junctions was also considered to be negligible.

Such an approach makes it possible to use the classical "different-layer model" of Petritz [16], which divides the sample into small "blocks" of *p–n–p* or *n–p–n* structures. The next simplification consists in assuming that a magnetic field is always directed parallel to the interface between the hole and electron layers. In this case, we considered the components of the current *I* separately, which are parallel (I_l) and perpendicular (I_t) with respect to the interface between *n*- and *p*-type regions. It is clear that the Hall voltages should be calculated for a sequence of *n–p–n*-type regions connected in parallel for the first case and the same regions connected in series for the second case. However, the calculation yields (see [7]) identical results in both cases:

$$R_H = [R_p\sigma_p D_p + R_n\sigma_n D_n]/[\sigma_p D_p + \sigma_n D_n]. \quad (2)$$

Here, R_i is the Hall coefficient for the *i*th region ($i = n, p$), σ_i is the conductivity of such a region, and D_i is the thickness of this region (for the current flow perpendicular to the *p–n*-junction boundary) or the area of this region (for the current flowing along the *p–n*-junction boundary). The conductivity for the current I_l can be easily written making allowance for the fact that, here, the regions with electron and hole conductivity operate as shunt resistances: $\sigma_l = \sigma_p D_p + \sigma_n D_n$. With respect to the "perpendicular" direction of the current I_l, the aforementioned regions are connected as series resistances and, thus, $\sigma_t = 1/[\sigma_p D_p + \sigma_n D_n]$. In the general case of random distribution of blocks of the *n–p–n* type, the conductivity can be written as

$$\sigma = \sum \sigma_l(D^{(i)})P^i + \sum \sigma_t(D^{i)})[1 - P^i]. \quad (3)$$

Here, P^i is the probability that the current flows in the direction parallel to the *p–n*-junction boundary for the *i*th block. The summation in (3) is performed over all the possible blocks of the sample. However, the calculation of such a complicated expression requires further simplification. In the simplest case [15], P^i was assumed to be independent of the number of a block and all σ_t and σ_l were assumed to be identical. In this case, expression (3) can be written in a form that makes calculation simple:

$$\sigma = \sigma_l P + \sigma_t[1 - P]. \quad (4)$$

Hereafter, expression (2) was calculated with allowance made for (4). The electron concentration in the *n*-type region was calculated with allowance made for intrinsic- and extrinsic-carrier concentrations. In a sim-

ilar way, we calculated the hole concentrations in the *p*-type region, but in this case, we also took into account the temperature dependence of filling the acceptors with the binding energy E_A. The minority-carrier concentration in both regions was assumed to be equal to their intrinsic concentrations.

The donor concentration N_D was determined from the R_H magnitude in the low-temperature region. The acceptor concentration, the ratio D_p/D_n, and the probability P were considered as adjustable parameters of the theory. For the electron and hole mobilities, we used the empirical formulas [17]. From the expressions obtained, it follows that the peaks of R_H and of the Hall mobility are interrelated. In this case, the best agreement between theory and the curves in Figs. 2 and 3 was attained for $D_p/D_n = 0.1$, $P = 0.5$, and $N_A = 2 \times 10^{15}$ cm^{-3}.

It should be noted that the ratio $D_p/D_n = 0.1$ is of the same order of magnitude as that obtained above from a simple estimate of the radius r (0.04). Better agreement could hardly be expected due to the multiple approximations made above. We give a simple qualitative interpretation of the peak observed in the curve $R_H(1/T)$. It is evident that R_H features no considerable anomalies in the matrix within the temperature range of the transition from intrinsic to impurity conductivity: it remains negative and attains magnitudes close to the difference $N_D - N_A$. This curve is superimposed by the dependence $R_H(1/T)$ in a system of extended *p*-type microclusters. In the region of intrinsic conductivity, the Hall coefficient sign is also negative (i.e., defined by more mobile electrons). However, when the conductivity passes to the hole impurity type, the sign of R_H becomes positive, while the Hall coefficient itself increases due to a decrease in the free-hole concentration with temperature. It is this fact that leads to the appearance of a small peak at the $R_H(1/T)$ curve for the matrix–microcluster system within the region of transition from intrinsic to impurity hole conductivity (in the microclusters) and to the further weak decrease in this coefficient with decreasing temperature.

When considering the experimental results obtained for the *p*-type samples, the following circumstance particularly caught our attention. If, in measuring R_H and ρ, we restrict ourselves to the temperature range above $T = 77$ K, these experimental data can lead to an erroneous conclusion (as was made in certain studies): the type of the carrier changes as a result of deformation (from *p*- to *n*-type). Actually, as can be seen from the comparison for the entire temperature range of the curves, nothing of the kind happens. As to the erroneous assumption, it is associated with the shift of the temperature of transition from intrinsic to impurity conductivity (the change of the sign of R_H) to lower temperatures for the deformed crystal.

We will examine this feature in more detail in the $R_H(1/T)$ dependence. The fact that the R_H inversion point shifts to lower temperatures with increasing concentration of deformation defects indicates, at first glance (as in the *n*-type crystals), that the resultant activity of the defects introduced by the deformation is of the donor type. However, in this case, the following contradiction arises: if an additional concentration of electrons associated with the deformation defects of the donor type turns out to be sufficient for conserving the negative sign of R_H in a certain temperature range of impurity conductivity, a change of sign is even less probable with a further decrease in temperature. In fact, the total hole concentration can only decrease with temperature, and for $T < 40$ K, it decreases exponentially due to the fact that the holes are frozen out at acceptors. At the same time, the electron concentration remains virtually constant due to the presence of a major impurity component (the donors are in the ionized state down to the lowest temperatures). However, an inversion is observed in experiment and R_H becomes positive at $T < 50$ K. The solution to this contradiction will likely be found in features of the temperature dependence of mobility of carriers in the deformed crystals. If there are two types of carriers with different signs (electrons and holes), the Hall coefficient is described by the expression $R_H = [(p - b^2n)/(p + bn)^2]/e$. In this case, the sign should change when the equality $p - b^2n = 0$ is fulfilled. It is easy to see that an abrupt decrease in the electron mobility (Fig. 3) can be the principal cause of the shift in the R_H inversion temperature (with the mobility of heavy holes decreasing negligibly) in the deformed crystals as the temperature decreases in the range of $T = 50$–100 K. Actually, variation in the factor b^2 turns out to be determining because, in the above range of T, the concentration of carriers varies only slightly, as can be seen from Fig. 2.

The variation in the coefficient b is evidently associated with the different influence of dislocations introduced by deformation on the mobility of electrons and holes. Qualitatively, it is possible to use a simple expression for the time of scattering by an edge dislocation: $1/\tau = N_{\text{dis}}\nu_t s$. Here, ν_t is the component of the velocity vector of a carrier scattered in the plane perpendicular to the dislocation axis; s is the cross section of scattering of carriers by dislocations and has the dimension of length, since the problem is two-dimensional. From this relationship, it can be seen that high-mobility electrons are scattered stronger than those with lower mobility if a certain concentration N_{dis} of dislocations is introduced. It is this circumstance that leads to an abrupt decrease in the parameter b.

Another feature of the *p*-type samples also requires explanation: a decrease in the activation energy of acceptors as N_{dis} grows and the transition to activation-free conductivity in the low-temperature range. In a homogeneous crystal, the transition to the activation-free conductivity (the Mott transition) is provided by overlap of the wave functions for acceptor states as the spacing between impurities decreases. For attaining this in *p*-type MCT, the acceptor concentration is required to be $N_A = (2$–$3) \times 10^{17}$ cm^{-3} [18]. Such a den-

sity of hole states is quite unlikely for the conditions under study. According to the experimental values of R_H, on the one hand, and the estimate of the density of states formed under plastic deformation, on the other hand, the concentration of holes cannot exceed 10^{16} cm^{-3} in the deformed crystals ($N_{dis} \approx 10^7$ cm^{-2}). Therefore, an explanation should evidently be sought in the inhomogeneity of a crystal with dislocations. Here, two main competing factors can be involved. As was shown in [19], the broadening of impurity levels induced by crystal inhomogeneity is proportional to the "degree of disorder" and is governed by the characteristic energy of the shift of the band edge over the correlation length of the inhomogeneity. In the case under consideration, the scale of such shifts for the band edges is defined by the properties of the SCR near the dislocation tubes and can attain a value on the order of 10 meV, according to the estimate for the aforementioned concentration of the introduced defects. This would be quite sufficient for broadening the acceptor level necessary for the transition to activationless conductivity; however, in the above estimate, a change in the degree of compensation of the crystal when introducing dislocations was ignored. As is known, an increase in the degree of compensation leads to increasing E_A and, thus, inhibits the transition to the conductivity without activation. A progressive decrease in the activation energy of acceptors with a growth in N_{dis} counts in favor of the first of the aforementioned factors. However, this mechanism cannot explain the features of R_H. Actually, the alternating-sign behavior of R_H with variation of T and the magnetic field points to the presence (the same as in the *n*-type samples) of two types of charge carriers with different signs, which introduce a comparable contribution to the conductivity of *p*-type crystals. The appearance of the electron component in the *p*-type crystals can only be explained by the formation of conductive channels of *n*-type as a result of deformation. These channels can emerge as dislocation tubes around cation chains. It is evident that the contribution of the electron component increases as the density of these tubes increases, particularly in the low-temperature region, where the contribution of the hole component must decrease.

Within the entire temperature range of extrinsic conductivity in *p*-type MCT crystals, a transition from *p*- to *n*-conductivity as a result of deformation was not observed in the experiments under consideration except in one sample. There are several causes of this fact. It is well known that *p*-type crystals are much more imperfect in comparison with *n*-type crystals. As a rule, the initial total concentration of uncompensated acceptors, including deep-level centers, exceeds 10^{16} cm^{-3} in *p*-type crystals (a relatively low concentration of impurity holes is attained by profound compensation). Deformation-induced donors can be assumed to be completely compensated, because the relationship $N_A > N_D$ remains valid even after deformation, and, thus, the crystal retains the hole type of conductivity. A certain increase in the hole density should probably be associated with the known mechanism for the recharging of defects by moving dislocations, which are present in the initial state of *p*-type crystals and lacking in *n*-type crystals.

Apparently, a lower initial concentration N_A is probably necessary in the sample for the transition from *p*- to *n*-conductivity. A convincing inversion of the conductivity type as a result of introducing dislocations ($N_{dis} \approx 10^7$ cm^{-2}) was observed in this study only for one of the investigated *p*-type MCT crystals with $N_A = (3–4) \times 10^{15}$ cm^{-2} and with relatively slight compensation. The last fact was also corroborated by the higher mobility of holes as compared with that in other samples. Another origin of the inversion of the conductivity type can be related to a higher degree of plastic deformation than in our experiments when the dislocation density greatly exceeds 10^7 cm^{-2}. However, in our opinion, this case is of lesser interest because it is uncommon in practice. An exclusion is the formation of MCT damaged layers of significant thickness as a result of cleavage [10] or in the process of the mechanical treatment of the surface [20]. As a result, high concentrations of dislocation loops and so-called mechanodonors arise in the crystal and lead to a change in the type of conductivity. However, in this case, it is difficult to consider the plastic deformation of the crystal as homogeneous.

REFERENCES

1. P. I. Baranskiĭ, Yu. N. Gavrilyuk, A. I. Elizarov, and V. A. Kulik, Fiz. Tekh. Poluprovodn. (Leningrad) **11**, 1560 (1977) [Sov. Phys. Semicond. **11**, 916 (1977)].
2. S. G. Gasan-zade, E. A. Sal'kov, and G. A. Shepel'skiĭ, Fiz. Tekh. Poluprovodn. (Leningrad) **17**, 1913 (1983) [Sov. Phys. Semicond. **17**, 1225 (1983)].
3. J. H. Tregigals, T. L. Polgreen, and M. C. Chen, J. Cryst. Growth **88**, 460 (1988).
4. S. G. Gasan-zade, I. P. Zhad'ko, É. A. Zinchenko, *et al.*, Fiz. Tekh. Poluprovodn. (Leningrad) **23**, 85 (1989) [Sov. Phys. Semicond. **23**, 52 (1989)].
5. B. Pelliciari and G. Beret, J. Appl. Phys. **62**, 3986 (1987).
6. S. Cole, A. F. W. Willoughby, and M. Brown, J. Cryst. Growth **59**, 370 (1982).
7. M. C. Chen, S. G. Parker, and D. F. Weirauch, J. Appl. Phys. **58**, 3150 (1985).
8. Yu. G. Arapov, B. B. Ponikarov, I. M. Tsidil'kovskiĭ, and N. G. Shelushinina, Fiz. Tekh. Poluprovodn. (Leningrad) **13**, 695 (1979) [Sov. Phys. Semicond. **13**, 409 (1979)].
9. Yu. A. Osipyan, V. F. Petrenko, G. K. Strukova, and I. I. Khodos, Phys. Status Solidi A **57**, 477 (1980).
10. J. P. Hirth and H. Erenreich, J. Vac. Sci. Technol. **3**, 367 (1985).
11. W. T. Read, Philos. Mag. **46**, 111 (1955).

12. V. I. Ivanov-Omskii, N. N. Berchenko, and A. I. Elizarov, Phys. Status Solidi A **103**, 11 (1987).
13. K. K. Parat, N. R. Taskar, I. B. Bhat, and S. K. Ghandhi, J. Cryst. Growth **102**, 413 (1990).
14. V. F. Gantmakher and Y. B. Levinson, *Carrier Scattering in Metals and Semiconductors* (Nauka, Moscow, 1984; North-Holland, New York, 1987).
15. H. F. Matare, *Defect Electronics in Semiconductors* (Wiley, New York, 1971; Mir, Moscow, 1974).
16. R. L. Petritz, Phys. Rev. **110**, 1254 (1958).
17. L. F. Lou and W. H. Frye, J. Appl. Phys. **56**, 2253 (1984).
18. A. I. Elizarov, V. V. Bogoboyashchiĭ, and N. N. Berchenko, Fiz. Tekh. Poluprovodn. (Leningrad) **18**, 455 (1984) [Sov. Phys. Semicond. **18**, 283 (1984)].
19. M. V. Strikha and F. T. Vasko, J. Phys.: Condens. Matter **9**, 663 (1997).
20. L. A. Bovina, V. N. Stafeev, A. V. Frolov, and A. G. Rubtsov, in *Proceedings of All-Union Workshop on Physics and Chemistry of Semiconductors, Pavlodar, 1987*, p. 218.

Translated by V. Bukhanov

Semiconductors, Vol. 37, No. 1, 2003, pp. 65–69. Translated from Fizika i Tekhnika Poluprovodnikov, Vol. 37, No. 1, 2003, pp. 65–69.

SEMICONDUCTOR STRUCTURES, INTERFACES, AND SURFACES

Silicon Carbide Transistor Structures as Detectors of Weakly Ionizing Radiation

N. B. Strokan*, A. M. Ivanov*^, M. E. Boĭko*, N. S. Savkina, A. M. Strel'chuk*, A. A. Lebedev*, and R. Yakimova**

** Ioffe Physicotechnical Institute, Russian Academy of Sciences, St. Petersburg, 194021 Russia*

^e-mail: alexandr.ivanov@pop.ioffe.rssi.ru

*** Linköping University, S-581 83 Linköping, Sweden*

Submitted June 5, 2002; accepted for publication June 17, 2002

Abstract—SiC-based nuclear radiation detectors figured prominently in the very first attempts of the 1960s to replace gas in ionization chambers with a more condensed semiconducting medium. However, the dynamics of improvement of SiC in those years was markedly inferior to the progress made in the development of competing materials. This study continues with the investigation of triode detector structures based on "pure" SiC films. It is established that for weakly ionizing radiation (as also in the case of strongly ionizing alpha particles) the signal is amplified by no less than a factor of several tens. This allows SiC films with a thickness of about 10 μm to be used to detect penetrating radiation, e.g., X-rays, since the effective thickness of the films is on the order of hundreds of micrometers. © *2003 MAIK "Nauka/Interperiodica".*

1. INTRODUCTION

For the ionization principle to be successfully implemented in semiconductor detectors, the starting material must possess a certain combination of properties. These are the following: a low impurity concentration (extended electric field domain in a diode structure typically used in detectors), bipolar conduction (no accumulation of space charge distorting the field), long drift displacement of carriers (carrier transport with efficiency close to unity), wide band gap ensuring weak thermal generation of carriers (low noise), and the possibility of creating high-voltage diode structures. Since tracks occupy only a small fraction of the detector volume, high local uniformity of carrier transport conditions throughout the detector volume is necessary.

Owing to the success achieved recently in controlling the properties of silicon carbide SiC, the above set of characteristics is rather well obtained in modern materials. Presently, the standard impurity concentration in SiC is 5×10^{14}–10^{15} cm^{-3}. This gives field regions with a width of $W \approx 30$ μm at a voltage of 500 V. Lifetimes on the order of hundreds of nanoseconds for less mobile holes, combined with high values of saturated drift velocity, ensure a nearly 100% efficiency of charge transfer. Particularly attractive are the radiation hardness [3, 4] and chemical stability of SiC, as well as the possibility of device operation at temperatures of hundreds of degrees centigrade [5–7].

Correspondingly, publications of recent years have given much attention to the investigation of the above-mentioned properties of SiC and to tests of SiC structures for detection and spectrometry of various kinds of nuclear radiation [8–10].

In this communication, we consider the possibility of recording penetrating radiation with SiC detectors (X-rays and gamma radiation, high-energy particles) when the feasibility of using SiC is far from obvious. Indeed, the most structurally perfect SiC is obtained under laboratory conditions in the form of films with a thickness of tens of micrometers [11–13]. Correspondingly, the detector signal generated by weakly ionizing radiation has a low amplitude.

In [1, 2], the possibility of detector signal amplification in the case of a transistor-type (instead of the conventional diode type) structure was demonstrated. Specifically, a superlinear rise in the signal with increasing bias across the structure was observed when recording single alpha particles. An amplification of the charge, introduced by a particle into the base, by a factor of ~50 was achieved. Short-range alpha particles generated in natural decay (with an energy of ~5 MeV) produce tracks with a carrier density on the order of 10^{16} cm^{-3} and belong to strongly ionizing radiation.

The present study is concerned with the response of triode structures to weakly ionizing radiation (X-rays and gamma radiation, high-energy particles). The experiment was performed with fluxes of X-ray and optical photons recorded in the induced-current measurement mode. It is rather important that a k-fold amplification of the signal generated by penetrating radiation be equivalent to an identical increase in the effective thickness of the film.

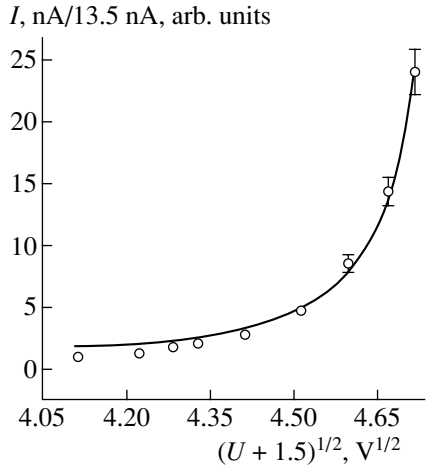

Fig. 1. Current induced by radiation from X-ray tube vs. the voltage across the triode detector structure. Solid line: fitting by formula (1) at current normalized to 13.5 nA. Parameters: film thickness d = 4.66 μm, electron diffusion length L_D = 0.35 μm. Tube anode voltage 20 kV.

2. EXPERIMENTAL

The current was recorded as a function of bias applied to a structure, with carriers generated by X-rays or optical radiation.

In the first case, samples were irradiated on a URS 1.0 installation at an X-ray tube anode voltage of 20 kV and current of 20 mA. Because of the small film thickness, the absorption of the radiation emitted by the tube was weak. Therefore, carrier generation was virtually equiprobable across the film thickness.

In the second case, the films were irradiated with the light of a mercury lamp. Separate parts of its emission spectrum were selected by using various filters.

The detectors were fabricated in the form of transistor structures. *p*-type 6*H*-SiC films grown on n^+-substrates by vacuum sublimation [12] served as the base region. The net concentration of impurities ionized at room temperature $|N_{A^-} - N_{D^+}| = (1–3) \times 10^{15}$ cm^{-3} at a film thickness of ~5 mm. A Schottky barrier fabricated by magnetron sputtering of Ni acted as the second electrode with *n*-type conduction. The area of the Ni electrode was 1.2 mm^2.

According to [1, 2], higher amplification is observed with the Schottky barrier as a collector. This predetermined the polarity of the bias applied to a detector connected in the floating-base mode.

3. RESULTS

Measurements of capacitance characteristics demonstrated that the *p*–*n* junctions of the structure are not identical. The Schottky barrier corresponds to an abrupt junction, whereas the transition to *p*-type conduction at the n^+-substrate occurs gradually.

(1) The response to the X-rays in the maximum-amplification mode shows superlinear behavior with increasing voltage U. Figure 1 presents a part of the dependence of the photocurrent on U as a function of $(U + 1.5)^{1/2}$, with the term 1.5 V accounting for the contact potential difference. The current is normalized to its value of 13.5 nA at $(U + 1.5)^{1/2} = 4.1$ V$^{1/2}$. It can be seen that the current increases steeply across a relatively narrow range of argument variation, with the initial current exceeded by a factor of 25.[1] Unfortunately, the steep rise in the dark current at higher biases provided no way of studying the behavior of the induced current in a wider range of voltages.

The data in Fig. 1 were processed under the assumption that the observed rise in current is due to amplification typical of a transistor in the common emitter mode. The emitter efficiency was taken to be $\gamma = 1$. It was also assumed that, during the separation of photocarriers created in the base, the main contribution to the current comes from the collector junction. Correspondingly, the expression for the collector current, presented in monograph [14], was used as the starting formula:

$$I_c = I_{\text{ph}}/(1 - \alpha_T),$$

where

$$\alpha_T = \{\cosh[(d - W)/L_D]\}^{-1}.$$

Here, I_{ph} is the primary current of photoelectrons entering the collector, α_T is the transfer coefficient of secondary electrons injected into the base owing to the photovoltage that appeared across the emitter–base junction, d is the film thickness, $W \propto (U + 1.5)^{1/2}$ is the width of the space charge region (SCR) of the collector, and L_D is the diffusion displacement of electrons in the base.

In writing an expression for I_{ph}, account was taken, similarly as in [1], of both the drift transport of photoelectrons from the W region and the contribution of their diffusion from the neutral base. Since, to a first approximation, $I_{\text{ph}} \propto W \propto U^{1/2}$, the main contribution to the dependence on bias comes from the denominator of the formula, which contains a hyperbolic cosine.

In approximating the dependence of current on voltage, account was taken of normalization. The expression for I_c was divided by the same expression at fixed W_n. This W_n value corresponded to the voltage U_n at which the normalization current I_n flows (I_n = 13.5 nA in the case in question). W was calculated with the concentration of ionized impurity in the base ($N_{A^-} - N_{D^+}$)

[1] It is noteworthy that, in the case of alpha particles, the energy introduced into the base is known to be 0.2 MeV/μm, which is in accordance with the Bragg curve. This allows the magnitude of the pulses observed to be expressed directly in units of energy. In measurements with X-ray and optical excitation of current, relative values are considered in order to circumvent calibration in the intensity of carrier generation.

assumed to be 1.2×10^{15} cm^{-3}, which was the value obtained from capacitance measurements. The film thickness $d = 4.66$ μm and $L_D \cong 0.35$ μm, found by fitting to the data in Fig. 1, are consistent with the film growth conditions.

(2) For the case of carrier generation by optical photons, a semitransparent Ni electrode was used. Figure 2 shows the dependence of the photocurrent on bias for a sample irradiated with a flux of photons from a DRSh-250 mercury lamp, which were passed through either a glass or a double (water + UFS6 glass) filter. The glass filter made carrier generation more uniform across the base thickness. The double filter enabled measurements in the UV spectral range. The current was normalized to 1 μA, and, therefore, its values along the ordinate axis correspond to an amplification factor of ~35. No noticeable differences in the behavior of the current are observed for the given filtration conditions.

The $I_c(U)$ data were approximated with account taken of the above-described normalization for the above impurity concentration in the base, $(N_{A^-} - N_{D^+}) = 1.2 \times 10^{15}$ cm^{-3}. This gave d = 4.67 μm, a value coinciding with that obtained in detection of X-rays. However, $L_D = 0.83$ μm exceeds the L_D value obtained from Fig. 1 more than twofold. This can be attributed to a difference of more than 2 orders of magnitude between the currents flowing in X-ray and optical excitation of carriers.

It should also be noted that the dark current–voltage dependence of the samples with semitransparent Ni exhibited a characteristic feature. With increasing voltage, a steep rise in current by 2–3 orders of magnitude occurred over a relatively narrow range of U variation (<1 V). In some cases, there occurred an S-type switching from a "high-voltage" state with $U \approx 25$ V to a "low-voltage" state with $U \approx 5$ V, similarly to the effects observed in [15] and related to breakdown and current pinching. However, in the case in question, these effects were manifested at current densities 2–3 orders of magnitude lower than those in [15]. Correspondingly, those portions of the current–voltage curve in which the dark currents were insignificant were chosen for measuring the voltage dependence of the photocurrent.

At a negatively biased Schottky barrier, the photocurrent also exceeds the dark current by orders of magnitude, but, in the range U = (10–100) V, the photocurrent is virtually independent of voltage.

(3) Additionally, the effect of a superlinear rise in signal was studied in relation to temperature. The experiment was carried out as in [1] with alpha particles and a detector having a more extended base. Figure 3 presents the behavior of the signal as a function of voltage expressed in energy units for amplifications of up to an order of magnitude at room temperature. The solid line represents the results of fitting at an impurity concentration $N_{A^-} - N_{D^+} = 1.16 \times 10^{15}$ cm^{-3}, which was found from capacitance measurements. Varying parameters such as the base width and L_D gave the values $d = 6.37$ μm and $L_D = 2.90$ μm.

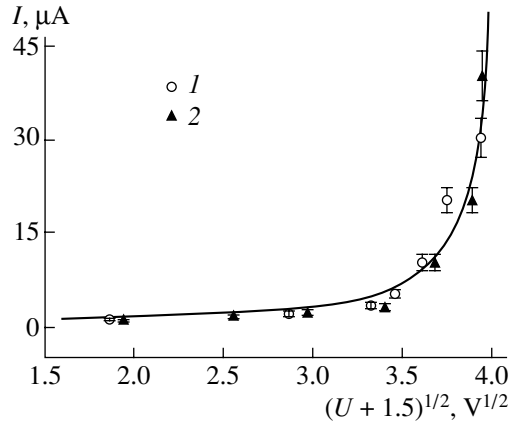

Fig. 2. Photocurrent induced by light from mercury lamp vs the voltage across the detector. The current is normalized to 1 μA. Solid line: results of fitting (as in Fig. 1) at $d = 4.67$ μm, $L_D = 0.83$ μm. Filters used: (1) glass and (2) water + UFS6 glass.

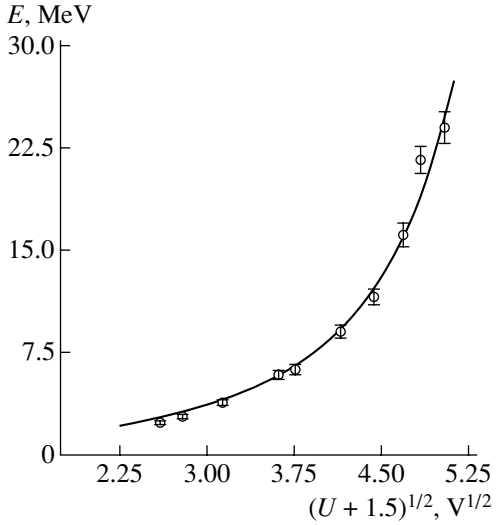

Fig. 3. Signal energy as a function of voltage in recording of ^{244}Cm alpha particles ($E_\alpha = 5.8$ MeV). Solid line: result of fitting by the algorithm of [1] at $d = 6.37$ μm and $L_D = 2.90$ μm. Energy absorbed in the detector base ~1.3 MeV.

At higher temperatures (up to $T = 135$°C), the room-temperature value of $d = 6.37$ μm was taken as the starting value in data processing. The parameters to be determined were $(N_{A^-} - N_{D^+})$ and L_D, which can vary with temperature. Experimentally, a significant decrease in L_D to 0.3 μm was observed. Figure 4 presents the dependence $(L_D)^2 = f(1000/T)$ reflecting a fall in the electron lifetime $\tau \propto (L_D)^2$.

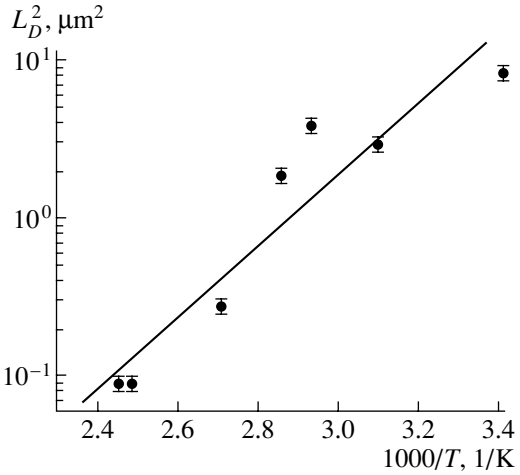

Fig. 4. Temperature dependence of the diffusion displacement of electrons in the *p*-base of the detector according to the results obtained in recording of alpha particles. L_D values found from curves similar to those in Fig. 3. The run of the dependence $(L_D)^2 = f(T)$ corresponds to variation of the electron lifetime $\tau(T)$.

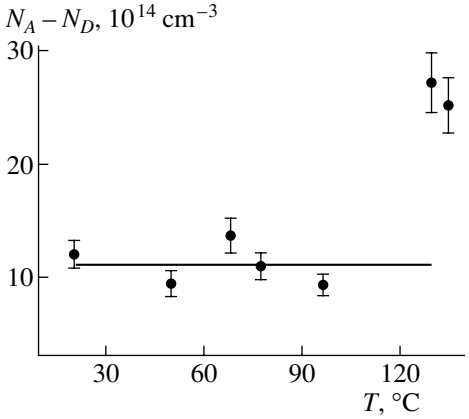

Fig. 5. Temperature dependence of the concentration of impurities ionized in the SCR of the collector junction according to the results obtained in recording of alpha particles. $(N_{A^-} - N_{D^+})$ values calculated from curves similar to those in Fig. 3.

The concentration of impurities (ionized within the SCR of the collector junction) remained virtually unchanged up to T = 100°C and then started to grow (see Fig. 5).

4. DISCUSSION

The data obtained in this study were described above in terms of the model [1], i.e., were attributed to amplification in the phototransistor structure. The model makes it possible to determine the main parameters of the *p*-base and seems to be reasonable for a triode structure.

Previously, superlinear behavior of the photocurrent in SiC with an SCR width (voltage) similar to that in Fig. 2 was observed in [16]. However, in contrast to the case being considered in this paper, diode structures fabricated on a heavily doped material were used in [16]. Correspondingly, the effect was attributed to impact ionization by nonequilibrium holes.

The signal amplification observed in this study is characterized by the insignificant role of the type of carrier generation. Diametrically opposite cases in this regard are those of irradiation with alpha particles and with X-rays. As mentioned above, single alpha particles create dense tracks consisting of carriers shaped as cylinders ~10 μm in diameter. X-rays produce carriers with a low density at equal probabilities throughout the detector base. However, a superlinear rise in signal, with about the same amplification factors, is observed in both cases. In the end, it turns out that the manner in which nonequilibrium carriers are created in the base by radiation is insignificant for the resulting signal. This is consistent with the phototriode model, in which the current flowing through the base is governed by the photovoltage across the emitter–base junction, which appears owing to the "primary" charge itself.

At the same time, it is difficult to provide a satisfactory explanation for the behavior of the measured parameters when the temperature increases. For example, it seems natural to relate the increase in the negative space charge of impurities $(N_{A^-} - N_{D^+})$ to the filling of centers having a higher energy with electrons from the valence band. The holes formed in this process drift toward the negative electrode and are carried away from the field region.

Less understandable is the observed decrease in L_D (in lifetime τ) for electrons in the *p*-base. The decrease contradicts the known fact that, in recombination via simple local centers, the lifetime grows with temperature and reaches a maximum upon transition to intrinsic conduction (see [17]).

In explaining the run of $L_D(T)$, account should be taken of the fact that the L_D values were found from the signal generated by single alpha particles. Under these conditions of pulsed ionization, the charge recorded in the experiment is governed both by the photovoltage across the emitter–base junction and by the duration of its existence. Thus, the question as to why the lifetime of majority carriers (holes, τ_h) decreases in the base arises in addition to the problem of transport of electrons injected from the emitter.

In principle, the decrease in τ_h can be understood as the manifestation of multicharge centers. With centers of this kind, a new level may appear when the Fermi level moves upwards, away from the ν-band, with increasing temperature. In order for this to occur, the old level must be filled. The center acquires a negative charge and its hole-capture cross-section increases. However, the filling of old levels with electrons must

reflect upon the space charge ($N_{A^-} - N_{D^+}$), which is only observed at $T > 100$°C.

In view of the aforesaid, it is apparent that no exhaustive explanation of the run of the $L_D(T)$ dependence could be found. It is also apparent that the experimental L_D value cannot be unequivocally attributed to electron diffusion and should be regarded as a parameter reflecting current relaxation in the external circuit of a triode structure under pulsed ionization.

5. CONCLUSION

The dependence of the signal on bias across a triode detector structure in recording weakly ionizing radiation was studied. Fluxes of photons from an X-ray tube or mercury lamp were used. In all cases, a superlinear rise in induced current was observed with increasing voltage across the structure. The signal was amplified by a factor of several tens with respect to the value chosen for normalization.

Qualitatively, the rise in signal can be accounted for by the amplification of the nonequilibrium charge introduced into the base, which is characteristic of a phototriode (as proposed in a previous communication [1]).

At room temperature, a quantitative description in terms of the phototriode model gives quite acceptable values for the base width, length of diffusion displacement of electrons, and space charge of ionized impurities. However, in additional experiments, the recording of single alpha particles demonstrated that the calculated electron diffusion length falls markedly with increasing temperature. This fact could not be explained adequately.

From the practical point of view, it is important that comparatively thin (on the order of 10 μm) SiC films can be used to detect penetrating radiation. Their effective thickness exceeds the geometrical value by a factor equal to the signal amplification factor.

ACKNOWLEDGMENTS

This study was supported in part by the Russian Foundation for Basic Research (project no. 00-15-96750).

REFERENCES

1. A. A. Lebedev, N. B. Strokan, A. M. Ivanov, *et al.*, Appl. Phys. Lett. **79**, 4447 (2001).
2. N. B. Strokan, A. M. Ivanov, N. S. Savkina, *et al.*, Fiz. Tekh. Poluprovodn. (St. Petersburg) **36**, 375 (2002) [Semiconductors **36**, 354 (2002)].
3. A. M. Ivanov, N. B. Strokan, D. V. Davidov, *et al.*, Appl. Surf. Sci. **184**, 431 (2001).
4. A. A. Lebedev, V. V. Kozlovskiĭ, N. B. Strokan, *et al.*, Fiz. Tekh. Poluprovodn. (St. Petersburg) **36**, 1354 (2002) [Semiconductors **36**, 1270 (2002)].
5. V. A. Tikhomirova, O. P. Fedoseeva, and G. F. Kholuyanov, Fiz. Tekh. Poluprovodn. (Leningrad) **6**, 957 (1972) [Sov. Phys. Semicond. **6**, 831 (1972)].
6. G. Violina, P. Shkreby, E. Kalinina, *et al.*, in *Proceedings of III International Seminar on Silicon Carbide and Related Materials, Novgorod the Great, Russia, 2000*, p. 125.
7. G. N. Violina, E. V. Kalinina, G. F. Kholujanov, *et al.*, Fiz. Tekh. Poluprovodn. (St. Petersburg) **36**, 750 (2002) [Semiconductors **36**, 710 (2002)].
8. G. Bertuccio, R. Casigaghi, and F. Nava, IEEE Trans. Nucl. Sci. **48**, 232 (2001).
9. M. Bruzzi, F. Nava, S. Russo, *et al.*, Diamond Relat. Mater. **10**, 657 (2001).
10. A. A. Lebedev, N. S. Savkina, A. M. Ivanov, *et al.*, Mater. Sci. Forum **338–342**, 1447 (2000).
11. R. Yakimova and E. Jansen, Diamond Relat. Mater. **9**, 432 (2000).
12. N. S. Savkina, A. A. Lebedev, D. V. Davydov, *et al.*, Mater. Sci. Eng. B **77**, 50 (2000).
13. T. Kimito, S. Nakazawa, K. Fujira, *et al.*, in *Technical Digest of International Conference on Silicon Carbide and Related Materials (ICSCRM2001), Tsukuba, Japan, 2001*, p. 189.
14. S. Sze, *Physics of Semiconductor Devices* (Wiley, New York, 1981; Mir, Moscow, 1984).
15. Yu. A. Vodakov, D. P. Litvin, V. I. Sankin, *et al.*, Pis'ma Zh. Tekh. Fiz. **10**, 303 (1984) [Sov. Tech. Phys. Lett. **10**, 128 (1984)].
16. A. O. Konstantinov, Fiz. Tekh. Poluprovodn. (Leningrad) **17**, 2124 (1983) [Sov. Phys. Semicond. **17**, 1358 (1983)].
17. S. M. Ryvkin, *Photoelectric Effects in Semiconductors* (Fizmatgiz, Leningrad, 1963; Consultants Bureau, New York, 1964).

Translated by M. Tagirdzhanov

Semiconductors, Vol. 37, No. 1, 2003, pp. 70–76. Translated from Fizika i Tekhnika Poluprovodnikov, Vol. 37, No. 1, 2003, pp. 70–76.

LOW-DIMENSIONAL SYSTEMS

Lateral Electronic Transport in Short-Period InAs/GaAs Superlattices at the Threshold of Quantum Dot Formation

V. A. Kul'bachinskii*, R. A. Lunin*, V. A. Rogozin*, V. G. Mokerov*, Yu. V. Fedorov*, Yu. V. Khabarov*, E. Narumi, K. Kindo**, and A. de Visser*****

** Moscow State University, Vorob'evy gory, Moscow, 119899 Russia*

*** Osaka University, Japan*

**** Van der Waals–Zeeman Institute, University of Amsterdam, the Netherlands*

Submitted April 8, 2002; accepted for publication April 9, 2002

Abstract—Temperature dependences of resistance at 0.7 K < T < 300 K, the Hall and Shubnikov–de Haas effects in magnetic fields of up to 40 T, photoluminescence (PL), and morphology of a heterointerface (using an atomic-force microscope) of short-period InAs/GaAs superlattices were investigated. The investigations were carried out for a region of subcritical and critical thickness Q = 2.7 monolayers (ML) of InAs. Upon exceeding the critical thickness, the self-organized growth of InAs quantum dots (QDs) set in. The formation of QD layers upon exceeding the critical thickness of InAs Q = 2.7 ML is accompanied by a transition of conductivity from metallic to hopping. It is found that at InAs layer thicknesses of Q = 0.33 ML and Q = 2.0 ML, the PL intensities and electron mobilities in the structures have clearly pronounced maxima. Anisotropy of conductivity, which depends on the thickness of the deposited InAs layers, was observed. © *2003 MAIK "Nauka/Interperiodica".*

1. INTRODUCTION

In recent years, one of most important trends in fundamental and applied solid-state physics has been the investigation of formation of nanostructures resulting from the reconstruction (self-organization) of a surface during heteroepitaxial growth in lattice-mismatched systems. Such processes are observed, for example, in InAs/GaAs semiconductor heterostructures [1–4]. Using these processes, it is possible to obtain, for example, quantum-dot (QD) structures, the investigation of which is of tremendous scientific interest.

The self-organized growth of InAs QDs on a GaAs surface sets in when the thickness of the InAs layer, which is generally measured in monolayers (ML), exceeds a certain critical value. There are numerous publications devoted to the investigation of the optical properties of QD structures. However, the electron-transport properties of InAs/GaAs structures in the region of the critical, and slightly below critical, thickness of the InAs layer are poorly understood.

In this study, the lateral transport of charge carriers in δ-Si-doped short-period InAs/GaAs superlattices is investigated. In essence, these superlattices represent quantum wells (QWs). Investigations were carried out in the region of subcritical and critical thickness of the InAs layers, which is necessary for the formation of the QDs.

2. SAMPLES

The samples investigated were grown by molecular beam epitaxy on semi-insulating GaAs(100) substrates. Each sample consisted of substrate, an undoped GaAs buffer layer 1 μm thick, a short-period InAs/GaAs superlattice (for a detailed description, see below), an undoped $Al_{0.2}Ga_{0.8}As$ spacer 10 nm thick, an Si δ-layer, an $Al_{0.2}Ga_{0.8}As$ layer (35 nm thick), and a GaAs cap layer 6 nm thick (Fig. 1).

The nominal thickness Q of the InAs layers in various superlattices varied from 0.33 to 2.7 ML. The thickness P of the GaAs layers was varied proportionally from 1.7 to 13.5 ML in order to keep the average composition of

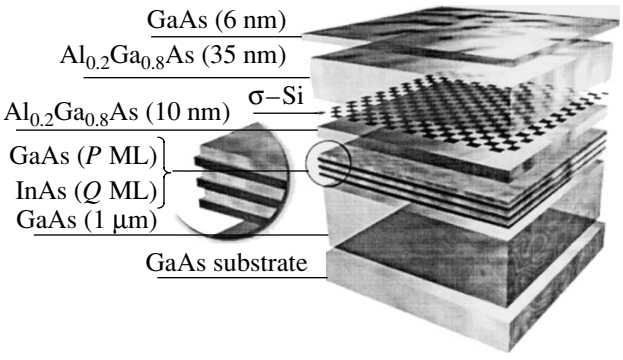

Fig. 1. Schematic representation of the sample structure. Letters P and Q denote the thicknesses of the GaAs and InAs in monolayers (ML), respectively.

Characteristics of the samples investigated

Sample	Q, ML	P, ML	Number of periods N	$h\nu_2$, $h\nu_1$, eV	$\Delta(h\nu_{max})$, meV	E_1–E_0, meV	n_H, 10^{11} cm^{-2}	n, 10^{11} cm^{-2}	μ_H, cm^2/(V s)
				Experiment		Calculation			
1	$In_{0.16}Ga_{0.84}As$ QW			1.434, 1.375	59	50	8.1	8.3	8100
2	0.33	1.7	24	1.419, 1.367	52	54	11.5	–	9400
3	0.67	3.4	12	1.411, 1.369	42	52	7.2	7.0	2060
4	1.00	5.0	8	1.411, 1.370	41	53	7.3	8.7	2450
5	1.33	6.7	6	1.418, 1.374	44	52	8.66	–	4220
6	1.58	8.0	5	1.404, 1.368	36	52	6.8	9.3	4910
7	2.00	10.0	4	1.406, 1.356	50	51	10.4	–	7060
8	2.70	13.5	3	1.390, 1.265	125	–	1.52	–	50

Note: Letters Q and P denote the number of InAs and GaAs monolayers, $h\nu_1$ and $h\nu_2$ are the peak energies of the PL spectrum $h\nu_{max}$ measured at 77 K, $\Delta(h\nu_{max})$ is the difference between the PL peaks, E_1–E_0 is the calculated difference between the electron energy levels, n_H is the Hall electron density, n is the electron density obtained from the Shubnikov–de Haas effect, and μ_H is the Hall mobility. Measurements were carried out at T = 4.2 K.

the superlattice equivalent to the $In_{0.16}Ga_{0.84}As$ solid solution. Such narrow GaAs barriers are penetrable, and, as it will be seen below, the superlattice represents a QW. The number of MLs is not an integer. This means that InAs (or GaAs) is distributed nonuniformly over the structure surface, thus forming separate islands in addition to a continuous layer. Depending on the layer thickness, the number of lattice periods varied from 24 to 3, so that the overall thickness of the superlattice was 14 nm in all of the samples. All superlattices were grown at a temperature T = 490°C, and the other layers were grown at T = 590°C. After the deposition of each InAs layer, the growth was interrupted for 30 s. We investigated eight samples. Some of the parameters of the samples are given in the table.

For comparison, a structure with a single QW was grown (sample 1). In this structure, a layer of $In_{0.16}Ga_{0.84}As$ solid solution was formed instead of a superlattice. This layer had the same thickness of 14 nm.

Data on photoluminescence (PL) (see section 3.3 below) and data obtained by atomic-force microscopy demonstrated that, if the InAs layer thickness exceeded 2.7 ML, then QDs are formed. Figure 2 shows an image obtained using an atomic-force microscope for sample 8 after the selective etching of its upper layers. The InAs islands (i.e., the QDs) are clearly seen.

In this study, we investigated lateral electron transport, i.e., transport over layers of superlattices. To measure the anisotropy of resistance and magnetoresistance, the samples were prepared in the form of L-shaped double Hall bridges using photolithography. The resistance of the structures was simultaneously measured for currents flowing along the [110] direction and along the $[\bar{1}10]$ direction. Magnetoresistance and the magnitude of the Hall effect at low temperatures in magnetic fields of up to 8 T were measured in a superconducting solenoid. A setup at the University of Amsterdam that generated pulsed magnetic fields was used for measurements in magnetic fields of up to 40 T.

3. RESULTS OF MEASUREMENTS AND DISCUSSION

3.1. Temperature Dependences of Resistance

The conductivity of the samples with short-period superlattices was investigated in the temperature range from room temperature to 70 mK (Fig. 3). For the samples with a nominal InAs thickness $Q \le 2.0$ ML, a metallic dependence of resistance on temperature is characteristic. In the region of low temperatures, a logarithmic fall in conductivity, which is characteristic of weak localization of charge carriers, is observed [5]. The absolute value of resistivity for these samples was significantly smaller than h/e^2, which conventionally

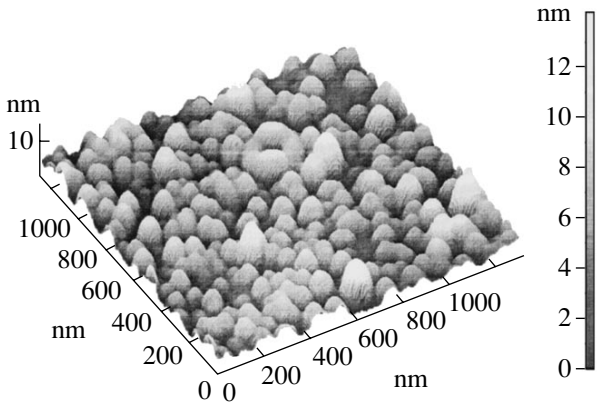

Fig. 2. Atomic-force microscopy image of the QD structure (sample 8) after selective etching of the upper layer.

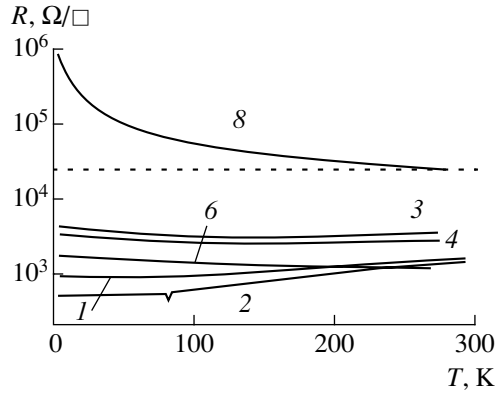

Fig. 3. Temperature dependences of resistance R per area for samples 1–6 with short-period superlattices and sample 8 with QD layers. A horizontal dotted straight line corresponds to the h/e^2 value. Curves are numbered according to sample numbers in the table.

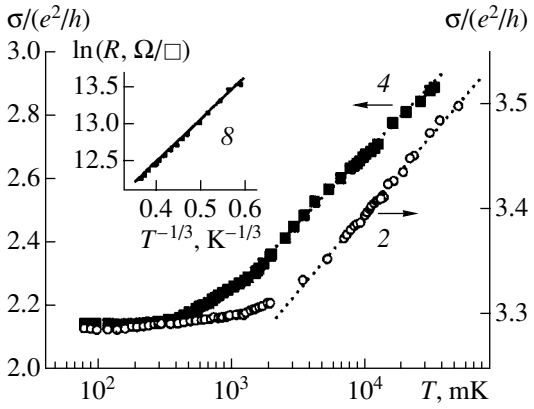

Fig. 4. Conductivity σ for samples 2 and 4 in units of the lowest metallic conductivity e^2/h at low temperatures. The dependence of resistance R on the temperature T for sample 8 in the coordinates corresponding to the Mott law is in the inset. Curves are numbered according to sample numbers in the table.

separates a two-dimensional (2D) metal and insulator. As an example, the temperature dependences of conductivity for samples 2 and 4 are shown in Fig. 4. The temperature scale in Fig. 4 is logarithmic. Due to this, the linear portions are clearly distinguished for each curve as the temperature decreases to ~2 K. At temperatures $T < 1$ K, the conductivity of superlattices with a nominal InAs thickness $Q \le 2.0$ ML levels off (see Fig. 4).

The resistance of sample 8 was larger than h/e^2 in the entire temperature range under consideration and increased as the temperature decreased. At temperatures below 20 K, the resistance was approximated well by a function corresponding to the Mott law for hopping conductivity with a variable hop range for the two-dimensional case. In this case, the approximation takes the form $\rho = \rho_0 \exp[(T_0/T^{1/3})]$ [6] (see inset in Fig. 4). The T_0 parameter for sample 8 equals ~200 K. This parameter is associated with the density of states at the Fermi level and the localization radius as $T_0 = C(g_{E_F} a^2)^{-1}$, where $C = 13.8$ is a numerical coefficient. The localization radius r thus obtained from the experimental data is approximately equal to 53 nm. Hence, a transition from the short-period superlattice to the QD layers upon exceeding the critical InAs concentration is accompanied by a transition from metallic conduction to the hopping one.

3.2. Magnetoresistance and the Shubnikov–de Haas effect

In weak magnetic fields at the liquid-helium temperature, all of the samples showed negative magnetoresistance. For the samples with $Q \le 2.0$ ML, the magnetic-field dependence of negative magnetoresistance was initially quadratic and then logarithmic, which is characteristic of weak localization [5].

In stronger magnetic fields, the Shubnikov–de Haas effect was observed for samples 1–7 with 0 ML $\le Q \le$ 2.0 ML. As an example, Fig. 5 shows the dependences of the magnetoresistance R_{xx} and the Hall resistance R_{xy} for samples 4 ($Q = 1$ ML) and 6 ($Q = 1.58$ ML) in fields up to 40 T. For both samples, clearly distinguishable plateaus in the magnetic-field dependence of R_{xy} are observed. These plateaus correspond to the filling factors of Landau levels $\nu = 1$, 2, and 3. The Fourier spectra of Shubnikov–de Haas oscillations for the same samples are shown in the insets to Figs. 5a and 5b. The presence of a single peak in the Fourier spectra indicates that only the subband of dimensional quantization is filled in the samples under investigation. The electron concentrations n, which were obtained based on the Shubnikov–de Haas oscillations, are given in the table, along with the concentrations n_H and mobilities μ_H obtained from the Hall effect in weak magnetic fields.

3.3. Photoluminescence and Energy Spectrum

Figure 6 shows the PL spectra for sample 1, which contains a single $In_{0.16}Ga_{0.84}As$ QW, and six samples whose superlattices are arranged according to an increase in the InAs layer thickness from $Q = 0.33$ ML to $Q = 2.7$ ML.

As can be seen from Fig. 6, the PL spectra for a sample with a single QW and for samples with superlattices, which contain an InAs layer with a thickness $Q \le$ 2 ML, are shaped similarly. All of these spectra contain two pronounced peaks. The first low-energy peak with a transition energy $h\nu_1$ lies in the range of 1.356–1.375 eV, while the second high-energy peak with a transition energy $h\nu_2$ lies in the range of 1.404–1.434 eV (see

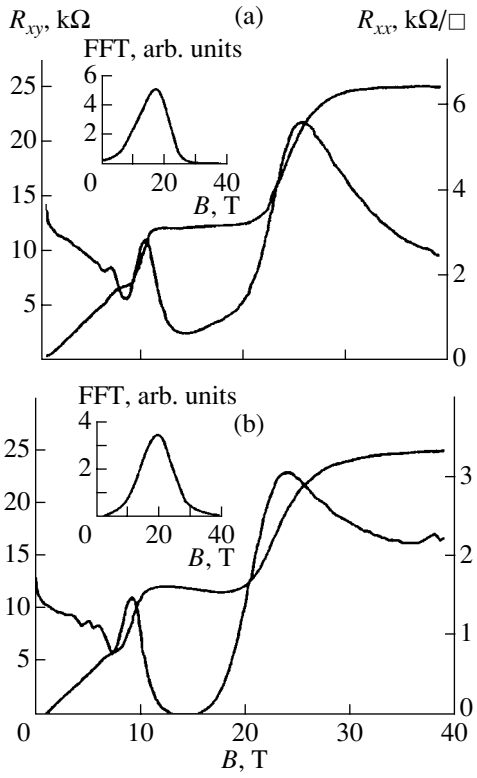

Fig. 5. Transverse magnetoresistance R_{xx} and Hall resistance R_{xy} of samples (a) 4 and (b) 6 at $T = 4.2$ K. Curves are numbered according to sample numbers in the table. The relevant Fourier spectra are shown in inset.

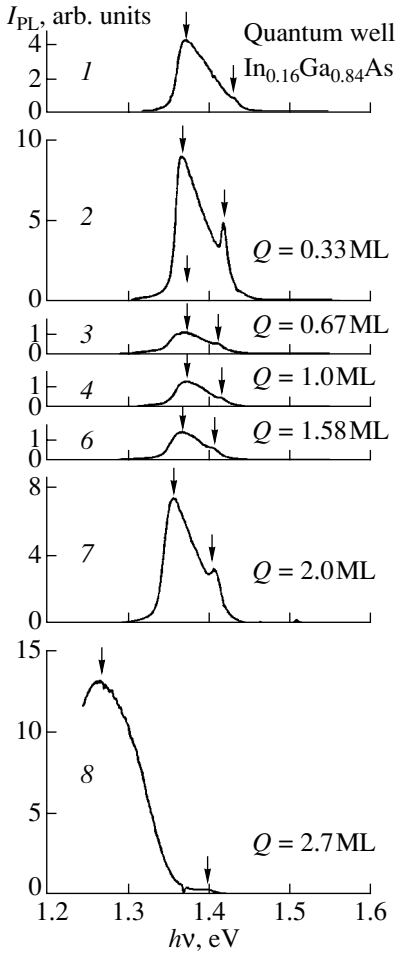

Fig. 6. Photoluminescence spectra of the investigated structures, which differ in the nominal thickness Q of the InAs layers. The scale on the axis of the PL intensity I_{PL} is identical for all drawings. Drawings are numbered according to sample numbers in the table. $T = 77$ K.

table). For all of the samples, the intensity of the first peak is higher than that of the second peak.

Upon reaching a nominal thickness $Q = 2.7$ ML (sample 8) for the InAs layers, radical changes are observed in the PL spectrum (see Fig. 6). A new broad and intense band with a peak at $h\nu = 1.265$ eV emerges in the low-energy region. According to [1], such changes in the spectrum represent a characteristic feature of a transition of an InAs layer from 2D to 3D growth, which leads to the formation of QDs. According to [7], the position of this peak in the PL spectrum allows one to estimate the QD size. In our case, such estimation yields a QD pedestal size of approximately 26 nm.

The electron mobilities μ_H for the samples investigated, which were obtained from the Hall effect, are also given in the table. It is obvious that the variation in the Hall mobility with an increase in the thickness Q of the InAs layers correlates with the Q dependence of the PL intensity I_{PL}. Thus, the mobility for the sample with $Q = 0.33$ ML is highest and equals $\mu_H = 9400$ cm^2/(V s). At $Q = 0.67$ ML, the mobility decreases to 2450 cm^2/(V s); it then increases and attains a value of 7060 cm^2/(V s) at $Q = 2.0$ ML (Fig. 7). For sample 1 with an $In_{0.16}Ga_{0.8}As$ QW, $\mu_H = 8100$ cm^2/(V s).

The results obtained allow us to assume the following. The structure of sample 1, which contains a strained $In_{0.16}Ga_{0.84}As$ QW, is rather homogeneous. In this case, the carrier mobility is determined by scattering, which is characteristic of alloys, and by elastic strains, which are caused by a mismatch of interatomic distances between GaAs and $In_{0.16}Ga_{0.84}As$ [8]. Sample 2 contains less than a single ML of InAs ($Q = 0.33$ ML), and the strains caused by lattice mismatch between InAs and GaAs are small. Due to this, these strains relax at small distances with the resulting formation of a QW. In this QW, scattering and nonradiative recombination are reduced, and the carrier mobility and PL intensity for this sample are highest. Upon reaching a thickness of $Q = 0.67$ ML in the InAs layers, the elastic strains become larger. This probably gives rise to fluctuations in the potential relief and reduces the mobility. A further increase in the thickness of the InAs layers results in a gradual decrease in the elastic strains and fluctuations caused by them, since an increase in the

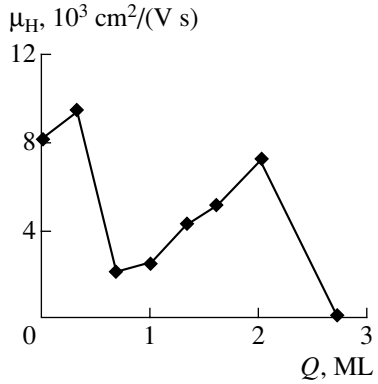

Fig. 7. Dependence of the Hall mobility μ_H on the thickness of the InAs layers (Q) at $T = 4.2$ K. The value $Q = 0$ ML corresponds to sample 1.

carrier mobility and PL intensity is observed with increasing thickness of the InAs layers. The radical reconstruction of the shape of the PL spectrum upon reaching the rated thickness $Q = 2.7$ ML of the InAs layers (sample 8) is indicative of the formation of InAs QDs. A low concentration of free charge carriers in this sample is explained by the localization (see above) of a considerable fraction of electrons in the formed QD arrays, which results in an extremely low Hall mobility in this sample. It is precisely these factors which lead to the nonmonotonic dependence of the PL intensity and the electron Hall mobility on the thickness of the InAs layers.

For all of the samples, the energy spectra and electron wave functions were calculated by the method of the self-consistent solution of the Schrödinger and Poisson equations [9, 10]. In the Schrödinger equation

$$\left[-\frac{\hbar^2}{2}\frac{d}{dz}\left(\frac{1}{m^*(z)}\frac{d}{dz}\right) + U(z)\right]\psi_i(z) = E_i\psi_i(z), \quad (1)$$

the potential energy is expressed by the sum $U(z) = U_H(z) + \Delta U_c + U_{xc}(z)U_H(z)$, where $U_H(z)$ is the electrostatic potential energy, which is determined from the Poisson equation

$$\frac{d}{dz}\left(\varepsilon_0\varepsilon(z)\frac{dU_H(z)}{dz}\right) = e^2[N(z) - n(z)]. \quad (2)$$

Here, $N(z)$ is the bulk concentration of ionized donors,

$$n(z) = \frac{m^*}{\pi\hbar^2}\sum_i (E_F - E_i)\theta(E_F - E_i)|\psi_i(z)|^2 \quad (3)$$

is the electron density at $T = 0$ K, and $\theta(x)$ is the unit-step function. ΔU_c is the offset of the conduction band bottom at the heterojunction, and U_{xc} is the exchange-correlation potential [11]

$$U_{xc} = -\left[1 + 0.0545 r_S \ln\left(1 + \frac{11.4}{r_S}\right)\right]\frac{2}{\pi\alpha r_S}\text{Ry}^*, \quad (4)$$

where

$$\alpha = \left(\frac{4}{9\pi}\right)^{1/3}, \quad r_S = \left(\frac{4\pi a_B^2 n(z)}{3}\right)^{-1/3},$$
$$a_B^* = \frac{4\pi\varepsilon_0\varepsilon\hbar}{m^* e^2}, \quad \text{Ry}^* = \frac{e^2}{8\pi\varepsilon_0\varepsilon a_B^*}. \quad (5)$$

In calculations, band offsets between GaAs layers and strained InAs layers were assumed to equal $\Delta U_c = 535$ meV and $\Delta U_v = 385$ meV [12] for the conduction-band bottom and the valence-band top, respectively. The effective electron mass for the strained InAs layers in the superlattices was assumed to equal $m_c^{st} = 0.0365 m_0$ [13].

As an example, Fig. 8 demonstrates the calculated profiles of the conduction-band bottom (E_c), the positions of two lower electron levels, and the profiles of

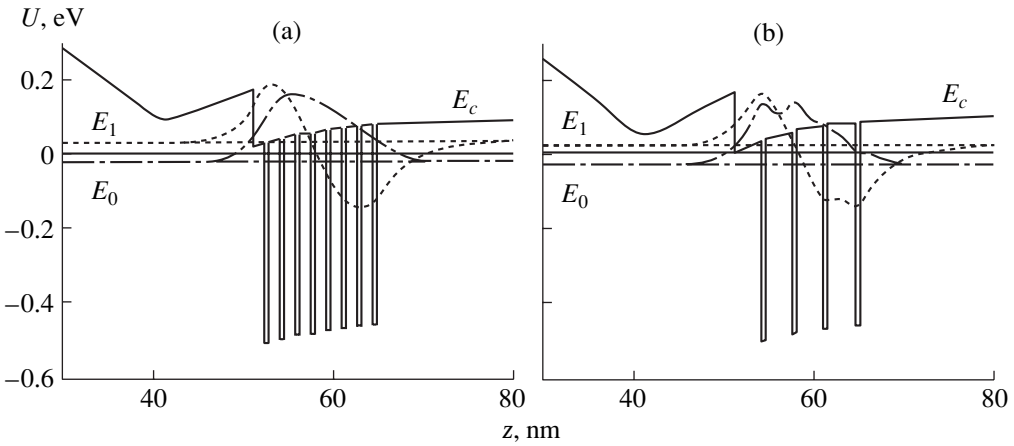

Fig. 8. Calculated profile of the conduction-band bottom (E_c), the position of the lower electron levels E_0 (dash-and-dot line) and E_1 (dashed line), as well as the profile of corresponding wave functions for samples (a) 4 and (b) 7. The letter z denotes the distance from the sample surface. The Fermi level is denoted by a solid horizontal line.

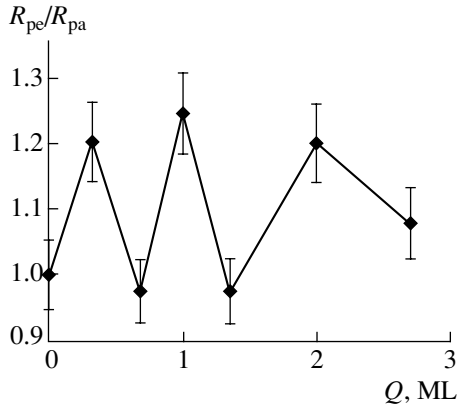

Fig. 9. Ratio of resistance in the [$\bar{1}$10] direction (R_{pe}) to the resistance in the [110] direction (R_{pa}) as a function of the thickness of the InAs layers (Q). The value Q = 0 ML corresponds to sample 1.

wave functions for samples 4 and 7. The Fermi energy is taken as the origin of the energy scale. For all of the samples, only the lower electron levels were occupied with electrons, which corresponds to the data obtained from the Shubnikov–de Haas effect. The calculated difference between the energies of the first and second electron levels is given in the table. It should be noted that the calculated difference between the energies of electron levels is close to the difference between the observed PL peaks. This indicates that it is the first and second electron subbands of dimensional quantization that contribute to the observed transitions.

The configuration of the wave functions in the superlattice for all of the samples resembles the configuration of the wave functions for a single $In_{0.16}Ga_{0.84}As$ QW. It differs from the latter by a modulation which correlates with the profile of the conduction-band bottom of the superlattice. This demonstrates that a short-period superlattice, in essence, represents a QW with profile modulations.

3.4. Anisotropy of Conductivity

For all of the samples, except for sample 1, anisotropy of resistance is observed. Figure 9 demonstrates the dependence of the ratio of resistance in the [$\bar{1}$10] direction to the resistance in the [110] direction on the thickness Q of the InAs layers. The spread of the anisotropy coefficient for a series of samples with the same Q is less than 10%. The anisotropy of resistance correlates with the asymmetry of dislocation distribution [14]. The anisotropy of resistance in a system of 2D electrons is typical of structures with the preferential growth of the deposited material in a single direction [15]. The dependence of anisotropy on the thickness of the InAs layers demonstrates that island growth, which leads to the anisotropy of conductivity, depends on the amount of InAs deposited.

4. CONCLUSION

In this study, the photoluminescence, the temperature dependences of resistance, and the Shubnikov–de Haas effect for short-period InAs/GaAs superlattices, which represent QWs, were investigated. During investigations, magnetic fields up to 40 T were applied in the temperature range of 0.07 K < T < 300 K. An $In_{0.16}Ga_{0.84}As$ QW can be grown as a solid solution or by the sequential fractional deposition of InAs and GaAs layers. In the latter case, at a certain thickness of the deposited InAs layer, specifically, at Q = 0.33 ML and Q = 2.0 ML, the PL intensities and electron mobilities of the structures have clearly pronounced maxima. This is apparently associated with more efficient strain relaxation compared with samples with other values of Q. Anisotropy of conduction is observed, which depends on the thickness of the deposited InAs layers.

It is found that a critical InAs concentration exists (Q = 2.7 ML). At concentrations higher than this value, quantum dots form in the layers. The formation of QDs leads to a sharp decrease in the electron Hall mobility and to a shift of the peak of the PL spectrum. Upon exceeding the critical thickness of the InAs layer, a transition from the short-period superlattice to the QD layer is accompanied by a transition from metallic conduction to hopping conduction with a variable hop range.

ACKNOWLEDGMENTS

This study was supported by the Russian Foundation for Basic Research (project no. 00-02-17493) and by the Ministry of Industry and Science of the Russian Federation.

REFERENCES

1. N. N. Ledentsov, V. M. Ustinov, V. A. Shchukin, *et al.*, Fiz. Tekh. Poluprovodn. (St. Petersburg) **32**, 385 (1998) [Semiconductors **32**, 343 (1998)].
2. D. Bimberg, M. Grundmann, and N. N. Ledentsov, *Quantum Dot Heterostructures* (Wiley, Chichester, 1998).
3. P. W. Fry, I. E. Itskevich, D. J. Mowbray, *et al.*, Phys. Rev. Lett. **84**, 733 (2000).
4. A. D. Yoffe, Adv. Phys. **50**, 1 (2001).
5. T. A. Polyanskaya and Yu. V. Shmartsev, Fiz. Tekh. Poluprovodn. (Leningrad) **23** (1), 3 (1989) [Sov. Phys. Semicond. **23**, 1 (1989)].
6. B. I. Shklovskiĭ and A. L. Efros, *Electronic Properties of Doped Semiconductors* (Nauka, Moscow, 1979; Springer-Verlag, New York, 1984).

7. J.-Y. Marzin, J.-M. Gérard, A. Israël, *et al.*, Phys. Rev. Lett. **73**, 716 (1994).
8. V. A. Kulbachinskii, V. G. Kytin, T. S. Babushkina, *et al.*, J. Low Temp. Phys., Nos. 5/6, 499 (1996).
9. T. Ando, J. Phys. Soc. Jpn. **51**, 3893 (1982).
10. V. A. Kul'bachinskiĭ, R. A. Lunin, V. G. Kytin, *et al.*, Zh. Éksp. Teor. Fiz. **110**, 1517 (1996) [JETP **83**, 841 (1996)].
11. *Theory of the Inhomogeneous Electron Gas*, Ed. by S. Lundqvist and N. H. March (Plenum, New York, 1983; Mir, Moscow, 1987).
12. J. Brübach, A. Yu. Silov, J. E. M. Haverkort, *et al.*, Phys. Rev. B **59**, 10315 (1999).
13. Y. Foulon and C. Priester, Phys. Rev. B **44**, 5889 (1991).
14. T. Schweizer, K. Kohler, W. Rothemund, and P. Ganser, Appl. Phys. Lett. **59**, 2736 (1991).
15. A. de Visser, V. I. Kadushkin, V. A. Kul'bachinskiĭ, *et al.*, Pis'ma Zh. Éksp. Teor. Fiz. **59**, 340 (1994) [JETP Lett. **59**, 363 (1994)].

Translated by N. Korovin

Semiconductors, Vol. 37, No. 1, 2003, pp. 77–81. Translated from Fizika i Tekhnika Poluprovodnikov, Vol. 37, No. 1, 2003, pp. 77–82.

LOW-DIMENSIONAL SYSTEMS

Investigation of Electronic Transitions in Coupled-Quantum-Well Structures with a Built-in Electric Field by Photoreflectance Spectroscopy

G. B. Galiev*, V. É. Kaminskiĭ*^, V. G. Mokerov*, L. P. Avakyants, P. Yu. Bokov**, A. V. Chervyakov**, and V. A. Kul'bachinskiĭ****

** Institute of Radio Engineering and Electronics, Russian Academy of Sciences, ul. Mokhovaya 18, Moscow, 103907 Russia*

*** Moscow State University, Vorob'evy gory, Moscow, 119899 Russia*

^e-mail: kamin@mail.cplire.ru

Submitted April 15, 2002; accepted for publication April 15, 2002

Abstract—Room-temperature photoreflectance spectra of coupled-quantum-well heterostructures with a built-in electric field are measured. The optical transition energies are determined and their dependences on the well width and the barrier thickness are examined. The experimental results are compared with the calculated energies of electron–hole transitions. Good agreement between calculations and experiment is found for narrow wells; in the case of wide wells, optical transitions are associated with groups of several closely spaced electron–hole transitions. © *2003 MAIK "Nauka/Interperiodica"*.

1. INTRODUCTION

In recent years, heterostructures with AlGaAs/GaAs/AlGaAs quantum wells (QWs) have been widely used to make photodetectors, optical modulators, high-power transistors, and other devices. Desired characteristics of the optoelectronic structures are often attained using a coupled-QW configuration representing two GaAs QWs separated by an AlAs barrier [1, 2]. It is known that parity selection rules hold for rectangular QWs, so that the overlap integrals between the electron and the hole wave functions equal either unity or zero. However, in most cases, the QWs are subjected to built-in and/or external electric fields. In this case, the parity selection rules are lifted and the overlap integrals can assume any value from zero to unity. This, in turn, causes a change in the conditions for light emission or absorption in such systems.

In addition to the quantization of the electron energy spectrum, the phonon spectrum is also quantized in AlGaAs/GaAs/AlGaAs heterostructures. Calculations indicate that this should bring about a reduction in electron–phonon scattering and, thus, an increase in electron mobility [3]. For QWs of specific sizes, introduction of a thin AlAs barrier should lead to a significant reduction in the intrasubband scattering rate and can provide for an additional increase in the mobility [4]; as a consequence, the transistor characteristics can be improved. All of this explains the current interest in studies of QW systems with thin barriers.

Electronic states in heterostructures have been investigated using a number of experimental techniques. Along with photoluminescence [5–8] and absorption spectroscopy [2, 9], methods of modulation spectroscopy are among those most widely used [10, 11]. The most common of these methods is the spectroscopy of photoreflectance or electroreflectance, which utilizes detection of the change in the reflection coefficient R of the sample under the influence of an electric field. In the photoreflectance (PR) approach, the modulation of the electric field in the semiconductor, which leads to the modulation of R, takes place due to the generation of electron–hole pairs by laser radiation.

In this paper, we report the results of experimental studies of heterostructures with coupled QWs using PR spectroscopy. The optical transition energies are determined from room-temperature PR spectra and compared with the energies of electron–hole transitions calculated theoretically.

2. GROWTH OF SAMPLES AND MEASUREMENTS OF PHOTOREFLECTANCE SPECTRA

The samples were grown by molecular-beam epitaxy on GaAs(100) substrates misoriented by 2° towards the [110] direction. First, a 0.5-μm-thick GaAs buffer layer was grown. Then, an $Al_{0.22}Ga_{0.78}As$ barrier, a GaAs QW, an AlAs barrier, a GaAs QW, and an $Al_{0.22}Ga_{0.78}As$ barrier were grown. Finally, a protective

The parameters of the samples, experimental and theoretical transition energies

Sample no.	W nm	L_b nm	E_g nm	E Experiment	E Calculation	M^2	Type of the transition
					1.415	0.172	1*e*-1*lh*
				1.421	1.416	0.136	1*e*-2*hh*
					1.428	0.268	1*e*-3*hh*
					1.431	0.317	2*e*-1*hh*
					1.439	0.332	1*e*-4*hh*
				1.437	1.441	0.531	1*e*-2*lh*
					1.444	0.541	2*e*-1*lh*
					1.446	0.266	2*e*-2*hh*
					1.45	0.155	1*e*-5*hh*
					1.464	0.278	3*e*-1*hh*
				1.468	1.468	0.254	1*e*-3*lh*
					1.477	0.125	3*e*-1*lh*
45*M*	26	0	1.42		1.491	0.149	3*e*-3*hh*
					1.498	0.245	2*e*-3*lh*
				1.514	1.504	0.239	3*e*-2*lh*
					1.522	0.135	4*e*-2*hh*
					1.533	0.12	2*e*-4*lh*
				1.561	1.574	0.175	4*e*-3*lh*
				1.608	1.609	0.022	4*e*-4*lh*
					1.65	0.128	4*e*-5*lh*
				1.414			
				1.437	1.443	0.595	1*e*-3*hh*
					1.443	0.505	2*e*-1*hh*
					1.46	0.113	1*e*-2*lh*
					1.462	0.609	2*e*-1*lh*
				1.492			
46*M*	26	1.8	1.414		1.522	0.197	3*e*-3*hh*
					1.54	0.213	3*e*-4*hh*
					1.541	0.127	4*e*-1*hh*
					1.58	0.127	4*e*-1*hh*
				1.605	1.606	0.178	4*e*-3*lh*
					1.638	0.101	4*e*-4*lh*
				1.413			
					1.440	0.435	2*e*-1*hh*
				1.442	1.456	0.449	1*e*-2*lh*
					1.457	0.664	2*e*-1*lh*
				1.507	1.512	0.032	1*e*-4*lh*
50*M*	26	0.9	1.413		1.53	0.133	3*e*-2*lh*
					1.531	0.222	3*e*-3*hh*
					1.532	0.111	4*e*-2*hh*
					1.593	0.196	4*e*-3*lh*
				1.611			
				1.413			
				1.431	1.438	0.467	2*e*-1*hh*
					1.452	0.595	1*e*-2*lh*
				1.457	1.454	0.685	2*e*-1*lh*
					1.455	0.164	1*e*-3*hh*
					1.455	0.12	2*e*-2*hh*
56*M*	26	0.5	1.413		1.475	0.15	1*e*-3*lh*
					1.523	0.186	2*e*-2*lh*
				1.526	1.526	0.298	3*e*-3*hh*

Sample no.	W nm	L_b nm	E_g nm	E Experiment	E Calculation	M^2	Type of transition
					1.528	0.128	4*e*-2*hh*
					1.579	0.179	3*e*-4*lh*
					1.586	0.198	4*e*-3*lh*
				1.599			
					1.408	0.102	1*e*-4*hh*
					1.41	0.2	1*e*-2*lh*
				1.413	1.411	0.22	2*e*-1*lh*
					1.413	0.128	2*e*-2*hh*
					1.418	0.176	1*e*-5*hh*
					1.422	0.227	3*e*-1*hh*
					1.426	0.267	2*e*-3*hh*
					1.432	0.414	1*e*-3*lh*
				1.425	1.435	0.448	3*e*-1*lh*
					1.437	0.196	2*e*-4*hh*
					1.437	0.25	3*e*-3*hh*
					1.438	0.391	2*e*-2*lh*
					1.448	0.287	4*e*-1*hh*
				1.451	1.454	0.278	1*e*-4*kh*
					1.462	0.178	4*e*-1*lh*
58*M*	35	0	1.413		1.471	0.129	3*e*-5*hh*
					1.476	0.104	4*e*-3*hh*
				1.479	1.482	0.184	2*e*-4*lh*
					1.484	0.221	3*e*-3*lh*
					1.488	0.197	4*e*-2*lh*
				1.514	1.509	0.146	2*e*-5*lh*
					1.533	0.14	3*e*-5*lh*
				1.551	1.543	0.105	5*e*-3*lh*
				1.59			
				1.625			
				1.413			
				1.429	1.438	0.191	1*e*-4*hh*
59*M*	35	1.8	1.413		1.438	0.627	1*e*-3*lh*
				1.463	1.473	0.165	2*e*-1*hh*
				1.525	1.529	0.313	2*e*-2*lh*
				1.546			
					1.563	0.209	3*e*-4*hh*
				1.629	1.616	0.101	3*e*-5*lh*
					1.621	0.018	3*e*-5*hh*
				1.413			
61*M*	6.5	0	1.413	1.479	1.48	0.307	1*e*-1*hh*
					1.507	0.35	1*e*-1*lh*
				1.413			
					1.465	1.469	0.173	1*e*-1*hh*
				1.486	1.488	0.316	1*e*-2*hh*
					1.498	0.386	1*e*-1*lh*
62*M*	13	0.5	1.413		1.528	0.534	1*e*-1*lh*
					1.531	0.154	2*e*-1*lh*
				1.604			
					1.473	0.41	1*e*-1*hh*
Surface GaAs layer	8	0	1.42	–	1.495	0.447	1*e*-1*lh*
					1.567	0.241	1*e*-2*lh*

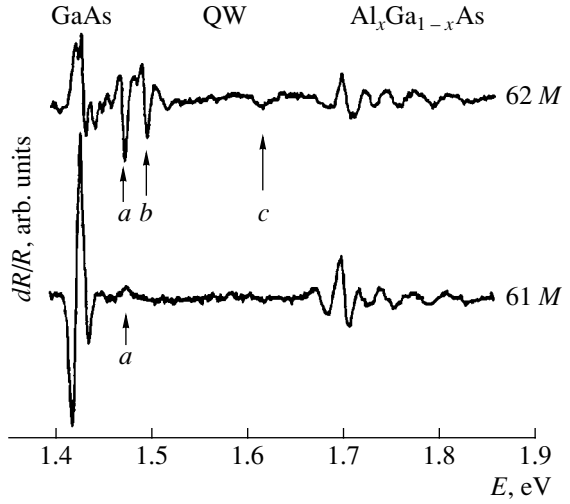

Fig. 1. Photoreflectance spectra of the samples with narrow QWs. Arrows *a–c* indicate the features related to the quantum-confinement levels in the wells.

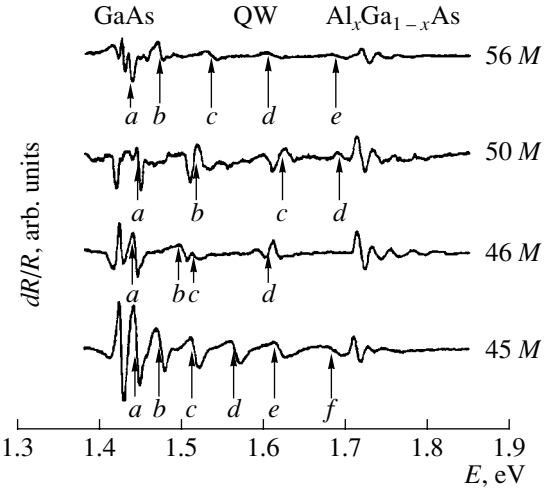

Fig. 2. Photoreflectance spectra of the samples with a 26-nm QW. Arrows *a–f* indicate the features related to the quantum-confinement levels in the wells.

8-nm-thick cap layer of GaAs was deposited. The growth temperature for the GaAs and AlAs layers was 600°C, and that for AlGaAs layers was 640°C. The ratio of the arsenic and gallium fluxes in the growth zone equaled 30. The thickness of AlGaAs barriers in all structures was 30 nm. The widths of the two QWs were equal to each other. The values of the AlAs barrier thickness and the total width of the QWs for all samples are listed in the table. For the purpose of comparison, some of the samples were grown without an AlAs barrier layer. Heterostructures were not intentionally doped during the growth process; according to our estimates, unintentional background doping was of donor type with a density of $\approx 5 \times 10^4$ cm^{-3}.

The PR spectra were recorded using an automated setup described elsewhere [12]. A He–Ne laser operating at 632.8 nm was used as a source of modulating radiation, with its power being 1 mW. The modulation frequency was 370 Hz. The width of the instrument response function of the spectrometer was less than 1 meV.

The PR spectra of the samples under study are shown in Figs. 1–3. To determine the energy position of the lines in these spectra, the shape of each of them was approximated by a formula corresponding to the low-field Aspnes model [13]:

$$\frac{dR_i}{R_i}(E) = \mathrm{Re}[Ae^{i\varphi}(E - E_i + i\Gamma)^{-m}]. \qquad (1)$$

Here, A and φ are the amplitude and the phase parameters, E is the energy of the probing radiation, E_i is the energy position of the spectral feature, and Γ is the broadening parameter. The index m is determined by the type of the critical point; we used $m = 2$ [13]. The energies of the optical transitions derived by this procedure are given in the table. The experimentally determined values of the band gap in the buffer GaAs layer are also presented.

3. CALCULATION OF THE QUANTUM TRANSITION ENERGIES AND DISCUSSION OF THE EXPERIMENTAL RESULTS

Since the structures were not intentionally doped, the space-charge region related to the surface potential is rather extended; for the donor density given above, its thickness is about 2 μm. Thus, the QWs are subjected to a uniform built-in electric field E_s. Assuming that the surface-barrier height is 0.7 V, we find that the field strength equals $\approx 4 \times 10^3$ V/cm. The band dia-

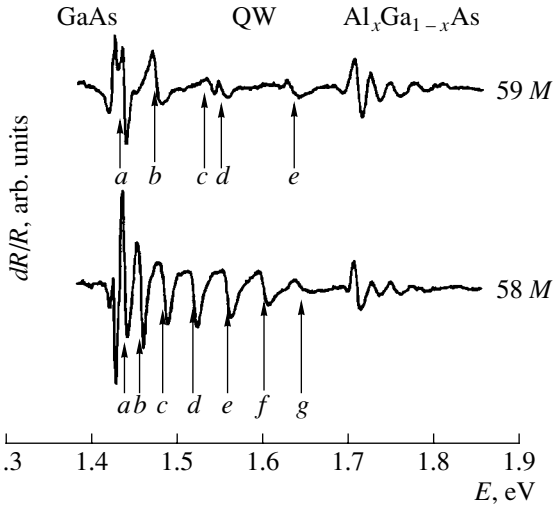

Fig. 3. Photoreflectance spectra of the samples with a 35-nm QW. Arrows *a–g* indicate the features related to the quantum-confinement levels in the wells.

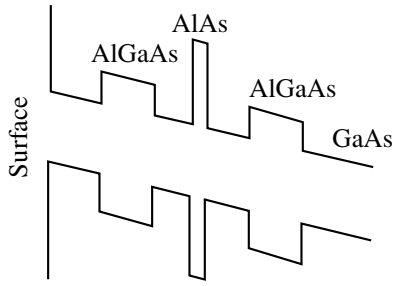

Fig. 4. The schematic energy-band diagram of the studied heterostructures with a built-in electric field.

gram of the heterostructure under these conditions is shown in Fig. 4.

The transition energies were calculated in the envelope-wave-function approximation by numerically solving the Schrödinger equation for the QWs:

$$\left(-\frac{\hbar^2}{2m}\frac{d^2}{dx^2} - qE_s x\right)\psi_n(x) = E_n\psi_n(x). \qquad (2)$$

Here, E_n are the energy eigenvalues and m is the charge-carrier effective mass for electrons (e), light holes (lh), and heavy holes (hh). Since the AlGaAs barriers are thick and their tunneling transparency is low, a Schrödinger equation for the case of semi-infinite barriers was considered. To obtain time-independent solutions to the Schrödinger equation, the built-in field E_s was assumed to be zero within the barriers. It was also assumed that the conduction-band offset at the heterointerface $\Delta E_c = 0.62\Delta E_g$. According to [14], we have $\Delta E_c = 0.19$ eV for $x = 0.22$. The calculated energies of the electron–hole transitions are listed in the table.

In addition, the table contains the values of the squared overlap integrals of the envelope wave functions:

$$M_{ij} = \int \psi_{ie}\psi_{jh}dx.$$

Note that the amplitude A in (1) is proportional to M_{ij}^2. For wide QWs (26 and 35 nm), only the transitions with $M_{ij}^2 > 0.1$ are included in the table. The results of the calculation for the QW formed by the surface cap layer are also presented. However, the actual size of this well exceeds the atomic thickness of the layer and is determined by the self-consistent potential at the surface. Thus, these results should be treated as approximate. It can be seen that the calculated transition energies are close to the experimentally determined ones. Thus, it may be assumed that they merge with QW optical transitions.

It follows from the energy-band diagram that a recorded spectrum represents a superposition of the PR signals from the bulk GaAs, the protective cap layer, the QW itself, and the triangular well for holes formed in the GaAs buffer next to the interface with the AlGaAs barrier. One can see from the table that good agreement between the calculated transition energies and those determined from the experiment exists for the structures with narrow QWs. It may be assumed that the absence of high-energy transitions (1.507–1.531 eV) in the experimental data is related to the small amplitude of the corresponding signals, which are difficult to isolate from noise.

For the structures with wide QWs, the situation is somewhat different. First, in the QWs without an inserted AlAs barrier, some of the electron–hole transitions merge with the band-to-band transitions in the GaAs buffer layer. Second, for all QWs, calculations indicate that the energy spacing within certain groups of electron–hole transitions is considerably smaller than the thermal energy kT (equal to 26 meV for the temperature at which the spectra were taken). Meanwhile, at equilibrium, the broadening parameter $\Gamma \approx kT$; note that, in general, each transition is characterized by its own value of Γ. Next, there is no equilibrium under the conditions of the PR measurements. For undoped GaAs, the equilibrium densities of electrons and holes are very low ($\approx 10^7$ cm^{-3}). Thus, irradiation of the sample leads to a considerable increase in the charge-carrier densities and to a significant deviation of the electron and hole distribution functions from equilibrium ones. Furthermore, nonequilibrium electrons and holes in the GaAs buffer layer drift in the built-in field. All these factors contribute (to differing extents) to an additional increase in Γ and a change in the conditions of absorption and reflection for each of the transitions in comparison with the equilibrium conditions. If the energy difference between the neighboring electron–hole transitions $\Delta E > \Gamma$, the number of spectral features in the PR curve coincides with the number of allowed optical transitions characterized by a sufficiently high M^2. In the case under study, this situation is realized for 6.5- and 13-nm-thick QWs. In wide QWs, (26 and 35 nm) $\Delta E < \Gamma$. Then, the number of lines observed in the PR spectra is always smaller than the number of electron–hole transitions and depends on the amplitude and phase relationships (1). Apparently, closely spaced transitions ($\Delta E < \Gamma$) will appear in the PR spectrum as a single line, whose position corresponds to the average energy of these transitions. Evidently, this occurs in the case of the optical transitions experimentally observed at 1.437 eV (sample 45*M*), 1.442 eV (sample 50*M*), and 1.425 and 1.473 eV (sample 58*M*).

If $\Delta E \sim \Gamma$, the number of spectral lines will correspond to the number of allowed electron–hole transitions. It may be surmised that this is the case for the electron–hole transitions calculated at 1.46 and 1.482 eV (sample 46*M*), 1.593 eV (sample 50*M*), and 1.579 and 1.586 eV (sample 56*M*). It should be noted that, for certain relationships between parameters, the amplitude of the PR signal can be lower than the noise level and, thus, the energy of the optical transition cannot be determined. Apparently, this occurs for the transitions

calculated at 1.53–1.532 eV (sample 50*M*) and 1.54 and 1.541 eV (sample 46*M*).

The experimental spectra of samples 45*M*, 46*M*, 50*M*, and 62*M* have a feature in the region of 1.6–1.611 eV which corresponds to $E_g + \Delta E_c$; thus, this feature is most probably related to transitions between the electron levels in the continuous spectrum and the first level of heavy holes (1*hh*) in the QW.

One can see from Figs. 1 and 2 and from the table that the shape of the spectra and the energy of the transitions change considerably as the QW width *W* increases from 6.5 to 26 nm. With a further increase in *W*, the transition energies vary insignificantly. For wide QWs, the insertion of an AlAs barrier and variation in its thickness L_b also have little influence on the transition energies; at the same time, it leads to a marked decrease in the magnitude of the features in the spectrum of $\Delta R/R$ (Figs. 2, 3). We believe that this behavior is related to the presence of a built-in field in the structure, which, in the case of wide QWs, results in the formation of triangular wells for electrons and holes. The position of the second boundary in such wells is determined by the shape of the self-consistent potential. Thus, the energy spectrum does not change considerably upon introduction of a barrier in the region where the potential energy exceeds the level energy. At the same time, these factors have a profound effect on the values of the overlap integrals between the electron and hole wave functions. In narrow QWs, the effect of a built-in field is minimal and the transition energies are mainly governed by the well width. Therefore, the use of wide QWs to control the reflection or absorption spectra by varying the surface electric field in devices like optical modulators or photodetectors is not effective.

4. CONCLUSION

To summarize, AlGaAs/GaAs/AlGaAs epitaxial structures with QWs of different thicknesses were studied by photoreflectance spectroscopy. It was shown that the spectrum of narrow QWs can be changed effectively by the insertion of a thin AlAs barrier in the center of the well; the desired optical transition energies can be obtained by varying the barrier thickness. For these structures, there is a one-to-one correspondence between the calculated energies of the optical transitions and the spectral position of the PR features. For wide QWs, the effect of the insertion of an AlAs barrier is much less pronounced. In this case, the lines observed in the PR spectra result from a superposition of the features originating from several closely spaced electron–hole transitions, with the spectral position of the lines being determined both by the QW configuration and the transition broadening parameters.

ACKNOWLEDGMENT

This study was supported by the Ministry of Industry, Science, and Technology of the Russian Federation within the program “Physics of Solid-State Nanostructures”.

REFERENCES

1. W. Trzeciakowski and B. D. McCombe, Appl. Phys. Lett. **55**, 891 (1989).
2. A. Lorke, U. Merkt, F. Malcher, *et al.*, Phys. Rev. B **42**, 1321 (1990).
3. J. Pozela, V. Jucene, and K. Pozela, Semicond. Sci. Technol. **10**, 1076 (1995).
4. J. Požela, K. Požela, and V. Juciene, Fiz. Tekh. Poluprovodn. (St. Petersburg) **34**, 1053 (2000) [Semiconductors **34**, 1011 (2000)].
5. A. Chiari, M. Colocci, F. Fermi, *et al.*, Phys. Status Solidi B **147**, 421 (1988).
6. S. K. Brierley, J. Appl. Phys. **74**, 2760 (1993).
7. A. V. Guk, V. É. Kaminskiĭ, V. G. Mokerov, *et al.*, Fiz. Tekh. Poluprovodn. (St. Petersburg) **31**, 1367 (1997) [Semiconductors **31**, 1178 (1997)].
8. Yu. V. Gulyaev, V. G. Mokerov, V. E. Kaminskii, *et al.*, Photon. Electron. **4**, 1 (1997).
9. Y. Hirayama, W.-Y. Choi, L. H. Peng, and C. G. Fonstad, J. Appl. Phys. **74**, 570 (1993).
10. H. Qiang, F. H. Pollak, Y.-S. Huang, *et al.*, Proc. SPIE **2139**, 11 (1994).
11. P. J. Hughes, B. L. Weiss, and T. J. S. Hosea, J. Appl. Phys. **77**, 6472 (1995).
12. L. P. Avakyants, V. S. Gorelik, A. V. Chervyakov, *et al.*, Kratk. Soobshch. Fiz., No. 2, 17 (1999).
13. D. E. Aspnes, Surf. Sci. **37**, 418 (1973).
14. L. Pavesi and M. Gizzi, J. Appl. Phys. **75**, 4779 (1994).

Translated by M. Skorikov

Semiconductors, Vol. 37, No. 1, 2003, pp. 82–91. Translated from Fizika i Tekhnika Poluprovodnikov, Vol. 37, No. 1, 2003, pp. 83–92.

AMORPHOUS, VITREOUS, AND POROUS SEMICONDUCTORS

Influence of Charged Defects on Detection of Electron Spin Resonance in Vitreous Chalcogenide Semiconductors

L. P. Ginzburg

Moscow Technical University of Communications and Information Science, Moscow, 111024 Russia

Submitted March 12, 2002; accepted for publication June 10, 2002

Abstract—A relationship between the concentrations of induced spins and native U^- centers is established on the basis of taking electronic processes accompanying band-to-band excitation into account. © *2003 MAIK "Nauka/Interperiodica".*

1. INTRODUCTION

Chalcogenide vitreous semiconductors (ChGS), such as *a*-Se, *a*-As_2Se_3, *a*-As_2S_3, *a*-GeSe, etc., have been attracting the attention of researchers for more than 30 years. This is not surprising since ChGS possess a number of very unusual and contradictory properties which can hardly be explained from a common standpoint. In particular, this has to do with effects accompanying photoexcitation. We will leave aside the whole set of relevant problems, since various aspects of these have been considered in numerous reviews (see, e.g., [1, 2] and references therein).

In this paper, we will concern ourselves with phenomena associated with photoexcitation of moderate intensity (~1 mW/cm^2) and limited duration ($\lesssim$10 min), i.e., effects commonly related to native defects. Such defects are charged centers with a negative effective correlation energy (U^- centers) [3–5]. In what follows, for these centers we will use commonly accepted designations: C_n^α (in the case of S, Se), P_n^α (in the case of As), and T_n^α (for Ge), where the symbol $\alpha = 0, +, -$ denotes the charge state, and the symbol $n = 1, 2, 3, \ldots$ the coordination.

Under the above conditions, the main effects induced by transitions of the band-to-band type (or nearly so) are the following [6–8]:

(1) photoluminescence (PL) with a large Stokes shift (~$E_g/2$, where E_g is the band gap);

(2) PL fatigue with a characteristic transient period of $\lesssim$10 min;

(3) electron spin resonance (ESR) signal not observed without irradiation;

(4) intragap absorption appearing together with the ESR signal.

Comparison of the kinetics for attaining a stationary mode by the above effects clearly indicates that defects of the same kind are involved in all cases. ESR experiments yielded the following spin concentrations [6, 7]:

$$N_s(a\text{-Se}) \approx 10^{16}\ \text{cm}^{-3},$$

$$N_s(a\text{-As}_2\text{Se}_3) \approx N_s(a\text{-As}_2\text{S}_3) \approx 10^{17}\ \text{cm}^{-3}, \quad (1)$$

$$N_s(a\text{-GeSe}_2) \approx 5 \times 10^{15}\ \text{cm}^{-3}.$$

In the case of *a*-As_2S_3 and *a*-As_2Se_3, these estimates of N_s correlate well with the defect concentration found from PL measurements: 10^{17}–10^{18} cm^{-3} [8]. Therefore, it is frequently assumed that $N_s \approx N_v$, where N_v is the concentration of U^- centers.

However, here we have a contradiction. First, the PL data are rather approximate, having been obtained without exact knowledge of the quantum efficiency [8]. Second, almost simultaneously with reports of PL data in [3, 4], an estimate of $N_v \approx 10^{18}$–10^{19} cm^{-3} was proposed which is different from (1).

The latter is possibly due to the following. There is reason to believe that, not only in *a*-Se, but in *a*-As_2S_3 and *a*-As_2Se_3 as well, U^- centers are C_3^+ and C_1^- defects [9]. Under these conditions, the concentration can be calculated by the formula

$$N_v = N_0 \exp(-U_c/2k_0T_g), \quad (2)$$

where N_0 is the concentration of chalcogen atoms, T_g is the glass transition point, U_c is the effective energy of Coulomb repulsion associated with the addition of an extra electron to a nonbonding level, and k_0 is the Boltzmann constant. The U_c value is unknown, with widely varying estimates found in the literature: from 0.2–0.4 [2] to 0.5–1.0 eV [5]. If we choose an intermediate value of, say, 0.5 eV, we obtain, using the known N_0 and T_g, from (2)

$$N_v(a\text{-Se}) = 2.6 \times 10^{18}\ \text{cm}^{-3},$$

$$N_v(a\text{-As}_2\text{Se}_3) = 4.2 \times 10^{19}\ \text{cm}^{-3},$$

$$N_v(a\text{-}As_2S_3) = 5.5\times10^{19}\ \text{cm}^{-3},$$

$$N_v = (a\text{-}GeSe_2) = 5.9\times10^{20}\ \text{cm}^{-3}.$$

It follows from the values presented that, raising U_c somewhat, we can achieve agreement with the data from [3, 4], but this can in no way be done for (1). Finally, attention is drawn to the fact that, according to ac conductivity data for a-As_2S_3 [10], the concentration of randomly distributed charged centers must be $\sim 2.0\times 10^{18}$ cm^{-3}. The last value is also in agreement with [3, 4] and markedly exceeds the data of [6, 7] in (1).

To better clarify the problem concerning the concentration of U^- centers, we used an alternative method to evaluate N_v, which is based on the fact that the low-frequency tail of the PL spectrum is due to the absolutely hard Coulomb gap (AHCG) formed by charged centers [11, 12]. In this case, N_v can be evaluated using the relation [13]

$$N_v \approx \left[\frac{\kappa(\hbar\omega_m - \hbar\omega_0)}{1.36e_0^2}\right]^3, \qquad (3)$$

where κ is the dielectric constant, e_0 is the elementary charge, and the difference of photon energies $(\hbar\omega_m - \hbar\omega_0)$ is the gap width. The reliability of (3) depends on two factors. First, the above-mentioned tail should be measured rather accurately in order to determine the photon energy $\hbar\omega_0$ corresponding to the onset of the PL spectrum, i.e., the point at which the intensity starts to rise from zero. Moreover, the conditions for the existence of the AHCG must be satisfied [11, 12]. When this is the case, we can take as $\hbar\omega_m$ the point at which the function

$$\eta(\hbar\omega) = \frac{d(I/\hbar\omega)^2}{d(\hbar\omega)}$$

(I is emission intensity) ceases to be linear [11]. For these reasons, we chose, for the application of (3), the data from [14, 15], where the $\hbar\omega_0$ point was indicated for a-As_2S_3 and a-As_2Se_3. A thorough analysis of these data using the least-squares method confirmed that all indications for the existence of AHCG are present. For dielectric constants $\kappa(a\text{-}As_2Se_3) = 7.6$ [16] and $\kappa(a\text{-}As_2S_3) = 6.4$ [17], it follows from (3) that

$$N_v(a\text{-}As_2Se_3) \approx 2.4\times10^{18}\ \text{cm}^{-3},$$
$$N_v(a\text{-}As_2S_3) \approx 2.5\times10^{18}\ \text{cm}^{-3}. \qquad (4)$$

These values are in good agreement with [3, 4, 10]. Unfortunately, we failed to find any experimental data that could enable the application of (3) to the case of a-Se. For a-$GeSe_2$, there are also no experiments that can give the value of $\hbar\omega_0$. Of some help in this sense is communication [18], which, although containing no exact evidence about $\hbar\omega_0$, presents a PL curve that closely approaches zero. Therefore, an approximation is possible that gives an estimate of $\hbar\omega_0 = 0.600$–0.622 eV. Processing of the data from [18] also confirms the presence of AHCG. It follows from (3) that

$$N_v(a\text{-}GeSe_2) \approx (1.4 - 5.3)\times10^{18}\ \text{cm}^{-3}. \qquad (5)$$

It is noteworthy that the value obtained is close to the estimate presented in [19]: $N_v(GeSe_2) \approx 5.0\times10^{18}$ cm^{-3}.

Thus, formula (3), applied with all the necessary conditions carefully verified, yields N_v given by (4) and (5). These values, which are in agreement with other indirect estimates, show that the N_s values obtained from ESR data are underestimated, compared with N_v, by an order of magnitude in the case of a-As_2S_3 and a-As_2Se_3 and by 3 (!) orders of magnitude in the case of a-$GeSe_2$.

The aim of this study is to ascertain a possible mechanism by which the N_s values obtained in [6, 7] differ from N_v. This mechanism is based on a certain model of electronic processes that must accompany photoexcitation of the band-to-band type. The model used in this study is not new and can be regarded as a refinement of the known models [3, 4, 8] used to interpret the effects described above. However, the refinement of the models allows for an important conclusion: under the established conditions, each generated paramagnetic center is surrounded by randomly arranged charged defects.

This paper is organized as follows. The model is considered in Section 2. The theory concerned with the influence exerted by charged atoms on ESR detection is developed in Section 3. The basic conclusion of the theory is that a relationship exists between the experimentally recorded spin concentration (N_s) and the N_v value. Section 4 compares the theoretical results with experiment.

2. ELECTRONIC PROCESSES ACCOMPANYING PHOTOEXCITATION

In terms of the model [3, 4], the basic scheme of processes accompanying band-to-band excitation is as follows. A generated electron and hole are captured, respectively, by the antibonding level C_3^+, converting it into C_3^0, and by the nonbonding level, making it C_1^-. The last level is responsible for the observed ESR [6, 7]. In principle, PL related to a reverse radiative transition is also possible:

$$C_3^0 + C_1^0 \longrightarrow C_3^+ + C_1^- + \hbar\omega. \qquad (6)$$

However, if the initial centers are not closely spaced and do not form a so-called "intimate" valence alternation pair (IVAP), the probability of instantaneous recombination is low [20, 21]. Because of the influence exerted by the lattice, an electron moves away from the C_3^0 center and becomes involved in thermalization via hopping. According to computer simulation in [21], only ~39% of electrons are involved in geminate recombination. The aforesaid means that ESR is

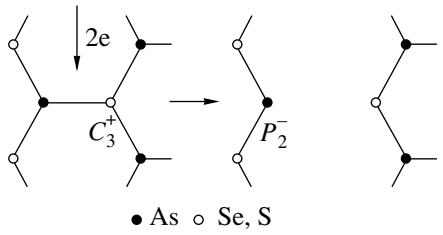

Fig. 1. Scheme of P_2^- center formation.

accounted for by ~61% of the C_1^0 centers created by irradiation.

It is noteworthy that the mechanism described is in rather good agreement both with the AHCG model responsible for the PL spectrum tail [12] and with the large Stokes shift. This shift is not necessarily related to abnormally strong polaronic deformation, which can be ascertained if we assume that the density of states, via which the electron moves, near the conduction band edge (E_0) decreases rapidly in the depth of the gap as, e.g., $g(E) = g_0\exp[-(E_0 - E)/\zeta]$ and assume that $\zeta \sim 0.1$ eV. It was shown in [20] that the electron energy decreases under these conditions by ~0.7 eV even after 10^{-9} s.

One question remains unanswered by the model presented above. What happens with that excited electron which is not involved in luminescence and moves a great distance away from its own hole? To the author's knowledge, this problem has not been analyzed in detail. Meanwhile, in my opinion, it is of key importance both for explaining (e.g., intragap absorption) and interpreting the results reported below.

It is clear that the electron must be localized somewhere, and, leaving behind a C_3^+ center, it must form a negatively charged nonparamagnetic state. In this respect, the situations in *a*-Se, on the one hand, and *a*-As_2S_3, *a*-As_2Se_3, and *a*-$GeSe_2$, on the other, differ significantly. In the first case, in accordance with the exothermic process

$$2C_3^0 \longrightarrow C_3^+ + C_1^-, \tag{7}$$

two "wandering" electrons, finding themselves at a C_3^+ center, must, having ruptured one bond, convert it into C_1^- and C_2^0 centers. In the cases of *a*-As_2S_3 and *a*-As_2Se_3, the situation is more complicated. If we disregard defects with improper bonds, then, as shown in [9], a process of the type shown in Fig. 1 is preferable. Here, the appearance of two electrons near the C_3^+ center results in the rupture of one bond, with one electron creating a normal center C_2^0 and the second giving rise to a P_2^- center owing to the appearance of a nonbonding orbital at the As atom. If we disregard the electron getting stuck at the interstice, then the scheme in Fig. 1 seems to be the only one possible under geminate recombination conditions. At the same time, this scheme is dubious, and the probability of formation of P_2^- centers may prove to be small. This statement follows from the results of [22], where it was shown that, because of the difference in electronegativity between As and Se (S), the nonbonding orbital of As must lie near the conduction band. Therefore, if the Fermi level does not lie far from the middle of the mobility gap, it is expected that a P_2^+ center will appear instead of P_2^-. Moreover, the energy U_c associated with the appearance of a second electron on the nonbonding orbital must be much higher in the case of As, compared with that for Se and S [22].

We believe that the above contradiction is resolved by communications [23, 24] (especially the latter). Indeed, wherever the electron is localized, it must induce a particular lattice deformation. As shown in [23, 24], this is sufficient for hybridization of states belonging to a dangling bond and to the nearest conduction band. This hybridization results in the defect level being markedly shifted, when occupied by electrons, deeper into the mobility gap. For example, if we assume that the P_2^+ level lies near the conduction band bottom (whose energy is taken as zero), then, according to [23, 24], for the energies of different P_n^α states we have

$$\begin{gathered} E(P_2^+) = 0, \quad E(P_2^0) = -\Delta W/2, \\ E(P_2^-) = U_c - \Delta W, \end{gathered} \tag{8}$$

where the positive ΔW value is determined by the degree of hybridization. It can be seen from (8) that

$$U^- = E(P_2^-) + E(P_2^+) - 2E(P_2^0) = U_c - \Delta W. \tag{9}$$

Moreover, it follows from a comparison of (8) and (9) that

$$E(P_2^-) = U^- - \Delta W. \tag{10}$$

The data presented in [23, 24] indicate that, even under moderate deformation, the value of ΔW can ensure that the condition $U^- < 0$ is satisfied. It follows from (10) that, irrespective of the value of U_c, the $E(P_2^-)$ level may descend deep into the band gap. (It is noteworthy that such a level can be used to interpret intragap absorption.)

Thus, the above model of processes occurring in *a*-As_2S_3 and *a*-As_2Se_3 under band-to-band excitation yields the following pattern. A certain portion of defects are involved in PL according to scheme (6). Under geminate recombination conditions, the concentration of such defects is $\sim 0.39N_v$. The remaining

defects decompose into C_1^0 centers responsible for ESR (concentration $\sim 0.61N_v$) and charged C_3^+ and P_2^- defects, each with a concentration of $\sim 0.305N_v$. Thus, the concentrations of the forming charged defects are as follows:

$$N(C_3^+) = 0.695N_v, \quad N(C_1^-) = 0.39N_v, \quad N(P_2^-) = 0.305N_v. \tag{11}$$

In the case of *a*-$GeSe_2$, the situation should, on the whole, be similar to that described above. However, an essential difference consists in that T_3^- centers should appear instead of P_2^- centers [9]. The T_3^- centers form a more rigid structure, and the effect of level lowering may be weakened. Under these conditions, the probability of interpair recombination may increase markedly at the expense of T_3^- center formation. Therefore, a weakening of PL fatigue would be expected. In view of the aforesaid, let us consider Fig. 7 in [7], showing how a percentage decrease in the PL intensity depends on time (t) for *a*-As_2Se_3 and *a*-$GeSe_2$. In interpreting the figure, let us take into account the fact that the quantity presented in it corresponds to the dependence $[I(0) - I(t)]/I(0)$, where $I(t)$ is the PL intensity. At $t = 0$, when the process has just begun, $I(0) \propto N_v$ [the concentration of C_3^+ and C_1^- centers appearing through conversion (6) is virtually zero]. In the steady state, $I(\infty) \propto \gamma N_v$, where γ is the fraction of recombining centers. Therefore,

$$[I(0) - I(\infty)]/I(0) \approx 1 - \gamma. \tag{12}$$

As already noted, according to [21], $\gamma \approx 0.39$ under the conditions of geminate recombination. This corresponds exactly to Fig. 7 of [7] for *a*-As_2Se_3. It can be readily verified that, in this case, $1 - \gamma = 0.61$ under conditions of saturation. In the case of *a*-$GeSe_2$, the corresponding value is much smaller: $1 - \gamma = 0.09$. This indirectly confirms the assumption about the contribution from interpair recombination.

Thus, with the following concentrations of charged defects, the concentration of C_1^0 must be $0.09N_v$ in the case of $GeSe_2$:

$$N(C_3^+) = 0.955N_v, \quad N(C_1^-) = 0.91N_v, \quad N(T_3^-) = 0.045N_v. \tag{13}$$

Finally, in the case of *a*-Se, according to (7) we have

$$N(C_3^+) = N(C_1^-) = 0.695N_v. \tag{14}$$

3. INFLUENCE OF CHARGED DEFECTS ON THE DETECTION OF ESR

It follows from the aforesaid that, in the steady state, each paramagnetic center C_1^0 must be surrounded by numerous randomly distributed positive and negative defects. According to the Holtsmark theorem [25], the uncompensated charge of a paramagnetic atom must, in the first place, sense the field of a nearest neighbor of each type (which is oscillating, rather than being immobile). Therefore, we have a certain kind of the known quantum problem of interaction between an atomic electron and a moving charged particle [26]. In this case, an additional term must appear in the Hamiltonian of the electron

$$H_c(t) = \pm\frac{e_0^2}{\kappa|\mathbf{R}(t) - \mathbf{r}|} \approx \pm\frac{e_0^2}{\kappa R(t)}. \tag{15}$$

It is assumed that the origin of coordinates lies at a paramagnetic center, $\mathbf{R}(t)$ is the time-dependent coordinate of the charged defect, and $\mathbf{r}$ is the coordinate of the spin carrier. Here, we take into account the fact that $R(t) \gg r$ under equilibrium conditions and use an assumption according to which characteristic changes in $R(t)$ (δR), related to variation in the position of the charged defect, are not beyond the condition

$$\delta R/R(t) \ll 1. \tag{16}$$

In what follows, we ascertain that (16) is satisfied with a large safety margin.

Since the phases of oscillation of separate charged atoms are uncorrelated, distance as a function of time, $R(t)$, should be considered random. Here, two situations should be distinguished with respect to the possible influence on ESR. If the characteristic time of $R(t)$ variation (δt) satisfies the condition $\delta t \gg \omega_1^{-1}$, where ω_1 is the frequency of a resonance transition, $\omega_1 \sim 10^{10}$ s^{-1} [6]. At the same time, we have $\delta t \sim \omega^{-1}$, where ω is the phonon frequency ($\omega \gtrsim 10^{13}$ s^{-1}). Thus, we have $\delta t \ll \omega_1^{-1}$ in the case in question. This means that, during the time of transition, the additional term (15) changes its value randomly and repeatedly. This fact must be reflected in the Hamiltonian, which becomes explicitly time dependent:

$$H(t) = H_0 + \frac{g\beta B}{\hbar}\hat{s}_z + H_c(t). \tag{17}$$

Here, H_0 is the Hamiltonian in the absence of a magnetic field (B) and a randomly varying electric field [i.e., $H_s(t)$], $\hat{s}_z$ is the electron spin operator, and β is the Bohr magneton

$$\beta = \frac{e_0\hbar}{2m_0} = 5.795 \times 10^{-5} \text{ eV/T}. \tag{18}$$

Henceforth, the g-factor appearing in (17) is considered to be equal to 2.

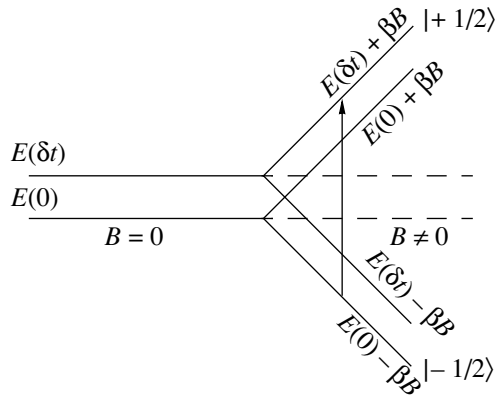

Fig. 2. Model of resonance transition under conditions of a weak shift of levels.

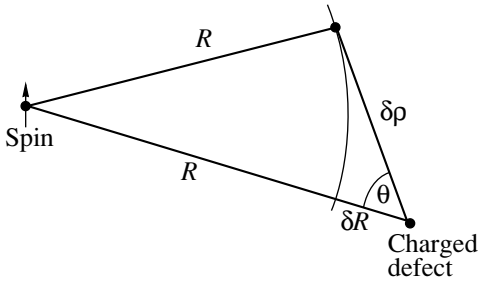

Fig. 3. Model of random variation of the distance between the spin and the charged defect.

It is shown in the Appendix that, under the given conditions, a microwave photon is absorbed with the energy determined by

$$\hbar\omega_1 = 2\beta B + [E(\delta t) - E(0)], \quad (19)$$

which is illustrated in Fig. 2. Since $E(\delta t)$ is a random quantity, the resonance is "smeared" when the characteristic scatter of the difference $E(\delta t) - E(0)$ (δE) exceeds the Zeeman splitting $2\beta B$. Therefore, the ESR signal observed can only be accounted for by centers for which the following inequality holds:

$$\delta E < 2\beta B. \quad (20)$$

According to (15) and (16), this means that the distance from the center to any charged defect of the ith type ($i = C_3^+, C_1^-, P_2^-, T_3^-$) must satisfy

$$R(t) > R_0(i) \approx \left(\frac{e_0^2}{\kappa}\frac{\delta R_i}{2\beta B}\right)^{1/2}. \quad (21)$$

Let us assume that the charged atom is shifted to a certain distance $\delta\rho(i)$. Then, its distance from the spin carrier will be incremented by δR_i, satisfying the condition (see Fig. 3)

$$\delta R_i \approx \delta\rho(i)\cos\theta. \quad (22)$$

Averaging δR_i^2 over all possible angles θ in a plane that is always formed by the centers in Fig. 3, we ascertain that

$$(\langle\delta R_i^2\rangle)^{1/2} = 0.707\delta\rho(i). \quad (23)$$

Using (23) as an estimate of δR_i in (21), we have

$$R(t) > R_0(t) \approx \left(\frac{e_0^2}{\kappa}\frac{0.707\delta\rho(i)}{2\beta B}\right)^{1/2}. \quad (24)$$

In the general case, for a characteristic value of $\delta\rho(i)$ [26] we can write

$$\delta\rho(i) = \left[\frac{\hbar}{m\omega_i}\left(n + \frac{1}{2}\right)\right]^{1/2}, \quad (25)$$

where m is the mass of an oscillating atom, ω_i is frequency, and

$$n = \left(\exp\frac{\hbar\omega_i}{k_0 T} - 1\right)^{-1}. \quad (26)$$

According to Poisson's distribution, the probability that condition (24) will be satisfied for the distance from the paramagnetic center to the ith defect is given by

$$\mathrm{Prob}[R(t) > R_0(t)] = \exp\left\{-\left[\frac{4\pi}{3}R_0(i)\right]^3 N(i)\right\}, \quad (27)$$

where $N(i)$ is the concentration of defects of the ith type.

If we assume that there is no correlation in the positions of defects (including those oppositely charged), then, based on (27), we can evaluate the recorded spin concentration from the relation

$$N_s = (1-\gamma)N_v\prod_i \exp\left\{-\left[\frac{4\pi}{3}R_0(i)\right]^3 N(i)\right\}. \quad (28)$$

4. COMPARISON WITH EXPERIMENT

It follows from (24) and (25) that, in order to compare (28) with the experiment, we must know the frequencies ω_i. To the author's knowledge, direct measurements of the vibration frequencies of the defects C_3^+, C_1^-, P_2^-, and T_3^+ have not been carried out for the semiconductors being considered here. Therefore, it is necessary to proceed from a number of general considerations that will allow evaluation of $R_0(i)$.

First, let us take into account the fact that all of the defects considered can be related to three types of molecular formations:

$$XY_3(C_3^+, T_3^-), \quad XY_2(P_2^-), \quad Y_1(C_1^-).$$

According to [19], each of these molecules is characterized by a certain set of orthogonal vibrations deter-

mined by the type of deformation. For example, we have, in the case of XY_3, bending vibrations with a frequency $\omega_{b3}(i)$ and stretching vibrations with a frequency $\omega_{s3}(i)$. If we take into account the fact that, under the conditions in question, $\omega(i) \gtrsim 10^{13}$ s^{-1} (see below) and that ESR experiments have been carried out at $T = 4.2$ K [6, 7], then, according to (26), we can neglect (here and in what follows) n in (25). Correspondingly, we have

$$\delta\rho(i) = [\delta\rho_{b3}^2(i) + \delta\rho_{s3}^2(i)]^{1/2} = \left[\frac{\hbar}{2m_X(i)}\right]^{1/2}\left[\frac{1}{\omega_{b3}(i)} + \frac{1}{\omega_{s3}(i)}\right]^{1/2}. \quad (29)$$

In the case of XY_2, we should also add to the vibrations mentioned above a rocking vibration with frequency $\omega_{r2}(i)$ [27]. Therefore, we have

$$\delta\rho(i) = \left[\frac{\hbar}{2m_X(i)}\right]^{1/2}\left[\frac{1}{\omega_{b2}(i)} + \frac{1}{\omega_{s2}(i)} + \frac{1}{\omega_{r2}(i)}\right]^{1/2}. \quad (30)$$

Finally, in the case of C_1^-, we have [19]

$$\delta\rho(i) = \left(\frac{\hbar}{2m_X(i)\omega_{s1}(i)}\right)^{1/2}. \quad (31)$$

If it were possible to regard all the defects as free molecules, then we could use the formulas presented in [28] to determine the frequencies appearing in (29) and (30):

$$\omega_{b3}^2 = \frac{3k_r}{m_X}\left[\frac{m_X}{3m_Y} + \cos^2\beta + \left(\frac{m_X}{3m_Y} + \sin^2\beta\right)\frac{12\cos^2\beta}{1 + 3\cos^2\beta}\nu\right], \quad (32)$$

$$\omega_{s3}^2 = \frac{3k_r}{2m_X}\left\{\frac{2m_X}{3m_Y} + \sin^2\beta + \frac{3[(2m_X/2m_Y)(1 + \cos^2\beta) + \sin^2\beta]}{1 + 3\cos^2\beta}\right\}, \quad (33)$$

$$\omega_{b2}^2 = \frac{2k_r}{m_X}\left[\frac{m_X}{2m_Y} + \cos^2\alpha + 2\left(\frac{m_X}{2m_Y} + \sin^2\alpha\right)\nu\right], \quad (34)$$

$$\omega_{s2}^2 = \frac{2k_r}{m_X}\left(\frac{m_X}{2m_Y} + \sin^2\alpha\right). \quad (35)$$

In the same approximation for C_1^-, it seems natural to use a reduced mass:

$$\omega_{s1}^2 = \frac{k_r}{m_X}\left(\frac{m_X}{m_Y} + 1\right). \quad (36)$$

In relations (32)–(36), k_r is the force constant for the X–Y bond; $\nu = k_\theta/k_r$, where k_θ is the force constant for displacements perpendicular to X–Y; β is the angle between an X–Y bond and the axis of symmetry of the molecule; and 2α is the angle at the point X between two X–Y bonds.

The use of formulas (32)–(36) presents the following problems. First, it is necessary to determine k_r and ν. Second, it is necessary to evaluate the angles β and α. Further, account should be taken of the fact that, in the case in question, the X atoms are charged.

It is also necessary to determine to what extent the free-molecule (FM) approximation is applicable. It is absolutely clear that, in the case in question, the Y atoms are bound and it is not improbable that the approximation of immobile Y atoms (IYA), considered in [19], is more precise. In this case, we must set $m_Y = \infty$ in (32)–(36).

Finally, the question of frequency ω_{r2} remains open.

The problem of the coefficients k_r and ν is resolved relatively easily. For the cases of *a*-As_2S_3, *a*-As_2Se_3, and *a*-$GeSe_2$, values of k_r were reported in [29]. The data presented in [29] can also be used to evaluate ν for P_2^- and T_3^-. For C_3^+ we took the value $\nu = 0.01$ [30]. Finally, the value of k_r for *a*-Se was found by the Gordy method [31].

The angles β and α were found as follows. In [32], attention was drawn to the fact that $\beta = 60°$ is a good approximation for many structures of the XY_3 type with different relative masses of X and Y atoms. We adopted this condition for C_3^+ and T_3^-. For the α angle, which is important for the P_2^- state, account was taken of the fact that chalcogen atoms (S, Se) are bonded to one another in As_2S_3 and As_2Se_3 lattices. Therefore, removing a single Y atom from the XY_3 structure (see Fig. 1) must not markedly affect the positions of the other two chalcogens. In this case, assuming that the covalent nature of the X–Y bond is invariable and proceeding from the condition [19, 28]

$$\sin\alpha = \frac{\sqrt{3}}{2}\sin\beta, \quad (37)$$

for $\beta = 60°$, we obtain $\alpha = 48.6°$.

The fact that the X atoms are charged may affect the following two factors. First, the equilibrium position is shifted [23, 24]. Second (and especially important for determining the frequencies), this reflects upon the force constants. Using the empirical formulas reported in [31] (and fitted to the k_r values presented in [29]), we analyzed in detail the influence exerted by charges on $\delta\rho(i)$. This effect is exceedingly weak and can affect N_s only to a second order of smallness. The main reason for this is that opposite charges affect k_r in different

Table 1. $\sigma\rho(i)$ values in accordance with (29)–(31)

IYA approximation				
Substance	$\delta\rho(C_3^+)$, 10^{-10} cm	$\delta\rho(C_1^-)$, 10^{-10} cm	$\delta\rho(P_2^-)$, 10^{-10} cm	$\delta\rho(T_3^-)$, 10^{-10} cm
a-As_2S_3	6.322	4.393	6.643	–
a-As_2Se_3	5.327	3.701	6.790	–
a-$GeSe_2$	5.226	3.632	–	5.079
a-Se	4.592	3.191	–	–
FM approximation				
Substance	$\delta\rho(C_3^+)$, 10^{-10} cm	$\delta\rho(C_1^-)$, 10^{-10} cm	$\delta\rho(P_2^-)$, 10^{-10} cm	$\delta\rho(T_3^-)$, 10^{-10} cm
a-As_2S_3	5.743	3.994	5.837	–
a-As_2Se_3	4.389	3.009	5.653	–
a-$GeSe_2$	4.285	3.104	–	4.481
a-Se	3.810	2.263	–	–

directions. In our case, the number of negative and positive defects is approximately the same.

The most difficult problem in determining $\delta\rho(i)$ is how to choose between FM and IYA approximations. As already mentioned, the IYA approximation was used in [19]. This approach was based on the fact that [19] was concerned with *v*-SiO_2, in which each Y (Si) atom in the C_3^+ structure, in addition to being bonded to an X (O^+) atom, has triple coordination, not to mention the fact that the mass of Si is nearly twice that of O. In our case, such a situation may only refer to C_3^+ defects in *a*-$GeSe_2$. In all other cases, drawing a conclusion in favor of one of the approximations considered is difficult. Therefore, both variants were considered here. Apparently, the correct value of N_s must lie between N_s for the FM approximation and that for the IYA approximation.

The final question concerning the frequency ω_{r2} was answered as follows. According to [27], the oscillation frequency of the bridging atom, i.e., O, S, and Se in, respectively, As_2O_3, As_2S_3, and $GeSe_2$, follows, with good precision, the dependence

$$\frac{\omega_{r2}(j)}{\omega_{r2}(i)} = \left(\frac{m_i}{m_j}\right)^{1/2}, \tag{38}$$

where m_i and m_j are the masses of the above-mentioned atoms. For *a*-As_2S_3 and *a*-As_2Se_3, As acts as the bridging atom in the P_2^- state (Fig. 1). Therefore, in accordance with (38), the frequencies $\omega_{r2}(P_2^-)$ were determined as

$$\omega_{r2}(P_2^-, As_2S_3) = \omega_{r2}(As_2S_3)\sqrt{\frac{m_S}{m_{As}}} = 1.97\times10^{13}\ s^{-1},$$
$$\omega_{r2}(P_2^-, As_2Se_3) = \omega_{r2}(Gese_3)\sqrt{\frac{m_{Se}}{m_{As}}} = 1.94\times10^{13}\ s^{-1}, \tag{39}$$

where the close proximity of the atomic masses of Ge and As was used in the latter case.

Table 1 presents all the values of $\delta\rho(i)$ obtained in accordance with (29)–(31) from (32)–(36) and (39) in FM and IYA approximations. Table 2 lists the corresponding $R_0(i)$ values obtained from (24) and N_s values calculated using formula (28). In this case, we

Table 2. Critical distances R_0 and concentrations N_v of U^- centers and N_s of spins

IYA approximation							
Substance	$R_0(C_3^+)$, 10^{-7} cm	$R_0(C_1^-)$, 10^{-7} cm	$R_0(P_2^-)$, 10^{-7} cm	$R_0(T_3^-)$, 10^{-7} cm	N_v, cm^{-3}	N_s, cm^{-3}	N_s, cm^{-3} (experiment [6, 7])
a-As_2S_3	5.215	4.347	5.345	–	2.4×10^{18}	2.5×10^{17}	$\sim10^{17}$
a-As_2Se_3	4.392	3.662	4.959	–	2.5×10^{18}	4.5×10^{17}	$\sim10^{17}$
a-$GeSe_2$	5.136	4.281	–	5.063	5.0×10^{18}	5.9×10^{15}	$\sim5\times10^{15}$
a-Se	4.590	3.826	–	–	1.65×10^{16}	1.0×10^{16}	$\sim10^{16}$
FM approximation							
Substance	$R_0(C_3^+)$, 10^{-7} cm	$R_0(C_1^-)$, 10^{-7} cm	$R_0(P_2^-)$, 10^{-7} cm	$R_0(T_3^-)$, 10^{-7} cm	N_v, cm^{-3}	N_s, cm^{-3}	N_s, cm^{-3} (experiment [6, 7])
a-As_2S_3	4.970	4.145	5.010	–	2.4×10^{18}	3.2×10^{17}	$\sim10^{17}$
a-As_2Se_3	3.897	3.302	4.525	–	2.5×10^{18}	6.4×10^{17}	$\sim10^{17}$
a-$GeSe_2$	5.136	3.958	–	4.756	5.0×10^{18}	8.2×10^{15}	$\sim5\times10^{15}$
a-Se	4.181	3.222	–	–	1.65×10^{16}	1.0×10^{16}	$\sim10^{16}$

used, on the basis of [6], a magnetic field $B = 3191$ G for a-As_2S_3, a-As_2Se_3, and a-S2, and $B = 3164$ G for a-$GeSe_2$. The $N(i)$ values were substituted from (11) for a-As_2S_3 and a-As_2Se_3, from (13) for a-$GeSe_2$, and from (14) for a-Se. The experimental values of N_s were taken from (1).

5. CONCLUSION

Commenting on the data presented in Tables 1 and 2, in the first place, according to (23), in all cases we have

$$\delta R_i/R_0(i) \lesssim 10^{-3}. \quad (40)$$

This confirms condition (16), which plays an important part in deriving the basic relationships.

Further, attention should be drawn to the following. The value of N_v was unknown beforehand for a-Se. The value of $N_v = 1.65 \times 10^{16}$ cm^{-3}, given in the table, is a result of fitting to the value $N_s = 10^{16}$ cm^{-3}, which must be obtained, according to [6, 7], if (28) is valid. Thus, if $N_v \lesssim 10^{16}$ cm^{-3}, then it follows from Table 2 that charged defects virtually do not affect ESR detection for both of the approximations used.

The situation is different for the cases of a-As_2S_3 and a-As_2Se_3. Here, the use of values of N_v following from formula (3) [see (4)] yields N_s values which are in good agreement with data from observations [6, 7] [see (1)] for both the FM and IYA cases. In other words, the higher concentration of native U^- centers compared with a-Se is responsible for the fact that the recorded N_s value is an order of magnitude smaller than N_v. This is even more clearly manifested in the case of a-$GeSe_2$. To be sure, a certain influence is also exerted by the smaller fraction of electrons involved in geminate recombination and by the relatively low dielectric constant. However, the fact that the N_s value is large, rather than small, is a decisive circumstance for the value of N_s being 3 orders of magnitude less than $N_v = 5 \times 10^{18}$ cm^{-3}, which corresponds to (3) and [19].

Finally, attention is called to the following. The main conclusion of the present study is that charged centers which originate under photoexcitation of moderate intensity from native U^- centers may, when the concentration of the latter is sufficient, markedly reduce the recorded concentration of induced spins. Of interest in this connection is such a material as v-SiO_2. The concentration of U^- centers in this material is, in all probability, high (~10^{19} cm^{-3} [13, 19]). Therefore, if, in addition, we take into account the smallness of the dielectric constant, the question arises as to whether it is even possible to observe photoinduced ESR in v-SiO_2. There have been reports of an observed photoinduced ESR signal in v-SiO_2 (see, e.g., [33]). In my opinion, however, the photoexcitation used in these studies cannot, strictly speaking, be classified as being of the band-to-band type. Moreover, the resonance curves observed in these studies are not quite identical in shape to those presented in [6, 7] and require additional interpretation.

At any rate, it is clear, in view of the results obtained in the present study, that the problem of photoinduced ESR in v-SiO_2 (which is equal to the set of problems encountered in studying photostructural transformations) invites further investigation.

APPENDIX

Let us denote by $V(t)$ a microwave perturbation and consider the Schrödinger equation

$$i\hbar\frac{\partial\Psi}{\partial t} = [H(t) + V(t)]\Psi. \quad (A.1)$$

To pass to the interaction representation, we assume that

$$\Psi = \exp\left[-\frac{i}{\hbar}\int_0^t H(s)ds\right]\Phi. \quad (A.2)$$

Substituting (A.2) into (A.1) and "multiplying" from the left by $\exp[(i/\hbar)\int_0^t H(s)ds]$, we obtain

$$i\hbar\frac{\partial\Phi}{\partial t} = \left[\exp\left(\frac{i}{\hbar}\int_0^t H(s)ds\right)H(t)\right.$$
$$\times\exp\left(-\frac{i}{\hbar}\int_0^t H(s)ds\right) - H(t) + \exp\left(\frac{i}{\hbar}\int_0^t H(s)ds\right)V(t) \quad (A.3)$$
$$\left.\times\exp\left(-\frac{i}{\hbar}\int_0^t H(s)ds\right)\right]\Phi.$$

In writing (A.3), account was taken of the fact that, according to (17),

$$[H(t), H(s)] = H_0(H_c(s) - H_c(t)) - (H_c(s) - H_c(t))H_0 \neq 0. \quad (A.4)$$

From (A.3) we have, to a first approximation of the perturbation theory,

$$\Phi(\delta t) = \frac{1}{i\hbar}\int_0^{\delta t} dt\left[\exp\left(\frac{i}{\hbar}\int_0^t H(s)ds\right)H(t)\right.$$
$$\times\exp\left(-\frac{i}{\hbar}\int_0^t H(s)ds\right) - H(t) + \exp\left(\frac{i}{\hbar}\int_0^t H(s)ds\right)V(t) \quad (A.5)$$
$$\left.\times\exp\left(-\frac{i}{\hbar}\int_0^t H(s)ds\right)\right]\Phi(0).$$

Let us introduce a spectrum of eigenfunctions

$$(H_0 + H_c(t))\varphi(t) = E(t)\varphi(t). \quad (A.6)$$

In addition, we introduce the spin functions $|-1/2\rangle$ and $|+1/2\rangle$, which satisfy the conditions

$$\hat{s}_z|\pm 1/2\rangle = \pm\frac{\hbar}{2}|\pm 1/2\rangle. \quad (A.7)$$

Assuming that, at $t = 0$, the system is in the state

$$\Phi(0) = \varphi(0)|-1/2\rangle \equiv |u_-(0)\rangle, \quad (A.8)$$

we can write, according to (A.5) and (A.7), for the magnitude of the transition into the state

$$u_+(\delta t) \equiv \varphi(\delta t)|+1/2\rangle \quad (A.9)$$

the following expression:

$$\langle u_+(\delta t)|\Phi(\delta t)\rangle = \frac{1}{i\hbar}\left\langle u_+(\delta t)\int_0^{\delta t} dt \exp\left(\frac{i}{\hbar}\int_0^t H(s)ds\right)V(t)\right. \quad (A.10)$$
$$\left.\times \exp\left(-\frac{i}{\hbar}\int_0^t H(s)ds\right)\middle| u_-(0)\right\rangle,$$

in which account is taken of the orthogonality of the spin functions. With (17), it can be readily understood that in (A.10) we have operations of the form

$$[H_0 + H_c(s)]\varphi(0), \quad [H_0 + H_c(s)]\varphi(\delta t),$$

which, in the general case (at $s \neq 0$, $s \neq \delta t$), are not defined. However, on the basis of (15), (16), and (A.6), we can write

$$[H_0 + H_c(s)]\varphi(0)$$
$$= \left[H_0 + H_c(0)\left(1 + \frac{H_c(s) - H_c(0)}{H_c(0)}\right)\right]\varphi(0) \quad (A.11)$$
$$\approx \left[H_0 + H_c(0)\left(1 - \frac{\delta R}{R(0)}\right)\right]\varphi(0) \approx E(0)\varphi(0),$$

where the following relation is used:

$$1/R(s) - 1/R(0) \approx \delta R/R^2(0).$$

In a similar manner, we can write

$$[H_0 + H_c(s)]\varphi(\delta t)$$
$$= \left[H_0 + H_c(\delta t)\left(1 + \frac{H_c(s) - H_c(\delta t)}{H_c(\delta t)}\right)\right]\varphi(\delta t)$$
$$\approx \left[H_0 + H_c(\delta t)\left(1 \mp \frac{\delta R}{R(\delta t)}\right)\right]\varphi(\delta t) \quad (A.12)$$
$$\approx E(\delta t)\varphi(\delta t).$$

From (A.11), (A.12), (A.7), and (17), it follows that

$$H(s)\varphi(0)|-1/2\rangle \approx [E(0) - \beta B]\varphi(0)|-1/2\rangle,$$
$$H(s)\varphi(\delta t)|+1/2\rangle \approx [E(\delta t) + \beta B]\varphi(\delta t)|+1/2\rangle. \quad (A.13)$$

Hence, assuming that

$$V(t) = \frac{\beta}{\hbar}B_1\hat{s}_x(e^{i\omega_1 t} + e^{-i\omega_1 t}), \quad (A.14)$$

where B_1 is the amplitude of an ac orthogonal magnetic field with a frequency ω_1, and substituting (A.13), (A.13), and (A.14) into (A.10), we have

$$\langle u_+(\delta t)|\Phi(\delta t)\rangle \approx \frac{1}{i\hbar^2}\int_0^{\delta t} dt e^{(1/\hbar)[E(\delta t) - E(0) + 2\beta B - \hbar\omega_i]t} \quad (A.15)$$
$$\times \langle \varphi(\delta t)|\varphi(0)\rangle \langle +1/2|\hat{s}_x|-1/2\rangle.$$

From (A.15) we obtain, by applying conventional methods, the resonance transition probability

$$|\langle u_+(\delta t)|\Phi(\delta t)\rangle|^2 \propto |\langle \varphi(\delta t)|\varphi(0)\rangle|^2 \quad (A.16)$$
$$\times \delta(E(\delta t) - E(0) + 2\beta B - \hbar\omega_1).$$

It can be seen from (A.16) that transitions are possible when, first, the overlapping condition $\langle\varphi(\delta t)|\varphi(0)\rangle \neq 0$ and, second, condition (19) are satisfied.

REFERENCES

1. K. Shimakawa, A. Kolobov, and S. R. Elliott, Adv. Phys. **44**, 475 (1995).
2. S. D. Baranovskiĭ and V. G. Karpov, Fiz. Tekh. Poluprovodn. (Leningrad) **21**, 3 (1987) [Sov. Phys. Semicond. **21**, 1 (1987)].
3. R. A. Street and N. F. Mott, Phys. Rev. Lett. **35**, 1293 (1975).
4. M. Kastner, D. Adler, and H. Fritzsche, Phys. Rev. Lett. **37**, 1504 (1976).
5. M. Kastner and H. Fritzsche, Philos. Mag. B **37**, 199 (1978).
6. S. G. Bishop, U. Strom, and P. C. Taylor, Phys. Rev. B **15**, 2278 (1977).
7. S. G. Bishop, U. Strom, and P. C. Taylor, in *Proceedings of 7th International Conference "Amorphous and Liquid Semiconductors", Edinburgh, 1977*, p. 595.
8. R. A. Street, Adv. Phys. **25**, 397 (1976).
9. R. A. Street and G. Lukovsky, Solid State Commun. **31**, 289 (1979).
10. K. Shimakawa and S. R. Elliott, Phys. Rev. B **38**, 12479 (1988).
11. L. P. Ginzburg, J. Non-Cryst. Solids **171**, 172 (1994).
12. L. P. Ginzburg and A. P. Zhilinskiĭ, Zh. Tekh. Fiz. **72** (2), 59 (2002) [Tech. Phys. **47**, 200 (2002)].
13. L. P. Ginzburg, J. Non-Cryst. Solids **171**, 164 (1994).
14. J. Chernogora, F. Mollot, and C. Benoit a la Guillaume, Phys. Status Solidi A **15**, 401 (1973).
15. F. Mollot, J. Chernogora, and C. Benoit a la Guillaume, Phys. Status Solidi A **21**, 281 (1974).
16. T. T. Nang, M. Okuda, and T. Matsushita, J. Non-Cryst. Solids **33**, 323 (1979).
17. N. F. Mott and E. A. Davis, *Electronic Processes in Non-Crystalline Materials* (Clarendon, Oxford, 1971; Mir, Moscow, 1974).

18. V. A. Vassilyev, M. Koos, and I. Kosa Somogyi, Solid State Commun. **22**, 633 (1977).
19. G. Lukovsky, Philos. Mag. B **39**, 513 (1979).
20. M. Kastner, J. Non-Cryst. Solids **35–36**, 807 (1980).
21. B. I. Shklovskii, H. Fritzsche, and S. D. Baranovskii, J. Non-Cryst. Solids **114**, 325 (1989).
22. D. Vanderbilt and J. D. Joannopoulos, Phys. Rev. B **23**, 2596 (1981).
23. K. D. Tséndin, Pis'ma Zh. Éksp. Teor. Fiz. **55**, 635 (1992) [JETP Lett. **55**, 661 (1992)].
24. K. D. Tséndin, in *Electronic Phenomena in Chalcogenide Vitreous Semiconductors*, Ed. by K. D. Tséndin (Nauka, St. Petersburg, 1996), p. 68.
25. J. Holtsmark, Phys. Z. **20**, 162 (1919).
26. A. S. Davydov, *Quantum Mechanics* (Nauka, Moscow, 1973; Pergamon, Oxford, 1976).
27. G. Lukovsky, C. K. Wong, and W. B. Pollard, J. Non-Cryst. Solids **59–60**, 839 (1983).
28. G. Herzberg, *Molecular Spectra and Molecular Structure*, Vol. 2: *Infrared and Raman Spectra of Polyatomic Molecules* (Van Nostrand, New York, 1945; Inostrannaya Literatura, Moscow, 1949), Chap. 2.
29. G. Lukovsky, R. J. Nemanich, S. A. Solin, and R. C. Keezer, Solid State Commun. **17**, 1567 (1975).
30. G. Lukovsky and R. M. Martin, J. Non-Cryst. Solids **8–10**, 185 (1972).
31. W. Gordy, J. Chem. Phys. **14**, 305 (1946).
32. G. Lukovsky, Phys. Rev. B **6**, 1480 (1972).
33. J. H. Stathis and M. Kastner, Phys. Rev. B **29**, 7079 (1984).

Translated by M. Tagirdzhanov

Semiconductors, Vol. 37, No. 1, 2003, pp. 92–96. Translated from Fizika i Tekhnika Poluprovodnikov, Vol. 37, No. 1, 2003, pp. 93–97.

AMORPHOUS, VITREOUS, AND POROUS SEMICONDUCTORS

Electrical Properties of Si:H/*p*-Si Structures Fabricated by Hydrogen Implantation

O. V. Naumova*, I. V. Antonova, V. P. Popov, and V. F. Stas'

Institute of Semiconductor Physics, Siberian Division, Russian Academy of Sciences, Novosibirsk, 630090 Russia

**e-mail: naumova@isp.nsc.ru*

Submitted April 9, 2002; accepted for publication April 24, 2002

Abstract—Hydrogenated silicon (Si:H) layers and Si:H/*p*-Si heterostructures were produced by multiple-energy (3–24 keV) high-dose (5×10^{16}–3×10^{17} cm^{-2}) hydrogen implantation into *p*-Si wafers. After implantation, current transport across the structures is controlled by the Poole–Frenkel mechanism, with the energy of the dominating emission center equal to $E_c - 0.89$ eV. The maximum photosensitivity is observed for structures implanted with 3.2×10^{17} cm^{-2} of hydrogen and annealed in the temperature range of 250–300°C. The band gap of the Si:H layer $E_g \approx 2.4$ eV, and the dielectric constant $\varepsilon \approx 3.2$. The density of states near the Fermi level is $(1–2) \times 10^{17}$ cm^{-3} eV^{-1}. © *2003 MAIK "Nauka/Interperiodica".*

1. INTRODUCTION

Interest in amorphous hydrogenated silicon (*a*-Si:H) films is primarily due to their possible applications as photodetectors [1, 2]. Conventionally, *a*-Si:H layers are deposited by PECVD. Previous studies have shown that, to improve and stabilize the parameters of *a*-Si:H devices, it is essential to be able to control the density of dangling Si–Si bonds, as well as the hydrogen density, and also to determine the optimal ratio between these densities [3]. Ion implantation allows controlled introduction of hydrogen in a wide concentration range. Thus, an attempt to produce Si:H layers by ion-implantation doping with hydrogen was justified. To obtain a uniform distribution of hydrogen in a layer, a source emitting hydrogen ions in a range of energies was used instead of a monoenergetic beam [4]. The goal of the present study was to investigate electrical properties of Si:H/*c*-Si structures produced by this method.

2. EXPERIMENTAL METHODS

p-Si with a carrier density of 7×10^{14}–10^{15} cm^{-3} was irradiated from a pulsed source with hydrogen ions with energies in the range E = 3–24 keV. The pulse width was 4 μs; the pulse separation, 30 s; and the current density, 40 mA cm^{-2}. The irradiation dose was varied in the range $D = 5 \times 10^{16}$–3.2×10^{17} cm^{-2}. The maximum ion range was 0.22 μm; the hydrogen density at the maximum irradiation dose was ~10^{22} cm^{-3}. After irradiation, the wafers were pretreated with oxygen plasma to remove organic contaminants from their surfaces and further cleaned chemically by boiling in acetone. Aluminum or gold contacts were deposited through a mask by sputtering in a vacuum, or mesa structures with Al contacts were fabricated. In several cases, a mercury probe was used as a contact. Measurements of capacitance–voltage (*C–V*) and current–voltage (*I–V*) characteristics, combined with layer-by-layer etching and deep level transient spectroscopy (DLTS), were used to study the parameters of Si:H/*c*-Si structures immediately after irradiation, and also after 1-h annealing in the temperature range T_{ann} = 180–700°C.

3. RESULTS AND DISCUSSION

Figure 1 shows *I–V* characteristics of Al/Si:H/*p*-Si structures for minimum and maximum doses of hydrogen irradiation (in all the figures, the forward bias corresponds to a negative voltage applied to an Si:H layer). As seen, the as-grown structures exhibit clearly pronounced rectifying *I–V* characteristics. The rectifica-

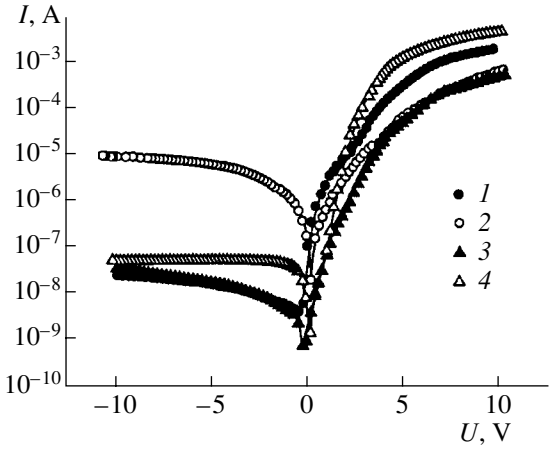

Fig. 1. *I–V* characteristics of Al/Si:H/*p*-Si structures implanted with hydrogen at a dose *D*: (*1*, *2*) 5×10^{16}, (*3*, *4*) 3.2×10^{17} cm^{-2}; (*1*, *3*) unannealed, (*2*, *4*) annealed at 260°C for 1 h. Forward bias corresponds to negative voltage at Si:H layer.

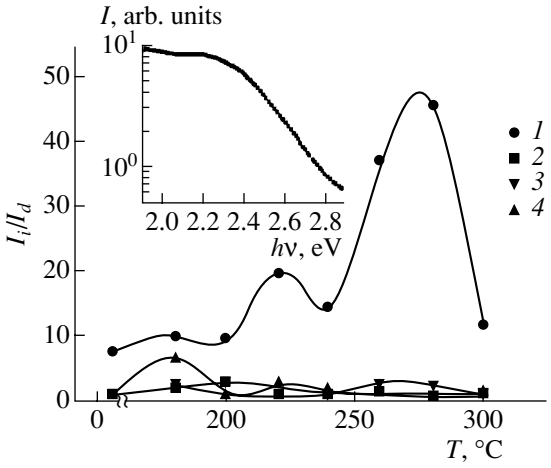

Fig. 2. Reverse current under illumination by the wavelength $\lambda = 0.7$ μm (at $U = -5$ V) related to dark current, I_i/I_d, vs. the annealing temperature T_{ann} for structures implanted with hydrogen at a dose D: (*1*) 3.2, (*2*) 2.7, (*3*) 1, and (*4*) 0.5×10^{17} cm^{-2}. Inset: spectral dependence of current after 1 h of annealing at $T_{ann} = 280$°C; $D = 3.2 \times 10^{17}$ cm^{-2}.

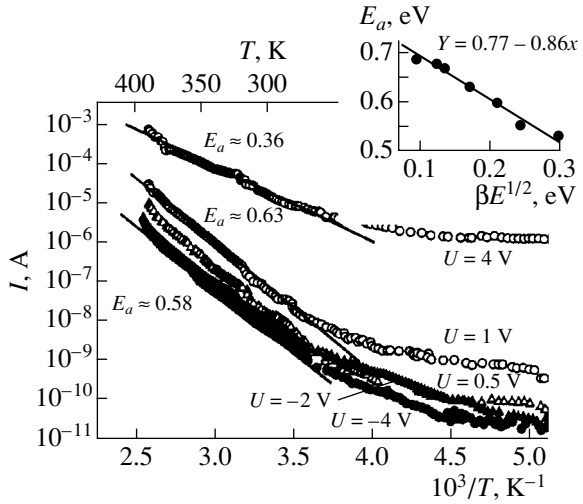

Fig. 3. Temperature dependences of current at different biases U for a structure implanted with $D = 3.2 \times 10^{17}$ cm^{-2}. Solid lines: simulation with the activation energy E_a (eV) shown near a curve. Inset: E_a vs. the barrier energy lowering in the electric field $\beta(E)^{1/2}$. The straight line corresponds to the equation presented in the inset.

tion coefficient (the ratio between the forward and reverse currents, I_f/I_r) is ~10^3–10^4 at $V = 10$ V bias across the structure. For structures with the maximum irradiation dose, the barrier properties are totally eliminated after annealing at $T_{ann} \sim 700$°C.

To determine which contact (i.e., metal/Si:H or Si:H/*c*-Si interface) is rectifying, the temperature dependences of current were recorded in structures with different contacts. The experiment has shown that, at one and the same bias across the structure, the temperature dependence of current is independent of the contact metal (Au, Al). This implies that the rectifying properties of structures (Fig. 1) are due to the formation of an internal barrier between the Si:H layer and *p*-Si substrate, rather than to the metal/Si:H Schottky barrier. As found from an analysis of (*C*–*V*) characteristics, the carrier density determined from the slope of $1/C^2(V)$ is virtually independent of the irradiation dose (7.5×10^{14} and 8.0×10^{14} cm^{-3} for, respectively, the minimum and maximum doses) and corresponds to the carrier density in the substrate. The DLTS study in the temperature range 77–300 K did not reveal deep levels in the depletion region of the structures. This implies that the depletion region is located in the single-crystal substrate rather than in the Si:H layer distorted by irradiation; i.e., heterostructures were fabricated by implantation.

To determine the band gap of the Si:H layer, the photoelectric properties were studied. Figure 2 shows the ratio of current I_i, measured when the structure was illuminated by photons with a wavelength $\lambda = 0.7$ μm, to the dark current I_d versus the temperature of isochronous ($t = 1$h) annealing. The data were recorded at a reverse bias of 5 V. As seen, maximum photosensitivity (I_i/I_d) is observed in the structures with an irradiation dose $D = 3.2 \times 10^{17}$ cm^{-2} and annealed at $T_{ann} = 250$–300°C. The inset of Fig. 2 shows the short-wavelength portion of the spectral dependence of current, which allowed us to estimate the band gap of the Si:H-layer, $E_g \approx 2.4$ eV. The extrapolation of the $1/C^2(V)$ dependence to the voltage axis yields the height of the internal barrier (Si:H/*p*-Si), $V_d \approx 1.1$ eV.

Since the structures under study include an irradiation-distorted Si:H layer and a barrier, it is reasonable to discuss *I*–*V* characteristics for an in-series connected resistor and diode [5]:

$$I = I_0 \exp[q(V - IR)/nkT]. \quad (1)$$

Here, n is the ideality factor of a *I*–*V* characteristic, and R is the resistance (of the irradiated layer, in the given case). For the maximum and minimum irradiation doses, we obtain $n \approx 36$, $R \approx 7$ kΩ, and $n \approx 20$, $R \approx 2$ kΩ, respectively. The junction depth d was determined from *I*–*V* measurements with layer-by-layer etching. Simple estimation shows that, with $d \approx 0.25$ μm and an area $S = 1.13$ cm^{-2}, the resistivity of hydrogenated layers is $\rho \approx 3 \times 10^6$ and 8×10^5 Ω cm for the extreme irradiation doses. A high value of the ideality factor indicates that the voltage applied across the structure falls mainly on the high-resistivity layer rather than on the barrier [5]. Indeed, partial removal of the Si:H layer shifts the forward *I*–*V* characteristic toward negative voltages. Therefore, the forward conductance of the structure is defined by the conductivity of the Si:H layer.

Figure 3 shows temperature dependences of current measured with different biases across the structures obtained by hydrogen implantation with $D = 3.2 \times$

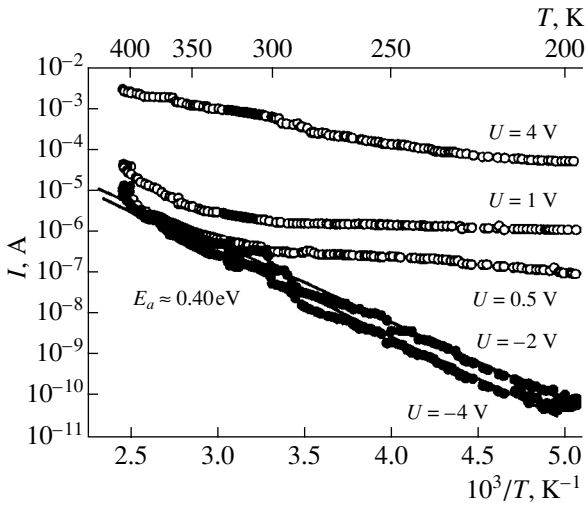

Fig. 4. Temperature dependences of current at different biases U for a structure implanted with $D = 3.2 \times 10^{17}$ cm^{-2} and annealed at 260°C for 1 h.

10^{17} cm^{-2}. As seen, the current increases exponentially in the temperature range 270–400 K, $I \sim \exp(E_a/kT)$. The experiment shows that the activated behavior of $I(T)$ is observed for all doses, 5×10^{16}–3.2×10^{17} cm^{-2}. The activation energy of conductivity E_a decreases with increasing bias across the structure. This suggests that a mechanism associated with field-assisted ejection of carriers from emission centers dominates in irradiated structures (under forward bias). For the volume-confined Frenkel effect [6],

$$I \propto \exp[F_v - \beta E^{1/2})/rkT]. \quad (2)$$

Here, F_v is the depth of the level related to the emission center, $\beta = (q^3/\pi\varepsilon_0\varepsilon)^{1/2}$ is the Frenkel constant, E is the electric field strength, and r is a parameter taking values between 1 and 2.

The inset of Fig. 3 shows the activation energy $E_a = F_v/r$ as a function of the barrier lowering $\beta(E)^{1/2}$. In calculating β, we used the dielectric constant $\varepsilon = 3.2$ obtained from *C–V* measurements. Then, $\beta = 2.68 \times 10^{-4}$ eV cm$^{1/2}$ V$^{-1/2}$. The energy of the dominating center, estimated by extrapolating the experimental curve to zero activation energy, is $E_a \approx 0.89$ eV.

It was found that, with respect to the electrical properties of the annealed samples, the samples implanted with $D = 5 \times 10^{16}$, 10^{17}, 2.7×10^{17}, and 3.2×10^{17} cm^{-2} can be divided into two groups: those implanted with doses in the range 5×10^{16}–2.7×10^{17} cm^{-2} and those with $D = 3.2 \times 10^{17}$ cm^{-2}. The samples of the first group, besides having virtually zero photosensitivity (Fig. 2), have the following specific feature. *C–V* studies combined with layer-by-layer etching have shown that, in the structures produced by hydrogen irradiation with $D = 5 \times 10^{16}$–2.7×10^{17} cm^{-2}, annealing at $T_{ann} = 250$°C forms an *n*-type surface layer with a carrier density of about 10^{16} cm^{-3}. The layer thickness is 30–50 nm. It is noteworthy that, under irradiation with a monoenergetic hydrogen beam at a dose above 10^{16} cm^{-2}, the *n*-layer in *p*-Si is formed at higher annealing temperatures (~300°C) [7].

The structures obtained at an implantation dose of 3.2×10^{17} cm^{-2} differed from those implanted at lower doses by the following specific features, which appeared after annealing in the temperature range of 250–300°C:

(i) The formation of a low-resistivity *n*-type surface layer was not observed;

(ii) *I–V* curves showed a saturation of current in the depletion mode (Fig. 1);

(iii) The mechanism of current transport across the structures changed (cf. Figs. 3 and 4);

(iv) The structures were photosensitive (Fig. 2).

The saturation of current in the structures with *p*-substrate (Fig. 1) indicates the presence of an electronic component of current from the substrate to the Si:H layer.

Figure 4 shows the temperature dependences of current in the structures implanted with $D = 3.2 \times 10^{17}$ cm^{-2} and annealed at 260°C. As seen from a comparison of Figs. 4 and 5, the temperature dependences of forward current exhibit not only an exponential portion, but also a portion in which the current is virtually temperature-independent, i.e., $I(T) \approx$ const, over some temperature interval. This interval becomes wider as the annealing temperature rises. Immediately after irradiation, $I(T) \approx$ const at $T < 250$ K (Fig. 3); after annealing at 260°C, this occurs at $T < 310$ K (Fig. 4), and after annealing at 300°C, at $T < 380$ K.

There are two known mechanisms of carrier transport across barrier structures with high-resistivity layers and in which current is constant; these are space-charge limited current (SCLC) and tunneling through the barrier. It is hardly probable that tunneling through an Si:H/*p*-Si barrier occurs at room temperature, since the electric field strength in the structure does not exceed 2×10^5 V cm^{-1} and the Fowler–Nordheim mechanism demands a higher field. To determine whether tunneling from an emission center can take place, we evaluated the barrier height. The experimental data were approximated with the relation $I \propto AV^2 \exp(-b/V)$, with the coefficient $b = 10.82$. Here $b = 23\pi m^{1/2}\phi d/6hq$, where ϕ is the height and d, the width of the potential barrier; m is the effective mass, and q is the elementary charge. Calculation has shown that, in order to obtain physically plausible values of the barrier height ($\gtrsim kT$) at $d \approx 1$ nm, it is necessary to assume that $m \ll 10^{-4} m_0$. Thus, it seems most probable that the SCLC mechanism is operative.

Space-charge-limited current is an injection current through a high-resistivity layer (in our case, Si:H) that is partially compensated by trapping at localized

levels. In the general case, SCLC is described by the relation [8]

$$I = aV + bV^{\gamma}.$$

The linear term (the ohmic portion of a *I*–*V* curve) is dominant at low fields. The parameter γ characterizes the energy distribution of local states (γ = 2 for monoenergetic traps in a layer). Under the experimental conditions, we obtained γ = 5.3 for T_{ann} = 260°C and γ = 4.2 for T_{ann} = 300°C. The lower value of γ implies that the energy distribution of carrier traps in Si:H is less uniform for the case of T_{ann} = 300°C.

We used the method of calculating the density of charged states from SCLC data [9] to estimate the density of states near the Fermi level. For the structures implanted at $D = 3.2 \times 10^{17}$ cm^{-2} and annealed at T_{ann} = 260°C and 300°C (1 h), the obtained values were, respectively, $r \approx 2.3 \times 10^{17}$ and $\approx 1.1 \times 10^{17}$ cm^{-3} eV^{-1}. At the same time, SCLC can be observed only if the density of thermally activated carriers in the high-resistivity layer is lower than the density of injected carriers. The fact that SCLC is observed only in a limited range of doses and temperatures implies that it is in this mode where generation–recombination centers in an Si:H layer are largely eliminated. Figure 5 shows the dark current I_d versus the temperature of structure annealing in the range T_{ann} = 180–300°C. As is seen, I_d increases as the annealing temperature rises; this indicates the formation of generation-recombination centers in the structures. However, the reverse current (which depends on the density of the recombination centers) is 1–2 orders of magnitude smaller in the structures with a maximum irradiation dose than in the structures implanted with $D = 5 \times 10^{16}$–2.7×10^{17} cm^{-2}. It is the structures implanted with $D = 3.2 \times 10^{17}$ cm^{-2} that are photosensitive.

Another specific feature of the structures under study is the metastable state of the system of defects in an Si:H layer. Thus, unannealed samples implanted at $D = 3.2 \times 10^{17}$ cm^{-2} and stored for some time (more than half a year) exhibited, after subsequent annealing, properties similar to those typical of structures implanted at lower doses (for example, an *n*-type low-resistivity surface layer was formed at T_{ann} above 250°C). At the same time, if annealing with T_{ann} > 250°C was carried out directly after irradiation, the electric properties of a structure remained unchanged with time.

It follows from these results that a heterostructure is formed in *p*-Si during implantation, similarly to PECVD fabrication of Si:H layers. However, a comparison of the electrical properties of structures produced by hydrogen implantation and conventional methods (glow discharge, sputtering, CVD) yields the following. In *a*-Si:H layers applicable for device fabrication and produced by conventional methods, the hydrogen content is 5–15 at. % [10]. This corresponds to passivation of the majority of defects. At a higher hydrogen concentration, the density of defect states in the layer and at the interface increases, thus enhancing recombination in the layer (with loss of photosensitivity) and leading to the total loss of modulation in the space charge region of barrier structures as a consequence of a high density of states at the interface. In the case of ion implantation, the structures are photosensitive at a hydrogen content ~29% ($D = 3.2 \times 10^{17}$ cm^{-2}); i.e., a higher hydrogen concentration is necessary for defect passivation. The band gap in ion-implanted Si:H layers is $E_g \approx 2.4$ eV, in contrast to $E_g \approx 1.9$ eV in films with the same hydrogen content (~29%) but produced by conventional methods [10]. The dielectric constant ε ≈ 11 for the latter films, and ε ≈ 3 for the films produced by implantation. At the same time, the value $E_g > 2$ eV is typical of porous silicon, whose dielectric constant (ε = 3.6 [9]) is also close to that of the structures under study (ε = 3.2). Therefore, analysis of our results leads to the conclusion that the difference between the electrical properties of Si:H layers produced by conventional methods and those produced by hydrogen ion implantation is most probably related to the presence of defects introduced during implantation and annealing, with the possible formation of vacancy-type clusters (pores).

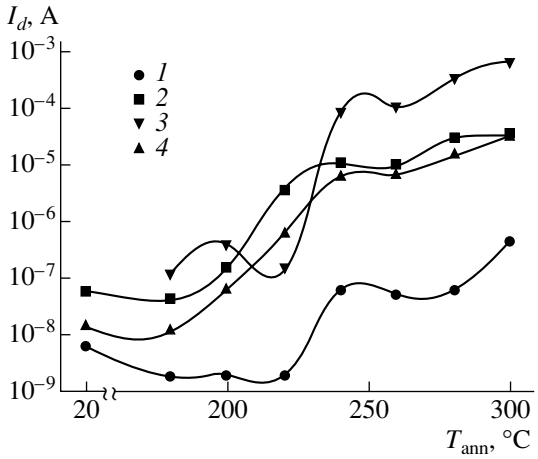

Fig. 5. Dark current (at U = –5 V) vs the annealing temperature for Al/Si:H/*p*-Si structures implanted with hydrogen at a dose D: (*1*) 3.2, (*2*) 2.7, (*3*) 1, and (*4*) 0.5×10^{17} cm^{-2}.

4. CONCLUSION

We established the following:

(i) Si:H/*p*-Si structures obtained by hydrogen implantation in the dose range $D = 5 \times 10^{16}$–3.2×10^{17} cm^{-2} exhibit rectification with the coefficient $I_f/I_r \approx 10^3$–10^4 and at 10 V bias across the structure. The resistivity of an Si:H layer is $\rho \approx 3 \times 10^6$ and $\rho \approx 8 \times 10^5$ Ω cm for maximum and minimum doses, respectively;

(ii) After implantation, the carrier transport across the structures at room temperature is associated with field-assisted ejection of carriers from emission centers (the Poole–Frenkel mechanism). The energy depth of

the level related to the dominating emission center is about 0.89 eV;

(iii) Maximum photosensitivity is obtained in structures implanted at $D = 3.2 \times 10^{17}$ cm^{-2} and annealed at T_{ann} = 250–300°C. The band gap of the Si:H layer in these structures is ≈ 2.4 eV. The carrier transport mechanism is space-charge limited current; the density of states near the Fermi level is ~$(1–2) \times 10^{17}$ cm^{-3} eV^{-1};

(iv) In the structures produced by irradiation in the dose range $D = 5 \times 10^{16}$–2.7×10^{17} cm^{-2} and annealed at $T_{ann} \approx 250$°C and higher, 30- to 50-nm-thick *n*-type surface layers with a carrier density of ~10^{16} cm^{-3} are formed.

ACKNOWLEDGMENTS

We are grateful to A.S. Yaroshevich for the measurements of the spectral dependences of current.

This study was supported by the International Science & Technology Center (grant no. 563).

REFERENCES

1. N. Jensen, U. Rau, and J. H. Werner, Mater. Res. Soc. Symp. Proc. **609**, A13.1.1 (2000).
2. R. De Rosa, M. L. Grill, G. Sasicala, *et al.*, Solid State Phenom. **67–68**, 563 (1999).
3. M. M. Mezdrogina, A. V. Abramov, G. N. Mosina, *et al.*, Fiz. Tekh. Poluprovodn. (St. Petersburg) **32**, 620 (1998) [Semiconductors **32**, 555 (1998)].
4. V. P. Popov, I. V. Antonova, A. K. Gutakovsky, *et al.*, J. Mater. Sci. Eng. B **73**, 120 (2000).
5. T. A. Burr, A. A. Seraphin, E. Werwa, and K. D. Kolenbranger, Phys. Rev. B **56**, 4818 (1997).
6. *Properties of Metal–Insulator–Semiconductor Structures*, Ed. by A. V. Rzhanov (Nauka, Moscow, 1976).
7. S. J. Pearton, J. W. Corbett, and T. S. Shi, Appl. Phys. A **43**, 153 (1987).
8. M. A. Lampert and P. Mark, *Current Injection in Solids* (Academic, New York, 1970; Mir, Moscow, 1973).
9. T. Matsumoto, H. Mimura, N. Koshida, and Y. Masumoto, J. Appl. Phys. **84**, 6157 (1998).
10. *The Physics of Hydrogenated Amorphous Silicon*, Ed. by J. D. Joannopoulos and G. Lucovsky (Springer-Verlag, New York, 1984; Mir, Moscow, 1988).

Translated by D. Mashovets

Semiconductors, Vol. 37, No. 1, 2003, pp. 97–102. Translated from Fizika i Tekhnika Poluprovodnikov, Vol. 37, No. 1, 2003, pp. 98–103.

AMORPHOUS, VITREOUS, AND POROUS SEMICONDUCTORS

Structural–Phase Transformations in SiO_x Films in the Course of Vacuum Heat Treatment

I. P. Lisovskyy, I. Z. Indutnyy*, B. N. Gnennyy, P. M. Lytvyn, D. O. Mazunov, A. S. Oberemok, N. V. Sopinskyy, and P. E. Shepelyavyi

Institute of Semiconductor Physics, National Academy of Sciences of Ukraine, Kiev, 03028 Ukraine

** e-mail: indutnyy@isp.kiev.ua*

Submitted March 25, 2002; accepted for publication May 15, 2002

Abstract—A thermally stimulated structural transformation of the Si–O phase in the SiO_x layers, which leads to the formation of Si nanoinclusions, was investigated using gravimetry, infrared spectroscopy, multiple-angle ellipsometry, and atomic-force microscopy. It is demonstrated that vacuum heat treatment leads to an increase in the concentration of O bridges in the structural network of oxide. Oxide is compacted, and its surface roughness is smoothened. Silicon and SiO_2 phases are precipitated due to the transfer of O atoms from lightly oxidized molecular clusters ($SiOSi_3$) to heavily oxidized ones (SiO_3Si). An analysis of ellipsometry data in the context of the effective medium model made it possible to estimate the fractions of the precipitated Si and SiO_2 phases. © *2003 MAIK "Nauka/Interperiodica".*

1. INTRODUCTION

The insulating and optical properties of amorphous films of silicon oxides (SiO_x) have been intensively investigated over the last three decades (see, for example, [1–5]). This is mainly due to the widespread use of such layers as passivating, insulating, or antireflecting coatings. Today, the investigation of this material is still of interest in connection with the possibility of obtaining Si nanoinclusions in an SiO_x matrix as a result of heat treatment. Particularly, photoluminescence (PL) bands related to the formation of Si nanocrystallites in annealed SiO_x films, which were obtained by plasmochemical deposition, have been observed recently [6, 7].

Recently, PL with bands at 650 and 730 nm was observed in annealed SiO_x films, which were obtained using vacuum thermal evaporation of SiO [8]. This method is very promising for the fabrication of large-area Si-based displays. The effect mentioned can be explained by the formation of Si nanoinclusions as a result of heat treatment. The structure of these inclusions (amorphous or crystalline) depends on the heat treatment temperature. In principle, the emergence of such Si inclusions is in good agreement with the known phenomenon of the separation of an SiO_x matrix into Si and SiO_2 phases at elevated temperatures [1, 4]: $2SiO_x \longrightarrow xSiO_2 + (2 - x)Si$. Because of this circumstance, the investigation of structural–phase transformations of silicon oxides upon heating is of great importance from the point of view of understanding the mechanisms of formation of Si nanoinclusions in an oxide matrix.

Annealing-induced variations in the characteristics of SiO_x layers obtained using vacuum thermal evaporation of SiO_x have been investigated in detail [3, 5, 8–10]. As a rule, heat treatment was carried out in an oxidizing medium (usually in air). Specifically, the purpose was to obtain a wide set of films with a variable stoichiometry coefficient. However, such an approach does not permit one to keep track of the phase separation of the film material itself during thermal treatment. This restriction is caused by external oxygen influx, which is associated with additional oxidation of the film. In the case of vacuum heat treatment [8, 10], prime attention was paid to the observation and characterization of the Si inclusions. At the same time, analysis of thermally stimulated changes in the structure and composition of the Si–O phase should give important additional information about the mechanism of formation of these inclusions. In this context, we carried out a detailed investigation of variations in the structural properties of SiO_x films as a result of heat treatment in vacuum. As was demonstrated previously [8], such treatment leads to the formation of Si nanoinclusions.

2. EXPERIMENTAL

The SiO_x layers were obtained by thermal evaporation of SiO (Cerac Inc.) with a 99.9% purity in vacuum at a residual pressure of $(1–2) \times 10^{-5}$ Torr. Two-sided polished Si wafers were used as the substrates. During deposition, the substrate temperature was 150°C. The film thickness, which varied within the range $d = 1–3$ μm, and the deposition rate were initially determined using a quartz oscillator, which was accurate to 3%. Typically, the deposition rate was 8–10 nm/s. The film thickness was further refined and made accurate to 5 nm using a Dektak 3030 profilometer. Some samples were annealed in vacuum at a residual pressure of $(1–2) \times 10^{-5}$ Torr for 20 min at 700°C.

Table 1. Characteristics of the SiO_x films investigated

Characteristic	As-grown film	Annealed film
Density, g/cm^3	1.90 ± 0.07	2.09 ± 0.10
Index of refraction	1.99 ± 0.03	1.90 ± 0.01
Absorption index	$(6.9 \pm 1) \times 10^{-3}$	$(9 \pm 1) \times 10^{-3}$
Position of the absorption band peak, cm^{-1}	1023	1053

Immediately after deposition and heat treatment, the film weight was measured using an Oertling NA164 analytical balance with an accuracy of 10^{-4} g. This permitted us to calculate the density (ρ) of the SiO_x layers being studied.

The refractive index (n) and absorption factor (k) of the films were determined using multiple-angle measurements on an LÉF-3M laser ellipsometer with a wavelength of 632.8 nm. When calculating n and k values for the oxide films, the known values of optical constants for single-crystal Si were used [11].

Infrared (IR) transmission spectra were measured in the range of 800–1400 cm^{-1} using an IKS-25M automated spectrometer. An Si substrate without an oxide film was used as a reference sample. It is known that the main absorption band for SiO_x is within the aforementioned range and the position of the ν_M peak varies within the wavenumber range of 1000–1100 cm^{-1}. This band was deconvolved into Gaussian profiles, whose main characteristics, specifically, positions and intensities of peaks, were analyzed in the context of the random bonding model. The purpose of the analysis was to determine the content of $Si–O_y–Si_{4-y}$ ($1 \le y \le 4$) molecular complexes in the structural network of an SiO_x matrix according to the approach that was previously suggested by us [12–14]. The accuracy of deconvolution was characterized by the standard deviation of the Gaussian sum from the experimental curve. In our experiments, this deviation was no larger than 10^{-2}.

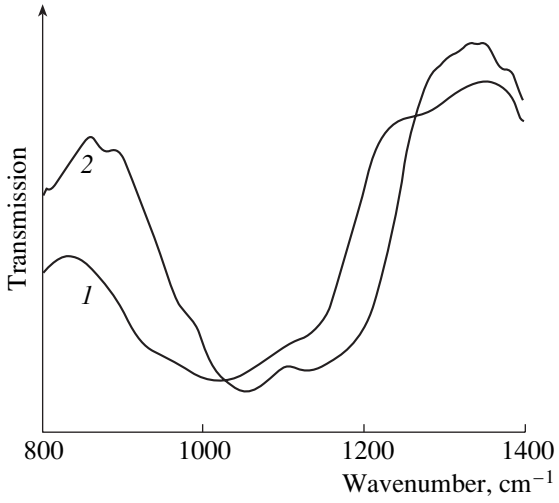

Fig. 1. Optical transmission spectra for (*1*) as-grown and (*2*) annealed SiO_x films.

The surface profile of the oxide films was investigated using a DI NanoScope IIIa atomic-force microscope. The measurements were carried out in periodic contact mode using CSG10 (NT-MDT) Si probes with an Au reflective coating. The nominal curvature of a probe tip was 10 nm. Prior to measurements, some samples were kept as long as 5 min in 1% HF solution in order to etch the SiO_2 phase.

3. RESULTS AND DISCUSSION

As-grown SiO_x films had characteristics (see Table 1) which correlated rather well with those obtained for this material in other studies [2, 3, 15]. Subsequent heat treatment in vacuum substantially affected all of the characteristics of the material. The thickness of the annealed films decreased by 7–9%, while their weight remained unchanged. The density attained after heat treatment was 2.09 g/cm^3. This value almost coincides with the results of calculation (2.1 g/cm^3) for SiO [16], as well as with the value 2.16 g/cm^3 [3] for the films deposited in rather high vacuum (5×10^{-6} Torr).

Figure 1 shows the transmission spectra of the as-grown and annealed SiO_x films. It can be seen that the fundamental-absorption band for the annealed oxide noticeably shifts to higher frequencies (see Table 1) and its area substantially increases. The former fact is usually attributed to variation in the phase composition of an oxide film [1, 3]. Moreover, using the position of the transmission-band peak ν_M and the known data on the ν_M dependence of x obtained for oxides grown using the same technology [3, 17], we can estimate the oxide composition. This estimation demonstrated that, for the SiO_x films investigated, $x \approx 1.25$ and 1.54 prior to and after heat treatment, respectively. Thus, during the thermal deposition of SiO_x films, atomizing SiO clusters are partially oxidized in an ambient of residual gases. Further variation in the phase composition of a film during heat treatment in vacuum proceeds due to the partial decomposition of silicon oxide into the Si and SiO_2 phases [1, 8]. This leads to an increase in the effective value of the stoichiometry index.

The characteristics of elementary Gaussian components, which were obtained by mathematical decomposition of the spectral curves of optical density for corresponding transmission bands, are given in Table 2. The main parameters of the components (their number, peak position, and full width at half maximum) almost coincide with those obtained previously for SiO_x films deposited by the CVD technique [12, 13], SiO_x layers obtained by ionic modification of SiO_2 [18], and for SIPOS films (semi-insulating polycrystalline oxygen-doped silicon) [19]. This coincidence, along with a detailed analysis of the uniqueness of the results of the mathematical deconvolution procedure for the spectra,

Table 2. Characteristics of elementary absorption bands for SiO_x films

Band	Peak position, cm^{-1}	Si–O–Si bond angle, deg	Mode	Origin	Area, arb. units	
					prior to heat treatment	after heat treatment
0	940			SiOH	18.0	6.7
1	995	115	TO	$SiOSi_3$	21.6	19.2
2	1033	127	TO	SiO_2Si_2	12.0	16.1
3	1067	136	TO	SiO_3Si	14.0	20.0
4	1100	145	TO	SiO_4	10.1	16.8
5	1145	115	LO	$SiOSi_3$	19.8	28.2
6	1205	126	LO	SiO_2Si_2	No Gaussian	24.0

which was carried out in these studies, suggests that the data we obtained are sufficiently credible. It can be seen from the results presented that the main absorption band for an oxide is mainly represented by the sum of four profiles. These profiles are related to transverse stretching vibrations of bridging O atoms which appear in the molecular complexes $Si–O_y–Si_{4-y}$ ($1 \le y \le 4$). The bands assigned to longitudinal stretching vibrations of the Si–O bond (bands 5 and 6) are related to the motion of the bridging O atoms. These atoms enter the same structural elements as the bands of transverse optical (TO) phonons 1 and 2, respectively. Heat treatment of the SiO_x layers leads to a substantial redistribution of the intensities of elementary bands. Consequently, the areas under the bands also vary (see Table 2). Specifically, the contribution of the band assigned to the $SiOSi_3$ complexes decreases. Alternatively, the fraction of vibrations determined by bridging O atoms, which appear in the SiO_3Si and SiO_4 complexes, increases. It is this fact that leads to the above-mentioned shift of the summary absorption band to higher frequencies. This may mean that heat treatment of SiO_x causes the decomposition of molecular complexes of lightly oxidized Si and the formation of both Si clusters and clusters containing heavily oxidized Si. A similar effect was previously observed for CVD-deposited SiO_x films [12, 13] and SIPOS films [19]. It seems likely that this effect is similar to the formation of O precipitates during heat treatment of single-crystal Si [20]. A substantial increase in the intensity of the bands of longitudinal optical (LO) phonons due to heat treatment was also observed previously [9, 10]. This effect may be associated with the heterogeneity of the annealed film due to the formation of phases of variable composition.

However, the aforementioned bands, which are associated with stretching vibrations of bridging O in an oscillating Si–O–Si "molecule", are insufficient to describe the lower-frequency wing of the main absorption band. An elementary 0 band, whose parameters coincide with those given in [21], is related to SiOH complexes. Their emergence in the as-grown SiO_x film is apparently caused by the presence of water vapors (or hydrogen) in residual gases or in SiO powder. A substantial decrease in the contribution of the relevant profile to the spectra of the annealed films is consistent with the results reported in [21]. According to [21], vanishing of the band at ~940 cm^{-1}, which is associated with the decomposition of SiOH groups, was observed due to heat treatment of silicon oxide layers for 1 h at 800°C.

A substantial (~30%) increase in the total area under the main absorption band of the SiO_x films due to heat treatment was mentioned above. This is indicative of an increase in the total number of oscillators, i.e., an increase in the concentration of bridging O atoms. A similar effect may arise from the formation of Si–O–Si bridges due to the completion of dangling bonds of Si and O, both of which initially existed in the as-grown oxide film and formed during the decomposition of the SiOH complexes. This conclusion is in good agreement with the measurements of the mechanical characteristics of the investigated films. According to these measurements, the as-grown SiO_x layer is characterized by a rather porous structure; i.e., there are numerous dangling Si and O bonds in the layer. To be sure, measurements of electron spin resonance demonstrated the presence of numerous P_b centers in similar samples [8].

The transformation of the surface relief of annealed SiO_x films is shown in Fig. 2. It can be seen that the roughness of the surface substantially decreases due to heat treatment.

The formation of clusters of heavily oxidized Si in the annealed SiO_x film, which was revealed in the course of an analysis of the shape of the IR spectra, can be seen upon treatment of the sample surface in hydrofluoric acid. A similar phenomenon was observed previously [13] for SiO_x films obtained using the CVD technology. For this purpose, we etched the surface of some films in 1% HF solution. The change in the surface nanorelief of an annealed sample due to subsequent etching is illustrated by Fig. 2c. It can be seen that the effect of the etchant on the surface of the annealed sample causes the roughness of the sample surface to increase substantially and even exceed the roughness of an as-

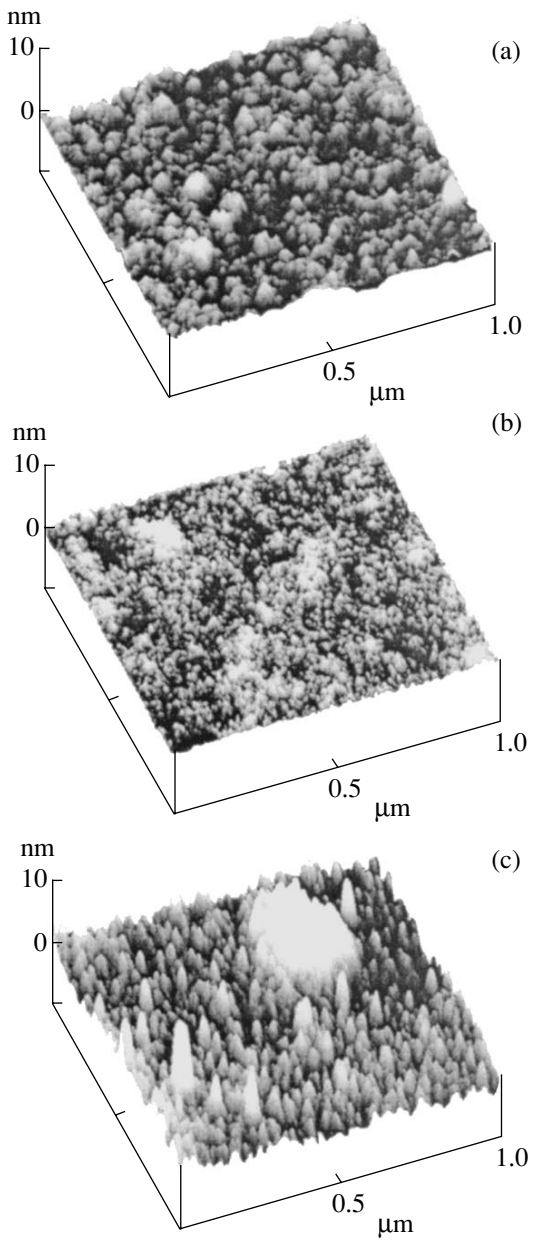

Fig. 2. Three-dimensional atomic-force microscopy images of the SiO_x film surface: (a) as-grown surface, (b) annealed surface, and (c) annealed surface after subsequent etching for 5 min.

grown film. Allowance should be made for the fact that a solution of hydrofluoric acid does not etch Si, while it slightly etches an oxide ($x < 2$), and etches SiO_2 well. In this context, the data presented clearly demonstrate the existence of phase reconstructions, which proceed at least at the surface of the SiO_x films upon heat treatment in vacuum and lead to the formation of SiO_2 inclusions.

Thus, summarizing the results obtained, we may conclude that the as-deposited $SiO_{1.25}$ films have a rather porous structure. This structure contains numerous dangling bonds, which are partially saturated with hydroxyl complexes, and a relatively high content of $SiOSi_3$ molecular clusters. Subsequent heat treatment in vacuum causes the escape of hydroxyl groups and the completion of dangling bonds of Si and O. Specifically, this leads to an increase in the concentration of O bridges in the structural network of an oxide. The oxide is compacted, and its surface relief is smoothened. Simultaneously, lightly oxidized molecular clusters, mainly $SiOSi_3$, start to lose oxygen and transform to $SiSi_4$ tetrahedra due to the formation of new Si–Si bonds. The interaction of released oxygen with heavily oxidized molecular clusters, for example, SiO_3Si, leads to their transformation into silicon–oxygen SiO_4 tetrahedra, thus increasing the number of SiO_2 molecules in the oxide film. Due to both processes, local precipitation of elemental Si and SiO_2 phases in an SiO_x matrix occurs.

Using the effective-medium model, we calculated the optical constants (n and k) of annealed SiO_x films. We assumed that the annealed films consisted of three phases: an SiO_x matrix, as well as SiO_2 and Si inclusions localized in the matrix. For this case, the Maxwell–Garnett formula can be written as [22]

$$(\varepsilon - \varepsilon_1)/(\varepsilon + 2\varepsilon_1) = f_2(\varepsilon_2 - \varepsilon_1)/(\varepsilon_2 + 2\varepsilon_1) + f_3(\varepsilon_3 - \varepsilon_1)/(\varepsilon_3 + 2\varepsilon_1), \quad (1)$$

where ε, ε_1, ε_2, and ε_3 are complex dielectric constants ($\varepsilon_i = (n_i + ik_i)^2$) of the $SiO_x/SiO_2/Si$ composite, SiO_x matrix, and SiO_2 and Si inclusions, respectively; and f_1, f_2, and f_3 are the volume fractions of these phases.

Performing simple transformations, we obtain

$$\varepsilon = \varepsilon_1(1 + 2A)/(1 - A), \quad (2)$$

where $A = f_3[a(\varepsilon_2 - \varepsilon_1)/(\varepsilon_2 + 2\varepsilon_1) + (\varepsilon_3 - \varepsilon_1)/(\varepsilon_3 + 2\varepsilon_1)]$, and $a = f_2/f_3$.

Expression (2) was used to calculate dependences of the indices of refraction and absorption of the three-phase composite on the volume fraction of the formed Si inclusions. In carrying out the calculations, the following circumstances were taken into account.

First, the $a = f_2/f_3$ quantity depends heavily on the composition of the as-grown SiO_x film, i.e., on the value of x. However, this quantity can be easily estimated in each particular case. Specifically, in the case under consideration ($x \approx 1.25$), the complete decomposition of the oxide into SiO_2 and Si phases is described by the equation

$$2SiO_{1.25} \longrightarrow 1.25SiO_2 + 0.75Si. \quad (3)$$

Since the SiO_2 and Si densities (2.217 and 2.328 g/cm^3, respectively [16]) differ slightly (within 10%), we may assume that the volumes of phases formed are proportional to the ratio of their masses. Using the known molecular weights of the components formed and taking into account the coefficients in the reaction

scheme (3), we can easily find the ratio of volumes of the SiO_2 and Si phases formed: $a \approx 3.75$.

Second, as long as there are no problems with the choice of optical constants of the vitreous SiO_2 phase and if the data in [23] are used ($n_2 \approx 1.46$, $k_2 \approx 0$ at a wavelength of 632.8 nm), optical constants for the Si inclusions depend substantially on both the structural state of Si and the size of inclusions mentioned. Because of this, the dependences $n(f_3)$ and $k(f_3)$ were calculated for three cases: (i) inclusions of crystalline Si (optical constants for single-crystal Si [11] were used), (ii) inclusions of amorphous Si (optical constants for amorphous Si films tens of nanometers thick [24] were used), and (iii) nanoinclusions of amorphous Si (optical constants for amorphous 1-nm-thick Si films [25] were used). The values of optical constants n_3 and k_3 for the Si phase are given in Table 3. The results of ellipsometric measurements carried out for as-grown (unannealed) samples were used to calculate the optical constants of the $SiO_{1.25}$ matrix (Table 1).

The results are shown in Fig. 3. The index of refraction for the annealed sample was obtained from the ellipsometric measurements and equaled $n = 1.9$. It follows from Fig. 3 that there are no possible f_3 values ($0\% \le f_3 \le 21.1\%$) that fit the calculated dependences $n(f_3)$ for the films with amorphous Si inclusions (Fig. 3a, curve *2*). Agreement between the experiment and calculations is possible for the composite with inclusions of crystalline Si (Fig. 3a, curve *1*) and nanoinclusions of amorphous Si (Fig. 3a, curve *3*). For crystalline inclusions, the value $n = 1.9$ is reached for the volume fraction of inclusions $f_3 = 18.2\%$. In this case, the volume fractions of SiO_2 and $SiO_{1.25}$ are 68 and 13.8%, respectively. The averaged compositions of the matrix in such Si/SiO_y composite corresponds to $y = (1.84 \pm 0.09)$. This value is substantially higher than the O content, which was obtained from the composition dependence of the IR-absorption band peak ($y = 1.54$). In addition, with the formation of crystalline inclusions, the effective absorption index for the composite should decrease (Fig. 3b, curve *1*) as its experimental value somewhat increases (Table 1).

In the case of amorphous Si nanoinclusions in an annealed sample, agreement with the experiment is attained for volume fractions of the Si, SiO_2, and $SiO_{1.25}$ phases equal to 6.8, 25.3, and 67.9%, respectively. In this case, the average O content in the $SiO_2/SiO_{1.25}$ matrix is $y = (1.43 \pm 0.06)$, which is rather close to the estimation of the matrix composition from the position of the IR band. The effective absorption index for the sample with such a composition is 2.2×10^{-2}; i.e., it exceeds the experimentally observed value by a factor of 2.4 (Table 1). This distinction can be attributed to the fact that the optical characteristics of thin Si layers were used in the calculation of the effective absorption index. At the same time, the inclusions formed during heat treatment are small clusters in which the fraction of surface atoms substantially exceeds the fraction of such atoms in the film. The formation of Si–O bonds on the cluster surface leads to a decrease in the effective absorption index in such clusters compared with that in the film. Similar effects were also observed for other structures. For example, for chalcogenide glass nanoparticles ~1–2 nm in size, the absorption index in the edge band-to-band transition region was substantially smaller (by a factor of 2–4) than in the film of the same glass [26].

Table 3. Optical constants for Si inclusions

Type of Si phase	n_3	k_3	References
c-Si	3.88	0.019	[11]
a-Si, film ~ 60 nm	4.20	0.41	[24]
a-Si, film ~ 1 nm	2.50	0.30	[25]

Thus, the best agreement between the calculated effective optical parameters of an annealed film and the measured characteristics can be attained if the optical constants for the Si inclusions are used as the parameters for the nanometer amorphous film. This circumstance is in agreement with previous experimental data [8], which indicate an amorphous structure of the Si

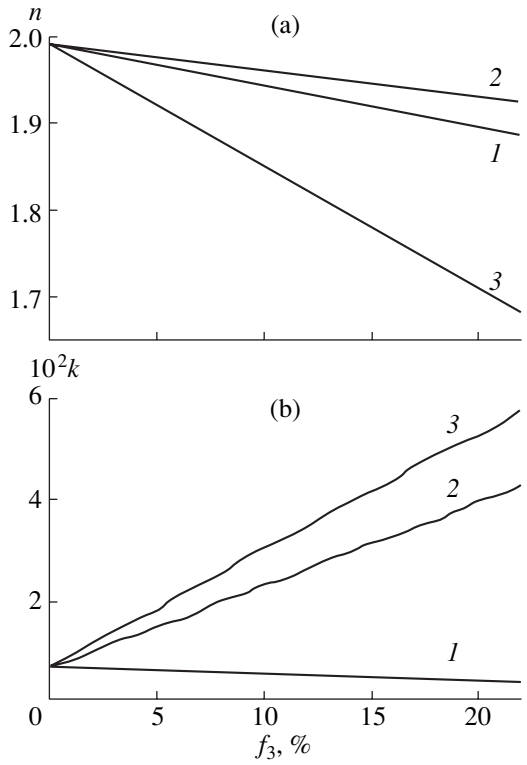

Fig. 3. Calculated (a) indexes of refraction *n* and (b) absorption indexes *k* at a wavelength of 632.8 nm for the three-phase $SiO_x/SiO_2/Si$ composite versus the volume fraction of Si inclusions of various types. See the text for details.

nanoinclusions formed as a result of heat treatment under similar conditions.

4. CONCLUSION

Heat treatment of SiO_x film deposited by thermal evaporation profoundly affects the physical properties of the film; this is associated with structural changes. Specifically, the density and absorption increase, while the refraction index decreases. We analyzed specific features of thermally stimulated variations of the IR spectra and simulated effective optical constants of annealed films. The results suggest that dangling bonds of Si and O are completed due to heat treatment. This refers both to dangling bonds that already existed in the as-grown oxide film and to those formed upon the decomposition of SiOH complexes, which leads to the compaction of the layer. In addition, molecular complexes of lightly oxidized Si also decompose and phases which contain heavily oxidized Si and amorphous Si nanoclusters are formed.

ACKNOWLEDGMENTS

We thank V.G. Litovchenko for his helpful participation in discussions.

REFERENCES

1. K. Hubner, Phys. Status Solidi A **61**, 665 (1980).
2. A. L. Shabalov and M. S. Feldman, Thin Solid Films **110**, 215 (1983).
3. M. Nakamura, Y. Mochizuki, K. Usami, *et al.*, Solid State Commun. **50**, 1079 (1984).
4. F. Rochet, G. Dudour, H. Roulet, *et al.*, Phys. Rev. B **37**, 6468 (1988).
5. G. Hollinger, Y. Jugnet, and T. M. Duc, Solid State Commun. **22**, 277 (1977).
6. F. N. Timofeev, A. Aidinli, Sh. Syuzar, *et al.*, Pis'ma Zh. Tekh. Fiz. **20**, 79 (1994) [Tech. Phys. Lett. **20**, 599 (1994)].
7. T. Inokuma, Y. Wakayama, T. Muramoto, *et al.*, J. Appl. Phys. **83**, 2228 (1998).
8. V. Ya. Bratus', V. A. Yukhimchuk, L. I. Berezhinskiĭ, *et al.*, Fiz. Tekh. Poluprovodn. (St. Petersburg) **35**, 854 (2001) [Semiconductors **35**, 821 (2001)].
9. L. I. Berezhinskiĭ, N. V. Sopinskiĭ, and V. S. Khomchenko, Zh. Prikl. Spektrosk. **68**, 103 (2001).
10. H. Rinnert, M. Vergant, and A. Burneau, J. Appl. Phys. **89**, 237 (2001).
11. D. F. Edwards, in *Handbook of Optical Constants of Solids*, Ed. by E. D. Palik (Academic, Orlando, 1985), p. 547.
12. I. P. Lisovskyy, V. G. Litovchenko, V. B. Lozinsii, *et al.*, J. Non-Cryst. Solids **187**, 91 (1995).
13. I. P. Lisovskiĭ, Ukr. Fiz. Zh. **43**, 949 (1998).
14. G. P. Romanova, V. G. Litovchenko, A. A. Efremov, *et al.*, in *Proceedings of 10th International Conference on SIMS-X, Münster, Germany, 1995*, p. 701.
15. A. Cachard, J. A. Roger, J. Pivot, and C. H. S. Dupuy, Phys. Status Solidi A **5**, 637 (1971).
16. W. Y. Ching, Phys. Rev. B **26**, 6610 (1982).
17. A. L. Shabalov, M. S. Fel'dman, and M. Z. Bashirov, Izv. Akad. Nauk Az. SSR, No. 3, 78 (1986).
18. I. P. Lisovskyy, V. G. Litovchenko, V. B. Lozinskii, *et al.*, Thin Solid Films **247**, 264 (1994).
19. I. P. Lisovskyy, V. G. Litovchenko, B. M. Gnennyy, *et al.*, Phys. Low-Dimens. Struct. **7/8**, 113 (2001).
20. A. Borghesi, B. Pivak, A. Sassella, and A. Stella, J. Appl. Phys. **77**, 4169 (1995).
21. V. A. Skryshevskiĭ and V. P. Tolstoĭ, *Infrared Spectroscopy of Semiconductor Structures* (Lybid', Kiev, 1991).
22. R. J. Becker, J. Appl. Phys. **61**, 1123 (1987).
23. V. I. Gavrilenko, A. M. Grekhov, D. V. Korbutyak, and V. G. Litovchenko, *Optical Properties of Semiconductors: a Handbook* (Naukova Dumka, Kiev, 1987).
24. H. Piller, in *Handbook of Optical Constants of Solids*, Ed. by E. D. Palik (Academic, Orlando, 1985), p. 571.
25. I. Bloomer and J. Lam, Data Storage **8**, 18 (2001).
26. I. Z. Indutnyy, P. E. Shepelyavyy, and Yu. P. Dotsenko, Ukr. Fiz. Zh. **44**, 1261 (1999).

Translated by N. Korovin